Topological Floquet states, artificial gauge fields in strongly correlated quantum fluids

Kirill Plekhanov

université PARIS-SACLAY

NNT: 2018SACLS264

Thèse de doctorat

Topological Floquet states, artificial gauge fields in strongly correlated quantum fluids

Thèse de doctorat de l'Université Paris-Saclay
préparée à l'Université Paris-Sud,
Laboratoire de Physique Théorique et Modèles Statistiques et
l'Ecole Polytechnique, Centre de Physique Théorique

École doctorale n° 564 Physique en Île-de-France
Spécialité de doctorat: Physique

Thèse présentée et soutenue à Orsay, le 7 septembre 2018, par

M. Kirill Plekhanov

Composition du Jury:

M. Nicolas Regnault Professeur — École Normale Supérieure, Laboratoire Pierre Aigrain	Président du Jury
M. Nathan Goldman Professeur — Université libre de Bruxelles, Physics of Complex Systems (CENOLI)	Rapporteur
M. Titus Neupert Professeur Associé — Universität Zürich, Institut für Theoretische Physik	Rapporteur
M. Mark Oliver Goerbig Directeur de Recherche — Université Paris-Sud, Laboratoire de Physique des Solides	Examinateur
M. Walter Hofstetter Professeur — Goethe-Universität Frankfurt, Institut für Theoretische Physik	Examinateur
M. Guido Pupillo Professeur — Université de Strasbourg, Institut de Science et d'Ingénierie Supramoléculaires	Examinateur
Mme Karyn Le Hur Directrice de Recherche — Ecole Polytechnique, Centre de Physique Théorique	Directrice de thèse
M. Guillaume Roux Maître de Conférences — Université Paris-Sud, Laboratoire de Physique Théorique et Modèles Statistiques	Directeur de thèse

– What're quantum mechanics?
– I don't know. People who repair quantums, I suppose.

Terry Pratchett

Acknowledgements

First and foremost, I would like to thank my thesis supervisors: Guillaume Roux and Karyn Le Hur. During these three years I had a great opportunity to learn from them and work on extremely interesting projects. Our numerous discussions were crucial for forming my current worldview, and I am proud to be their student.

I am also very grateful to the reviewers of my thesis Nathan Goldman and Titus Neupert, as well as the Jury members Mark Oliver Goerbig, Walter Hofstetter, Guido Pupillo, and Nicolas Regnault. I am thankful that they had time to attend my PhD defense, read very carefully the manuscript to evaluate my work and participate in our mini-workshop. I appreciated very much the question session that followed the defense, the discussions, and the talks of the mini-workshop.

During my PhD I had an opportunity to visit several other laboratories and discuss about the physics with brilliant scientists. Such discussions were enlightening to me and allowed to see what other people are interested in, learn new techniques and explore different approaches of doing science. In this context, I would like to particularly thank Ivana Vasic and Walter Hofstetter for taking part in a challenging yet enjoyable collaborative project we worked on together. I also appreciated very much the discussions with Hans Peter Buchler, Piers Coleman, Antoine Georges, Steven Girvin, Leonid Glazman, Jelena Klinovaja, Daniel Loss and Lode Pollet, as well as during my visit of the Stewart Blusson Quantum Matter Institute, on the CIFAR conferences, and FOR 2414 DFG meetings. Finally, I am very grateful to Eugene Bogomolny and Gregoire Misguich for playing a crucial role in my PhD and following my progress as a parrain and a tutor.

My PhD time was shared between two laboratories: the LPTMS and the CPHT. I would like to thank very much their directors: Emanuel Trizac, Jean-René Chazottes and Bernard Pire, and the administrative teams. Without their help this thesis would simply be impossible. I am also very proud to be a part of the student/postdoc equipes at LPTMS and CPHT. It was a pleasure to meet such wonderful people, share the same offices (yes, there are two of them), go for a lunch and enjoy the tea/coffee time (and not only) together. I am happy that I could spend a significant part of these three years with Aurelien, Ariane, Ines, Loïc Z. and Tal. Unfortunately, there was lesser time I could spend with you, Alex, Aleksey, Bertrand, Fan, Ivan, Loïc H., Luca, Matthieu, Nina, Samuel, Thibault B. and Thibault G., and with my friends outside of the labs: Camille, Félix, Marc, Marie, Paul, Shuwei and Thibault L.. But still I am glad that you were there.

Finally, my greatest thanks go to my parents for encouraging and supporting me.

Contents

Acknowledgements iii

Introduction 1

1 Condensed matter in the age of topological phase transitions 5
1.1 New look at the phase transitions . . . 6
1.1.1 Ginzburg-Landau paradigm of phase transitions . . . 6
1.1.2 Beyond Ginzburg-Landau theory . . . 7
1.2 Conventional band theory . . . 10
1.2.1 Block-diagonalization in the momentum space . . . 10
1.2.2 Bogoliubov transformations . . . 12
A. Fermions . . . 12
B. Bosons . . . 12
1.2.3 Interactions and approximations. BCS theory example . . . 13
1.3 Few words about topology . . . 14
1.3.1 A coffee cup or a doughnut? . . . 14
1.3.2 Relevant definitions . . . 15
A. Basics of topological spaces and manifolds . . . 15
B. Covectors, tensors and differential forms . . . 17
C. Parallel transport: connection and curvature . . . 18
D. Topological invariants . . . 20
1.3.3 Homotopy and cohomology . . . 21
A. Homotopy groups . . . 21
B. De Rham cohomology groups . . . 22
1.3.4 Basics of fibre bundles . . . 23
A. Fibre bundles in geometry and in physics . . . 23
B. Connection and curvature in fibre bundles . . . 25
C. Topology of fibre bundles . . . 27
1.4 Topological band theory . . . 29
1.4.1 Berry's connection and Berry's phase . . . 29
A. Adiabatic evolution argument . . . 29
B. Zak phase . . . 32
1.4.2 Berry's curvature and the first Chern number . . . 33
A. Definitions . . . 33
B. Many sides of the first Chern number through the examples 34
1.4.3 Topological phase transitions . . . 36
1.4.4 Symmetry protected topological states . . . 38
1.4.5 Bulk-boundary correspondence . . . 40
1.5 Role of topology in strongly correlated quantum systems . . . 41
1.5.1 Fractional quantum Hall states . . . 42
A. Laughlin states . . . 42
B. Generalizations . . . 43
1.5.2 Interacting SPT states and intrinsic topological order . . . 45

1.5.3 Frustrated quantum magnetism and spin liquids 46

2 Chiral phases of the Haldane Chern insulator **49**
2.1 Dirac materials and Chern insulators 50
2.1.1 Graphene as a Dirac material 51
2.1.2 Haldane model as a Chern insulator 53
A. Opening a gap at Dirac points 53
B. Topological phase transition 54
2.1.3 Anisotropy and generalizations of the Haldane model 57
2.2 Anisotropic Haldane model for bosons with interactions 57
2.2.1 Overview of the problem 59
2.2.2 Superfluid phases 60
A. Zero-momentum phase 60
B. Critical value of NNN hopping amplitude 62
C. Finite-momentum phase 64
D. Interaction effects 67
2.2.3 Excitation properties 69
2.2.4 Mott insulator phase 70
2.3 Interacting bosons on brickwall ladder geometry 72
2.3.1 Band structure in free case 73
2.3.2 Interactions and bosonization 74
A. Strong t_1 phase 76
B. Strong t_2 phase 77
2.3.3 Perspectives 78

3 Phases of the bosonic Kane-Mele Hubbard model **81**
3.1 Kane-Mele model and topological insulators 82
3.1.1 Introduction to the model and symmetries 83
3.1.2 $\mathbb{Z}_2$ topological invariant 85
3.1.3 Interactions in the Kane-Mele model 87
3.2 Bosonic Kane-Mele-Hubbard model 88
3.2.1 Overview of the problem 89
3.2.2 Mott – superfluid phase transitions 90
3.2.3 Mott phase and emergent magnetism 91
3.3 Effective frustrated spin-1/2 XY model 93
3.3.1 Classical phase diagram 94
3.3.2 Magnetically ordered states 95
A. Fidelity metric 96
B. Static structure factors 96
3.4 Disordered spin state 99
3.4.1 Chiral spin liquids 99
3.4.2 Chern-Simons field theory arguments 100
A. Jordan-Wigner transformation in 2D 100
B. Free fermionic problem 102
C. Physical interpretation 105
D. Explicitly broken symmetries 105
3.4.3 Chiral spin state 106
3.4.4 Laughlin's pump and topological order 109
A. Ground-state degeneracy 109
B. Twisted boundary conditions 110
C. Berry curvature and first Chern number 111

4 Quantum simulator engineering and probing exotic states of matter 113
4.1 Quantum simulators . . . 114
A. Ultra-cold atoms . . . 115
B. Photonic circuits . . . 115
4.2 Periodically driven systems . . . 116
4.2.1 Floquet theory . . . 116
A. Floquet Hamiltonian . . . 117
B. Effective Hamiltonian . . . 118
4.2.2 High-frequency approximations . . . 119
A. Magnus expansion . . . 120
B. Degenerate perturbative expansion . . . 120
4.2.3 The role of interactions . . . 121
4.3 Floquet engineering of artificial gauge fields . . . 121
4.3.1 Ultra-cold atoms . . . 122
4.3.2 Photonic lattices . . . 124
A. Magnetic fields under a resonance condition . . . 124
B. NNN hoppings using Floquet theory . . . 125
C. Higher order terms . . . 126
4.3.3 Numerical verification . . . 127
4.4 Dynamical probe of the Zak phase in the photonic SSH model . . . 131
4.4.1 SSH model . . . 131
4.4.2 Circuit model . . . 132
4.4.3 Measuring the Zak phase . . . 134
4.5 Purification spectroscopy protocol . . . 137
4.5.1 Purification spectroscopy . . . 137
A. Numerical simulations at finite temperature . . . 137
B. Purification spectroscopy . . . 138
C. Numerical verification . . . 139
4.5.2 Experimental proposal . . . 139
4.5.3 Fock state spectroscopy and many-body localization . . . 141

Conclusion and perspectives 143

A Numerical methods 145
A.1 Exact diagonalization . . . 146
A.1.1 Lanczos algorithm . . . 146
A.1.2 Davidson algorithm . . . 148
A.1.3 Basis states . . . 149
A.1.4 Symmetries . . . 149
A.1.5 Simple way to sample clusters . . . 151
A.2 Density matrix renormalization group . . . 152
A.2.1 Singular-value decomposition . . . 153
A.2.2 Matrix product states . . . 154
A.2.3 Matrix product operators . . . 157
A.2.4 DMRG in the MPS language . . . 157

B Chern-Simons field theory and fractional quantum Hall states 159
B.1 Chern-Simons field theory . . . 159
B.2 Quantum Hall effects . . . 160
B.2.1 Integer case and quantized Hall conductivity . . . 160
B.2.2 Fractional case and composite fermions . . . 160

B.3 Lattice approach: known solutions and difficulties 161

C Edge modes in Haldane Chern insulators **163**

D Anisotropic Haldane model for bosons: intermediate regime of the FM phase **167**

E Out-of plane classical solution of the frustrated spin-1/2 XY model **171**
E.1 Zero external magnetic field 171
E.2 Effect of the external magnetic field 172

F Résumé en français **173**
F.1 Introduction générale 173
F.2 Dans cette thèse 175

Bibliography **177**

Introduction

Since long time ago, a question that attracted a lot the attention of scientists was to classify different states of matter and the transitions between them. The theory developed in the middle of the 20th century, that had a great success in describing such phenomena, was called Ginzburg-Landau theory. It met a great success, allowing to understand the phase transitions in terms of symmetry groups, as well as classifying them according to different universality classes. However, with the discovery of the integer and fractional quantum Hall effects several decades ago, it was found that the Ginzburg-Landau description is not comprehensive. Understanding new states of matter, intractable by means of the Ginzburg-Landau theory in terms of symmetry groups, has been possible thanks to topology. Now one could definitely say that this discovery revolutionized the concept of phase transitions, giving birth to a completely new domain of condensed matter physics – the topological condensed matter.

Topology gave new insights both on the fundamental understanding of properties of quantum matter and for practical issues related to the questions of quantum computation and quantum information. This is because topological states of matter cannot be described in terms of local order parameters and are protected against perturbations and disorder. The effect of strong interactions in such systems could also lead to exotic many-body phenomena such as the formation of quasi-particles with anyonic statistics and fractional charges. The most famous examples of such quasi-particles are excitations in quantum spin liquids and fractional quantum Hall states, Majorana zero modes and parafermions. This fractionalization is also intrinsically related to the topological degeneracy of the ground-state depending on the genus of the physical space – a property known under the name of topological order.

However, the interplay between topology and many-body effects is far from being well understood. Moreover, experimental realizations of related systems are challenging. Often, models that have a simple / exact analytical solution are hard to implement in laboratories, *e.g.* as a result of peculiar interactions or complicated configurations of gauge fields. From another side, real materials or artificial systems (quantum simulators) cannot always be described in terms of simple / exactly solvable models. As a consequence, a further analytical investigation of such questions is required and new protocols should be designed in order to observe experimentally these exotic phenomena.

In this thesis, we address some of the above mentioned questions. In this respect, we use various analytical and numerical methods, while exploring different microscopical models and quantum simulator protocols. First, in Chapter 1 we make a short introduction to the main concepts of topological condensed matter. Next, in Chapters 2 and 3 we describe our work on analyzing the effect of interactions in condensed matter models with topological bands. Issues related to experimental realizations of such systems are addressed in Chapter 4. Below we provide a more detailed description of the thesis content.

In this thesis

Chapter 1 of this thesis is dedicated to a general introduction to topology in mathematics and condensed matter physics. Starting from an experimental discovery of the integer quantum Hall effect, which led to a breakthrough in the current understanding of condensed matter physics, we discuss first non-interacting and non-topological, then non-interacting and topological, and finally interacting and topological states of matter. Non-interacting topological systems we consider in the thesis correspond to one and two-dimensional symmetry protected topological states. Bulk properties of such systems are described by topological numbers, such as winding numbers or Chern numbers. Via the bulk-boundary correspondence, the bulk description is related to the presence of gapless boundary excitations robust against disorder – a property representing a huge interest in the domain of quantum information. The physics of such non-interacting topological states of matter is relatively well understood nowadays. However, the problem of classifying interacting many-body states still remains largely unresolved. This context provides a motivation for the remaining part of the thesis, which consists in understanding the interplay of topology and interactions in condensed matter systems.

In Chapter 2 we address the questions related to the properties of the Haldane mode. This is a model for non-interacting fermions defined on the honeycomb lattice, also known as a model for quantum anomalous Hall effect. Its bands are described by a non-vanishing value of a $\mathbb{Z}$ topological invariant – the first Chern number, associated with the presence of chiral edge modes in a system with boundaries. Starting from Section 2.2, following the work presented in Ref. [1] (publication 1 in the list at the end of this introduction), we present our study of the many-body properties of the Haldane model, that arise if instead of fermions we consider bosons with Bose-Hubbard interactions. We discuss the emergence of exotic finite-momentum superfluid phases, and construct a phase diagram of the model. We consider different geometries: a usual two-dimensional, but with an anisotropic configuration of hopping interactions, and a ladder one.

In Chapter 3 we consider the bosonic Kane-Mele-Hubbard model. The Kane-Mele model for fermions is known as a model for quantum spin Hall effect. It can be understood as two copies of the two-dimensional Haldane model for fermions, arranged in such a way that the $\mathbb{Z}$ topological invariant is reduced to a new $\mathbb{Z}_2$ topological invariant. The change in the bulk description is also accompanied by a vanishing of chiral edge modes and the emergence of new helical edge modes. In this chapter, after making a quick introduction to the single-particle case, we present our exploration of the effect of interactions. As previously, instead of fermions we consider interacting bosons. We show that the regime of strong interactions of the resulting model leads to the emergence of an effective frustrated spin-1/2 XY model. This model has a very rich phase diagram with a variety of symmetry broken spin states. One of such spin states has been a candidate for the chiral spin liquid of Kalmeyer and Laughlin, hosting exotic anyonic excitations. Starting from Section 3.3, we explore in details the magnetic properties of the frustrated XY model, by looking especially for magnetically disordered spin liquid states with topological order. The results presented in this Chapter have been already presented in Ref. [2] (publication 2 in the list).

In the first part of Chapter 4 we present our work on the quantum simulator protocols, that could be used to realize the systems of Chapters 2 and 3. These protocols require a generation of artificial gauge fields, achievable through the application of periodic time-dependent modulations. This procedure, known under the name of Floquet engineering, has got a lot of attention recently. After giving an introduction to the domain of Floquet engineering and an overview of the approach, that has been recently applied for ultra-cold atoms, we describe in Section 4.3 our proposal to use periodic time-dependent modulations to generate artificial gauge fields for excitations in photonic lattices. This approach has been described previously in Refs. [1] and [3] (publications 1 and 3 in the list).

In last two sections of Chapter 4, we consider in greater details two experimental protocols to explore quantum systems. First, following Ref. [4] (publication 4 in the list), we propose an approach to realize the Su-Schrieffer-Heeger model with *LC* circuits. We also describe a way to measure its topology, encoded in the winding number of Berry's phase. Second, following Ref. [5] (publication 5 in the list), we propose a purification protocol to measure the spectral properties of quantum systems. It consists in making two copies of the same system and measuring the outcome of a quench (*i.e.* an abrupt time evolution of the system after a sudden change of parameters, or starting from a particularly prepared initial state). This method has an advantage of being applicable not only in the experimental context, but also for numerical simulations, if systems of sufficiently large sizes can be handled.

Thesis publications

1. *Floquet Engineering of Haldane Chern insulators and Chiral bosonic phase transitions.*
Kirill Plekhanov, Guillaume Roux, Karyn Le Hur.
Article. Phys. Rev. B 95, 045102 (2017); arXiv:1512.06442.

2. *Emergent Chiral spin state in the Mott phase of a bosonic Kane-Mele-Hubbard model.*
Kirill Plekhanov, Ivana Vasić, Alexandru Petrescu, Rajbir Nirwan, Guillaume Roux, Walter Hofstetter, Karyn Le Hur.
Article. Phys. Rev. Lett. 120, 157201 (2018); arXiv:1707.07037.

3. *Many-Body Quantum Electrodynamics Networks : Non-Equilibrium Condensed Matter Physics with Light.*
Karyn Le Hur, Loïc Henriet, Alexandru Petrescu, Kirill Plekhanov, Guillaume Roux, Marco Schiró.
Review. C. R. Physique (2016) 808-835; arXiv:1505.00167.

4. *Topological Zak phase in strongly coupled LC circuits.*
Tal Goren, Kirill Plekhanov, Félicien Appas, Karyn Le Hur.
Article. Phys. Rev. B Rapid. Comm. 97, 041106 (2017); arXiv:1711.02034.

5. *Purification spectroscopy.*
Bradraj Pandey, Kirill Plekhanov, Guillaume Roux.
Article. Submitted to Phys. Rev. Lett.; arXiv:1802.04638.

6. *Driven dissipative dynamics and topology of quantum impurity systems.*
Karyn Le Hur, Loïc Henriet, Loïc Herviou, Kirill Plekhanov, Alexandru Petrescu, Tal Goren, Marco Schiro, Christophe Mora, Peter P. Orth.
Review. C. R. Physique (2018) 1631-0705; arXiv:1702.05135.

Chapter 1

Condensed matter in the age of topological phase transitions

The main goal of this chapter is to provide a general introduction to the recently developed concept of topological phase transitions in condensed matter physics. First, in Section 1.1 we give a rapid historical overview of how the topological aspects have become so popular and what are the most striking experimental discoveries that gave birth to the domain. Second, in Section 1.2 we make a short reminder of the conventional band theory. This section will mainly serve to us as a way to fix the notation and define some transformations and approaches, that we will use several times throughout the work. Then, in Section 1.3 we make an introduction to topology. We define some precise, rather mathematical notions, but do not go into details of technical proofs. This section will allow us to better understand the meaning of mathematical objects used in physical calculations, such as the connection and curvature on fibre bundles and Chern classes. Next, in Section 1.4 we provide a connection between topology and physics, showing how some concepts introduced in the previous section naturally arise in the real world problems. All the content of this section concerns only single-particle problems, relatively well understood at this current stage. In particular, we briefly discuss some general considerations allowing to classify all non-interacting states of matter. Several models appearing in this section will be considered in greater details in the following chapters, either in the context of perspective experimental realizations, or as a platform to study many-body effects. Finally, in Section 1.5 we outline the main problems that arise today, which consist in classifying the many-body topological states of matter. We show, why this problem is hard to solve, and mention some known results. We also discuss the main directions of the ongoing research and the connection between them. This section will serve to us as a motivation for the studies presented in the remaining chapters of the thesis.

Contents of the chapter

1.1 New look at the phase transitions 6
1.1.1 Ginzburg-Landau paradigm of phase transitions 6
1.1.2 Beyond Ginzburg-Landau theory 7
1.2 Conventional band theory 10
1.2.1 Block-diagonalization in the momentum space 10
1.2.2 Bogoliubov transformations 12
A. Fermions 12
B. Bosons 12
1.2.3 Interactions and approximations. BCS theory example 13

1.3 Few words about topology . . . 14
1.3.1 A coffee cup or a doughnut? . . . 14
1.3.2 Relevant definitions . . . 15
A. Basics of topological spaces and manifolds . . . 15
B. Covectors, tensors and differential forms . . . 17
C. Parallel transport: connection and curvature . . . 18
D. Topological invariants . . . 20
1.3.3 Homotopy and cohomology . . . 21
A. Homotopy groups . . . 21
B. De Rham cohomology groups . . . 22
1.3.4 Basics of fibre bundles . . . 23
A. Fibre bundles in geometry and in physics . . . 23
B. Connection and curvature in fibre bundles . . . 25
C. Topology of fibre bundles . . . 27
1.4 Topological band theory . . . 29
1.4.1 Berry's connection and Berry's phase . . . 29
A. Adiabatic evolution argument . . . 29
B. Zak phase . . . 32
1.4.2 Berry's curvature and the first Chern number . . . 33
A. Definitions . . . 33
B. Many sides of the first Chern number through the examples 34
1.4.3 Topological phase transitions . . . 36
1.4.4 Symmetry protected topological states . . . 38
1.4.5 Bulk-boundary correspondence . . . 40
1.5 Role of topology in strongly correlated quantum systems . . . 41
1.5.1 Fractional quantum Hall states . . . 42
A. Laughlin states . . . 42
B. Generalizations . . . 43
1.5.2 Interacting SPT states and intrinsic topological order . . . 45
1.5.3 Frustrated quantum magnetism and spin liquids . . . 46

1.1 New look at the phase transitions

1.1.1 Ginzburg-Landau paradigm of phase transitions

For several decades the central idea in the theory of phase transitions was formulated in the context of a Ginzburg-Landau paradigm. It relies on the concept of an order parameter and a closely related notion of spontaneous symmetry breaking. It consists in the following: suppose that we have two phases. Transition from one phase to another occurs at a critical point either as a function of the temperature T, or as a function of some parameter p of the Hamiltonian, which interpolates between two non-commuting terms

$$H = H_1 + pH_2, \quad [H_1, H_2] \neq 0 \,. \tag{1.1}$$

In the following we will refer to the first situation as a classical phase transition, and to the second situation as a quantum phase transition. Two different phases have to be distinct from the point of view of symmetries describing the system. One of the phases is then called an ordered phase, and another – a disordered phase. As the names imply, the disordered phase is described by a larger symmetry group, and the ordered phase – by a smaller one. For example, in the liquid-solid phase

transition the disordered liquid phase is described by a continuous symmetry group of translations in the real space, while the ordered solid phase is described only by a discrete group of lattice translations. Another example is ferromagnetism: above the Curie temperature the system has a continuous spin rotation symmetry (all spins are disordered), which is broken to a discrete spin-inversion symmetry (all spins are aligned). We thus see that at the critical point the larger symmetry group associated with the disordered phase is broken into its smaller counterpart associated with the ordered phase. The order parameter quantifies the amount of such symmetry breaking. In particular, it must vanish in the disordered phase and acquires a non-zero value in the ordered regime.

The physical origin is different in the classical and quantum phase transitions. In the case of a classical phase transition, the macroscopic order (such as a crystal structure of a solid or alignment of spins in a magnet) is destroyed by thermal fluctuations, while in quantum phase transitions, the order is destroyed solely by quantum fluctuations originating from the Heisenberg uncertainty principle. However, the same phenomenological approach could be used to understand the phase transition in both cases. In fact, even though the order parameter is zero in the disordered phase, its fluctuations can be non-zero. When approaching the critical point, the correlation length of such fluctuations diverges, implying the scale-invariance of the system. Some universal parameters (critical exponents) emerge then, describing how fast the divergence occurs. This behavior establishes the critical properties of the system. A remarkable fact consists in the universality of such phenomena: the critical behavior is determined only by the symmetries of the order parameter and the space dimension of the system, and defines the so-called universality class. Even more remarkably however, during the last few decades, theoretical investigations and experimental developments have shown that several phase transitions are not straightforwardly related to the question of symmetries, and are hence situated beyond the Ginzburg-Landau paradigm. In order to understand some of such phases one needs to explore the topology of the system, and the associated phase transition are then called **topological phase transitions**.

1.1.2 Beyond Ginzburg-Landau theory

The first theoretical result indicating that the physical properties of some systems cannot be described by the spontaneous symmetry breaking paradigm, was found in the seminal independent works by Berezinskii [6, 7], Kosterlitz and Thouless [8]. They studied the two-dimensional XY model. According to Mermin-Wagner theorem [9, 10], there cannot be a spontaneous breaking of a continuous symmetry at finite temperature in systems with sufficiently short-range interactions in dimensions $d \leq 2$. Nevertheless, the authors have shown that a phase transition still occurs in the XY model, but has a very different nature. The low-temperature phase in this model corresponds to a regime with bound topological excitations – vortex-antivortex pairs. The high-temperature phase in its turn corresponds to the phase where the vortices and antivortices become free.

Another important work, giving also a first experimental motivation to explore the questions of topology, was the discovery of the integer (IQHE) and fractional (FQHE) quantum Hall effects [11, 12]. The experimental setup of the quantum Hall effect is schematically shown in Fig. 1.1(a). It comprises a 2D electron gas subjected to a strong magnetic field. Because of the effect of the magnetic field, the circular trajectory of electrons is quantized, which leads to the formation of highly degenerate

Landau levels at energy $\epsilon_n = \hbar\omega_c(n + 1/2)$, with $\omega_c = eB/m$ – the cyclotron frequency, B – the strength of the magnetic field, and e and m – respectively the charge and the mass of the electron. Such quantization effect occurs at low temperatures, when thermal energy is much smaller than the spacing between different Landau levels. The number of states N_B in each Landau level is equal to the ratio of the total flux Φ piercing the sample to the flux quantum $\Phi_0 = h/e$ (h being the Planck constant)

$$N_B = \Phi/\Phi_0 \,. \tag{1.2}$$

N_B is thus the total number of flux quanta in the system. Because of the disorder, necessarily present in a real experimental sample, each Landau level has a finite width, as shown in Fig. 1.1(b). Naively, one would expect that such system would describe either a conductor, when the chemical potential lies exactly inside one of the Landau levels, or an insulator, when the chemical potential lies in the gap between them. This occurs to be almost true, in the sense that such behaviour is observed, but only regarding the usual longitudinal conductivity of the sample. When the transversal (Hall) conductivity is considered however, a surprising effect appears: the Hall conductivity σ_{xy} (the inverse of the Hall resistance R_H) does not vanish, changes by plateaus and takes perfectly quantized values

$$\sigma_{xy} = 1/R_H = \nu e^2/h \,. \tag{1.3}$$

Here the constant $\nu = N/N_B$ is the filling factor (N is the number of particles), which can take either integer $\nu \in \mathbb{Z}$ or fractional values $\nu \in \mathbb{Q}$. In the first case an integer number of Landau levels is occupied and the observed effect corresponds to the IQHE. In the second case a fraction of the Landau level (usually the lowest one) is occupied and one speaks about the FQHE. The result of such an experimental measurement from the work by Eisenstein and Stormer [13] is shown in Fig. 1.1(c).

The first theoretical understanding of the quantum Hall conductivity and its strikingly perfect quantization was obtained by Laughlin, based on a gedanken topological pump argument [14]. Here we want to briefly explain this argument, presented in a slightly modified form, following Ref. [15]. Let us imagine a quantum Hall experiment performed on a Corbino disk (Fig. 1.1(d)). We apply a tangential electric field $E(r,t)$ to such system, by changing the magnetic flux $\Phi(t)$ piercing the disk through the hole in its center

$$E(r,t) = \partial_t\Phi(t)/(2\pi r) \,. \tag{1.4}$$

Here r is the distance to the disk center. The transverse Hall conductivity thus becomes

$$\sigma_{xy} = J/E(r,t) = I/\partial_t\Phi(t) \,. \tag{1.5}$$

Here $I = 2\pi r J$ is the radial current, and J is the current density. We change the magnetic flux cyclically by pumping a quantum flux $\Delta\Phi = \Phi_0$ over the period of time ΔT. The charge transferred in such a way will be

$$\Delta Q = I\Delta T = \sigma_{xy}\, h/e \,. \tag{1.6}$$

After several full cycles the flux is equal to an integer times the flux quantum $\Phi(\nu\Delta T) = \nu\Phi_0$. Hence, the system, at this moment, cannot be distinguished from the starting state $\Phi(0) = 0$: the spectrum and the wavefunctions of the electrons have to remain the same. The assignments of an energy to an eigenstate may however have been interchanged. We conclude thus that only an integer number of charges can be

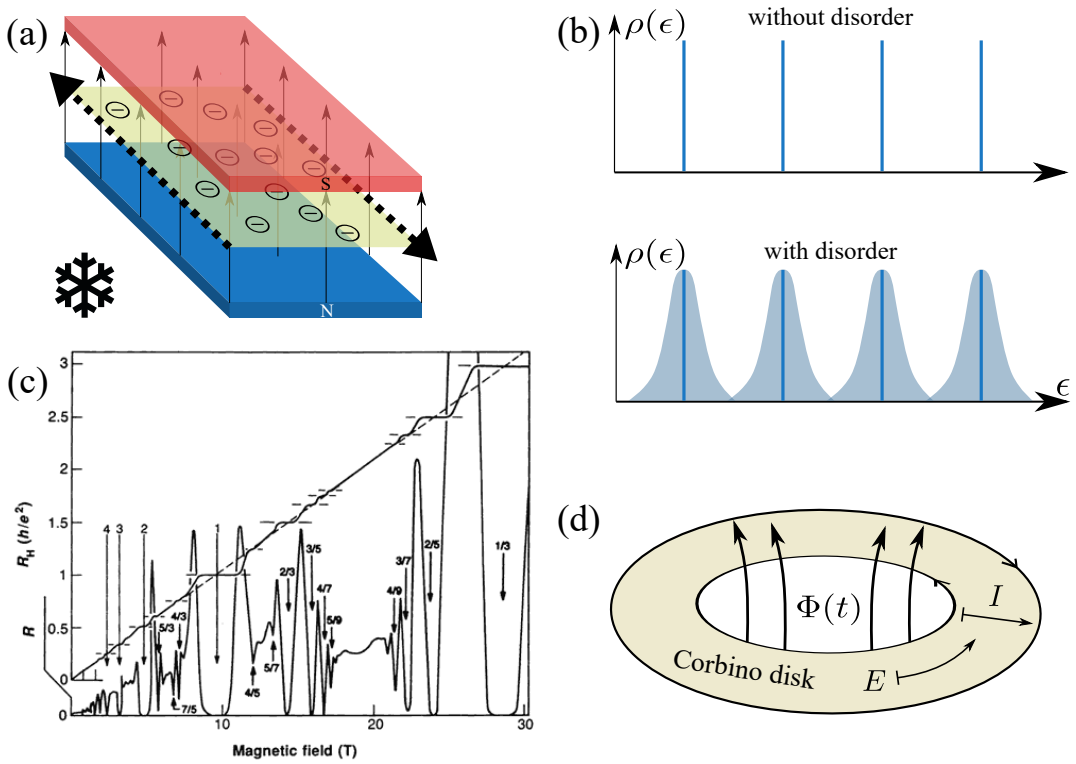

FIGURE 1.1: Quantum Hall effect. **(a)** Experimental setup which comprises a two-dimensional electron system at a very low temperature, under a strong applied external magnetic field. **(b)** Application of the strong magnetic field leads to the quantisation of the cyclotron radius, leading to the emergence of highly degenerate Landau levels. In the perfect scenario such Landau levels would lead to a Dirac comb-like energy distribution $\rho(\epsilon)$. When the disorder is taken into account, the energy distribution of Landau levels acquires a finite width. **(c)** When the temperature is much smaller than the spacing between different Landau levels, we observe the quantum Hall effect, *i.e.* the formation of plateaus with vanishing longitudinal conductivity and quantized Hall conductivity along the boundaries of the sample: $\sigma_{xy} = 1/R_H = \nu e^2/h$. For the integer quantum Hall effect the plateaux appear at integer values of the quantization constant ($\nu \in \mathbb{Z}$), while for the fractional quantum Hall effect the constant is fractional ($\nu \in \mathbb{Q}$). The experimental results shown here are taken from Eisenstein and Stormer [13]. **(d)** The Corbino disk geometry used to prove the quantization of the Hall conductivity using the Laughlin's pump argument in the main text.

pumped between the edges: $\nu \in \mathbb{Z}$. By making a substitution into the above equation, we deduce that the quantum Hall conductivity has to be quantized following the Eq. (1.3), with an integer ν. In the original Laughlin's argument, a cylinder is used instead of the Corbino disk, in order to take into account the periodic boundary conditions, but the argument remains exactly the same.

In the following sections of this chapter, we will present in greater details the mathematical and physical arguments which lie behind the observation of the quantum Hall effect. We will show a precise mathematical meaning of the topological invariant ν, which appear in the expression of the integer quantum Hall conductivity, in Sections 1.3 and 1.4. We will also say few words about the generalizations of such topological invariant and a more elaborate description of the topological states of matter, which has been developed since the discovery of the quantum Hall effects, and led to the development of new notions, such as Chern and topological insulators, symmetry protected topological states, etc. We also notice that we have not said anything about the FQHE, and how the value of ν can become fractional. While the physics of the IQHE can be understood at a single-particle level, taking into account interactions is necessary to understand the FQHE. We will discuss this in more details in Section 1.5.

1.2 Conventional band theory

In this section we want to make a short introduction to the formalism used to describe the translation invariant tight-binding lattice models for non-interacting particles, *i.e.* in the cases when the Hamiltonian in the second quantization form is quadratic in creation and annihilation operators. Since the statistics of the particles does not play an important role at the single-particle level and does not affect the band-structure, at the beginning of this section we will not distinguish between bosons and fermions. The difference will however arise if we focus on the ground-state properties, in the way we perform the Bogoliubov transformation or, most importantly, if we take into account the effect of interactions and consider the many-body case, as in Section 1.5.

1.2.1 Block-diagonalization in the momentum space

For the beginning, let us consider a model defined on the Bravais lattice $\mathcal{L}$ generated by the set of linearly independent (primitive) vectors $\{\boldsymbol{R}_i\}$. Any Bravais lattice site $\boldsymbol{r}_j$ which belongs to $\mathcal{L}$ can be expressed as

$$\boldsymbol{r}_j = \sum_i m_i(\boldsymbol{r}_j)\boldsymbol{R}_i, \quad m_i(\boldsymbol{r}_j) \in \mathbb{Z}\,. \tag{1.7}$$

We also assume that the total number of unit cells in $\mathcal{L}$ equals N_c. The most generic second-quantized tight-binding Hamiltonian describing the non-interacting model defined on the lattice $\mathcal{L}$ has the following form

$$H = \sum_{\boldsymbol{r}_i \in \mathcal{L},\sigma} \mu_{\sigma,\boldsymbol{r}_i} c^\dagger_{\sigma,\boldsymbol{r}_i} c_{\sigma,\boldsymbol{r}_i} + \sum_{\boldsymbol{r}_i,\boldsymbol{r}_j \in \mathcal{L}^2,\sigma,\sigma'} \left(t^{\sigma\sigma'}_{\boldsymbol{r}_i\boldsymbol{r}_j} c^\dagger_{\sigma,\boldsymbol{r}_i} c_{\sigma',\boldsymbol{r}_j} + \Delta^{\sigma\sigma'}_{\boldsymbol{r}_i\boldsymbol{r}_j} c^\dagger_{\sigma,\boldsymbol{r}_i} c^\dagger_{\sigma',\boldsymbol{r}_j} + \Delta^{\sigma\sigma'\,*}_{\boldsymbol{r}_i\boldsymbol{r}_j} c_{\sigma,\boldsymbol{r}_i} c_{\sigma',\boldsymbol{r}_j} \right)\,, \tag{1.8}$$

where $c^\dagger_{\sigma,\boldsymbol{r}_i}(c_{\sigma,\boldsymbol{r}_i})$ is a creation (annihilation) operator of a particle of species σ on the Bravais lattice site $\boldsymbol{r}_i$. In this notation the specie σ could be used to describe a

fermionic spin, a bosonic specie (for example in a multi-component bose gas experiment) or an intra-cell position of a particle in the case of a multi-site unit cell (*i.e.* in the case of a honeycomb lattice the unit cell contains two inequivalent sites). The Hamiltonian comprises several terms. $\mu_{\sigma,\boldsymbol{r}_i}$ is the chemical potential term. $t^{\sigma\sigma'}_{\boldsymbol{r}_i\boldsymbol{r}_j}$ is the amplitude of hopping of a particle from site $\boldsymbol{r}_j$ to site $\boldsymbol{r}_i$, which takes into account possible specie exchange processes such as spin exchanges or intra-cell hoppings. $\Delta^{\sigma\sigma'}_{\boldsymbol{r}_i\boldsymbol{r}_j}$ describes the pairing term, which is at the origin of the phenomenon of superconductivity. For convenience, we also introduce the parameter N_σ which describes the number of species $\{\sigma\}$.

In order to treat the problem described by the Hamiltonian (1.8), it is convenient to work in the momentum space. For this purpose, we introduce the vector $\boldsymbol{k}_i$ which belongs to the reciprocal lattice generated by another set of primitive vectors $\{\boldsymbol{Q}_i\}$:

$$\boldsymbol{k}_j = \sum_i n_i(\boldsymbol{k}_j)\boldsymbol{Q}_i, \quad n_i(\boldsymbol{k}_j) \in \mathbb{Z}\ , \tag{1.9}$$

defined in such a way that

$$\boldsymbol{Q}_i \cdot \boldsymbol{R}_j = 2\pi\delta_{ij}\ , \tag{1.10}$$

where δ_{ij} is the Kronecker delta function. We also assume that $\boldsymbol{k}_i$ belongs to the first **Brillouin zone** (BZ) defined to be the (Wigner-Seitz) primitive cell of the reciprocal lattice centered at 0. We perform the Fourier transform

$$c_{\sigma,\boldsymbol{r}_i} = \frac{1}{\sqrt{N_c}} \sum_{\boldsymbol{k}_j\in \mathrm{BZ}} e^{i\boldsymbol{r}_i\cdot\boldsymbol{k}_j} c_{\sigma,\boldsymbol{k}_j}, \quad c_{\sigma,\boldsymbol{k}_j} = \frac{1}{\sqrt{N_c}} \sum_{\boldsymbol{r}_i\in\mathcal{L}} e^{-i\boldsymbol{r}_i\cdot\boldsymbol{k}_j} c_{\sigma,\boldsymbol{r}_i}\ . \tag{1.11}$$

Using this transformation, one can block-diagonalize the Hamiltonian of Eq. (1.8) in the momentum space

$$H = \sum_{\boldsymbol{k}\in\mathrm{BZ}} H_{\boldsymbol{k}} = \sum_{\boldsymbol{k}\in\mathrm{BZ}} \psi^\dagger_{\boldsymbol{k}} \cdot \mathcal{H}(\boldsymbol{k}) \cdot \psi_{\boldsymbol{k}}\ . \tag{1.12}$$

Here different terms $H_{\boldsymbol{k}}$, which appear in the decomposition of H, commute with each other

$$[H_{\boldsymbol{k}}, H_{\boldsymbol{k}'}] = 0\ . \tag{1.13}$$

Depending on the presence of the pairing terms $\Delta^{\sigma\sigma'}_{\boldsymbol{r}_i\boldsymbol{r}_j}$, the block-diagonalization should be performed in different ways. If the pairing is absent, all Fourier modes $\boldsymbol{k}$ are decoupled from each other and vectors $\psi_{\boldsymbol{k}}$ can be written as follows:

$$\psi_{\boldsymbol{k}} = \begin{pmatrix} c_{1,\boldsymbol{k}} \\ c_{2,\boldsymbol{k}} \\ \vdots \end{pmatrix}\ . \tag{1.14}$$

The size of vectors $\psi_{\boldsymbol{k}}$ is equal to N_σ and their elements satisfy $\psi^\sigma_{\boldsymbol{k}} = c_{\sigma,\boldsymbol{k}}$. The matrix $\mathcal{H}(\boldsymbol{k})$ is a square matrix of the same size as $\psi_{\boldsymbol{k}}$. It can be understood as the first-quantized Fourier-transformed **Bloch Hamiltonian** of the system. It can be diagonalized in the usual way via a unitary transformation. However, if the paring terms $\Delta^{\sigma\sigma'}_{\boldsymbol{r}_i\boldsymbol{r}_j}$ are non zero, Fourier modes $\boldsymbol{k}$ and $-\boldsymbol{k}$ become coupled. As a consequence, one

should use the generalization of Nambu spinors defined as

$$\psi_{\boldsymbol{k}} = \begin{pmatrix} c_{1,\boldsymbol{k}} \\ c_{2,\boldsymbol{k}} \\ \vdots \\ c^{\dagger}_{1,-\boldsymbol{k}} \\ c^{\dagger}_{2,-\boldsymbol{k}} \\ \vdots \end{pmatrix} . \tag{1.15}$$

Components of $\psi_{\boldsymbol{k}}$ verify $\psi^{\sigma}_{\boldsymbol{k}} = c_{\sigma,\boldsymbol{k}}$ and $\psi^{N_\sigma+\sigma}_{\boldsymbol{k}} = c^{\dagger}_{\sigma,-\boldsymbol{k}}$. Both $\psi_{\boldsymbol{k}}$ and $\mathcal{H}(\boldsymbol{k})$ now are of the size $2N_\sigma$ and, in order to diagonalize $\mathcal{H}(\boldsymbol{k})$, one should employ the Bogoliubov transformation.

1.2.2 Bogoliubov transformations

We now describe the way to solve the problem described by Eqs. (1.8) and (1.12) in the general case when the pairing terms $\Delta^{\sigma\sigma'}_{\boldsymbol{r}_i\boldsymbol{r}_j}$ do not vanish and the vector $\psi_{\boldsymbol{k}}$ acquires the form (1.15). We must treat separately the case for bosons and for fermions.

A. Fermions

Let us first consider the fermionic case. Fermionic operators $c_{\sigma,\boldsymbol{k}}$ verify anticommutation relations

$$\left\{c_{\sigma,\boldsymbol{k}}, c^{\dagger}_{\sigma',\boldsymbol{k}'}\right\} = \delta_{\sigma\sigma'}\delta_{\boldsymbol{k}\boldsymbol{k}'}, \quad \{c_{\sigma,\boldsymbol{k}}, c_{\sigma',\boldsymbol{k}'}\} = 0 , \tag{1.16}$$

which can be written in the vector form as

$$\psi_{\boldsymbol{k}} \cdot \psi^{\dagger}_{\boldsymbol{k}'} + \psi_{\boldsymbol{k}'} \cdot \psi^{\dagger}_{\boldsymbol{k}} = \delta_{\boldsymbol{k}\boldsymbol{k}'} I_{2N_\sigma} , \tag{1.17}$$

where I_{2N_σ} is the identity matrix of the size $2N_\sigma$ (we remind that in the previous subsection we defined N_σ to be the number of species $\{\sigma\}$). The idea of the Bogoliubov transformation for fermions consists in finding a canonical transformation which diagonalizes the matrix $\mathcal{H}(\boldsymbol{k})$ while preserving the fermionic anticommutation relations. We denote the diagonalized matrix by $\mathcal{D}(\boldsymbol{k})$ and the canonical transformation by $\mathcal{T}(\boldsymbol{k})$:

$$\begin{aligned} &\psi_{\boldsymbol{k}} = \mathcal{T}(\boldsymbol{k}) \cdot \gamma_{\boldsymbol{k}}, \quad \mathcal{T}^{\dagger}(\boldsymbol{k})\mathcal{H}(\boldsymbol{k})\mathcal{T}(\boldsymbol{k}) = \mathcal{D}(\boldsymbol{k}) , \\ &\gamma_{\boldsymbol{k}} \cdot \gamma^{\dagger}_{\boldsymbol{k}'} + \gamma_{\boldsymbol{k}'} \cdot \gamma^{\dagger}_{\boldsymbol{k}} = \delta_{\boldsymbol{k}\boldsymbol{k}'} I_{2N_\sigma} . \end{aligned} \tag{1.18}$$

The condition above means simply that $\mathcal{T}(\boldsymbol{k})$ should be orthogonal.

B. Bosons

Bosonic operators $b_{\sigma,\boldsymbol{k}}$ (for clarity we introduced here another index for bosons) verify commutation relations

$$\left[b_{\sigma,\boldsymbol{k}}, b^{\dagger}_{\sigma',\boldsymbol{k}'}\right] = \delta_{\sigma\sigma'}\delta_{\boldsymbol{k}\boldsymbol{k}'}, \quad [b_{\sigma,\boldsymbol{k}}, b_{\sigma',\boldsymbol{k}'}] = 0 , \tag{1.19}$$

which in the vector form transforms into

$$\psi_{\boldsymbol{k}} \cdot I^{-}_{2N_\sigma} \cdot \psi^{\dagger}_{\boldsymbol{k}'} - \psi_{\boldsymbol{k}'} \cdot I^{-}_{2N_\sigma} \cdot \psi^{\dagger}_{\boldsymbol{k}} = \delta_{\boldsymbol{k}\boldsymbol{k}'} I^{-}_{2N_\sigma} , \tag{1.20}$$

where

$$I^{-}_{2N_\sigma} = \begin{pmatrix} I_{N_\sigma} & 0 \\ 0 & -I_{N_\sigma} \end{pmatrix} . \tag{1.21}$$

The condition which should be verified by the canonical transformation to preserve the bosonic commutation relations also transforms into

$$\mathcal{T}^{-1}(\boldsymbol{k}) I^{-}_{2N_\sigma} \mathcal{T}(\boldsymbol{k}) = I^{-}_{2N_\sigma} , \tag{1.22}$$

which means that $\mathcal{T}(\boldsymbol{k})$ is symplectic for bosons. We also observe that matrices $\mathcal{H}(\boldsymbol{k})$ and $\mathcal{D}(\boldsymbol{k})$ verify

$$\mathcal{T}^{-1}(\boldsymbol{k}) I^{-}_{2N_\sigma} \mathcal{H}(\boldsymbol{k}) \mathcal{T}(\boldsymbol{k}) = I^{-}_{2N_\sigma} \mathcal{D}(\boldsymbol{k}) , \tag{1.23}$$

which means that matrices $I^{-}_{2N_\sigma}\mathcal{H}(\boldsymbol{k})$ and $I^{-}_{2N_\sigma}\mathcal{D}(\boldsymbol{k})$ are similar and should have identical spectrum. As a consequence, if we are interested in the spectrum of Bogoliubov quasiparticles only, it is sufficient to diagonalize $I^{-}_{2N_\sigma}\mathcal{H}(\boldsymbol{k})$.

We see that eigenfunctions of both fermionic and bosonic problems correspond to the superposition of particles (associated to operators $c_{\sigma,\boldsymbol{k}}$ or $b_{\sigma,\boldsymbol{k}}$) and holes (associated to operators $c^\dagger_{\sigma,-\boldsymbol{k}}$ or $b^\dagger_{\sigma,-\boldsymbol{k}}$). In particular, the ground-state of such system (which we will denote by $|\mathrm{GS}_\gamma\rangle$) does not correspond anymore to the vacuum state $|\mathrm{GS}_\psi\rangle$ of the original particles. It is equal up to a renormalization constant to

$$|\mathrm{GS}_\gamma\rangle \sim \prod_{\boldsymbol{k}\in \mathrm{BZ}} \prod_{\sigma} \gamma^\sigma_{\boldsymbol{k}} |\mathrm{GS}_\psi\rangle , \tag{1.24}$$

and verifies

$$\gamma^\sigma_{\boldsymbol{k}} |\mathrm{GS}_\gamma\rangle = 0, \quad \psi^\sigma_{\boldsymbol{k}} |\mathrm{GS}_\gamma\rangle = c_{\sigma,\boldsymbol{k}} |\mathrm{GS}_\gamma\rangle \neq 0 . \tag{1.25}$$

1.2.3 Interactions and approximations. BCS theory example

In Bardeen, Cooper, and Schrieffer theory of superconductivity [16, 17] the apparition of the paring term $\Delta^{\sigma\sigma'}_{\boldsymbol{r}_i\boldsymbol{r}_j}$ that we introduced in Eq. (1.8) is due to the effective many-body interactions between electrons mediated by the phononic modes of the lattice. Cooper showed [16] that even a very small attractive force will lead to the formation of bound states called Cooper pairs. This phenomenon is accompanied by the formation of the gap to the lowest excitations, which means that it costs finite energy to break the Cooper pair. To be more explicit, the interaction between electrons takes the form

$$H_{\mathrm{H}} = \sum_{\boldsymbol{k}_1\sigma_1\boldsymbol{k}_2\sigma_2\boldsymbol{k}'_1\sigma'_1\boldsymbol{k}'_2\sigma'_2} V_{\boldsymbol{k}_1\sigma_1\boldsymbol{k}_2\sigma_2\boldsymbol{k}'_1\sigma'_1\boldsymbol{k}'_2\sigma'_2}\, c^\dagger_{\boldsymbol{k}'_1\sigma'_1} c^\dagger_{\boldsymbol{k}'_2\sigma'_2} c_{\boldsymbol{k}_2\sigma_2} c_{\boldsymbol{k}_1\sigma_1} . \tag{1.26}$$

Such problem cannot be solved exactly in 2D and approximations should be used. One of the possibilities consists in using the Bogoliubov-de Gennes mean field treatment [18] *i.e.* to assume that

$$c_{\boldsymbol{k}_2\sigma_2} c_{\boldsymbol{k}_1\sigma_1} \approx \langle c_{\boldsymbol{k}_2\sigma_2} c_{\boldsymbol{k}_1\sigma_1} \rangle , \tag{1.27}$$

which means that the pairing fraction has a finite expectation value and can be treated as a classical variable. The problem can be solved exactly using the Bogoliubov transformation.

Finally, we notice that the methods presented in this section allow us to calculate the band-structures and deduce the phase transitions originating from the band deformation. One could, for example, describe the simple case of superconductivity or capture the transition from bulk conductors to bulk insulators (in the case of fermions) or between different superfluid phases (in the case of bosons). Nevertheless, as we already pointed out in Section 1.1, this description lacks an important ingredient which had a significant impact on the modern condensed matter. In order to fill this gap, in the following two sections we will make a short introduction to the topology and its role in the band theory description.

1.3 Few words about topology

In this section we want to make a short yet general introduction to topology, by paying special attention to properly defining the most relevant basic concepts. As a result, this section is perhaps the most technical part of the manuscript. Nevertheless, we will unfortunately not be able to prove the statements, formulas and relevant theorems (related for example to the application of the homotopy and cohomology theories to classify the fibre bundles), since it is a topic which goes far away beyond the scope of this work. Our motivation is rather to give a general picture of what are various mathematical structures hidden in the background of simple calculations we will do, how these beautiful mathematical concepts are integrated in the world of physics, and what are different objects we will use in the following part of this work. In particular, combining the mathematical background presented in this section and the conventional band theory presented in Section 1.2 will allow us to understand the topological band theory from Section 1.4.

1.3.1 A coffee cup or a doughnut?

Topology is a domain of mathematics concerned with the geometrical description of objects and their properties, which are unaffected by smooth transformations. The famous example is a coffee cup and a doughnut, which are meant to be indistinguishable by topologists since any doughnut could be reshaped to the form of a cup and vice versa. Both objects are also distinct from a bun and the difference is encoded in an integer topological invariant called the genus, which corresponds to the number of holes, as shown in Fig. 1.2. Transformations required to change the value of the topological invariant can not be smooth and objects with different values of a topological invariant should necessarily be topologically distinct (the opposite statement is however not true in general).

A more rigorous formulation of the above statement can be formulated based on the Gauss–Bonnet theorem and using the language of differential geometry. We will try to make it clear in the rest of this subsection. In the second part, we introduce self-consistently all required definitions. In the third part, we briefly address the notion of two different kinds of topology: homotopy, and cohomology. Finally, in the last part, we answer the question of what fibre bundles and Chern classes are and what is their role in physics. The notion of the first Chern number, which is obtained from the Chern classes in some particular cases, will be massively used throughout this work.

The content of this section is based on several excellent sources. In particular, we were inspired by the mathematical books for physicists by Nakahara [19], Naber [20] and the lecture notes of the Les Houches summer school [21].

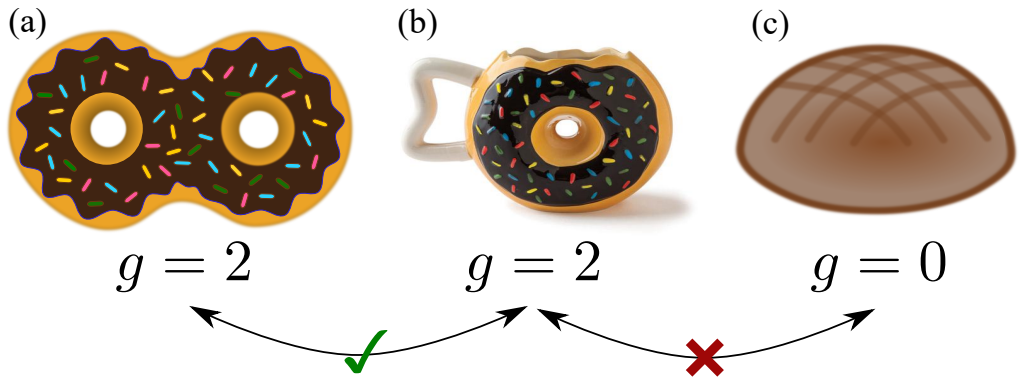

FIGURE 1.2: A doughnut with 2 holes **(a)**, a cup in form of a doughnut **(b)**, and a bun **(c)**. Both the doughnut and the cup have a genus g equal to 2, while the bun has a genus equal to 0. This implies that the bun is topologically distinct from the rest and can not be smoothly deformed. The cup can however be smoothly deformed into a doughnut.

1.3.2 Relevant definitions

A. Basics of topological spaces and manifolds

We first define the notion of a **topological space** as a set of points X with particular relations between different points. More precisely, to each point x in X, we associate a **neighborhood** N which should verify the following axioms

$$\begin{aligned}
&\text{1) If } N \text{ is a neighborhood of } x \text{ it contains } x\text{:} \quad x \in N \text{ ;} \\
&\text{2) If a subset } M \text{ of } X \text{ includes the neighborhood } N \text{ of } x\text{:} \quad N \subset M \text{ ,} \\
&\quad \text{it is itself another neghborhood of x ;} \\
&\text{3) Intersection of any two neighborhoods of } x \\
&\quad \text{is another neghborhood of x ;} \\
&\text{4) If } M \text{ and } N \text{ are 2 neighborhoods of } x \text{ and } N \subset M \text{ ,} \\
&\quad M \text{ is a neighborhood of all the points in } N \text{ .}
\end{aligned} \tag{1.28}$$

The topology in this definition refers to the exact manner the relation between different points takes form in terms of neighborhoods. For example, a trivial topology corresponds to the situation when all points are indistinguishable *i.e.* belong to the unique neighborhood which is the set X itself. A discrete topology refers to the case when each subset of points can be separated from the rest of X. Alternative definitions can also be formulated in terms of **open sets**, *i.e.* subsets of X which are neighborhoods to all their points, or **closed sets**, which are complementary to some open sets of X.

Since in the following we will use a lot the idea of mappings between different topological spaces, it will be convenient to define the notion of continuous functions and homeomorphisms. A function from the topological space X to the topological space Y is **continuous** at a point $x \in X$ if and only if for every neighborhood W of $f(x)$ in Y, the inverse image $f^{-1}(W)$ is a neighborhood of x. Equivalently, the inverse image of a continuous function of any open subset of Y should remain an open subset in X. An **homeomorphism** is a function between two topological spaces X and Y, which is a continuous bijection and has an inverse, which is continuous as well.

In physics, we are often interested in a particular type of topological spaces

which are called **topological manifolds** and, even more precisely, **differential manifolds**. They are defined as topological spaces which resemble locally the usual $\mathbb{R}^n$ space (for some $n \in \mathbb{N}$). Mathematically speaking, this means that the manifold is locally homeomorphic to $\mathbb{R}^n$. Local resemblance implies that the manifold should be provided with an atlas, *i.e.* a set of charts $\{U_i, \varphi_i\}$ each of which is a couple of an open subset U_i of the manifold and a homeomorphism φ_i from U_i to an open subset of $\mathbb{R}^n$

$$\varphi_i : U_i \to \varphi_i(U_i) \subset \mathbb{R}^n \ . \tag{1.29}$$

All subsets U_i in the atlas should cover the entire manifold. The differentiability of the coordinate transformations between two overlapping charts

$$\varphi_j \circ \varphi_i^{-1} : \varphi_i(U_i \cap U_j) \to \varphi_j(U_i \cap U_j) \tag{1.30}$$

establishes the differentiable structure of the manifold. If the coordinate transformations have k continuous derivatives, the atlas is said to be C^k. If $k \geq 1$ the manifold is called differential, and if $k = \infty$ the manifold is called smooth. If we have two smooth manifold M and L, the map between them could also be a smooth function. Such map is then called a **diffeomorphism**, and M and L are said to be diffeomorphic (which is denoted as $M \simeq L$).

The notion of manifolds represents a generalization of the familiar ideas about curves and surfaces. Our definition roughly means that to each point x of the n-dimensional manifold M we can associate a set of coordinates $\{x^\mu\}$ [1] and a set of **tangent vectors** of $\mathbb{R}^n$ which will generate an Euclidean hyper-plane of dimension n – the so called **tangent space** T_xM. If we consider a particular path on M, and if we look at the infinitesimal variation of this path close to some point x of M, we intuitively see the emergence of a vector tangent to the surface of the manifold at this particular point x defined as a directional derivative. $\{\boldsymbol{e}_\mu\} = \{\partial/\partial x^\mu\} = \{\partial_\mu\}$ is a natural choice of the basis of the tangent space, generated in such a way. Any vector $\boldsymbol{v}$ in the tangent space can thus be written as

$$\boldsymbol{v} = v^\mu \boldsymbol{e}_\mu \ . \tag{1.31}$$

It is obvious however that tangent vectors do not live on the manifold itself and the tangent space exists independently of the specification of the coordinates. The visualization of this construction is shown for a particular example of a sphere S^2 in Fig. 1.3.

By analogy with the Euclidean geometry, it is useful to introduce the distance which separates different points in a given set. In general case, such distance is introduced by means of a metric g. A metric is a particular type of function that takes as an input two points x and y in the set X and returns a real number, while verifying the following properties

$$\begin{aligned}
&\text{1) Non-negativity:} \quad g(x,y) \geq 0 \ ; \\
&\text{2) Identity of indiscernibles:} \quad g(x,x) = 0 \ ; \\
&\text{3) Symmetry:} \quad g(x,y) = g(y,x) \ ; \\
&\text{4) Triangle equality:} \quad g(x,z) \leq g(x,y) + g(y,z) \ .
\end{aligned} \tag{1.32}$$

The set of points equipped with the metric is called a metric space. The metric also

[1] Coordinates x^μ are in reality coordinate functions $x^\mu : M \to \mathbb{R}$ explicitly determined by the associated chart φ_i in the atlas.

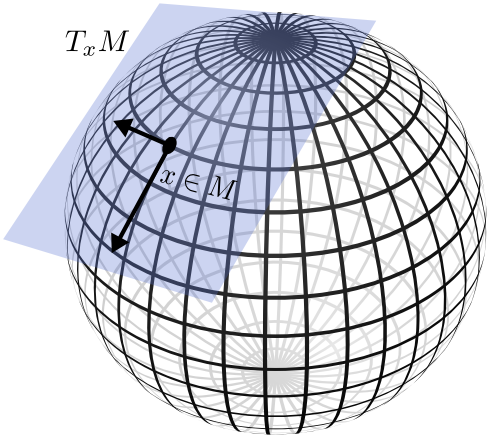

FIGURE 1.3: Sphere $M = S^2$ as a typical example of a two-dimensional differential manifold. At each point x of the sphere an Euclidean plane T_xM is attached.

naturally induces the notion of neighborhoods such that any metric space is a topological space. We are however particularly interested in the situation where the metric space is also a smooth manifold. In this case, we should define the so called **metric tensor** which is a tensor field taking as an input two tangent vectors $\boldsymbol{u}$ and $\boldsymbol{v}$ in the tangent space T_xM at each point x of the manifold M and returning a real number:

$$g(\boldsymbol{u}, \boldsymbol{v}) = g_{\mu\nu} u^\mu v^\nu = \langle \boldsymbol{u}, \boldsymbol{v} \rangle \in \mathbb{R} \,. \tag{1.33}$$

This is a natural generalization of the inner product between two vectors in $\mathbb{R}^n$. To outline the similarity we used the inner product notation $\langle \square, \square \rangle$. In quantum mechanics this is also equivalent to $\langle \square \,|\, \square \rangle$ in the bra-ket notation. In the limit of infinitesimally small tangent vectors, the metric tensor plays the same role as the metric and returns an infinitesimal distance on the manifold. A smooth manifold equipped with a positive definite metric tensor is called a **Riemannian manifold**. In the following, we are mostly interested in a particular case of Riemannian manifolds.

B. Covectors, tensors and differential forms

Differential forms are objects, which could be simply thought as a generalization of the integrands over smooth manifolds of various forms and dimensions (*i.e.* curves, surfaces, volumes). More precisely, let T_xM be a tangent space defined at a point x of a smooth n-dimensional manifold M. T_xM is a vector space and, as we said previously, vectors $\{\boldsymbol{e}_\mu\} = \{\partial_\mu\}$ form its basis. To each vector space we can associate a dual space whose elements are linear functions from the vector space to $\mathbb{R}$. In the particular case of a tangent space this dual vector space is called a **cotangent space** T_x^*M. Elements of T_x^*M are functions $\omega : T_xM \to \mathbb{R}$ called **covectors** (cotangent vectors) or **differential 1-forms**. The set of all differential 1-forms over the manifold M will be denoted as $\Omega^1(M)$. One of the simplest example of a 1-form is the differential of a scalar function f:

$$\mathrm{d}f = \frac{\partial f}{\partial x^\mu} \, \mathrm{d}x^\mu \,. \tag{1.34}$$

Here we see that covectors $\{e^{*\mu}\} = \{\mathrm{d}x^\mu\}$ play the role of a dual basis of the cotangent space. In particular, they verify

$$e^{*\mu}(e_\nu) = \frac{\partial x^\mu}{\partial x^\nu} = \delta^\mu_\nu \ . \tag{1.35}$$

Any differential 1-form ω can thus be written in such basis

$$\omega = \omega_\mu \, \mathrm{d}x^\mu \ . \tag{1.36}$$

In the case of a Riemannian manifold, the metric tensor induces a natural mapping between vectors and covectors: $\omega_\mu = g_{\mu\nu}\omega^\nu$. The introduction of covectors also allows us to properly define what tensors are. A **tensor** is simply a function, which takes as an input n vectors and m covectors and returns a number.

Starting from the expression of a differential 1-form, let us now try to generalize this definition. We want to define a differential r-form $\omega \in \Omega^r(M)$ as a map $\omega : (T^*_x M)^r \to \mathbb{R}$. By enforcing the analogy with the usual Euclidean space and the cross product between $\mathbb{R}^3$ vectors, we also want to impose the antisymmetricity condition on ω (the cross product is anticommutative $\boldsymbol{u} \times \boldsymbol{v} = -\boldsymbol{v} \times \boldsymbol{u}$ and the Jacobian determinant changes sign when we switch the order of two arbitrary vectors). In order to do so, we first introduce the notion of a wedge product $\wedge$ of r differential 1-forms as a totally antisymmetric tensor product

$$\mathrm{d}x^{\mu_1} \wedge \cdots \wedge \mathrm{d}x^{\mu_r} = \sum_{\mathcal{P}} \mathrm{sign}(\mathcal{P}) \, \mathrm{d}x^{\mathcal{P}(\mu_1)} \otimes \cdots \otimes \mathrm{d}x^{\mathcal{P}(\mu_r)} \ . \tag{1.37}$$

Here the summation is performed over all possible permutations $\mathcal{P}$ of the set $\{\mu_1, \ldots, \mu_r\}$. These objects form a basis of the differential r-forms. In particular, any **differential r-form** can be written as

$$\omega = \frac{1}{r!} \omega_{\mu_1 \ldots \mu_r} \, \mathrm{d}x^{\mu_1} \wedge \cdots \wedge \mathrm{d}x^{\mu_r} \ , \tag{1.38}$$

where $\omega_{\mu_1 \ldots \mu_r}$ is a totally antisymmetric tensor. Now, we can also give a proper definition to the differentiation operator we used at the beginning in Eq. (1.34). An operator $\mathrm{d}_r : \Omega^r(M) \to \Omega^{r+1}(M)$ is called an **exterior derivative** and it maps a form $\omega \in \Omega^r(M)$ to a form $\mathrm{d}_r\omega \in \Omega^{r+1}(M)$ through the following relation

$$\mathrm{d}_r\omega = \frac{1}{r!} \left(\frac{\partial}{\partial x^\nu} \omega_{\mu_1 \ldots \mu_n} \right) \mathrm{d}x^\nu \wedge \mathrm{d}x^{\mu_1} \wedge \cdots \wedge \mathrm{d}x^{\mu_n} \ . \tag{1.39}$$

C. Parallel transport: connection and curvature

Tangent vectors defined at different points of the Riemannian manifold cannot be naively compared to each other. In order to perform the comparison we should first understand how vectors (and in more general case tensors) behave when they are transported along a smooth path on the manifold. We intuitively understand that vectors should be re-calibrated to stay orthogonal to the surface of the manifold at each new point along the path, which explains why our task is not trivial. The process of the re-calibration is called a parallel transport and is described by means of a special structure called connection. A **connection** Γ takes two vectors $\boldsymbol{u}$ and $\boldsymbol{v}$ (a vector which should be transported and a direction of the transport) in the tangent space and returns another vector $\boldsymbol{w}$ (which is the transported vector in the nearby

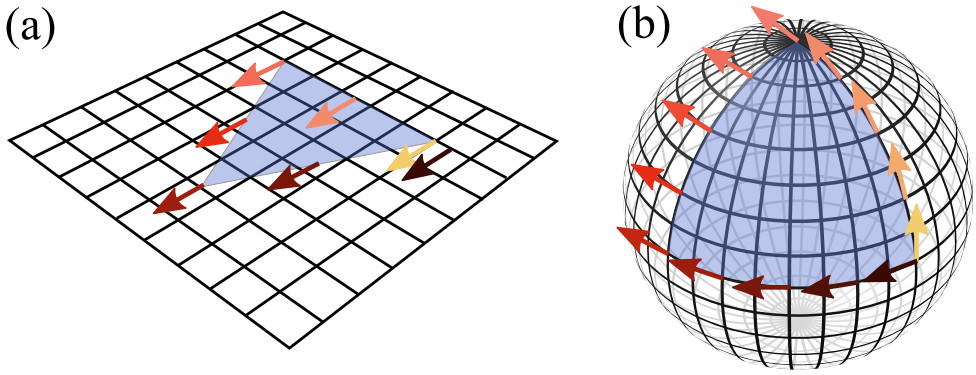

FIGURE 1.4: Parallel transport of a vector along the closed triangular path in an Euclidean plane **(a)** and on a sphere **(b)**. After returning to the initial point, the vector remains the same on a plane and is rotated on a sphere. The color of the vector represents the progression along the path: the color is brighter at the beginning and darker at the end.

tangent space minus the identity):

$$w^\rho = \Gamma^\rho_{\mu\nu} u^\mu v^\nu \ . \tag{1.40}$$

There are many valid rules of parallel transport, each of which is endowed with its own particular choice of the connection. For example, one could require that the component u^μ of the vector $\boldsymbol{u}$ is constant for a parallel transport along the vector $\boldsymbol{e}_\mu$, as in the case of the Euclidean space $\mathbb{R}^n$. However, if we know the expression of the metric tensor, a connection can be written down in a particular convenient form expressed in terms of Christoffel symbols:

$$\Gamma^\rho_{\mu\nu} = \frac{g^{\rho\lambda}}{2}\left(\partial_\mu g_{\lambda\nu} + \partial_\nu g_{\lambda\mu} - \partial_\lambda g_{\mu\nu}\right) \ . \tag{1.41}$$

The connection allows us to define the **covariant derivative** [2]

$$\nabla_\nu u^\mu = \partial_\nu u^\mu + \Gamma^\mu_{\nu\lambda} u^\lambda \ , \tag{1.42}$$

or, more generally

$$\nabla_{\boldsymbol{v}} \boldsymbol{u} = v^\nu \left(\partial_\nu u^\mu + \Gamma^\mu_{\nu\lambda} u^\lambda\right) \boldsymbol{e}_\mu \ . \tag{1.43}$$

The covariant derivative explains how the basis vectors are changed when we move on the manifold: $\nabla_\mu \boldsymbol{e}_\nu = \Gamma^\rho_{\mu\nu} \boldsymbol{e}_\rho$.

Now, let us consider a parallel transport of a vector along a closed loop on M. In Fig. 1.4 we show a particular example in the case of a sphere. Remarkably, we notice that the final orientation of the vector depends on the path we have chosen. This phenomenon, called **holonomy**, does not occur in the Euclidean space $\mathbb{R}^n$, thus, it is expected to originate from the intrinsic notion of the curvature of the manifold, independent of our choice of coordinates. The connection Γ can not be employed as an universal description of how much the manifold is curved since, as we have said previously, it is not uniquely determined [3]. An intrinsic object which answers the

[2] Vice versa, the connection can be established by first introducing the covariant derivative, *i.e.* an operator ∇ that assigns to every vector v a linear map ∇_v verifying the Leibniz rule.

[3] Moreover, Γ is not even a tensor.

above question is called a **Riemann curvature tensor**

$$R^{\rho}_{\mu\nu\sigma} = \partial_\mu \Gamma^{\rho}_{\nu\sigma} - \partial_\nu \Gamma^{\rho}_{\mu\sigma} + \Gamma^{\rho}_{\mu\lambda}\Gamma^{\lambda}_{\nu\sigma} - \Gamma^{\rho}_{\nu\lambda}\Gamma^{\lambda}_{\mu\sigma} \, . \tag{1.44}$$

Riemann curvature tensor describes how much the vector is changed when moved around an infinitesimal loop on the manifold. It takes as an input three vectors $\boldsymbol{u}$, $\boldsymbol{v}$ and $\boldsymbol{w}$ (two vectors specify the plane in which the loop is contained and act on indices ν and σ, the last vector acting on the index μ is the vector which should be transported) and returns another vector $\boldsymbol{z}$ (which is the transported vector).

It will be useful for us to write the connection and the curvature in the differential form (based on the Cartan's formalism). In order to do this, we define the matrix-valued connection 1-form as

$$\omega^{\nu}_{\mu} = \Gamma^{\nu}_{\mu\alpha} \mathrm{d}x^{\alpha} \, , \tag{1.45}$$

and the curvature 2-form as

$$R^{\nu}_{\mu} = \frac{1}{2} R^{\nu}_{\mu\alpha\beta} \mathrm{d}x^{\alpha} \wedge \mathrm{d}x^{\beta} \, . \tag{1.46}$$

They are related through the Cartan's structure equation

$$\mathrm{d}_1 \omega^{\nu}_{\mu} + \omega^{\nu}_{\alpha} \wedge \omega^{\alpha}_{\mu} = R^{\nu}_{\mu} \, . \tag{1.47}$$

D. Topological invariants

Up to now we introduced the language which could be used to describe different topological spaces and, in particular, the Riemannian manifolds. Now we would like to go back to the question we asked at the beginning of this section and reformulate it in a more general (and exact) way. We are interested in how one could compare different topological spaces and, more concretely, whether there exist characteristics which are invariant under any smooth deformation of the topological spaces (*i.e.* which are the same if the spaces are diffeomorphic)? We have already mentioned that such characteristics exist and they are called **topological invariants**. In particular, the number of holes piercing the doughnut is one of them, according to the statement of the celebrated Gauss-Bonnet theorem.

In two dimensions (*i.e.* for two-dimensional manifolds embedded in a three-dimensional space) the Riemann curvature can be written in a simpler form in terms of a Gaussian curvature G defined as follows

$$R^{\rho}_{\mu\nu\sigma} = G g^{\rho\lambda} \left(g_{\lambda\mu} g_{\nu\sigma} - g_{\lambda\nu} g_{\mu\sigma} \right) \, . \tag{1.48}$$

Gauss-Bonnet theorem relates the geometry of a compact orientable [4] two-dimensional Riemannian manifold M without boundaries expressed in terms of the Gaussian curvature integrated over the total surface, to its topology defined in terms of the Euler-Poincaré characteristic $\chi(M)$:

$$\frac{1}{2\pi} \oint_M G \mathrm{d}S = \chi(M) = 2 - 2g \, , \tag{1.49}$$

where g is the genus of the surface.

[4] Orientable surfaces have a consistent choice of surface normal vector at every point. For example, the cylinder and the torus are two orientable surfaces, while the Möbius strip and the Klein bottle are not.

1.3.3 Homotopy and cohomology

Preliminary: equivalence classes

When starting to write this section, we understood that the notion of equivalence classes is better to have an explicit definition. This paragraph is simply meant to define this notion and could be thought of as a big footnote or an appendix. Let us consider a set X. Let x and y be two elements of X. One could define an equivalence relation between x and y denoted as $x \sim y$ as a binary relation verifying three following properties:

$$\begin{aligned} &\text{1) Reflectivity:} \quad x \sim x \ ; \\ &\text{2) Symmetricity:} \quad x \sim y \Leftrightarrow y \sim x \ ; \\ &\text{3) Transitivity:} \quad x \sim y,\ y \sim z \Rightarrow x \sim z \ , \end{aligned} \tag{1.50}$$

where z is another element of X. A subset of all elements of X equivalent to x is called an equivalence class and is denoted by $[x]$. Clearly, homeomorphisms and diffeomorphisms define an equivalence relation in the set of topological spaces and manifolds. In the following, we will see two other examples relevant to us.

A. Homotopy groups

In homotopy we are interested in continuous deformation of maps between different topological spaces. To illustrate this idea, we provide a simple example. Let us consider a collection of different paths $\{\gamma_i\}$ in the topological space M. Any path can be defined as a continuous map $\gamma_i : [0,1] \to M$ such that its starting point is $\gamma_i(0) \in M$ and the ending point is $\gamma_i(1) \in M$. If $\gamma_i(0) = \gamma_i(1)$, the path corresponds to a closed curve. If we consider two such closed curves γ_1 and γ_2, they are said to be homotopic if they can be continuously deformed one into another. More precisely, there should exist a continuous function

$$f : [0,1] \times [0,1] \to M \ , \tag{1.51}$$

satisfying

$$f(x,0) = \gamma_1(x) \ , \quad f(x,1) = \gamma_2(x) \ . \tag{1.52}$$

Homotopy is an equivalence relation of closed paths. It defines an equivalence class $[\gamma_i]$ which denotes the set of all closed paths homotopic to γ_i. The set $\{[\gamma_i]\}$ equipped with an operation of concatenation of different paths forms a group $\pi_1(M)$ which is called the fundamental group or the **first homotopy group**. If the first homotopy group is trivial $\pi_1(M) = \emptyset$, all the paths can be shrunk to a single point and the space is said to be simply connected. This notion can also be generalized: **higher homotopy groups** $\pi_r(M)$ are obtained by considering the mappings from the r-sphere S^r to M.

More generally, we are interested in the equivalence relation of continuous maps between arbitrary topological spaces: $f, g : X \to Y$. Maps f and g are said to be **homotopic** (denoted as $f \sim g$) if there exists a continuous map

$$F : X \times [0,1] \to Y \tag{1.53}$$

such that

$$F(x,0) = f(x), \quad F(x,1) = g(x) \ . \tag{1.54}$$

The map F is called an **homotopy** between f and g. In addition, spaces X and Y are said to be of the same **homotopy type**, denoted as $X \simeq Y$, if there exist continuous maps $c : X \to Y$ and $d : Y \to X$, such that $c \circ d \sim \mathrm{id}_Y$ and $d \circ c \sim \mathrm{id}_X$. Here we defined by $\mathrm{id}_X : X \to X$ and $\mathrm{id}_Y : Y \to Y$ two identity maps over X and Y. The homotopy type is another example of an equivalence relation between the set of topological spaces. In particular, any pair of homeomorphic manifolds is also homotopic. However, homotopic manifolds are not necessarily homeomorphic. For example, the point x in the Euclidean space $\mathbb{R}^n$ is homotopic (but not homeomorphic) to the entire space $\mathbb{R}^n$. The hyper-sphere S^n is homotopic (but not homeomorphic) to $\mathbb{R}^n - \{0\}$ (if $n = 1$ we obtain the equivalence relation for a circle, if $n = 2$ – for a sphere). Both cylinder and a Möbius strip are homotopic (but not homeomorphic) to a circle.

Finally, we notice one of the most important property of the homotopy groups and homotopy type. We understand intuitively that since they are intended to describe the equivalence relations of the continuous maps, they belong to the category of topological invariants we are looking for.

B. De Rham cohomology groups

Basic objects used in de Rham cohomology are differential forms. Let ω be a differential r-form in $\Omega^r(M)$. If ω is the image of another differential form $f \in \Omega^{r-1}(M)$ through the application of the differentiation operator $\omega = \mathrm{d}_{r-1} f$, it is called an **exact form**. The set of all exact r-forms is a group which we will denote by $B^r(M) \subset \Omega^r(M)$. In other words, exact forms are in the image of the operator d_{r-1}. From the other side, if ω is such that $\mathrm{d}_r \omega = 0$, it is called a **closed form**. The set of all closed r-forms is another group $Z^r(M) \subset \Omega^r(M)$. Similarly, one could say that closed forms are in the kernel of the operator d_r.

Clearly, because of the antisymmetricity condition of differential r-forms, $\mathrm{d}_r \mathrm{d}_{r-1} = 0$, meaning that any exact form is also a closed form: $Z^r(M) \subset B^r(M)$. In 2D this statement takes a very familiar form: the rotational of a gradient is always zero. The opposite is however not true in general. For example, the 1-form

$$\omega = \frac{-y}{x^2 + y^2} \mathrm{d}x + \frac{x}{x^2 + y^2} \mathrm{d}y \tag{1.55}$$

is closed, but not exact on $\mathbb{R}^2 - \{0\}$. Using this property, one could deduce another equivalence relation on M. It consists in identifying two closed r-forms ω_1 and ω_2 in $Z^r(M)$ if $\omega_1 - \omega_2 = \mathrm{d}_{r-1}\eta$ for some $\eta \in \Omega^{r-1}(M)$. The set of corresponding equivalence classes $\{[\omega_i]\}$ is the quotient group called r-th **de Rham cohomology group** $H^r(M)$

$$H^r(M) = \frac{\text{closed } r\text{-forms on } M}{\text{exact } r\text{-forms on } M} = \frac{Z^r(M)}{B^r(M)} \,. \tag{1.56}$$

Elements $\{[\omega_i]\}$ of the de Rham cohomology group are also called **cohomology classes**.

Most importantly (and most interestingly), the de Rham cohomology group is another topological invariant. If we apply a diffeomorphic transformation to a smooth manifold, the de Rham cohomology group remains unaffected. An equivalent statement is also: two diffeomorphic manifolds are described by the same de Rham cohomology group. Different quantities (such as, for example, characteristic classes) could be obtained from the de Rham cohomology groups and serve as universal tools to distinguish between topologically distinct manifolds. In particular, as we

will see in the following, Chern classes, which are used to describe fibre bundles, can be expressed in terms of the de Rham cohomology groups.

Finally, we would like to mention an interesting relation to our previous discussion, where we addressed the notion of topology described in terms of the Euler characteristics $\chi(M)$ and the Riemann curvature R of a Riemannian manifold M (see for example Eqs. (1.48) and (1.49)). It occurs that the Euler-Poincaré characteristics can be written using the cohomology groups of the manifold M as follows

$$\chi(M) = \sum_{r=1}^{n} (-1)^r b^r(M) \, . \tag{1.57}$$

Here $b^r(M) = \dim H^r(M)$ are called Betti numbers of M. Remarkably, this equation relates again a purely topological observable (which is the Euler characteristics) and an analytic set of equations implying the conditions $\mathrm{d}_r\omega = 0$ and $\omega = \mathrm{d}_{r-1}f$.

1.3.4 Basics of fibre bundles

A. Fibre bundles in geometry and in physics

As we have previously seen in this section, a manifold is a topological space which looks locally like $\mathbb{R}^n$. A fibre bundle is a generalization of the notion of a topological manifold. A rough definition consists in saying that a **fibre bundle** is a topological space which looks locally like a direct product of two other topological spaces. Alternatively, it could be described as a topological space at each point of which another topological space is attached (please see also Fig. 1.5). To be more precise, to construct a fibre bundle one should mix the following ingredients:

1) A topological manifold P called the **total space** ;

2) A topological manifold M called the **base space** ;

3) A topological manifold F called the **fibre** ;

4) A surjection $\pi : P \to M$ called the **projection** ;

5) A set $\{U_i, \varphi_i\}$ of open subsets U_i of the base space M and homeomorphisms φ_i
$$\varphi_i : U_i \times F \to \pi^{-1}(U_i) \, ,$$
These maps are called **local trivializations** ;

6) A topological group G [5]acting on F on the left and a set of continuous maps $t_{ij} : M \to G$ such that for $x \in U_i \cap U_j \neq \emptyset$ we have $\varphi_i(x, f) = \varphi_j(x, t_{ij}(x) \cdot f)$.
The group G is called a **structure group** and $\{t_{ij}\}$ are called **transition functions** .

(1.58)

Let us now spend some time to clarify the definition above. We want the total space P to be locally homeomorphic to the direct product $M \times F$. This local similarity is formulated by means of local trivializations $\{U_i, \varphi_i\}$. They play exactly the same role as charts in the case of a simple manifold and map open sets $U_i \times F$ of the product

[5]A topological group is a topological space which is also a group. If the topological space is a manifold, the group is a Lie group. The action of the group G on a set X is a map $\phi : G \times X \to X$ expressed as $\phi(g, x) = g \cdot x$ for a left action or $\phi(g, x) = x \cdot g$ for a right action. Here $g \in G$ and $x \in X$. The action of the group should verify $e \cdot x = x$ and $(gh) \cdot x = g \cdot (h \cdot x)$, where h is another element of G, e is the identity element of G and we wrote down the binary operation between elements g and h of the group as a product gh.

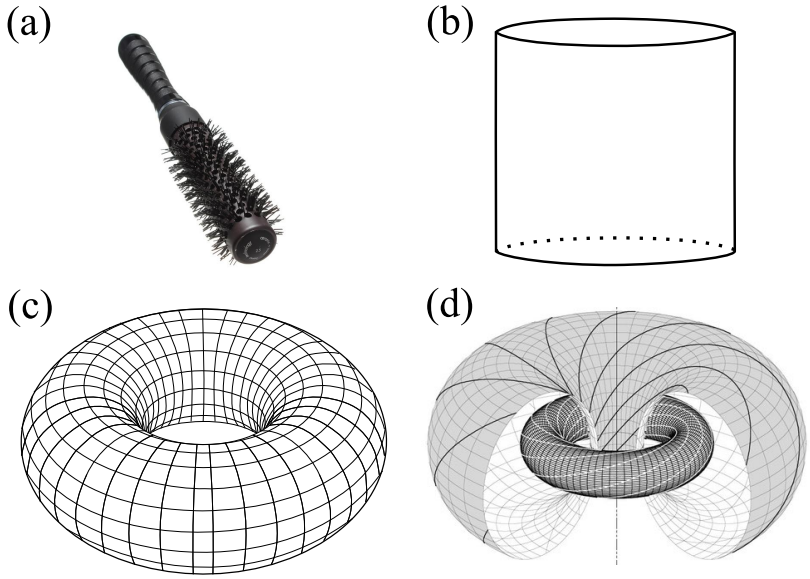

FIGURE 1.5: In a fibre bundle the total space T looks locally like a base space M with a fibre F attached to each point of M. Here we show few examples of fibre bundles. In a cylindrical hairbrush **(a)** M is a cylinder and F is a bristle (*i.e.* a line segment of a fixed length). In a cylinder **(b)** M is a circle and F is a line segment. In a torus **(c)** both M and F are two circles. In the Hopf fibration **(d)** M is a sphere and F is a circle.

space $M \times F$ to open sets of the total space P and vice versa. The projection π describes the link between the total space P and the base space M. It should commute with all local trivializations and allows to express the open set of the total space P as $\pi^{-1}(U_i)$, where U_i is the open set of M. The inverse image $s(x) = \pi^{-1}(x)$ at each point x of M is homeomorphic to the fibre F. A smooth function $s : M \to F$ which associates to each point x of M an element of the fibre F is called a section. Finally, we have not described how different maps φ_i communicate with each other. In particular, if a particular point x is such that $\pi(x)$ belongs to an intersection of several open sets $U_i \cap U_j$ in M, we also have several maps φ_i and φ_j which accomplish the trivialization. We then assign to the point x two elements of F, one by φ_i^{-1} and another by φ_j^{-1}:

$$\varphi_i^{-1}(x) = (x, f_i), \quad \varphi_j^{-1}(x) = (x, f_j) \, . \tag{1.59}$$

The structure group G and the transition functions t_{ij} take into account this inconsistency by relating f_i and f_j via $f_i = t_{ij}(x) \cdot f_j$. We notice that the structure groups describe only how different local trivializations are related to each other at the same point x of the base manifold M. Information on the connection between different points is yet unclear to us and requires an additional structure to be defined.

A trivial example of the fibre bundle is a topological space homeomorphic to $P = M \times F$. The difference as compared to the general definition is that the similarity is global instead local. In particular, in this case all the transition maps can be taken to be identity maps. A less trivial example of the fibre bundle is a so called tangent bundle TM over a topological manifold M. It is a manifold which collects all the

tangent spaces T_xM at each point $x \in M$:

$$TM = \bigcup_{x \in \mathcal{M}} T_xM \,. \tag{1.60}$$

In this case the manifold M is the base manifold and the fibre at each point $x \in M$ is the vector space T_xM. In Fig. 1.5 we also show several other examples of fibre bundles which have a nice visualization.

The definition of a fibre bundle could seem very abstract for a physicist. Nevertheless, it has a very big relevance in physics and appear in various domains. Let us justify our statement by providing few simple examples. The first example is the quantum mechanical wavefunction defined in n-dimensional physical space, *e.g.* a usual space-time. As we know, in quantum mechanics the wavefunction has a gauge freedom interpreted in terms of a local phase symmetry. This phase ambiguity determines a $U(1)$ fibre, while the original n-dimensional space-time forms the base space of the fibre bundle. By developing this idea, we see that the similar description applies to the case of the Standard Model where the non-abelian gauge theory with the symmetry group $U(1) \times SU(2) \times SU(3)$ is used to describe electroweak interactions and the quantum chromodynamics. Another example we want to mention comes from hydrodynamics, where one could be interested in describing for example the velocity field (fibre) at various point of the real space (base space). Vortices could be related to non-trivial topology of the resulting fibre bundle. The notion of fibre bundles is also widely used in general relativity. Finally, we notice that in the context of condensed matter physics we are often interested in using the translation symmetry and employing the Fourier transform to go to the momentum space (see for example Section 1.2). In this case, our problem consists in studying a fibre bundle, where the fibre corresponds to some gauge theory group, while the base manifold is a n-dimensional torus, *i.e.* a circle in 1D, usual torus in 2D etc. In this case we will sometime refer to our fibre bundle as a **Bloch bundle**.

To conclude on this part, let us say few words about the classification of fibre bundles based on the particularity of their geometrical structure. First of all, the fibre bundle is often said to be an F bundle over M, if F is its fibre and M is its base space. When F is a vector space, the fibre bundle is called a **vector bundle**. An example of a vector bundle is the tangent space TM. Another type of fibre bundles which is of particular interests (and use) to us is called a **principal bundle**. In principal bundles the fibre F is homeomorphic to the structure group G (*i.e.* we could define a right action of the group G on the fibre bundle which preserves its fibres and acts freely and transitively on them). We could thus proceed as if the fibre was the structure group itself. The principal bundle with the structure group G over the base manifold M is said to be a G-bundle over M. Principal bundles are exactly the objects which lie in the basis of gauge theories in physics.

B. Connection and curvature in fibre bundles

In a Riemannian manifold M, vectors living in tangent spaces T_xM and T_yM at two neighboring points x and y are connected to each other via a connection Γ. This concept can be generalized for fibre bundles. In this case the question we are interested in transforms into: how two distinct fibres at two points x and y of the base manifold M are related to each other? Clearly, if the fibre is a tangent space TM of a Riemannian manifold, Christoffel symbols could be employed (see for example Eq. (1.41)). The situation is however significantly different in general case, when

the fibre is not a vector space or there is no metric tensor defined on the base manifold. In particular, we expect that properties depend less on the exact structure of the base manifold, and the behavior of the fibres themselves (connection between fibres) often represents even more interest for us.

In this part, we will discuss how this construction could be accomplished and which results does it lead to in the case of a principal G-bundle over M. We suppose that M is a Riemannian manifold and G is a Lie group. In order to describe the parallel transport, we need to properly separate the tangent space T_pP at each point p of the total space P into a vertical space V_pP tangent to the fibre and a complementary horizontal space H_pP. The parallel transport describes how the point p moves in the fibre when it follows some path in M tangent to the horizontal space H_pP. This can be achieved by introducing a matrix-valued connection 1-form ω over P as in Eq. (1.45). It is a matrix-valued 1-form that takes values in the Lie algebra $\mathfrak{g}$ of the Lie group G. Notice that ω is defined globally. However, manipulating the objects defined in the total space P is not convenient for us. Moreover, in physics we are able to describe the connection on fibre bundles by using the functions defined on the base space M only. In fact, similarly to the physical case, one could pull the connection 1-form ω back to the horizontal space H_pP to get a set of new connection 1-forms $\mathcal{A}_i$ over the base manifold M, which are called **gauge potentials**. These forms can act only on the open subsets $U_i \subset M$ appearing in the local trivializations of the fibre bundle. Similarly to the case of Riemannian manifolds, the choice of the connection is not unique. However, it must be consistent with the choice of transition functions t_{ij} and the structure of the Lie group G, which translates into the following gauge transformation

$$\mathcal{A}_j = t_{ij}^{-1}\mathcal{A}_i t_{ij} + t_{ij}^{-1}\mathrm{d}t_{ij} \,, \tag{1.61}$$

where indices i and j refer to two distinct local trivializations such that $U_i \cap U_j \neq \emptyset$. We notice that one local gauge potential does not know about the global topology of the fibre bundle (except if the topology is trivial). Only the collection of all gauge potentials will allow us to learn about possibly non-trivial topological properties.

Here we do not seek to present the general approach to construct a connection (or gauge potentials), which is a rather technical problem and goes beyond the scope of this work. Instead, we prefer to discuss in more details the particular case of our interests, which is a principal $U(1)$-bundle over a n-dimensional Riemannian manifold M describing the simplest gauge symmetry in physics. The general form of the gauge potential as a differential 1-form over the manifold M becomes

$$\mathcal{A}_j = \mathcal{A}_{j\mu}\mathrm{d}x^\mu \,. \tag{1.62}$$

We notice that this gauge potential has only one component, as compared to the connections in Riemannian manifolds and the Christoffel symbols which have three components. This originates from the fact that the object we want to transport lives in a one-dimensional fibre, thus two remaining indices become superfluous. The transition functions are given by

$$t_{ij}(x) = e^{i\chi(x)} \,, \tag{1.63}$$

where $x \in U_i \cap U_j$ is a point in the base manifold M, and $\chi(x)$ is a $U(1)$ phase factor (a gauge phase). The compatibility condition transforms into

$$\mathcal{A}_j = \mathcal{A}_i + i\mathrm{d}\chi \,. \tag{1.64}$$

Similarly to the simple case of Riemannian manifolds, we can define the curvature associated to the connection $\mathcal{A}_j$ using Eq. (1.47). The relation is very intuitive in our case: the **curvature** is simply a 2-form obtained from the connection by applying the exterior derivative d_1 [6]

$$\mathcal{B}_j = \mathrm{d}_1 \mathcal{A}_j \ . \tag{1.65}$$

In components we get

$$\mathcal{B}_{j\mu\nu} = \partial_\mu \mathcal{A}_{j\nu} - \partial_\nu \mathcal{A}_{j\mu} \ , \tag{1.66}$$

where, again, we have less indices than in the general case because the fibre is one-dimensional.

We notice that in gauge theories in physics, in addition to the gauge potentials $\mathcal{A}_i$ by themselves, that live in the principal fibre bundle, we have matter fields, that live in some vector bundle. The fibre in the vector bundle at each point of the base manifold corresponds to the usual quantum-mechanical Hilbert space $\mathcal{HS}$. The relation between the two fibre bundles is provided by defining the representation of the Lie group G in the Hilbert space $\mathcal{HS}$.

C. Topology of fibre bundles

The description of fibre bundles is not an easy problem. As a consequence, it is useful to have some measurable quantities, which would allow us to identify in a straightforward and non-ambiguous way that two fibre bundles are non-equivalent. The objects which represent the greatest interest for us are of course the topological invariants, and the equivalence between different fibre bundles is determined by means of diffeomorphisms. More precisely, we say that two fibre bundles are equivalent if we can find a smooth differentiable map transforming one into another. Now we have all the tools required to address these questions, but first we would like to give some simple examples of very similar, but still topologically distinct fibre bundles, which will allow us to understand intuitively, what are the observables we are looking for.

Let us first take an example of a right circular cylinder (see Fig. 1.6(a)). In the language of fibre bundles the cylinder is composed of a circle S^1, which plays the role of a base manifold B, and a line segment – the fibre F. Let us assume without any loss of generality that the line segment is $[0, 1]$. The projections π maps all the points which lies on the line perpendicular to the plane of the circle, to the only point of the circle which crosses this line. A single local trivialization is sufficient to describe this structure: the fibre bundle is thus trivial ($P = S^1 \times [0, 1]$ globally). In particular, the structure group G has only one generator responsible for the infinitesimal shift of the line segment. The connection, which parallel transports points of the cylinder, moves one value in one fibre to the same exact value in the nearby fibre. After one full cycle on the circle, the point will return to the initial position.

Now, let us cut the edge of the cylinder vertically, invert one of the boundaries and glue it together again. The result of such transformation in Fig. 1.6(b). The surface we obtain in such a way is called a Möbius strip. It is still a fibre bundle with a base manifold – the circle, and a fibre – the line segment $[0, 1]$. However, this is not a trivial bundle anymore, one local trivialization is not sufficient to take into account the twist. The structure group G has two generators: one responsible for the translation and another responsible for the rotation of the unit interval around

[6] In the general case we should distinguish between the vertical and horizontal spaces. We should use an exterior covariant derivative, which acts only on the components of the vectors in the horizontal space.

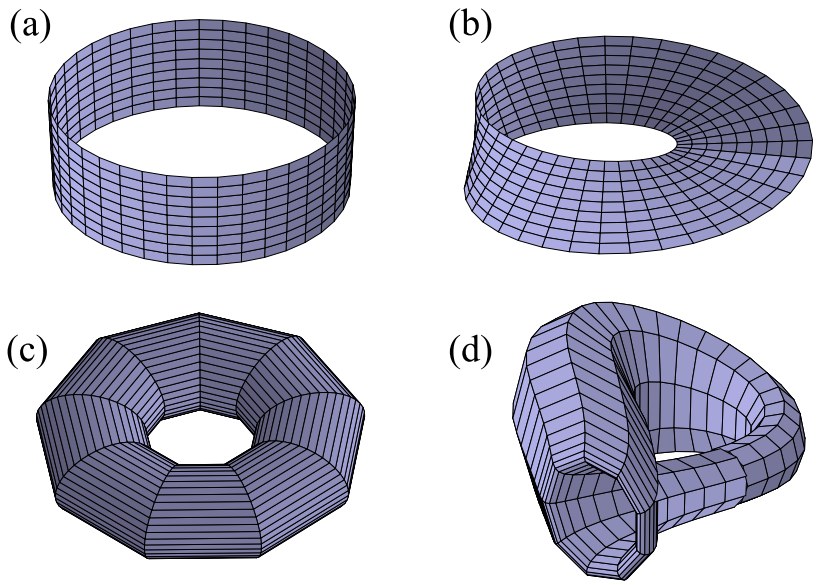

FIGURE 1.6: Non-trivial topology of fibre bundles with the same base manifolds and fibres. A cylinder **(a)** and a Möbius strip **(b)** are both fibre bundles with the base manifold being a circle S_1 and the fibre being a line segment $[0, 1]$. Nevertheless, they can not be transformed from one into the other by means of any homeomorphism: the procedure of cutting-inverting-gluing is necessary. A torus **(c)** and a Klein bottle **(d)** are both fibre bundles with the base manifold and the fibre being a circle S^1. Similarly, we cannot obtain one from the other without using the scissors and the glue.

its center. If we perform a parallel transport along the circle of the base space as previously, we see that the point which started to be transported from the initial position $x \in [0, 1]$ will arrive after one full cycle to the position $1 - x \in [0, 1]$, and the entire line segment will be rotated by 180°. Only after two full cycles it will arrive at the same starting position.

Another simple example is the case of a torus and a Klein bottle (see Fig. 1.6(c-d)). Both these surfaces could be described as S^1 fibre bundles over S^1. The torus is a trivial fibre bundle with $P = S^1 \times S^1$ globally. The Klein bottle however can be obtained by cutting one of the loops of the torus, changing the orientation of one of the boundaries (one of the circles on the edge of the resulting cylinder) and gluing it again. This procedure cannot of course be performed in real life, since it is necessery to make the manifold self-intersect.

Similarly to the case of the Riemannian manifolds (see for example Eqs. (1.48) and (1.49) for details), the geometry of the fibre bundles described in terms of connections (and their curvature) is intimately related to their topology. We could already see this in the case of a Möbius strip and a cylinder: when the topology is trivial, the parallel transport is trivial as well. When the topology is described by a twist, a point is not transported to the same initial position after a full closed path in the base space (this phenomenon generalizes the notion of the holonomy). The relation between the topology and the geometry in complex vector bundles is explained by the Chern-Weil theory of characteristic classes. Characteristic classes describe a way to associate to each principal G-bundle over P a cohomology class of P. At this point we would like to remind the reader of the nature of these cohomology classes. In fact, they are nothing but the elements of the de Rham cohomology groups $H^r(P)$

we already defined in Eq. (1.56)!

As we have seen, the de Rham cohomology groups are topological invariants. Thus, there is no inconsistency in our statement. The idea of the Chern-Weil theory is to understand the topology of the complex vector bundle by simply looking at the special relation between particular closed and exact forms on the base manifold. Like in the previously described case of the Gauss-Bonnet theorem, one could expect that the characteristic classes associated with the curvature 2-form $\mathcal{B}$ would allow us to deduce the topological invariants characterizing the intrinsic curvature or twisting of the fibre bundle. In this context, a very important role is played by so called **Chern classes**. Let us develop this notion in more details. The total Chern class $c(\mathcal{B})$ is defined as

$$c(\mathcal{B}) = \det\left(I + \frac{i\mathcal{B}}{2\pi}\right) = 1 + c_1(\mathcal{B}) + c_2(\mathcal{B}) + \dots \tag{1.67}$$

Different terms $c_i(\mathcal{B})$ that appear in the right hand side of the equation are called Chern classes. The first terms in the sum can be written down explicitly as

$$\begin{aligned} c_1(\mathcal{B}) &= \frac{i}{2\pi}\mathrm{tr}\,(\mathcal{B}) \ , \\ c_2(\mathcal{B}) &= \frac{1}{8\pi^2}\left[\mathrm{tr}\,(\mathcal{B}\wedge\mathcal{B}) - \mathrm{tr}\,(\mathcal{B})\wedge\mathrm{tr}\,(\mathcal{B})\right] \ . \end{aligned} \tag{1.68}$$

We remind the reader that the gauge potentials $\mathcal{A}_j$ and the curvatures $\mathcal{B}_j$ take their values in the Lie algebra $\mathfrak{g}$ of the Lie group G. Hence, the determinant and trace operators are employed in the equation to take this dependency into account. If we are interested in an oriented manifold M, we could integrate the Chern class over the manifold to get an integer topological invariant – the **Chern number**. We notice also that if the dimension of M is equal to $2n$, all the Chern classes higher than n vanish exactly. Thus, the two-dimensional manifolds are described by the unique non-vanishing constant – the first Chern number Ch_1, the 4-dimensional manifolds can have 2 non-vanishing constants (Ch_1 and Ch_2), 6-dimensional manifolds – 3 constants etc.

1.4 Topological band theory

Learning the mathematical tools described in Section 1.3 would be useless for us if we do not find any real application for them in physics. Hopefully, we know already that such mathematical concepts are used in practice, in particular to describe the gauge theories in physics. In this section we want however to provide a few more concrete examples of possible applications, and explain how the notion of topology has become so important in the domain of condensed matter physics of today. By going from the simple examples to more general concepts, we will introduce the notion of topological phases and phase transitions. Finally, we will discuss the role of symmetries in the classification of different types of phase transitions in non-interacting systems, and the bulk-boundary correspondence – one of the most striking experimentally measurable consequence of such topological description.

1.4.1 Berry's connection and Berry's phase

A. Adiabatic evolution argument

Let us reproduce the physical argument, which was initially mentioned by Pancharatnam [22] and later developed and popularized by Berry [23]. We consider

a general model (in any dimensions) for either bosons or fermions described by an Hamiltonian $H(\boldsymbol{X})$. Here $\boldsymbol{X} = \left(X^1, X^2, \ldots, X^r\right)$ refers to a r-dimensional vector which parametrizes the Hamiltonian, *e.g.* the momentum $\boldsymbol{k}$ associated with the translation symmetry as in Section 1.2, the twisted boundary condition phases we will introduce in Section 3.4.4, or any parameter of the physical problem such as the hopping amplitude or the interaction strength. We suppose that the Hamiltonian $H(\boldsymbol{X})$ is diagonalized and its eigenstates are labeled by $|n;\boldsymbol{X}\rangle$, while associated eigenenergies are $\epsilon_n(\boldsymbol{X})$

$$H(\boldsymbol{X})\,|n;\boldsymbol{X}\rangle = \epsilon_n(\boldsymbol{X})\,|n;\boldsymbol{X}\rangle \ . \tag{1.69}$$

Here the index n should be understood as an index associated with the band or energy level. Without any loss of generality we could assume that n is discrete. The set of eigenstates $\{|n;\boldsymbol{X}\rangle\}$ of $H(\boldsymbol{X})$ provides an orthonormal basis of the Hilbert space $\mathcal{HS}(\boldsymbol{X})$ defined at each point of the parameter space.

We prepare a system in the initial state $|\phi(0)\rangle = |n;\boldsymbol{X}_0\rangle$ and we evolve this state adiabatically in time [24] by changing the Hamiltonian through the associated parameter $\boldsymbol{X}$ such that $\boldsymbol{X} = \boldsymbol{X}(t)$ and $\boldsymbol{X}(0) = \boldsymbol{X}_0$. Under such time-dependent protocol the state evolves into

$$|\phi(t)\rangle = \exp\left(-i\int_0^t \epsilon_n\left[\boldsymbol{X}(\tau)\right]\mathrm{d}\tau\right)\exp\left\{i\gamma_n\left[\boldsymbol{X}(t)\right]\right\}|n;\boldsymbol{X}(t)\rangle \ . \tag{1.70}$$

Here we see the apparition of several relevant terms. First of all, if the drive is slow enough, the new state will be an instantaneous eigenstate $|n;\boldsymbol{X}(t)\rangle$ of the Hamiltonian $H\left[\boldsymbol{X}(t)\right]$ up to a phase factor [24]. This phase factor is composed of two terms: the first term in the Eq. (1.70) is the dynamic phase factor which equals the integral of the instantaneous eigenenergy $\epsilon_n\left[\boldsymbol{X}(\tau)\right]$, while the second term $\gamma_n\left[\boldsymbol{X}(t)\right]$ originates from the geometrical properties of the parameter space of the Hamiltonian [23] and is of the primal interest to us. We notice an important condition that ensures the validity of our reasoning based on the adiabatic theorem: we must suppose that the eigenenergy associated with the index n is non-degenerate for any value of the parameter

$$\forall \boldsymbol{X},\ m \neq n \Rightarrow \epsilon_m(\boldsymbol{X}) \neq \epsilon_n(\boldsymbol{X}) \ , \tag{1.71}$$

In such a way that any other state $|m \neq n;\boldsymbol{X}(t)\rangle$ cannot be populated in the process of the adiabatic evolution. Hence we can restrict ourselves to study each band n separately.

By inserting the expression (1.70) into Schroedinger's equation, we find that the geometric phase should verify

$$\frac{d\gamma_n\left[\boldsymbol{X}(t)\right]}{\mathrm{d}t} = i\,\langle n;\boldsymbol{X}(t)|\nabla_{\boldsymbol{X}}|n;\boldsymbol{X}(t)\rangle\cdot\frac{\mathrm{d}\boldsymbol{X}}{\mathrm{d}t} \ . \tag{1.72}$$

As a consequence, when moving along any oriented path $\mathcal{P}$ in the space of $\{\boldsymbol{X}\}$ the state $|\phi(t)\rangle$ will acquire the following additional geometric phase

$$\gamma_n(\mathcal{P}) = i\int_{\mathcal{P}} \mathrm{d}\boldsymbol{X}\cdot\langle n;\boldsymbol{X}|\,\nabla_{\boldsymbol{X}}\,|n;\boldsymbol{X}\rangle \ , \tag{1.73}$$

where $\mathrm{d}\boldsymbol{X}$ is an infinitesimal element of the path. For any given band n the differential 1-form

$$\mathcal{A}^n(\boldsymbol{X}) = \mathcal{A}^n_\mu(\boldsymbol{X})\mathrm{d}X^\mu = i\langle n;\boldsymbol{X}|\nabla_{\boldsymbol{X}}|n;\boldsymbol{X}\rangle\cdot\mathrm{d}\boldsymbol{X} = i\langle n;\boldsymbol{X}|\,\mathrm{d}\,|n;\boldsymbol{X}\rangle \tag{1.74}$$

is called a **Berry's connection**. In components it is written down as

$$\mathcal{A}^n_\mu(\boldsymbol{X}) = i\left\langle n;\boldsymbol{X}\left|\frac{\partial}{\partial X^\mu}\right|n;\boldsymbol{X}\right\rangle\ . \tag{1.75}$$

The integral of the Berry's connection along the oriented closed contour $\mathcal{C}$, *i.e.* the geometric phase acquired over the course of a cyclic adiabatic evolution is called a **Berry's phase** and will be denoted by γ_{Berry} in the rest of the manuscript:

$$\gamma_{\text{Berry}} = i\oint_{\mathcal{C}}\mathrm{d}\boldsymbol{X}\cdot\langle n;\boldsymbol{X}|\nabla_{\boldsymbol{X}}|n;\boldsymbol{X}\rangle\ . \tag{1.76}$$

Let us now have another look at the physical problem we just presented. In quantum mechanics the states $|n;\boldsymbol{X}\rangle$ cannot be distinguished (except if we perform an interference experiment) if they differ only by a phase factor: $|n;\boldsymbol{X}\rangle \sim e^{i\chi}|n;\boldsymbol{X}\rangle$. Physical states are thus expressed in terms of the equivalence classes

$$[|n;\boldsymbol{X}\rangle] = \{g\,|n;\boldsymbol{X}\rangle\,|g\in U(1)\}\ , \tag{1.77}$$

forming the so-called projective Hilbert space [7]. If the phase factor $g(\boldsymbol{X}) = e^{i\chi(\boldsymbol{X})}$ depends on the parameter $\boldsymbol{X}$ this is the formulation of gauge invariance. Now, we see that our system corresponds to a principal bundle, where the base manifold M is the parameter space $\{\boldsymbol{X}\}$ and the fibre G is the abelian unitary group $U(1)$ [8]. The projection from the total space to the base manifold is given by $\pi(g\,|n;\boldsymbol{X}\rangle) = |n;\boldsymbol{X}\rangle$. The adiabatic evolution is nothing else, but the parallel transport of the state $|\phi\rangle = |n;\boldsymbol{X}\rangle$ in the parameter space $\{\boldsymbol{X}\}$. It is completely determined by the Hamiltonian $H(\boldsymbol{X})$ – an additional structure we have in the physical system as compared to the bare principal bundle definition. The parallel transport in the manifold M could be studied by defining a connection 1-form, which is exactly the Berry's connection $\mathcal{A}^n(\boldsymbol{X})$. We notice that Berry's connection is gauge-dependent and transforms under the gauge transformation $|n;\boldsymbol{X}\rangle \to e^{i\chi(\boldsymbol{X})}|n;\boldsymbol{X}\rangle$

$$\mathcal{A}^n_\mu(\boldsymbol{X}) \to \mathcal{A}^n_\mu(\boldsymbol{X}) + \frac{\partial\chi(\boldsymbol{X})}{\partial X^\mu}\ . \tag{1.78}$$

This is exactly the re-expression of Eq. (1.61).

On the contrary, Berry's phase is quasi gauge-independent in the sense that it can change only by an integer multiple of 2π. For any oriented closed contour $\mathcal{C}$ and a gauge phase $\chi(\boldsymbol{X})$ (we suppose that the contour lies entirely in the open subset U, where the gauge transformation is defined) we have

$$\oint_{\mathcal{C}}\mathrm{d}\boldsymbol{X}\cdot\nabla_{\boldsymbol{X}}\chi(\boldsymbol{X}) = 0\ . \tag{1.79}$$

In the equation above, the only way a non-zero value can appear is when the fibre bundle is non-trivial, so that we cannot use the same vector potential defined everywhere and several gauge transformations are required. Nevertheless, even in

[7] We assume in addition that we work with the set of normalized states.

[8] Notice that the assumption of having non-degenerate eigenenergies $\{\epsilon_n\}$ is crucial here.

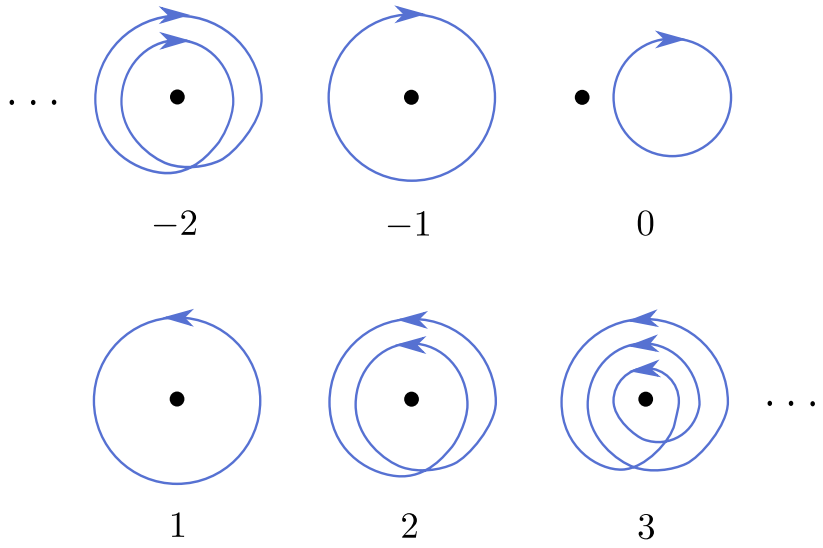

FIGURE 1.7: In 1D non-interacting condensed matter systems with chiral symmetry described by Eq. (1.81), the Hamiltonian H corresponds to a mapping from a circle S^1 composed of the momenta k in the first BZ, to another circle S^1 which describes how the operator acts on the Hilbert space. Such mapping has a non-trivial first homotopy group $\pi_1(S^1)$ and a topological invariant – the winding number. The winding number represents the total number of times the curve $H(k)$ travels clockwise or counter-clockwise around the origin. If we imagine such curves in the plane $\mathbb{R}^2 - \{0\}$, which is homotopic to a circle, we intuitively see that there is no way the curve with the winding number n can be deformed into a curve with the winding number $m \neq n$ without crossing the origin.

this case the integral should necessarily be a multiple of 2π and account for the discontinuities in the choice of χ. This does not imply however that the Berry's phase itself has to remain zero for any closed path. As was first pointed out by Simon [25], the geometrical meaning underlying the Berry's phase is the holonomy associated to the parallel transport in the parameter space. The cases when such holonomy is non-trivial are the most interesting to us.

B. Zak phase

Finally, we want to make a connection to the topological characterization of condensed matter systems by mentioning a few particular examples of such systems which are known to host topological phases (*i.e.* phases described by some non-trivial topological invariants). For instance, we would like to limit ourselves to the case of 1D systems and we will address the question of 2D systems in Section 1.4.2.

In 1D systems, due to translation invariance, the bulk Hamiltonians are described by the Zak phase [26], which is nothing but the integration of the Berry connection over the first BZ:

$$\gamma^n_{\text{Zak}} = i \oint_{\text{BZ}} \mathrm{d}k \, \langle n;k| \, \partial_k \, |n;k\rangle \ . \tag{1.80}$$

Here the role of the parameter $\boldsymbol{X}$ is played by the momentum k associated with the translation symmetry, which is a 1D parameter living on a circle S^1 (see Section 1.2). This is one of simplest possible Bloch bundles over a one-dimensional base space.

Let us suppose that we work with a two-band Bloch Hamiltonian, in which two bands will be denoted as $|\pm;k\rangle$. Such Hamiltonian can be written in the most general form as follows

$$\mathcal{H}(k) = \mu I_2 + d\left(u^j(k)\sigma_j\right) \ . \tag{1.81}$$

Here I_2 is the identity 2×2 matrix, σ_j are 3 Pauli matrices, $\boldsymbol{u}(k)$ is some unitary three-dimensional vector, and μ and d are two constants which have the dimension of the energy. The expression of $\boldsymbol{u}(k)$, μ and d depends on the exact form of the Hamiltonian. The integral (1.80) determines a topological invariant associated to the mapping from a circle S^1 to a sphere S^2 described by the vector $\boldsymbol{u}(k)$. It is intimately related to the first homotopy group $\pi_1(S^2)$. We know however that such homotopy group is trivial: any closed path on a sphere can be shrunk to a single point. Hence, our conclusion is that in general case any phase describing a 1D condensed matter system does not differ from a trivial phase from the topological point of view. Here, by a topologically trivial phase we mean a trivial insulator, described for example by $\boldsymbol{u}(k) = \boldsymbol{e}_z$.

Hopefully, this is not the end of the story. In reality, we have additional constraints – the symmetries, which restrict the space of available Hamiltonians we should consider. We will discuss this phenomenon in much greater details in Section 1.4.4. Here we just want to mention a few relevant examples. In the presence of chiral symmetry, the Hamiltonian is described by a vector $\boldsymbol{u}(k)$ living in the xy plane (*i.e.* $u^z(k) = 0$). Thus, instead of a mapping from a circle to a sphere, the system is described by a mapping from a circle to a circle, and we know that the associated first homotopy group $\pi_1(S^1) = \mathbb{Z}$ is non-trivial. Indeed, in the case of such two-band models, the eigenstates are

$$|\pm;\, k\rangle = \begin{pmatrix} u_x - iu_y \\ \pm 1 \end{pmatrix} \ , \tag{1.82}$$

and the Zak phase could be written as

$$\gamma^{\pm}_{\text{Zak}} = \frac{1}{2}\oint_{\text{BZ}} \mathrm{d}k\,(\boldsymbol{u}\times\partial_k\boldsymbol{u})\cdot\boldsymbol{e}_z = \frac{1}{2}\oint_{\text{BZ}} \mathrm{d}k\left(u_x\partial_k u_y - u_y\partial_k u_x\right) \ . \tag{1.83}$$

It acquires two distinct values, equal to 0 or π, depending on the parameters of the problem. It is also related to the winding number representing the total number of times the curve described by $\boldsymbol{u}(k)$ travels clockwise or counter-clockwise around the origin (see Fig. 1.7). Celebrated examples of 1D models describing such kind of systems are Su-Schrieffer–Heeger model for polyacetylene [27, 28] (see Section 4.4) and the p-wave superconducting Kitaev's wire [29, 30].

1.4.2 Berry's curvature and the first Chern number

A. Definitions

Previously (see Section 1.4.1), we have introduced the notions of Berry's connection and Berry's phase, which, among others, play an important role to describe the topological phase transitions. In the case where the oriented closed contour $\mathcal{C}$ in the parameter space $\{\boldsymbol{X}\}$ represents the boundary of a higher-dimensional manifold $\mathcal{S}$, Stokes' theorem can be employed to rewrite the expression of the Berry's phase in a

more convenient form, which involves the external derivative of the Berry's connection, called **Berry's curvature**

$$\mathcal{B}^n(\boldsymbol{X}) = \mathcal{B}^n_{\mu\nu}(\boldsymbol{X})\, \mathrm{d}X^\mu \mathrm{d}X^\nu = \mathrm{d}A^n(\boldsymbol{X}) = (\mathrm{d}\,\langle n;\boldsymbol{X}|) \wedge (\mathrm{d}\,|n;\boldsymbol{X}\rangle)\ . \tag{1.84}$$

In components it is written as follows

$$\mathcal{B}^n_{\mu\nu}(\boldsymbol{X}) = \frac{\partial A^n_\nu(\boldsymbol{X})}{\partial X^\mu} - \frac{\partial A^n_\mu(\boldsymbol{X})}{\partial X^\nu}\ . \tag{1.85}$$

In particular, according to Stokes' theorem, we have

$$\gamma_{\text{Berry}} = \oint_{\mathcal{C}} \mathrm{d}X^\mu \mathcal{A}^n_\mu(\boldsymbol{X}) = \int_{\mathcal{S}} \mathrm{d}X^\mu \wedge \mathrm{d}X^\nu\ \mathcal{B}^n_{\mu\nu}(\boldsymbol{X})\ , \tag{1.86}$$

where $\mathrm{d}X^\mu \wedge \mathrm{d}X^\nu$ is an infinitesimal element of the surface $\mathcal{S}$. Berry's curvature defined in this way is a real antisymmetric second-rank tensor and corresponds exactly to the curvature 2-form from Eq. (1.65). For a 2D parameter space it is also written sometimes as a rotational of the vector $\boldsymbol{\mathcal{A}}^n(\boldsymbol{X})$ as

$$\boldsymbol{\mathcal{B}}^n(\boldsymbol{X}) = \nabla_{\boldsymbol{X}} \times \boldsymbol{\mathcal{A}}^n(\boldsymbol{X})\ , \tag{1.87}$$

where the vector $\boldsymbol{\mathcal{A}}^n(\boldsymbol{X})$ is associated to the Berry's connection 1-form $\mathcal{A}^n(\boldsymbol{X})$ [9]. We notice that Berry's curvature is explicitly gauge invariant (in particular, the rotational of the gradient is zero). This will allow us to use it more efficiently in numerical calculations.

The integral of the Berry's curvature over any closed 2D manifold $\mathcal{S}$ is quantized to be 2π times an integer Ch^n_1. This is a result of the Chern-Weil theory of classification of fibre bundles, and the integer Ch^n_1 is a topological invariant called **first Chern number** (see Eqs. (1.67) and (1.68) or more generally Section 1.3 for more details):

$$Ch^n_1 = \frac{1}{2\pi} \oint_{\mathcal{S}} \mathrm{d}X^\mu \wedge \mathrm{d}X^\nu\ \mathcal{B}^n_{\mu\nu}(\boldsymbol{X})\ . \tag{1.88}$$

We also notice the similarity between the Berry's connection $\boldsymbol{\mathcal{A}}^n(\boldsymbol{X})$ and the electromagnetic vector potential, as well as between the Berry's curvature $\boldsymbol{\mathcal{B}}^n(\boldsymbol{X})$ and the magnetic vector field. Our notation is made explicit to outline this similarity and an intuitive understanding of the objects we introduced based on classical electrodynamics. In particular, the first Chern number could be understood in this interpretation as a magnetic Dirac monopole.

B. Many sides of the first Chern number through the examples

Sometimes, it could be convenient to write the Berry curvature and the Chern number in terms of a projector operator on the n-th band $\mathcal{P}_n(\boldsymbol{X}) = |n;\boldsymbol{X}\rangle\,\langle n;\boldsymbol{X}|$ in the following way [31]

$$Ch^n_1 = \frac{i}{2\pi} \int_{\text{BZ}} \mathrm{tr}\,(\mathrm{d}P_n(\boldsymbol{X}) \wedge [P_n(\boldsymbol{X})\mathrm{d}P_n(\boldsymbol{X})])\ . \tag{1.89}$$

For example, if we are interested in a fermionic system, which has a given number of occupied bands below, and empty bands above the Fermi energy ϵ_F, we could use

[9] We remind that any covector *i.e.* a differential 1-form can be "converted" to a vector using the metric.

the projector $P_{\text{occ}}(\boldsymbol{X}) = \sum_{\epsilon_n < \epsilon_F} P_n(\boldsymbol{X})$ on all the occupied bands in order to calculate the Chern number associated to such separation.

Let us now consider a particular case of a topological description of the 2D Bloch bundle. If we have a 2D model with translation symmetry, the Hamiltonian can be diagonalized in momentum space, so that the momentum $\boldsymbol{k}$ plays the role of a 2D parameter $\boldsymbol{X}$, living on a two-dimensional torus $T^2 = S^1 \times S^1$. The Berry connection and the Berry curvature can then be written as

$$\begin{aligned} \boldsymbol{\mathcal{A}}^n(\boldsymbol{k}) &= i \langle n;\boldsymbol{k}| \left(\partial_{\boldsymbol{k}} |n;\boldsymbol{k}\rangle\right) , \\ \mathcal{B}^n_{xy}(\boldsymbol{k}) &= -2\mathfrak{Im}\left(\partial_{k_x} \langle n;\boldsymbol{k}| \right)\left(\partial_{k_y} |n;\boldsymbol{k}\rangle\right) . \end{aligned} \tag{1.90}$$

The first Chern number Ch_1^n is expressed in terms of the Berry's phase acquired by the state $|n;\boldsymbol{k}\rangle$ when moving around the boundary of the first BZ (defining the closed oriented contour $\mathcal{C}$):

$$Ch_1^n = \frac{1}{2\pi} \oint_{\mathcal{C}} \mathrm{d}\boldsymbol{k} \cdot \boldsymbol{\mathcal{A}}^n(\boldsymbol{k}) = \frac{1}{2\pi} \int_{\text{BZ}} \mathrm{d}k_x \mathrm{d}k_y \mathcal{B}^n_{xy}(\boldsymbol{k}) . \tag{1.91}$$

By rewriting Eq. (1.89) in this particular case, we get:

$$Ch_1^n = \frac{i}{2\pi} \int_{\text{BZ}} \mathrm{d}k_x \mathrm{d}k_y \ \text{tr}\left(\mathcal{P}_n(\boldsymbol{k}) \cdot \left[\partial_{k_x}\mathcal{P}_n(\boldsymbol{k}), \partial_{k_y}\mathcal{P}_n(\boldsymbol{k})\right]\right) . \tag{1.92}$$

For any 2-band Hamiltonian

$$\mathcal{H}(\boldsymbol{k}) = \mu I_2 + d\left(u^j(\boldsymbol{k})\sigma_j\right) , \tag{1.93}$$

the projectors on the upper and lower bands could be indexed by $\pm$ and written in a simple form

$$\mathcal{P}_{\pm}(\boldsymbol{k}) = \frac{I_2 \pm u^j(\boldsymbol{k})\sigma_j}{2} . \tag{1.94}$$

This leads to the following simplified expression of the first Chern number

$$Ch_1^{\pm} = \mp \frac{1}{4\pi} \int_{\text{BZ}} \mathrm{d}k_x \mathrm{d}k_y \ \left(\boldsymbol{u}(\boldsymbol{k}) \cdot \left[\partial_{k_x}\boldsymbol{u}(\boldsymbol{k}) \times \partial_{k_y}\boldsymbol{u}(\boldsymbol{k})\right]\right) . \tag{1.95}$$

Here we recognize the expression of a topological invariant associated to the mapping from a torus T^2 to a sphere S^2. This topological invariant is an integer number that belongs to the homotopy group of a torus $\pi_2(T^2) = \mathbb{Z}$, known to be non-trivial. It corresponds to a winding number counting the amount of times the unit vector $\boldsymbol{u}(\boldsymbol{k})$ wraps around the origin while $\boldsymbol{k}$ is spanning the whole BZ. Well known examples of systems which exhibit a topological phase transition detectable via calculation of the Chern number, and which are described by the Hamiltonian (1.93), are the Haldane model for the quantum anomalous Hall effect [32] (see Section 2.1) and the $p_x + ip_y$ chiral superconductors [33, 34].

Another important example of non-interacting systems whose phases are described by the first Chern number is the integer quantum Hall effect which occurs in 2D semiconductor materials subjected to strong magnetic fields. As was originally shown by Thouless, Kohmoto, Nightingale, and den Nijs [35, 36], the transverse conductivity σ_{xy} of the quantum Hall system can be expressed using the Kubo formula

in the following way

$$\sigma_{xy} = ih \sum_{\epsilon_n < \epsilon_F < \epsilon_m} \int_{\mathrm{BZ}} \frac{\mathrm{d}k_x \mathrm{d}k_y}{(2\pi)^2} \frac{\langle n;\boldsymbol{k} \,|\, J_y \,|\, m;\boldsymbol{k}\rangle \langle m;\boldsymbol{k} \,|\, J_x \,|\, n;\boldsymbol{k}\rangle - \langle n;\boldsymbol{k} \,|\, J_x \,|\, m;\boldsymbol{k}\rangle \langle m;\boldsymbol{k} \,|\, J_y \,|\, n;\boldsymbol{k}\rangle}{(\epsilon_m(\boldsymbol{k}) - \epsilon_n(\boldsymbol{k}))^2} \,. \tag{1.96}$$

Here the index n runs over the filled bands, m runs over unfilled bands and the Fermi energy ϵ_F is supposed to lie in the gap between them. Operator

$$\boldsymbol{J} = e\nabla_{\boldsymbol{k}} H/h \tag{1.97}$$

is called a current operator and e denotes the electron charge. By using the identity

$$\langle n;\boldsymbol{k} \,|\, \partial_{k_i} H \,|\, m;\boldsymbol{k}\rangle = (\epsilon_m - \epsilon_n) \langle n;\boldsymbol{k}| \left(\partial_{k_i} |m;\boldsymbol{k}\rangle\right) = (\epsilon_n - \epsilon_m) \left(\partial_{k_i} \langle n;\boldsymbol{k}|\right) |m;\boldsymbol{k}\rangle \,, \tag{1.98}$$

it is easy to show that the quantum Hall conductivity is proportional to the sum of the Chern numbers of all filled bands

$$\sigma_{xy} = \frac{e^2}{h} \sum_{\epsilon_n < \epsilon_F} Ch_1^n \,, \tag{1.99}$$

which explains its experimentally observed robustness and perfect quantization.

Remark on the numerical implementation

In our work we were often interested in calculating numerically Berry's connection, Berry's curvature and the first Chern number. Naively it seems that the best way to proceed consists in applying directly Eqs. (1.75) and (1.85) (or in some more particular cases Eqs. (1.90)). Clearly, calculating the Berry's connection directly should be avoided, since this is not a gauge invariant quantity. One does not expect however to have problems in calculating other two quantities of our interest. Nevertheless, the disadvantage of the straightforward application of Eq. (1.85) (or also Eq. (1.90)) is that it employs derivatives of the states $|n;\boldsymbol{X}\rangle$. The only way to calculate such derivatives numerically is by using finite difference methods. These methods however are not gauge invariant since we need to calculate sums or differences of several states at different points in the parameter space, each of which comes with its own choice of the gauge. As a consequence, if we want to proceed in this way, we are obliged to fix the gauge. Still, other possibilities are available. In particular, Eqs. (1.92) and (1.96) provide us with an explicitly gauge independent formulas. Otherwise, the Wilson loop approach could also be employed [37].

1.4.3 Topological phase transitions

In the previous subsections we tried to give a first glance on various topological phases which appear in condensed matter systems. In particular, we have shown several examples of systems which could host phases described by non-trivial topological invariants, such as the holonomy of a quantum state in 1D (see Section 1.4.1) or the first Chern number in 2D (see Section 1.4.2). Now, we would like to generalize this notion, and address the question of what happens at the transition between such phases.

First of all, we notice that by defining the Hamiltonian $H(\boldsymbol{X})$ we actually introduce a mapping from the parameter space $\{\boldsymbol{X}\}$ to the space of hermitian operators

$\mathcal{HO}(N)$ acting on the Hilbert space $\mathcal{HS}(\boldsymbol{X})$

$$H : \{\boldsymbol{X}\} \to \mathcal{HO}(N) \ . \tag{1.100}$$

Here N denotes the dimension of the Hilbert space. The set of eigenstates $\{|n;\boldsymbol{X}\rangle\}$ of $H(\boldsymbol{X})$ provides an orthonormal basis of $\mathcal{HS}(\boldsymbol{X})$ at each point $\boldsymbol{X}$ of the parameter space. For example, if $N = 2$, the basis is formed by two spinors, and the Hamiltonian operator has a general matrix form presented in Eq. (1.81). Let us now consider an adiabatic evolution of a state $|n;\boldsymbol{X}\rangle$ along some path $\mathcal{P}$ in the parameter space $\{\boldsymbol{X}\}$. We suppose that at each point $\boldsymbol{X}$ the set of eigenvalues $\{\epsilon_n(\boldsymbol{X})\}$ of $H(\boldsymbol{X})$ is non-degenerate, so that the adiabatic theorem is applicable. By using a smooth homotopy transformation

$$F : \{\boldsymbol{X}\} \times [0,1] \to \mathcal{HO}(N) \ , \tag{1.101}$$

such that

$$F(\boldsymbol{X},0) = H(\boldsymbol{X}), \quad F(\boldsymbol{X},1) = H'(\boldsymbol{X}) \ , \tag{1.102}$$

we can transform the Hamiltonian H into another Hamiltonian H'. In such a way we deform the adiabatic evolution along the path P and change the energy structure of the problem. However, a smooth transformation cannot affect the topology of the bands, *i.e.* energy levels $\{\epsilon'_n(\boldsymbol{X})\}$ will still remain non-degenerate everywhere in the parameter space and along the path $\mathcal{P}$. Hence, topological description of the system will be unaffected as well.

The only way to change the topology of the system consists in applying a discontinuous transformation, which leads to the emergence of degeneracies in the spectrum

$$\exists\, m, \boldsymbol{X} \text{ s.t. } \epsilon'_n(\boldsymbol{X}) = \epsilon'_m(\boldsymbol{X}) \ . \tag{1.103}$$

In this scenario, we cannot apply the Berry's argument anymore because of the invalidity of the adiabatic theorem. In other words, instead of a simple $U(1)$ principal bundle, we should follow the parallel transport in the vector bundle, where the fibre vector space is generated by two (or even more) states $|n;\boldsymbol{X}\rangle$ and $|m;\boldsymbol{X}\rangle$ of the Hilbert space. At this particular moment, which is called a **critical regime**, transforming the Hamiltonian by a continuous transformation F allows to "rotate" one basis state into another one. It is thus possible to "re-glue" the principal bundle in a different way when moving away from the critical point and change its topological properties. Such critical regime could correspond to a point in the parameter space, called **critical point**, or to a line called **critical line**, etc.

Finally, this reasoning allows us to define more generally the notion of **topological phases** in condensed matter. We say that the phase is topological, if it cannot be deformed into a topologically trivial phase by means of any continuous transformation without passing through the critical regime. The notion of a topologically trivial phase should be introduced separately, but usually it refers to a trivial product state in quantum mechanics. Such state could be described for example by a set of diagonal matrices $D_N \in \mathcal{HO}(N)$ with coefficients $D_{N,ij} = i\delta_{ij}$ defined at each point $\boldsymbol{X}$ in the parameter space. If we are interested in studying a gapped fermionic ground-state, the relevant matrix associated to a topologically trivial state could be chosen as

$$\begin{pmatrix} I_n & 0 \\ 0 & -I_m \end{pmatrix} \ , \tag{1.104}$$

where n is the number of empty bands above the Fermi energy, which is supposed to

be fixed inside the gap, m – the number of occupied bands below the Fermi energy, and $n + m = N$.

1.4.4 Symmetry protected topological states

Often we are interested in restricting the space of allowed hermitian operators $\mathcal{HO}(N)$ from Eq. (1.100), acting on the Hilbert space $\mathcal{HS}(\boldsymbol{X})$ over the parameter space $\{\boldsymbol{X}\}$. This happens when the model we are interested in has some symmetry constraints. In this case the topological properties of the states will be protected as long as two conditions are verified: the system is not at (or has not passed through) the critical regime, and the symmetry in question is preserved. This leads to the definition of a **symmetry protected topology** (SPT) and symmetry protected topological states.

We have already mentioned the role of the translation symmetry in Section 1.2. It implies in particular that the Hamiltonian $H(\boldsymbol{X})$ should be block-diagonal, with each block $H_{\boldsymbol{k}}(\boldsymbol{X})$ corresponding to a different momentum sector $\boldsymbol{k}$. Previously, $\boldsymbol{X}$ represented to us a set of parameters of the model and we omitted writing it explicitly. It occurs that such consideration of symmetries is very useful to perform a general classification of the topological phases of matter. However, not all the symmetries are crucial for us. To justify this point, let us first recall how symmetries work. We suppose that an automorphism S is a symmetry transformation acting on the Hilbert space $\mathcal{HS}$. It should leave invariant the physical properties of the system, *i.e.* preserve the absolute value of the scalar product. Then, according to Wigner's theorem, only two possibilities could happen: either S is linear and unitary

$$\langle S\psi, S\left(\lambda_1\phi_1 + \lambda_2\phi_2\right)\rangle = \lambda_1\langle\psi,\phi_1\rangle + \lambda_2\langle\psi,\phi_2\rangle \ , \tag{1.105}$$

or S is antilinear and antiunitary

$$\langle S\psi, S\left(\lambda_1\phi_1 + \lambda_2\phi_2\right)\rangle = \lambda_1^*\langle\phi_1,\psi\rangle + \lambda_2^*\langle\phi_2,\psi\rangle \ . \tag{1.106}$$

The symmetries that are the most interesting for us correspond to antiunitary transformations. This is due to the fact that a unitary symmetry transformation has to commute with the Hamiltonian operator. Hence, we can always block-diagonalize the Hamiltonian and reduce the problem to the independent study of each separate block. Antiunitary symmetries however impose certain constraints on the irreducible blocks of the Hamiltonian. We also notice that any antiunitary transformation S can be written as a product of a unitary transformation U and a complex conjugation operator K

$$S = UK \ . \tag{1.107}$$

As a result, it should necessarily square to I_N or $-I_N$.

The two symmetries which play a particularly important role in physics are time-reversal symmetry and particle-hole symmetry. In particular, exactly these two symmetries lie at the basis of the topological classification of non-interacting states of matter, known also as the ten-fold way. The time-reversal symmetry operator T maps the time-evolution operator at t to the time-evolution operator at $-t$

$$T\exp\left(-itH\right)T^{-1} = \exp\left(itH\right), \quad THT^{-1} = H \ . \tag{1.108}$$

For fermions in second quantization, the corresponding operation can be described by the action of T on the creation and annihilation operators

$$Tc_jT^{-1} = U_{T,jk}c_k, \quad TiT^{-1} = -i \ , \tag{1.109}$$

	T^2	P^2	C^2	d	1	2	3	4	5	6	7	8
A	0	0	0		$\varnothing$	$\mathbb{Z}$	$\varnothing$	$\mathbb{Z}$	$\varnothing$	$\mathbb{Z}$	$\varnothing$	$\mathbb{Z}$
AIII	0	0	1		$\mathbb{Z}$	$\varnothing$	$\mathbb{Z}$	$\varnothing$	$\mathbb{Z}$	$\varnothing$	$\mathbb{Z}$	$\varnothing$
AII	−1	0	0		$\varnothing$	$\mathbb{Z}_2$	$\mathbb{Z}_2$	$\mathbb{Z}$	$\varnothing$	$\varnothing$	$\varnothing$	$\mathbb{Z}$
DIII	−1	+1	+1		$\mathbb{Z}_2$	$\mathbb{Z}_2$	$\mathbb{Z}$	$\varnothing$	$\varnothing$	$\varnothing$	$\mathbb{Z}$	$\varnothing$
D	0	+1	0		$\mathbb{Z}_2$	$\mathbb{Z}$	$\varnothing$	$\varnothing$	$\varnothing$	$\mathbb{Z}$	$\varnothing$	$\mathbb{Z}_2$
BDI	+1	+1	+1		$\mathbb{Z}$	$\varnothing$	$\varnothing$	$\varnothing$	$\mathbb{Z}$	$\varnothing$	$\mathbb{Z}_2$	$\mathbb{Z}_2$
AI	+1	0	0		$\varnothing$	$\varnothing$	$\varnothing$	$\mathbb{Z}$	$\varnothing$	$\mathbb{Z}_2$	$\mathbb{Z}_2$	$\mathbb{Z}$
CI	+1	−1	+1		$\varnothing$	$\varnothing$	$\mathbb{Z}$	$\varnothing$	$\mathbb{Z}_2$	$\mathbb{Z}_2$	$\mathbb{Z}$	$\varnothing$
C	0	−1	0		$\varnothing$	$\mathbb{Z}$	$\varnothing$	$\mathbb{Z}_2$	$\mathbb{Z}_2$	$\mathbb{Z}$	$\varnothing$	$\varnothing$
CII	−1	−1	+1		$\mathbb{Z}$	$\varnothing$	$\mathbb{Z}_2$	$\mathbb{Z}_2$	$\mathbb{Z}$	$\varnothing$	$\varnothing$	$\varnothing$

TABLE 1.1: Periodic table of topological insulators and superconductors showing ten symmetry classes of the non-interacting fermion problem. The first column represents the Altland-Zirnbauer symmetry classes. The columns labeled by T, P and C show the presence (± 1) or the absence (0) of time-reversal, particle-hole, and chiral symmetries. The entry is 1 if the symmetry transformation squares to I_N or -1 if it squares to $-I_N$. The last column describes the set of topological invariants associated to each symmetry class depending on the space dimension d of the system.

where U_T is a unitary rotation. The particle-hole symmetry transformation (called also a charge conjugation) maps a particle to its "antiparticle". In second quantization, it is expressed as

$$Pc_jP^{-1} = U_{P,jk}c_k^\dagger, \quad PiP^{-1} = -i\,, \tag{1.110}$$

where U_P is another unitary operator. Finally, we notice that the product $C = PT$ also represents a symmetry transformation, called a chiral symmetry. This is a unitary symmetry

$$Cc_jC^{-1} = U_{P,jk}U_{T,kl}c_l^\dagger, \quad CiC^{-1} = i\,. \tag{1.111}$$

Usually (but not always), it corresponds to a lattice $\mathbb{Z}_2$ symmetry. Thus, it is often called a sublattice symmetry. Its presence in this list is justified by the fact that even if T and P are not symmetries of the Hamiltonian, their product can still be a symmetry.

If now we count all the possibilities, there are $3 \times 3 = 9$ possible scenarios corresponding to different values of T and P, which we denote as 0 if they are not symmetries, or ± 1 depending on whether they square to I_N or $-I_N$. If both T and P are 0, we could have C equal to 0 or 1, which gives us the total number of $3 \times 3 - 1 + 2 = 10$ symmetries of the ten-fold way. Such classification was first performed by Altland and Zirnbauer [38], who made the connection to the classification of symmetric spaces in differential geometry discovered by Cartan in 1926. It generalized the preceding work by Wigner and Dyson [39] who relied on the time-reversal symmetry only. The 10 different symmetry classes, also called Altland-Zirnbauer classes, are presented in Table 1.1. For each symmetry class of the ten-fold way and a real space dimension d of the problem, entries $\mathbb{Z}$, $\mathbb{Z}_2$ or $\varnothing$ denote the set of accessible values of topological invariants. There exist several approaches to deduce these entries. One of the approaches proposed by Kitaev is based on the precise analysis of the algebraic structure of Clifford algebras and the so-called K-theory [40]. Another approach developed by Ryu, Schnyder, Furusaki and Ludwig is based on the Anderson localization theory [41, 42]. It relies on the remarkable property of topological

states – the presence of edge modes stable against a very large range of perturbations (we will describe this phenomenon in Section 1.4.5), and the long wavelength description of the associated Anderson localization problem in terms of a non-linear sigma model in the given symmetry class. Both approaches and the underlying concepts are also described in much greater details in the excellent reviews [43–45].

To be more explicit, let us provide a few well known examples of models with topological phase transitions. All the systems in this classification correspond to either insulators or superconductors, that originates from the necessity of having non-critical, *i.e.* gapped states of matter. The class *A* unifies the systems with no symmetries. In 2D such systems are described by $\mathbb{Z}$ topological invariant – the first Chern number. This corresponds to the celebrated integer quantum Hall effect [11, 35], or also the Haldane model for quantum anomalous Hall effect [32] (see Section 2.1). "Generalization" of the Haldane model – the Kane-Mele model [46, 47], is composed of two "copies" of the Haldane model with restored time-reversal symmetry. It belongs to the *AII* Altland-Zirnbauer class and is described by $\mathbb{Z}_2$ topological invariants (see Section 3.1). If instead of the time-reversal symmetry we have added a particle-hole (or charge conjugation) symmetry, we would arrive at the class *D*, which describes, for example, 2D *p*-wave superconductors. In one dimension, most of the phases are reminiscent of the Kitaev *p*-wave superconductor [29] and the Su-Schrieffer-Heeger model [27] (see Section 4.4), that belong to the *BDI* class.

Finally, we notice that the topological classification briefly presented in this section is a valid classification for fermionic ground-states, but not for bosonic ones. A priori, all non-interacting state of bosons have to be topologically trivial for a simple reason that the bosons do not see an intricate structure of the energy levels. Instead, they condense at the bottom of the lowest energy band and form a superfluid phase. Nevertheless, this is true only if we study the equilibrium properties of the ground-state. Various approaches could allow us to study the non-equilibrium properties of the system and probe the non-trivial topology of the band by using bosons. Such approaches could be based on photonic excitations in quantum circuits or bosonic particles in ultra-cold atoms experiments (see Chapter 4 for more details).

1.4.5 Bulk-boundary correspondence

After reading a long discussion on the topological properties of various condensed matter systems, one could ask a question, what are the physical impact and the utility of such concepts? The first experimental motivation originates from the discovery of the integer quantum Hall effect by Klitzing, Dorda and Pepper [11], who observed that the semiconductor materials confined in a 2D geometry subjected to strong magnetic fields are described by the presence of very robust, perfectly quantized edge modes crossing the gap between different Landau levels. Only later this property was related to the topological description of the systems [35] and intrinsic properties of the materials independent of the strength of the applied external magnetic field [32]. Developing this idea allowed to discover both theoretically [46–48] and experimentally [49] the role of symmetries and new kinds of topological phases, as well as new kinds of edge modes. A breakthrough in this direction occurred with the seminal work by Kane and Mele [46, 47] and the discovery of the quantum spin Hall effect, which does not require the presence of any magnetic field at all (this model will be described in greater details in Section 3.1). The subsequent topological classification [40–42] went further beyond the quantum Hall materials paradigm. Nevertheless, one of the main physical consequences still remains the

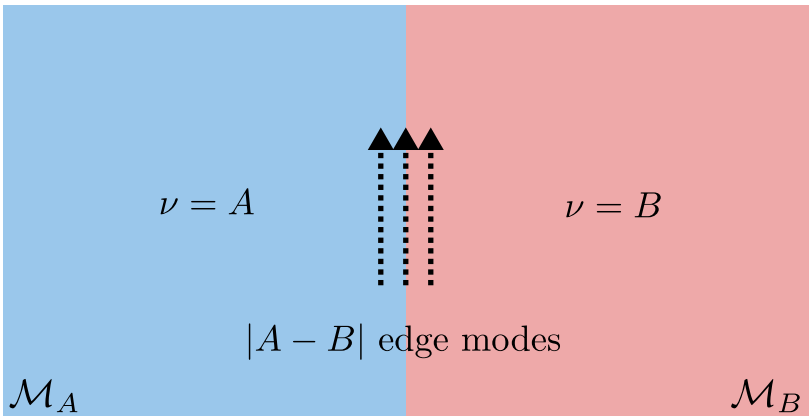

FIGURE 1.8: Schematic representation of the bulk-boundary correspondence. $\mathcal{M}_A$ and $\mathcal{M}_B$ denote two semi-infinite materials, characterized by two different values A and B of the bulk topological invariant ν (*i.e.* a topological invariant which describes an infinite-size sample). Two materials are then approached to each other and glued together at the edge. Since topological description of two system is distinct, it is impossible to continuously change through the common boundary of the materials without closing the gap, which implies the formation of $|A - B|$ gapless edge modes. The chirality of these edge modes is determined by the sign of $A - B$.

same: the topological phases are described by the presence of robust gapless boundary modes in systems with open boundary conditions, on the lattice defects or inside the vortex cores. In SPT systems however such states are protected by the symmetry in the sense that they will be stable against any perturbation which does not break the symmetry.

To be more precise, the bulk-boundary correspondence claims that an interface between two materials, which belong to the same symmetry class, characterized by two distinct bulk invariants A and B, has exactly $|A - B|$ gapless edge modes, as schematically presented in Fig. 1.8. One can roughly justify this statement by noticing that the "band structure" cannot interpolate continuously between different topological phases. This forces the gap to close at the interface leading to the emergence of a metallic state of topological origin. No proof of the bulk-boundary correspondence for topological phases exists in general. However, several particular cases or even particular symmetry classes have been studied in great details [50–55]. We also notice that the situation is different in the interacting cases: some interacting topological states do not have any edge mode. Instead, they are described by a particular form of the entanglement entropy, the presence of excitations with fractional charge and statistics, and the topological degeneracy of the ground-state on a manifold with non-zero genus (we will describe these notions in more details in Section 1.5).

1.5 Role of topology in strongly correlated quantum systems

As we have seen previously in this chapter, since last decades the topological aspects of mathematics started to play an important role in describing the states of matter, with the best known example being the experimental discovery of the IQHE [11, 35]. Developing these ideas allowed theorists to generalize the notion of quantum

Hall states [32, 46–48], and establish a topological classification based on the symmetries of the system and its dimension [40–42], that we mentioned in Section 1.4.4. The IQHE and the SPT states in such classification can however be completely understood already on a single-particle level. Nevertheless, starting with the discovery of the FQHE [12], people also understood that the effect of strong interactions could lead to new, even more exotic many-body phenomena. Some concrete examples comprise the formation of quasi-particles with anyonic charge and statistics, as well as the topological order, formulated in terms of a topological degeneracy of the ground-state on the manifold with non-zero genus.

In this section we will discuss in greater details the notions related to the complicated interplay between topology and interactions in condensed matter systems. We will start from the celebrated FQHE and Laughlin states. We will continue by saying a few words about the interacting SPT states and their long-range entangled partners – the intrinsically topologically ordered states. We will detail these notions by listing the most known and most relevant examples. Finally, we will conclude by making a connection to the theory of frustrated quantum magnetism and fascinating quantum spin liquids.

1.5.1 Fractional quantum Hall states

The FQHE was observed experimentally for the first time only few years after the discovery of the IQHE. Tsui, Stormer and Gossard [12] found that as the disorder in the 2D sample is decreased, the integer Hall plateaux become less prominent, and another plateau emerges. This plateau has a new, fractional value of the Hall conductivity

$$\sigma_{xy} = \nu e^2/h, \quad \nu \in \mathbb{Q}\,, \tag{1.112}$$

with $\nu = 1/3$. Later, several other plateaus at different fractional values of ν have been observed. Currently we know about the presence of a much greater number of fractional Hall states, as can be seen in Fig. 1.1(c).

Even though the experimental observation of the IQHE and FQHE is phenomenologically very similar, it is clear that the microscopic nature of the effects has to be significantly different. FQHE occurs, when the Landau level is only partially occupied. In this situation, one would naively expect that the system is gapless, since the low energy excitations are possible within the same Landau level. Nevertheless, this contradicts to the experimental observations showing the presence of a gap in the system. One thus understand that a simple Landau level picture cannot be employed. Moreover, the Laughlin's pump thought experiment can again be employed (see Section 1.1 for more details). It suggests that in the case of the FQHE, a particle with a fractional charge has to be transferred from one edge of the system to another. Both observations result in the conclusion that it is impossible to understand the FQHE on a single-particle level: the many-body physics has to be taken into account.

A. Laughlin states

FQHE occurs when the Coulomb interactions between the electrons becomes relevant. As a consequence, the problem one needs to solve also becomes notoriously difficult, because of the exponentially growing Hilbert space and impossibility to qualitatively perform a perturbative analysis. Historically, the first theoretical work enlightening the nature of the FQH states was done by Laughlin [56], based on an educated guess. Laughlin discovered that the following wavefunction describes very

well the FQH states at filling $\nu = 1/m$, with $m \in \mathbb{N}$

$$\Phi_L(z_1, \ldots, z_N) = \prod_{i<j}(z_i - z_j)^m \exp\left[-\sum_k |z_k|^2/(4l_B^2)\right] . \tag{1.113}$$

Here $z_i = x_i + iy_i$ is the complex coordinate of an electron in the plane, and $l_B = \sqrt{h/(2\pi eB)}$ is the magnetic length. We omitted to write the normalization constant for the purpose of keeping the notation simple. Such states are incompressible fluids that do not break any continuous spatial symmetry. The highest power of the complex particle position in (1.113) is equal to $(N-1)m$, where N is the number of particles. It also has to be equal to the number of flux quanta $N_B = \Phi/\Phi_0$ (we remind that according to the convention of Section 1.1, Φ is the total magnetic field piercing the system, and $\Phi_0 = h/e$ is the flux quantum). Hence, the filling fraction of a Laughlin state is indeed

$$\nu = \frac{N}{N_B} = \frac{N}{(N-1)m} \sim \frac{1}{m} . \tag{1.114}$$

Parameter m is odd for fermionic particles, and in particular for electrons, which were studied in experiments. One could however consider a generalization and include the cases when m is even. Such scenario would correspond to the case of bosonic particles.

Up to this moment, we mentioned only the ground-state properties of the FQH states. One can also construct and study the excitations above such ground-state [56]. Here we are interested in elementary excitations, which can be obtained by changing the number of fluxes $N_B = \Phi/\Phi_0$. If we increase the flux, we get the quasihole excitation described by the following wavefunction

$$\Phi_{\text{qh}}(z_0, z_1, \ldots, z_N) = \prod_i (z_i - z_0) \prod_{i<j}(z_i - z_j)^m \exp\left[-\sum_k |z_k|^2/(4l_B^2)\right] . \tag{1.115}$$

The maximal value of the exponent of each particle in this expression is indeed increased by one. In addition, the wavefunction vanishes whenever the coordinate z_j approaches z_0, showing the hole-like nature of the excitation. Alternatively, one can construct the quasiparticle excitations, by decreasing the number of flux quanta in the system. The corresponding wavefunction has the following form

$$\Phi_{\text{qp}}(z_0, z_1, \ldots, z_N) = \prod_i \left(2\frac{\partial}{\partial z_i} - \frac{\bar{z}_0}{l_B^2}\right) \prod_{i<j} (z_i - z_j)^m \exp\left[-\sum_k |z_k|^2/(4l_B^2)\right] . \tag{1.116}$$

Since the filling factor ν has to remain fixed, the charge of such quasihole and quasiparticle excitations is respectively equal to $\pm e/m$ and is fractional! Moreover, by adding two such excitations one can deduce that they have anyonic statistics, since the exchange of them will lead to an apparition of the phase factor π/m instead of the usual π (for fermions) or 2π (for bosons) [57–60]! These predictions also have been observed experimentally in the shot noise experiments [61, 62].

B. Generalizations

Laughlin's ansatz describes well the FQH states at $\nu = 1/m$, but does not clarify the emergence of plateaus with the numerator distinct from one. However, such states

have been observed soon after the discovery by Tsui, Stormer and Gossard. Some of these states can be understood following the idea of a hierarchical structure by Haldane [63] and Halperin [57], and the composite fermion approach proposed by Jain [64–66]. Inspired by the structure of a quasihole wavefunction, one can in fact interpret Laughlin wavefunction as a state of particles bound to magnetic fluxes. Jain suggested to write it in the following form

$$\Phi_{\mathrm{L}}(z_1,\ldots,z_N) = \prod_{i<j}(z_i - z_j)^{m-1}\chi_1(z_1,\ldots,z_N)\,, \tag{1.117}$$

where χ_1 is the wavefunction of a completely filled lowest Landau level

$$\chi_1(z_1,\ldots,z_N) = \prod_{i<j}(z_i - z_j)\exp\left[-\sum_k |z_k|^2/(4l_B^2)\right]\,. \tag{1.118}$$

The multiplicative factor before χ_1 in Eq. (1.117) represents an attachment of $m-1$ fluxes. The crucial difference consists however in the fact that these fluxes are not fixed in space, but are attached to the coordinates z_i, *i.e.* to real fermions, that explains the name of composite fermions. If the system is fermionic, m is odd, and each particle is bound to an even number of flux quanta, retaining its fermionic character. One can thus understand the resulting state as an IQH state of composite fermions at filling $\nu^* = 1$. More generally however, one could imagine such composite fermions to fill not one, but multiple Landau levels. The multiplicative factor before χ_1 in Eq. (1.117) can thus be replaced by $\prod_{i<j}(z_i - z_j)^{2s}$, leading to an effective attachment of $2s$ flux quanta, that again does not affect the statistics of fermions. The remaining $N_B^* = N - 2sN$ free flux quanta determine, how many effective Landau levels will be occupied. This leads to an effective IQHE of composite fermions with filling factor equal to

$$\nu^* = \frac{N}{N_B^*} = \frac{1}{1/\nu - 2s} \in \mathbb{Z}\,, \tag{1.119}$$

or equivalently $\nu = \nu^*/(2\nu^* s + 1)$. It corresponds exactly to the series of plateaus at

$$\begin{aligned} &1/3, 2/5, 3/7, \ldots \quad (s=1)\,,\\ &1/5, 2/9, 3/13, \ldots \quad (s=2)\,, \end{aligned} \tag{1.120}$$

observed in experiments.

If the magnetic field of vortices is antiparallel to the external magnetic field (*i.e.* there are more vortices in the composite fermion language, than it was for initial fermions), the expression above changes to $\nu = \nu^*/(2\nu^* s - 1)$. If instead of composite fermions, composite holes are formed, it transforms into $\nu = 1 - \nu^*/(2\nu^* s \pm 1)$. Moreover, one can enchain the process of making composite fermions / holes. Physically, this corresponds to the presence of weak residual interactions between composite particles [67]. This allows to recover almost all the FQH states observed experimentally. The only remaining exception corresponds to an even denominator FQH states [68]. In fact, using the composite fermion approach one should conclude that such filling describes a compressible Fermi-liquid state (the magnetic field must vanish exactly in the composite fermions representation). Nevertheless, $5/2$ FQH plateau has been observed experimentally. This phenomenon originates from the pairing effect, similar to the BCS instability giving rise to the superconductivity [16, 17]. A wavefunction which accounts for such interactions was proposed by Moore

and Read [69]. Moreover, the authors showed that the excitations above the ground-state in such system satisfy non-Abelian anyonic statistics, that represents a particular interest in relation with the ideas of topological quantum computing [70–72].

Finally, we notice that the FQHE is naturally described using a special form of field theory – the Chern-Simons (ChS) theory [60, 73–76]. This originates from the particular type of interactions between the matter and the gauge fields, that allow to attach particles and fluxes together – exactly what we need to get FQH states. This connection will be described in greater details in Appendix B of this manuscript.

1.5.2 Interacting SPT states and intrinsic topological order

We are now aware that when interactions are taken into account, the IQHE can be transformed into the FQHE, more exotic and interesting from the point of view of practical applications. A more profound question one could however ask is, what happens more generally to all the non-interacting topological states we introduced in Section 1.4.4, if we switch on strong correlations. Unfortunately, the answer to this question is not completely determined yet. Nevertheless, in the next paragraphs we will try our best to make a summary, of what is known nowadays on this subject. This subsection is greatly inspired by the reviews [77–79].

When interactions are taken into account in a model, which was initially described by some non-trivial topological invariants, three scenarios are possible. First of all, nothing could happen: as we have seen, topology in many cases is very robust against perturbations. Secondly, the topological phase could be changed on a non-quantitative level: the topological invariant could be modified, the system could move from one topological phase to another or become trivial. Finally, and most interestingly, the properties of the system could change on a quantitative level, so that there is no free particle counterpart of an observed effect. This last scenario is exactly what occurs in the FQHE [10].

Following the current understanding of the subject, it is important to distinguish between two different types of topological states of matter, based on the ground-state entanglement properties. One distinguishes the long-range entangled states, also called intrinsically topologically ordered states, and their short-range entangled counterparts, generalizing the class of SPT states. The notion of **topological order** was first introduced by Wen [80], and relies on several key properties. The first property is the topological ground-state degeneracy: on a manifold without boundary, the ground-states of a system with topological order has to be gapped and degenerate in the large system size limit. The degeneracy has to depend on the topological properties of the manifold (*e.g.* a genus of an orientable surface). The second property is the presence of exotic bulk excitations, which are deconfined, have fractional statistics and possibly fractional quantum numbers. When equipped with some global symmetries, an intrinsic topological order is often called a symmetry-enriched topological order. We notice that according to the definition of topological order, it cannot exist in 1D systems. In 2D, famous examples of systems with topological order are the FQH states (FQH states are in fact "enriched" by the $U(1)$ symmetry responsible for the conservation of the total number of particles), and the quantum spin liquids, that we will discuss in more details in Section 1.5.3.

[10] We notice that we indeed have an interpretation of the FQHE as an IQHE of composite fermions, so that we can say that there is a free fermion counterpart of the FQHE. However, the most striking property of the FQHE, which is the fractionalization, *i.e.* the presence of excitations with fractional statistics, does not have any analogue in the non-interacting world.

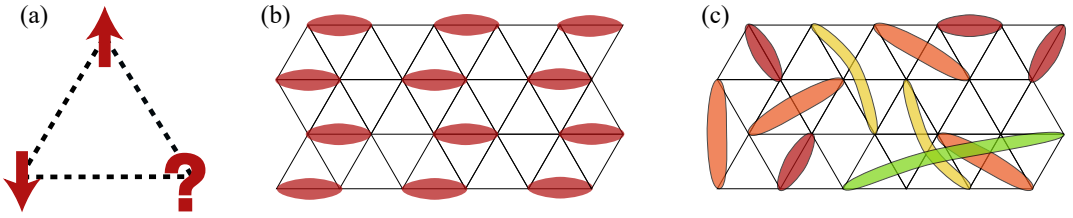

FIGURE 1.9: **(a)** Triangular loop of spins-1/2, with antiferromagnetic NN interactions. When trying to construct the ground-state, one can never satisfy all three constraints imposed by the interactions, so that the direction of one of the spins will be undetermined. By applying this reasoning to each of three spins, we deduce that the ground-state is six-fold degenerate. **(b)** Valence-bond-solids is an ordered structure of valence bonds – singlet states of spins with zero magnetization. This state clearly breaks the translation (translation by an even number of unit cells in one direction is inequivalent to the the translation by an odd number of unit cells) and rotation symmetry (bonds are formed in one particular direction). **(c)** Translation and rotation invariance of a valence-bond-solid is restored, by considering a superposition of singlet states at different distances and in different directions. The resulting state is called a resonating valence-bond state.

In the opposite limit of topologically ordered states, SPT states lack exotic bulk properties. Nevertheless, they exhibit non-trivial physics at the boundary, protected as long as the symmetry is maintained. As a result of strong interactions, excitations with fractional statistics and fractional quantum numbers can still exist in such systems, but only at the boundary. This effect is called a **symmetry fractionalization**, and unlike in the case of topologically ordered states, it can occur even in 1D. Celebrated example of such SPT states is the exact solution of the one-dimensional Heisenberg model proposed by Affleck, Lieb, Kennedy and Tasaki [81], and more generally the Haldane phase of odd-integer-spin chain [82–85]. While the classification of SPT phases of 1D systems [86, 87] and bosonic systems in $d > 1$ [88] has been proposed, the question of what happens in more general situations still remains unsolved.

1.5.3 Frustrated quantum magnetism and spin liquids

Another example of systems which could possess intrinsic topological order corresponds to quantum spin liquids. Spin liquids are strongly-correlated states of matter that do not order even at very low or zero temperature as a result of quantum fluctuations. In this subsection we want to make a short overview of this notion, based on several excellent reviews [89–93].

The idea of spin liquid states was first proposed by Anderson [94] in 1973 as a possible outcome of frustration in 2D magnetic systems. The phenomenon of **frustration** appears in some specific situations, when competing exchange interactions cannot be all simultaneously satisfied. In particular, this leads to a large degeneracy of the classical ground-state. The simplest possible frustrated system is a single triangular loop composed of spins-1/2, with antiferromagnetic interactions between them, as shown in Fig. 1.9(a). In such system, there is no possibility to satisfy more than two antiferromagnetic constraints at the same time, and the ground-state is 6-fold degenerate.

One of the possibility to obtain a non-magnetic ground-state consists in using maximally entangled valence bonds, *i.e.* pairs of spins forming a singlet state with

total magnetization equal to zero. If valence bonds are combined in an ordered structure, so that each spin is entangled with only one another, chosen in a specific manner, this corresponds to a valence-bond-solid, shown in Fig 1.9(b). Such state breaks however the translation symmetry and thus cannot be a spin liquid state. Anderson proposed a way [94] of forming a translation invariant "quantum liquid" state, which consists in using a superposition of all possible valence-bond partitionings – the so-called resonating valence-bond state (see Fig. 1.9(c)). The idea of Anderson attracted a lot of attention 14 years later because of a possible connection to the physics of recently discovered cuprate superconductors [95, 96].

In parallel to the works by Anderson, the connection between spin liquids and FQH states was found by Kalmeyer and Laughlin [97]. They discovered a new type of spin liquids – a **chiral spin liquid** state, which was associated with the bosonic FQH state. Such spin liquids have been shown to be described by two broken discrete symmetries – the parity symmetry R and the time-reversal symmetry T, and an associated order parameter – the scalar spin chirality [98]

$$\chi_{ijk} = \left\langle \boldsymbol{S}_i \cdot \left(\boldsymbol{S}_j \times \boldsymbol{S}_k \right) \right\rangle \ . \tag{1.121}$$

The concept of intrinsic topological order [80] was introduced by Wen in order to describe exactly these chiral spin liquids. Later, a $\mathbb{Z}_2$ time-reversal and parity invariant spin liquid was discovered [99–101]. In this context, a particularly appraised work was done by Kitaev, who proposed an exactly solvable $\mathbb{Z}_2$ spin liquid model [70], and showed how the excitations present in the model could be used as a basis of the topological quantum computing.

Gauge theory plays a central role in the current understanding of the nature of spin liquids, starting from the seminal work by Wen [102]. In this work Wen introduced the projective symmetry group to classify different possible spin liquids by their gauge structures at low energy. The electric and magnetic charges that appear in the gauge theories are naturally associated with the non-local exotic quasiparticles of highly entangled phases in spin liquids. Similarly to the phase transition in the XY model, some regions of the phase diagram host deconfined excitations, and at other regions non-local quasiparticles cannot be created at finite energy cost. In particular, the low-energy physics of chiral and $\mathbb{Z}_2$ spin liquids is described using respectively Chern-Simons and $\mathbb{Z}_2$ field theories. These field theories describe the systems with no gapless excitations. However, this is not a rule of thumb, and the later discovered $U(1)$ and $SU(2)$ spin liquids, or the Kitaev exactly solvable model for deconfined Majorana modes on the honeycomb lattice [103], are gapless. Such states are not yet fundamentally understood, and the question of their stability remains largely unsolved. Finally, we notice that not all the spin liquid states have a topological order, in the sense defined by Wen. The question of whether SPT-like state can exist in the context of spin liquids remains unanswered as well.

Chapter 2

Chiral phases of the Haldane Chern insulator

In this chapter we present our contribution to the study of the phase diagram of variations of the Haldane model on the honeycomb lattice. First, in Section 2.1, after making a short introduction to the physics of graphene and, more generally, Dirac materials, we describe the most striking properties of the Haldane model and, more generally, Chern insulators. In particular, we show how the topological description of single-particle states involving the first Chern number can be applied to the Haldane model. Next, motivated by an experimental context, in Section 2.2 we present our study of the bosonic anisotropic Haldane model with Bose-Hubbard interactions. We calculate the phase diagram of this model. Our results are based on analytical calculations and numerical simulations using exact diagonalization. We describe rich properties of the bosonic ground-state associated with a finite-momentum superfluid phase, emerging as a result of gauge fields of the model. Moreover, even though the bosonic ground-state does not allow to probe the topology of the system, Bogoliubov excitations (emerging as a result of Bose-Hubbard interactions) are sensitive to the topological properties. Finally, in Section 2.3 we explore the phase diagram of the bosonic Haldane model on a ladder geometry. The phases that appear in this model are qualitatively the same as in the two-dimensional case. However, the phase transition is quantitatively different, and leads to the emergence of flat bands in the single-particle band structure. While far away from the transition point we are able to use the Luttinger liquid theory to explain numerical results, the physics at the transition remains unclear to us. We notice that some of the results of this chapter have already been presented in Ref. [1].

Contents of the chapter

2.1 Dirac materials and Chern insulators . . . 50
2.1.1 Graphene as a Dirac material . . . 51
2.1.2 Haldane model as a Chern insulator . . . 53
A. Opening a gap at Dirac points . . . 53
B. Topological phase transition . . . 54
2.1.3 Anisotropy and generalizations of the Haldane model . . . 57
2.2 Anisotropic Haldane model for bosons with interactions . . . 57
2.2.1 Overview of the problem . . . 59
2.2.2 Superfluid phases . . . 60
A. Zero-momentum phase . . . 60
B. Critical value of NNN hopping amplitude . . . 62
C. Finite-momentum phase . . . 64
D. Interaction effects . . . 67

2.2.3 Excitation properties 69
2.2.4 Mott insulator phase 70
2.3 Interacting bosons on brickwall ladder geometry 72
2.3.1 Band structure in free case 73
2.3.2 Interactions and bosonization 74
A. Strong t_1 phase 76
B. Strong t_2 phase 77
2.3.3 Perspectives 78

2.1 Dirac materials and Chern insulators

The notion of Dirac, Majorana and Weyl fermionic fields was introduced to describe elementary particles in high-energy physics [104]. In the 4-dimensional space of signature $(1,3)$, all spin-1/2 massive particles are described by the Dirac equation [105]: $(i\gamma^\mu\partial_\mu - m)\Psi = 0$. Here Ψ is the wave function of the particle and γ^μ are four 4×4 gamma matrices that satisfy the Clifford algebra: $\{\gamma^\mu,\gamma^\nu\} = 2\eta^{\mu\nu}$ with $\eta^{\mu\nu}$ – the Minkowski tensor. In the Weyl (chiral) representation of the algebra, the Dirac equation can be rewritten for two chiral spinors Ψ_L and Ψ_R of the Dirac fermionic field as follows:

$$\begin{aligned}(i\sigma_0\partial_t + i\sigma_i\partial_i)\Psi_R &= m\Psi_L\,,\\ (i\sigma_0\partial_t - i\sigma_i\partial_i)\Psi_L &= m\Psi_R\,.\end{aligned} \tag{2.1}$$

where σ_μ are usual Pauli matrices ($\sigma_0 = I$). We see that Ψ_L and Ψ_R are coupled through the mass term m and become decoupled when the mass vanishes. In this case we deduce two equations describing Weyl fermionic fields [106]. Finally, the fermionic particle which also represents its own anti-particle is described by a Majorana field $\Psi^* = \Psi$ [107].

Interestingly, in the domain of condensed matter the relativistic Dirac and Weyl equations can be directly used to describe the low-energy fermionic excitations, that behave as Dirac or Weyl particles. This behavior establishes a new class of materials, called **Dirac materials** [108, 109]. The variety of corresponding systems is very large, ranging from graphene [110–112], topological insulators in 2D [46–49, 113–116] and 3D [113–117], to superfluid ^{3}He [34, 118], and Weyl and Dirac semimetals [119–122]. Such materials are usually narrow (or zero) gap semiconductors. As we have seen in Section 1.2, on lattice geometries solutions are described by Bloch waves and are labeled by quasi-momentum $\boldsymbol{k}$ periodic over the first BZ. As a result of this periodicity, Weyl or Dirac equations cannot hold true over the entire momentum space and are valid only in the neighborhood of particular points in the BZ which are called Dirac points. Dirac points play a very important role in the description of the related systems, so that Dirac materials with a completely different physical origin have some universal equilibrium properties, as well as response functions and susceptibilities.

In this section we will first make an introduction to the physics of Dirac materials, by considering a seminal example of graphene, and describing its celebrated Dirac cone energy structure. We will then develop these ideas by showing how adding a Haldane's term can lead to an opening of a gap in such system, and transform it into a **Chern insulator** – an insulator whose bands are described by non-vanishing values of the first Chern number.

2.1.1 Graphene as a Dirac material

It was predicted and shown experimentally that graphene, the two-dimensional layer of carbon atoms, should host massless Dirac-Weyl fermions [110–112]. The "relativistic" behavior of this material originates from its lattice structure, giving rise to a particular form of the coupling. It is similar to the spin-orbit coupling, but originates from the sublattice index rather than the real electron spin. Graphene can be described using the single orbital tight-binding model on the honeycomb lattice of atoms composed of two interpenetrating triangular Bravais sublattices, denoted by indices A and B. Triangular sublattices are spanned by vectors

$$\boldsymbol{R}_1 = \sqrt{3}a\boldsymbol{e}_x, \quad \boldsymbol{R}_2 = \frac{\sqrt{3}a}{2}\boldsymbol{e}_x + \frac{3a}{2}\boldsymbol{e}_y \,, \tag{2.2}$$

as shown on Fig. 2.1. The corresponding reciprocal lattice vectors are

$$\boldsymbol{Q}_1 = \frac{2\pi}{\sqrt{3}a}\boldsymbol{e}_x - \frac{2\pi}{3a}\boldsymbol{e}_y, \quad \boldsymbol{Q}_2 = \frac{4\pi}{3a}\boldsymbol{e}_y \,. \tag{2.3}$$

Here a is the length of the side of honeycombs in the lattice. The graphene tight-binding Hamiltonian is

$$H = -t_1 \sum_{\langle i,j \rangle} \left(a_i^\dagger b_j + b_j^\dagger a_i \right) \,, \tag{2.4}$$

where $a_i^\dagger(a_i)$ and $b_i^\dagger(b_i)$ are creation (annihilation) operators of a particle on the site i of sublattices A and B. In a real material the t_1-term in the Hamiltonian describes the hopping of electrons between the p_z-orbitals of two adjacent carbon atoms. This term connects any A-site to its three nearest neighbors (NN) in directions $\boldsymbol{u}_j$, defined as follows (see also Fig. 2.1):

$$\boldsymbol{u}_1 = \frac{\sqrt{3}a}{2}\boldsymbol{e}_x - \frac{a}{2}\boldsymbol{e}_y, \quad \boldsymbol{u}_2 = -\frac{\sqrt{3}a}{2}\boldsymbol{e}_x - \frac{a}{2}\boldsymbol{e}_y, \quad \boldsymbol{u}_3 = a\boldsymbol{e}_y \,. \tag{2.5}$$

The summation over NN is denoted in the equation by $\langle i, j \rangle$.

Using the approach presented in Section 1.2, we diagonalize the Hamiltonian and deduce the eigenstates and eigenergies of H. We find that

$$H = -t_1 \sum_{\boldsymbol{k}} a_{\boldsymbol{k}}^\dagger b_{\boldsymbol{k}} \left(e^{ia\left(\frac{\sqrt{3}}{2}k_x - \frac{1}{2}k_y\right)} + e^{ia\left(-\frac{\sqrt{3}}{2}k_x - \frac{1}{2}k_y\right)} + e^{iak_y} \right) + \text{h.c.} \tag{2.6}$$

In the $\boldsymbol{k}$-space the Hamiltonian becomes diagonal by blocks of size 2×2:

$$H = \sum_{\boldsymbol{k}} \psi_{\boldsymbol{k}}^\dagger \cdot \mathcal{H}(\boldsymbol{k}) \cdot \psi_{\boldsymbol{k}} \,, \tag{2.7}$$

with

$$\psi_{\boldsymbol{k}} = \begin{pmatrix} a_{\boldsymbol{k}} \\ b_{\boldsymbol{k}} \end{pmatrix}, \quad \text{and} \quad \mathcal{H}(\boldsymbol{k}) = -d_\mu(\boldsymbol{k})\sigma^\mu \,. \tag{2.8}$$

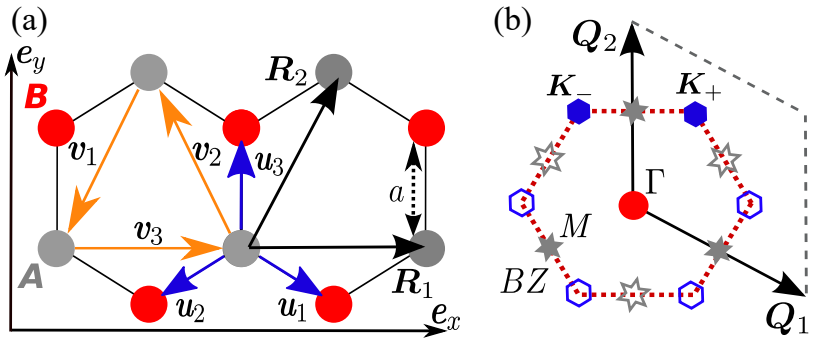

FIGURE 2.1: **(a)** Honeycomb lattice. Two triangular Bravais lattices, denoted by indices A and B can be generated by vectors $\boldsymbol{R}_1$ and $\boldsymbol{R}_2$ from Eq. (2.2). The length of the honeycomb side equals a. Vectors $\boldsymbol{u}_i$ connect each site of the sublattice A to its three nearest neighbors on the sublattice B. Vectors $\boldsymbol{v}_i$ connect each site on both sublattices to its six next nearest neighbors. **(b)** Vectors $\boldsymbol{Q}_1$ and $\boldsymbol{Q}_2$ generate the reciprocal lattice vectors according to Eq. (2.3). The honeycomb depicts the boundary of the first BZ. Points $\boldsymbol{K}_\pm$, $\boldsymbol{\Gamma}$ and $\boldsymbol{M}$ are special points in the first BZ.

Functions d_μ depend on the momentum $\boldsymbol{k}$ in the BZ and the parameters of the problem. For the graphene Hamiltonian, they take the following form:

$$\begin{aligned} d_0(\boldsymbol{k}) &= d_z(\boldsymbol{k}) = 0, \\ d_x(\boldsymbol{k}) &= t_1 \sum_j \cos(\boldsymbol{k}\cdot\boldsymbol{u}_j), \\ d_y(\boldsymbol{k}) &= t_1 \sum_j \sin(\boldsymbol{k}\cdot\boldsymbol{u}_j)\,. \end{aligned} \tag{2.9}$$

For each value of $\boldsymbol{k}$, we diagonalize the 2×2 matrix and calculate the corresponding eigenvalues

$$\begin{aligned} \epsilon_\pm(\boldsymbol{k}) &= \pm\, t_1 \left| e^{ia(\frac{\sqrt{3}}{2}k_x - \frac{1}{2}k_y)} + e^{ia(-\frac{\sqrt{3}}{2}k_x - \frac{1}{2}k_y)} + e^{iak_y} \right| \\ &= \pm\, t_1 \sqrt{3 + 2\cos(\sqrt{3}ak_x) + 4\cos(\frac{3}{2}ak_y)\cos(\frac{\sqrt{3}}{2}ak_x)}\,. \end{aligned} \tag{2.10}$$

Two bands defined by positive and negative solutions in Eq. (2.10) cross themselves at two Dirac points located at

$$\boldsymbol{K}_\pm = \pm\frac{2\pi}{3\sqrt{3}a}\boldsymbol{e}_x + \frac{2\pi}{3a}\boldsymbol{e}_y \tag{2.11}$$

on a reciprocal lattice. In the neighborhood of these points at $\boldsymbol{q} = \boldsymbol{k} - \boldsymbol{K}_\pm$ the energy becomes equal to

$$\epsilon_\pm(\boldsymbol{k}) \approx \pm v_F|\boldsymbol{q}|\,, \tag{2.12}$$

with $v_F = 3t_1a/2$ – the Fermi velocity. Such shape of the dispersion curve is called a Dirac cone. At the same time, the Hamiltonian describing the system takes the form of the Weyl Hamiltonian acting on the sublattice index [108–112]:

$$\mathcal{H}(\boldsymbol{k}) = v_F\left[\pm d_x(\boldsymbol{k})\sigma^x + d_y(\boldsymbol{k})\sigma^y\right] \tag{2.13}$$

where the $\pm$ sign depends on whether $\boldsymbol{K}_+$ or $\boldsymbol{K}_-$ was considered. The resulting matrix clearly takes the same form as in Eq. (2.1) with the mass m equal to zero. We notice that this effect is a pure consequence of the geometric configuration of the lattice. As a result, it can easily be generated in quantum simulator setups. In particular, it has been realized in ultra-cold atoms and photonic lattices (see Chapter 4 for more details).

2.1.2 Haldane model as a Chern insulator

A. Opening a gap at Dirac points

The presence of Dirac points in graphene is protected by two symmetries: the parity symmetry R and the time-reversal symmetry T [108, 109, 114, 115]. Breaking one of these symmetries leads to an opening of the gap and apparition of a mass term for the low-energy fermionic excitations. In the rest of this section we will describe two ways to perform such symmetry breaking.

A simple way of opening the gap consists in adding to the Hamiltonian $\mathcal{H}(\boldsymbol{k})$ a constant term $M\sigma_z$ which breaks the parity symmetry R. This unitary symmetry can be interpreted as a center-bond reflection which maps the sublattice A to the sublattice B. In second quantization, it reads

$$Ra_iR^{-1} = b_i, \quad Rb_iR^{-1} = a_i, \quad RiR^{-1} = i\,. \tag{2.14}$$

Please notice that this is not the chiral (or sublattice) symmetry from Section 1.4.4. Since the particle-hole symmetry is absent, the chiral symmetry is absent as well. Practically, such symmetry breaking term is realized by creating a difference in chemical potential between the two sublattices in the context of an ultra-cold atoms experiment or by considering a photonic circuit with different cavity frequencies. This term was introduced for the first time in [123] and is usually referred to as the Semenoff mass term.

Another possibility consists in breaking the antiunitary time-reversal symmetry T. This can be accomplished by considering a system with local staggered magnetic fluxes going through the lattice. In order to preserve the spatial Bloch space-periodicity of the eigenstates, one can consider fluxes that sum up to zero over the entire unit cell. The model realizing such a system is the celebrated Haldane model for anomalous quantum Hall effect, proposed by Haldane in [32]. The following tight-binding Hamiltonian incorporates both suggested modifications:

$$\begin{aligned} H = &\sum_i \left[(\epsilon_0 + M)\, a_i^\dagger a_i + (\epsilon_0 - M)\, b_i^\dagger b_i\right] - t_1 \sum_{\langle i,j\rangle} \left(a_i^\dagger b_j + b_j^\dagger a_i\right) \\ &- t_2 \sum_{\langle\langle i,j\rangle\rangle} \left(e^{i\phi_{ij}} a_i^\dagger a_j + e^{-i\phi_{ij}} b_i^\dagger b_j\right) + \text{h.c.} \end{aligned} \tag{2.15}$$

Here M is the Semenoff mass (staggered chemical potential term), ϵ_0 is the constant chemical potential. t_2 is the next nearest neighbor (NNN) hopping rate. The sum over i runs over all unit cells of the lattice. The sum $\langle\langle i,j\rangle\rangle$ is taken over all couples

of NNN sites on the same sublattice, distanced from each other by vectors v_j:

$$\begin{aligned} v_1 &= u_2 - u_3 = -\frac{\sqrt{3}a}{2}e_x - \frac{3a}{2}e_y, \\ v_2 &= u_3 - u_1 = -\frac{\sqrt{3}a}{2}e_x + \frac{3a}{2}e_y, \\ v_3 &= u_1 - u_2 = \sqrt{3}a e_x \, . \end{aligned} \tag{2.16}$$

The phase $\phi_{ij} = -\phi_{ji}$ is the unimodular phase acquired for NNN hoppings. We use the convention such that this phase is equal to ϕ_H for jumps in the anticlockwise direction, and $-\phi_H$ for jumps in the clockwise direction, as shown in Figure 2.2(a).

We simplify Eq. (2.15) by going again to the momentum space. We obtain that the Bloch Hamiltonian can be expressed as $\mathcal{H}(k) = -d_\mu(k)\sigma^\mu$ with

$$\begin{aligned} d_0(k) &= -\epsilon_0 + 2t_2\cos(\phi_H)\sum_j \cos(k\cdot v_j), \\ d_x(k) &= t_1\sum_j \cos(k\cdot u_j), \\ d_y(k) &= t_1\sum_j \sin(k\cdot u_j), \\ d_z(k) &= -M + 2t_2\sin(\phi_H)\sum_j \sin(k\cdot v_j) \, . \end{aligned} \tag{2.17}$$

We also find the dispersion relation

$$\epsilon_\pm(k) = d_0(k) \pm \sqrt{|d|^2(k)} = d_0(k) \pm \sqrt{d_x^2(k) + d_y^2(k) + d_z^2(k)} \, . \tag{2.18}$$

In particular, we see that around two Dirac points $q = k - K_\pm$ we can approximately write

$$\epsilon_\pm^2(q) = v_F^2|q|^2 + d_z^2(K_\pm) \, . \tag{2.19}$$

This means that the term $d_z(K_\pm) = -M \pm 3\sqrt{3}t_2\sin(\phi_H)$ can be associated with the pseudo-relativistic mass m exactly as in Eq. (2.1).

B. Topological phase transition

The most exciting properties of the Haldane model are not however related to the simple presence of the pseudo-relativistic mass term. We can see already in the expression $d_z(K_\pm) = -M \pm 3\sqrt{3}t_2\sin(\phi_H)$ that two symmetry breaking terms act differently: the Semenoff mass term has the same sign at two Dirac points, while the term induced by the NNN complex hopping changes sign. It occurs that this difference is crucial in the context of the topological description of the model.

Let us go back to the classification of topological states of matter we presented in Section 1.4.4 and, more precisely, to Table 1.1. If the time-reversal symmetry (T) breaking terms are non-zero, our problem belongs to the Altland-Zirnbauer symmetry class A, *i.e.* no symmetries are present in the model. In two dimensions this implies that the model is described by a $\mathbb{Z}$ topological invariant. This invariant is nothing else but the first Chern number Ch_1^n from Eq. (1.91), describing the twist of the $U(1)$ Bloch bundle associated with the conduction (or equivalently a valence)

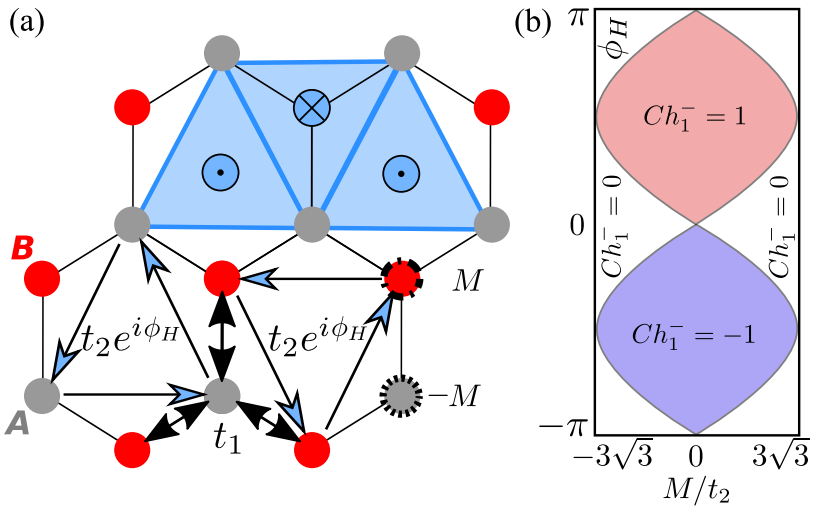

FIGURE 2.2: **(a)** Schematic presentation of the Haldane model for the quantum anomalous Hall effect on the honeycomb lattice. The model comprises the term of NN hoppings with the amplitude t_1, NNN hoppings with the amplitude $t_2e^{\pm i\phi_H}$ and the Semenoff mass term M. The phase factor $\pm\phi_H$ is positive for the hoppings in the anticlockwise direction and negative in the clockwise one. The Semenoff mass term breaks the parity symmetry R: the model is not invariant under the exchange of two sublattices. The complex hopping term $t_2e^{\pm i\phi_H}$ breaks the time-reversal symmetry T by adding staggered magnetic fluxes which sum up to zero inside the unit cell, as schematically represented using blue triangles. **(b)** Phase diagram of the Haldane model showing the first Chern number of the lowest band Ch_1^- as a function of the Haldane phase ϕ_H and the ratio M/t_2. The value of the topological constant changes at the critical line $M = 3\sqrt{3}t_2\sin(\phi_H)$, where the gap closes at one of the Dirac points.

band. We remind the reader that we obtained it by integrating the Berry curvature over the base manifold of the fibre bundle, which is the the first BZ forming a torus. More generally, insulating states of matter with broken time-reversal symmetry described by a non-vanishing value of the first Chern number are called **Chern insulators**.

By chance, we previously found (see Section 1.4.2) a convenient expression of the Chern number for a general two-band problem, written in terms of the unit vector $\boldsymbol{u}(\boldsymbol{k}) = \boldsymbol{d}(\boldsymbol{k})/|\boldsymbol{d}(\boldsymbol{k})|$:

$$Ch_1^{\mp} = \pm\frac{1}{4\pi}\int_{\mathrm{BZ}} \mathrm{d}k_x \mathrm{d}k_y \left(\boldsymbol{u}(\boldsymbol{k}) \cdot \left[\partial_{k_x}\boldsymbol{u}(\boldsymbol{k}) \times \partial_{k_y}\boldsymbol{u}(\boldsymbol{k})\right]\right) . \tag{2.20}$$

Hence, in this case we can simply interpret the topological invariant as an element of the homotopy group $\pi_2(T^2) = \mathbb{Z}$. Following Refs. [124, 125] we can further simplify the equation above to get the discrete expression

$$Ch_1^{\mp} = \pm\frac{1}{2}\sum_{\boldsymbol{k}\in[\boldsymbol{K}_\mu]} \mathrm{sign}\left(\left[\partial_{k_x}\boldsymbol{u}(\boldsymbol{k}) \times \partial_{k_y}\boldsymbol{u}(\boldsymbol{k})\right] \cdot \boldsymbol{e}_z\right) \mathrm{sign}\left(u^z(\boldsymbol{k})\right) . \tag{2.21}$$

In this equation the sum is going over all Dirac points, *i.e.* over all momenta $\boldsymbol{K}_\mu$ where the gap of the simplified Hamiltonian $d^x(\boldsymbol{k})\sigma_x + d^y(\boldsymbol{k})\sigma_y$ closes. The first term describes the winding number of the vector $\boldsymbol{u}_\perp(\boldsymbol{k}) = u^x(\boldsymbol{k})\boldsymbol{e}_x + u^y(\boldsymbol{k})\boldsymbol{e}_y$ around such Dirac points, while the second term corresponds to the sign of the mass term $d^z(\boldsymbol{k})$. In graphene, there are only two Dirac points and they have an opposite winding number of the vector $\boldsymbol{u}_\perp(\boldsymbol{k})$ equal to ± 1. Thus, the mass term has to change sign between two Dirac points in order to host the topological phase. This reasoning allows us to obtain the phase diagram of the Haldane model shown in Fig. 2.2(b). It comprises several phases characterized by different values of the Chern number Ch_1^- associated to the lower band. The Chern number of the upper band is the opposite, since the total Chern number of two bands $Ch_1^{\mathrm{tot}} = Ch_1^- + Ch_1^+$ is always zero. In the topological insulator phase $\left|Ch_1^{\pm}\right| = 1$, while in the normal insulator phase $\left|Ch_1^{\pm}\right| = 0$. The transition between two phases occurs when $M = 3\sqrt{3}t_2\sin(\phi_H)$ and it is marked by a semi-metal state, where the gap between two bands closes.

If the system is realized on a finite geometry with open boundary conditions (along one or two directions), the non-trivial topological description of the bulk will imply the presence of topologically protected localized modes at the boundary. This is the consequence of the bulk-boundary correspondence we introduced in Section 1.4.5. Here one of the two topological materials corresponds to the slice of the Haldane model, and the second one is simply the vacuum. According to the bulk-boundary correspondence, and since the difference of the topological invariants cannot be bigger that 1 in absolute value, exactly one edge mode must be localized at the boundary of the system. This is completely analogous to the integer quantum Hall effect, with the only difference that strong magnetic fields are not required to observe such phenomenon. It is why the Haldane model is also called a model for the quantum anomalous Hall effect. The corresponding edge states describe the perfectly quantized quantum Hall conductivity and are called **chiral edge states**. In Appendix C we show an analytic proof of the presence of edge modes in the Haldane model and the comparison to the numerical simulation results.

2.1.3 Anisotropy and generalizations of the Haldane model

As we have seen, the mass term which changes sign at two Dirac points is crucial to observe the topological phase transition in the Haldane model. Hence, we expect that any perturbation that preserves the structure of Dirac points and this sign constraint, will keep the Chern number invariant. Motivated by the past [126, 127] and perspective [1, 3] experimental realizations, we were however interested in exploring more precisely how the effect of anisotropy could affect the properties of the Haldane model.

We studied the anisotropic Haldane model with absent horizontal NNN hoppings, as shown in Fig. 2.3(a-b). We found that the missing link does not affect the possibility of topological bands (thanks to the presence of closed loops of vector potentials involving kite geometries), but modifies the critical point of the topological versus non-topological phase transition and the edge-mode dispersion relation. More precisely, in the anisotropic Haldane model we find that $d_z(\boldsymbol{K}_\pm) = -M \pm 2\sqrt{3}t_2 \sin(\phi_H)$. Thus, in the regime $t_2 > M/(2\sqrt{3})$, the Berry's phase acquired by the wavefunction wrapping around the BZ does not vanish. In this case, according to the bulk-boundary correspondence, by fixing the chemical potential of the system to the gap between two bands, one should be able to observe edge modes that go across the boundary of our system in real space. These modes should disappear in the regime $t_2 < M/(2\sqrt{3})$, after moving through the topological phase transition at $t_2 = M/(2\sqrt{3})$, where the gap between two bands closes and the system becomes conducting.

These calculations are verified numerically by diagonalizing the Hamiltonian in the strip geometry, i.e. with periodic boundaries along x and open boundaries along y (zigzag boundary conditions). The band structure is calculated for different values of t_2/M and edge modes are detected, as seen on Fig. 2.3(c-e). Moreover, we adapt methods previously used in works of Refs. [128] and [129] and presented in Appendix C to derive an analytical calculation of the dispersion relation for edge modes of the anisotropic Haldane model, by considering an exponentially decaying ansatz. In Fig. 2.3(f), we compare the analytical and numerical solutions. We outline that if $t_2 > M/(2\sqrt{3})$, even weak values of t_2 (compared to t_1) allow for the observation of edge modes.

One could also be interested in further generalizing the Haldane model by including longer range hopping terms. It was shown that such modifications can lead to the apparition of new Dirac points in the spectrum, which could increase the maximum value of the Chern number [125, 130] and allow to study the merging of Dirac points [34, 125, 130, 131]. Such terms could also be useful to flatten the bands, that could lead to the emergence of FQHE states and a new kind of materials called fractional Chern insulators [79, 132–141].

2.2 Anisotropic Haldane model for bosons with interactions

Previously in this chapter we described intriguing properties of Dirac materials and Chern insulators, related in particular to the topological description of non-interacting gapped bands. Such properties can be probed in a straightforward manner with fermions: in order to see the emergence of edge modes one only needs to fix the chemical potential between two bands described by different topological invariants. With bosons such task is slightly less trivial. As we will see in Chapter 4, the use of non-equilibrium probes is required in this case.

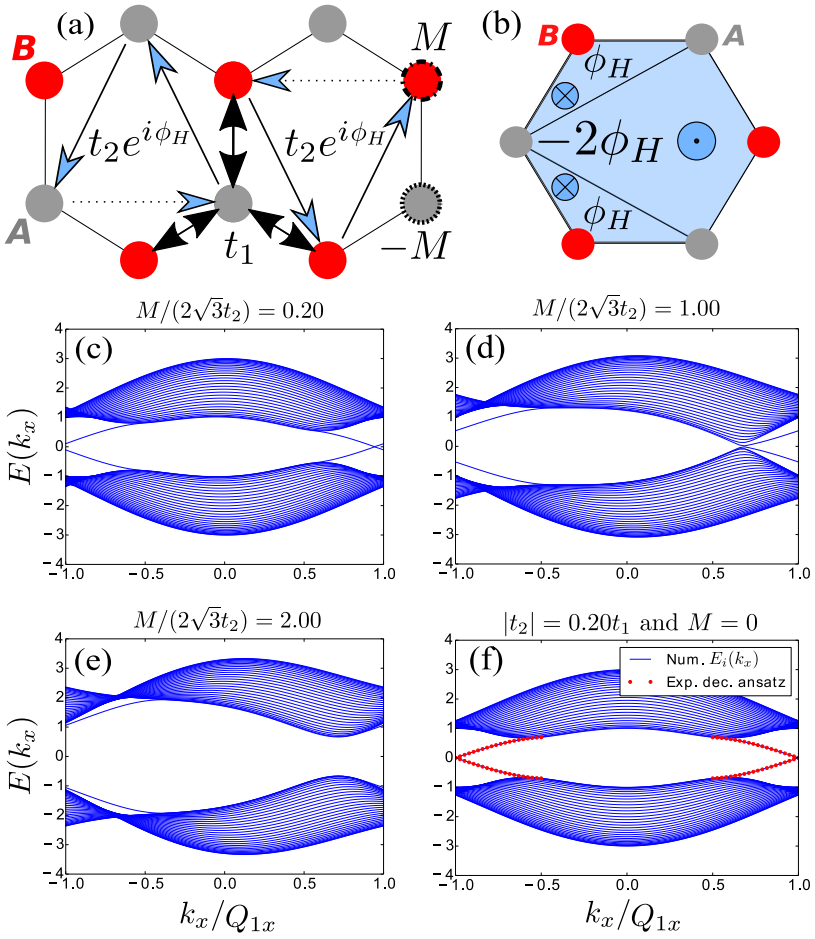

FIGURE 2.3: **(a)** Anisotropic Haldane model. Coloured bold lines represent NNN hoppings with amplitude modulus t_2. Dotted lines correspond to the hopping absent in the model. **(b)** Magnetic flux distribution in the anisotropic Haldane model. The total magnetic flux through the unit cell sums up to zero, with closed loops of vector potentials involving kite geometries rather then triangles as in the isotropic case. **(c-e)** Numerical calculations of the band structure for the anisotropic Haldane model in the strip geometry with zigzag edges (cut along the x axis of Fig. 2.1), showing the topological phase transition. Edge modes cross the gap between two bands for $M/t_2 < 2\sqrt{3}$. The gap closes at $M/t_2 = 2\sqrt{3}$. Edge modes do not cross the gap anymore for $M/t_2 > 2\sqrt{3}$. **(f)** Comparison between numerical results (solid blue lines) and analytical solution for edge modes based on an exponentially decaying ansatz [128, 129] (red doted lines). Band structure represented in this way is periodic with period $2Q_{1x}$, where $\boldsymbol{Q}_1$ is the reciprocal lattice vector defined in Fig. 2.1.

However, realizing the Haldane model for bosonic systems allows one to investigate rich properties of lattice bosons subjected to gauge fields. Previously explored experimental setups which give access to such properties consist of bosonic ultracold atoms systems in 1D [142, 143] or ladder geometries [144], on triangular [145, 146] and square [147] lattices. Alternatively, one could use exotic polariton superfluids [148] or photonic Bose-Einstein condensates (BECs) [149]. In this section we will show in details, how one could study the condensation of bosons at non-zero momentum [150–153] by performing such experiments on the honeycomb lattice. This effect is interesting thanks to its similarity to the Fulde-Ferrell-Larkin-Ovchinnikov (FFLO) phase [154, 155]. By taking as a starting point known results on the isotropic Haldane model [153], we will study how the presence of anisotropy can affect the phase transition. This consideration is indeed important, in light of a recent experimental realization [126] with ultra-cold atoms and a proposal for photonic lattices [1, 3] (see also Section 4.3) of the Haldane model, that involves exactly its anisotropic, rather than isotropic, version.

2.2.1 Overview of the problem

We consider the Hamiltonian $H = H_{\text{Haldane}} + H_{\text{BH}}$, where

$$\begin{aligned} H_{\text{Haldane}} &= \epsilon_0 \sum_i \left(a_i^\dagger a_i + b_i^\dagger b_i \right) - t_1 \sum_{\langle i,j \rangle} \left(a_i^\dagger b_j + b_j^\dagger a_i \right) \\ &\quad - t_2 \sum_{\langle\langle i,k \rangle\rangle}^{\text{anis}} \left(e^{\pm \frac{i\pi}{2}} a_i^\dagger a_k + e^{\mp \frac{i\pi}{2}} b_i^\dagger b_k + \text{h.c.} \right) , \\ H_{\text{BH}} &= \frac{U}{2} \sum_i \left[a_i^\dagger a_i \left(a_i^\dagger a_i - 1 \right) + b_i^\dagger b_i \left(b_i^\dagger b_i - 1 \right) \right] . \end{aligned} \tag{2.22}$$

Here the first term is the Haldane Hamiltonian from Eq. (2.15). We consider the anisotropic case, where one of the hopping terms (the horizontal one) is missing, as in Section 2.1.3. For the sake of clarity, we also assume that the Semenoff mass term M, producing charge density wave orders, is exactly zero, and the Haldane phase is $\phi_H = \pi/2$. The second term in the Hamiltonian (2.22) is the Bose-Hubbard interaction between bosons at same site i.

Based on the analysis of the single-particle Hamiltonian H_{Haldane}, we expect that when interactions are absent or sufficiently weak, the system is characterized by the presence of two distinct phases corresponding to the formation of either a zero-momentum superfluid (*ZMSF* phase) or a finite-momentum superfluid (*FMSF* phase) analogous to FFLO states. These phases appear since H_{Haldane} has minima at different points in the lowest band. When $t_2 \ll t_1$, we have a usual graphene dispersion with global minimum at point $\mathbf{\Gamma}$ in the middle of the BZ. By increasing t_2/t_1, we see the emergence of a critical value t_2^c, above which the maximum shifts away from $\mathbf{\Gamma}$, leading to the emergence of a non-uniform condensate order parameter. In Fig. 2.4 we show the variation of the band structure as a function of the ratio t_2/t_2^c. The *ZMSF–FMSF* transition between two phases is characterized by a change in the macroscopic occupation of the corresponding momenta in reciprocal space

$$n(\boldsymbol{k}) = \left\langle a_{\boldsymbol{k}}^\dagger a_{\boldsymbol{k}} \right\rangle + \left\langle b_{\boldsymbol{k}}^\dagger b_{\boldsymbol{k}} \right\rangle . \tag{2.23}$$

Another important observable is the expectation value of the bond current operators

$$J_{ik} = -2\mathfrak{Im}\left(t_{ik}\left\langle c_i^\dagger c_k\right\rangle\right) , \tag{2.24}$$

where c_i denotes either a_i or b_i, and t_{ik} is the amplitude of the corresponding tunneling. In our model only two types of current exist. The first type is NN currents flowing along one of the three vectors $\boldsymbol{u}_i$, that we will denote as $J_{AB,\boldsymbol{u}_i}$. The second type corresponds to NNN currents along one of the three vectors $\boldsymbol{v}_i$, denoted as $J_{AA,\boldsymbol{v}_i}$ and $J_{BB,\boldsymbol{v}_i}$. By symmetry, we have $J_{AA,\boldsymbol{v}_i} = -J_{BB,\boldsymbol{v}_i}$.

The nature of the *ZMSF–FMSF* transition is different in isotropic and anisotropic configurations of the Haldane model. In the first case the global minimum in the *ZMSF* phase transforms into a local maximum in the *FMSF* phase. Whereas in the second case the global minimum in the *ZMSF* phase still stays a minimum in the *FMSF* phase, but becomes local. Moreover, in the isotropic Haldane model the *FMSF* is characterized by the condensation of bosons at two Dirac points independently on the ratio t_2/t_1, while in the anisotropic Haldane model it moves continuously with t_2/t_1. This effect is due to the breaking of C_3 symmetry between the two models. We notice also that while finite momentum BECs were predicted [156–158] and observed experimentally [159, 160] with p-wave band superfluids and for a near-resonant hybridization of s and p-bands of bosons [161, 162], considering a model with artificial gauge fields as in our case is the only possibility to observe the *FMSF* phase using s-bands.

2.2.2 Superfluid phases

A. Zero-momentum phase

In the anisotropic model the *ZMSF* phase occurs as long as $t_2 < t_2^c = \sqrt{3/8}t_1$, while the isotropic model has a critical value $t_2^c = t_1/\sqrt{3}$. At zero temperature, bosons condense at zero momentum at the center $\mathbf{\Gamma}$ of the BZ, meaning that we can approximately write

$$a_i \approx a_{\mathbf{\Gamma}}/\sqrt{N_c}, \qquad b_j \approx b_{\mathbf{\Gamma}}/\sqrt{N_c} . \tag{2.25}$$

We remind that according to our notation, N_c is the total number of unit cells of the lattice. It is equal to half of the total number of sites $N_s = 2N_c$. Within this approximation, the Hamiltonian simplifies to

$$H \approx \epsilon_0\left(a_{\mathbf{\Gamma}}^\dagger a_{\mathbf{\Gamma}} + b_{\mathbf{\Gamma}}^\dagger b_{\mathbf{\Gamma}}\right) - 3t_1\left(a_{\mathbf{\Gamma}}^\dagger b_{\mathbf{\Gamma}} + b_{\mathbf{\Gamma}}^\dagger a_{\mathbf{\Gamma}}\right) + \frac{U}{2}\left[a_{\mathbf{\Gamma}}^\dagger a_{\mathbf{\Gamma}}\left(\frac{a_{\mathbf{\Gamma}}^\dagger a_{\mathbf{\Gamma}}}{N_c} - 1\right) + b_{\mathbf{\Gamma}}^\dagger b_{\mathbf{\Gamma}}\left(\frac{b_{\mathbf{\Gamma}}^\dagger b_{\mathbf{\Gamma}}}{N_c} - 1\right)\right] . \tag{2.26}$$

We next introduce the filling $n = N/N_s$, equal to the ratio of the total number of particles N to the total number of sites N_s. The complex order parameter in sublattice A is expressed as

$$\langle a_i\rangle = \langle a_{\mathbf{\Gamma}}\rangle/\sqrt{N_c} = \sqrt{n}e^{i\theta_A} , \tag{2.27}$$

with a similar expression for sublattice B, assuming an equal filling in both sublattices. The superfluid order parameter is uniform (it does not depend on the position i). The superfluid phases $\theta_{A/B}$ in each sublattice are pinned by the t_1 hopping term, such that $\theta_A = \theta_B$. This corresponds to the presence of one Goldstone mode. The

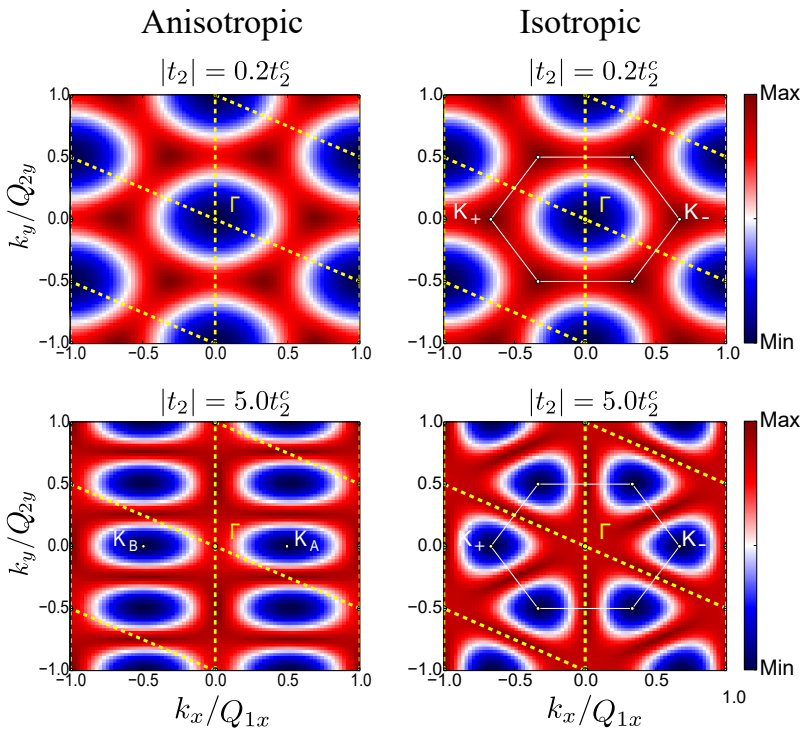

FIGURE 2.4: The lowest energy band of the anisotropic Haldane model (on the left) and of the isotropic Haldane model (on the right) in the non-interacting case ($U = 0$), plotted for different values of t_2 (different lines). Here t_2^c is the "critical" value of the coupling when minima move away from the point $\mathbf{\Gamma}$. Yellow dotted lines represent reciprocal lattice generated by vectors $\boldsymbol{Q}_1$ and $\boldsymbol{Q}_2$ defined in Fig. 2.1(b). Presence of artificial gauge fields (complex NNN hoppings in our case) is required for observation of minima at points in the BZ different from the point $\mathbf{\Gamma}$.

groundstate energy then reads

$$\epsilon_{GS} = N_s \left[(\epsilon_0 - 3t_1)\, n + \frac{U}{2} n(n-1) \right] . \tag{2.28}$$

We remark that the contribution of t_2-terms effectively vanishes in the groundstate. In the *ZMSF* phase, currents between NNN sites in the direction of vectors $\boldsymbol{v}_1$ or $\boldsymbol{v}_2$ are

$$J_{AA,\boldsymbol{v}_1} = J_{AA,\boldsymbol{v}_2} = -2\mathfrak{Im}\left(-it_2 n\right) = 2nt_2 . \tag{2.29}$$

We observe that in the anisotropic case we do not have NNN hoppings along $\boldsymbol{v}_3$, meaning that the corresponding currents are always zero: $J_{AA,\boldsymbol{v}_3} = 0$. Currents between NN sites $J_{AB,\boldsymbol{u}_i}$ are all exactly zero as well:

$$J_{AB,\boldsymbol{u}_1} = J_{AB,\boldsymbol{u}_2} = J_{AB,\boldsymbol{u}_3} = -2\mathfrak{Im}\left(-t_1 n\right) = 0 . \tag{2.30}$$

B. Critical value of NNN hopping amplitude

As we increase the NNN hopping amplitude t_2 up to the critical value t_2^c, the minimum of the single-particle band structure at the point $\boldsymbol{\Gamma}$ splits into two new minima that then start moving away from the center of the BZ. As we already mentioned previously, this behaviour is specific for the anisotropic Haldane model and has not been observed in the isotropic version of the model, where the condensation occurs at two Dirac points independently on the ratio t_2/t_1 for $t_2 > t_2^c$. Numerical simulations of the Fig. 2.4 and symmetry arguments imply that for any value of t_2, position of minima along the y-axis does not change. Thus, it should be sufficient for us to perform calculations only along the $k_y = 0$ axis in the BZ. In Fig. 2.5 we show some examples of the analytical energy structure compared to results of ED simulations for the single-particle Hamiltonian in different regimes of t_2 for $k_y = 0$, $k_x \in \left[0, 4\pi/\sqrt{3}a\right]$.

The goal of this subsection is to deduce the precise value of the critical NNN hopping amplitude t_2^c in the anisotropic Haldane model. Let us consider that the condensation in the general case occurs at points $\boldsymbol{k} = \pm\left(z\pi/\sqrt{3}a\right)\boldsymbol{e}_x$, for some real $z \in [0,2]$, defined up to a reciprocal lattice vector. Eigenvalues of the single-particle Hamiltonian H_{Haldane} at these points are

$$\epsilon_{\pm}(z) = \epsilon_0 \pm \sqrt{5t_1^2 + \left(16t_2^2 - 4t_1^2\right)\sin^2\left(\frac{\pi z}{2}\right) + 4t_1^2\cos\left(\frac{\pi z}{2}\right)} . \tag{2.31}$$

The extrema z_c of the lower band energy correspond to zeros of $\partial\epsilon_-(z)/\partial z$. They are solutions of the following set of equations:

$$\left[\begin{array}{rcl} \sin(\frac{\pi z_c}{2}) & = & 0\,, \\ \cos(\frac{\pi z_c}{2}) & = & \frac{1}{2}\left(\frac{t_1^2}{4t_2^2 - t_1^2}\right) . \end{array} \right. \tag{2.32}$$

We deduce three main regimes in the evolution of the energy band structure along the $k_y = 0$ line.

The first regime is determined by $|t_2| < \sqrt{1/8}t_1$. In this region the solution of the second equation exists and corresponds to the maximum of the band at two Dirac points. If we increase t_2, starting from zero, the value of z_c corresponding to these maxima increases (Dirac points move away from extremities of the BZ) until

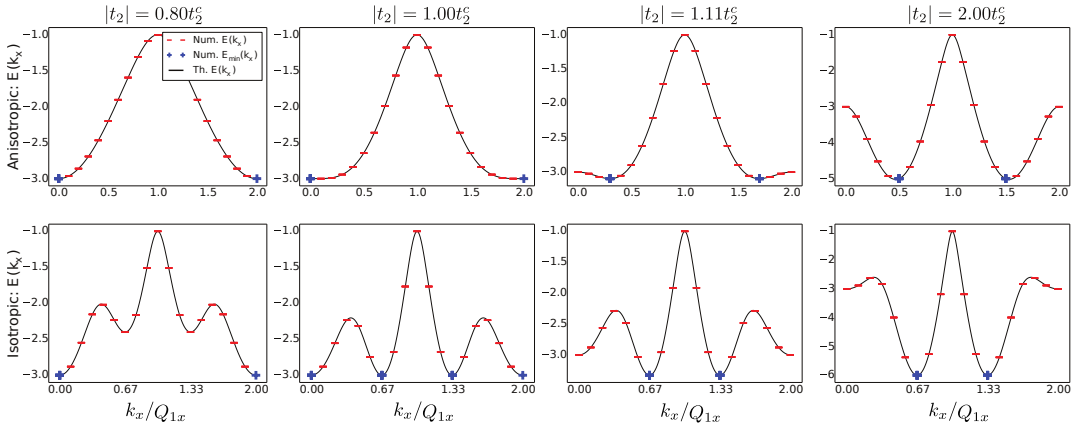

FIGURE 2.5: Cut of the lowest energy band of the single-particle system along the $k_y = 0$ line. Analytical calculations (black solid line) are superposed to the results of ED (red dashes). **Upper panel**: Anisotropic model. Structure of the ED cluster is 10×2 cells (40 sites) with tilt $t_h = -1$. Values of t_2 are chosen is such a way that the condensation occurs precisely at the points allowed by the geometry of the ED cluster. The value $t_2 = 2t_2^c$ is high enough to see the physics of the $t_2 \gg t_2^c$ regime. In this last case, shown on the rightmost figure, only the small distinction between analytical and numerical results (due to finite size effects) is observed. **Lower panel**: Isotropic model. Structure of the ED cluster is 9×2 cells (36 sites) with tilt $t_h = -1$.

it reaches the value $z_c = 2$. The minimum of the band is localized at point $\mathbf{\Gamma}$, that corresponds to the solution of the first equation for $z_c = 0$. In the second region $\sqrt{1/8}t_1 < |t_2| < \sqrt{3/8}t_1$ there is no solution of the second equation and the band possesses only one minimum at $z_c = 0$ and one maximum at $z_c = 2$. Finally, in the region $|t_2| > \sqrt{3/8}t_1$ the solution of the second equation starts existing again and corresponds to two new minima of the band. At the same time, the solution of the first equation at $z_c = 0$ transforms into a local maximum and the solution at $z_c = 2$ stays a global maximum of the band. This defines the precise point of the *ZMSF – FMSF* transition: $t_2^c = \sqrt{3/8}t_1$. The transitions between these three regimes can be seen in the upper panel of Fig. 2.5. The shape of the energy band at the critical point, expressed in terms of the parameter z is

$$\epsilon_-(z) \underset{z\to 0}{\approx} \epsilon_0 - 3t_1 + \frac{t_1}{12}\left(\frac{\pi z}{2}\right)^4 . \tag{2.33}$$

Thus, at the transition the well becomes much wider: the second power in the dispersion relation is replaced by the fourth power. In the following we will study in more details the behaviour of the time-dependent system in the regime of the effective NNN hopping amplitude t_2 close to t_2^c.

We notice that the displacement of the condensation point for different parameters of the problem affects the procedure of the numerical ED. Numerical simulations of the infinite lattice require considering a particular set of points on the lattice, forming a cluster, and of periodic boundary conditions (PBC) gluing together different clusters. This defines the set of quantum numbers associated to irreducible representations of the group of translations along two Bravais vectors of the lattice. Each quantum number corresponds to one point in the BZ and the amount of quantum numbers equals the number of possible translations in the cluster. Thus, by increasing the cluster size, we increase the resolution in the BZ. According to our previous

discussion, in order to capture the *ZMSF – FMSF* transition in the anisotropic model, one can restrict ourselves to the case $k_y = 0$. This motivates us to consider a particular choice of clusters, maximizing the resolution in the BZ along k_x at the price of minimizing the resolution along k_y. We make such clusters by composing $L_1 \times L_2$ unit cells of the honeycomb lattice in the geometry of the parallelogram generated by vectors $L_1\boldsymbol{R}_1$ and $L_2\boldsymbol{R}_2$. Each parallelogram is then translated with spanning vectors $\boldsymbol{S}_1 = L_1\boldsymbol{R}_1$ and $\boldsymbol{S}_2 = L_2\boldsymbol{R}_2 - t_h\boldsymbol{R}_1$ to fill the full lattice. Here t_h denotes the (horizontal) tilt of the lattice. This defines our implementation of PBC. More details on the tilted cluster construction are presented in Section A.1.5 of Appendix A.

C. Finite-momentum phase

The *FMSF* phase arises when t_2 reaches the critical value $t_2^c = \sqrt{3/8}t_1$. In the limit $t_2 \gg t_1$, the two sublattices become decoupled and bosons condense at the two inequivalent points $\boldsymbol{K}_A = \left(\pi/\sqrt{3}a\right)\boldsymbol{e}_x$ (on sublattice A), and $\boldsymbol{K}_B = -\left(\pi/\sqrt{3}a\right)\boldsymbol{e}_x$ (on sublattice B), as shown on Fig. 2.4. We begin with the study of the properties of the finite momentum BEC, by considering first this simpler case.

(i) Limit of two decoupled lattices. In the limit of two decoupled sublattices, one can use the following approximation for the real space annihilation (and creation) operators:

$$a_i \approx \frac{e^{-i\boldsymbol{r}_i\cdot\boldsymbol{K}_A}}{\sqrt{N_c}}a_{\boldsymbol{K}_A}, \qquad b_j \approx \frac{e^{-i\boldsymbol{r}_j\cdot\boldsymbol{K}_B}}{\sqrt{N_c}}b_{\boldsymbol{K}_B}\,. \tag{2.34}$$

In the following we will also use the notation

$$\langle a_i^\dagger a_i\rangle = n_A = N_A/N_c, \qquad \langle b_j^\dagger b_j\rangle = n_B = N_B/N_c\,, \tag{2.35}$$

such that $(n_A + n_B)/2 = n = N/N_s$ is the filling, since $N_c = N_s/2$. Within the mean-field approximation, we simply write

$$\langle a_{\boldsymbol{K}_A}\rangle \approx \sqrt{N_A}e^{i\theta_A}, \qquad \langle b_{\boldsymbol{K}_B}\rangle \approx \sqrt{N_B}e^{i\theta_B}\,, \tag{2.36}$$

where θ_A and θ_B are the superfluid phases associated with the two condensates. As a result, we obtain that the superfluid order parameter becomes non-uniform (it oscillates as a function of the position), similarly to the FFLO states:

$$\langle a_i\rangle \approx \sqrt{n_A}e^{-i\boldsymbol{r}_i\cdot\boldsymbol{K}_A}e^{i\theta_A}, \quad \langle b_j\rangle \approx \sqrt{n_B}e^{-i\boldsymbol{r}_j\cdot\boldsymbol{K}_B}e^{i\theta_B}\,. \tag{2.37}$$

By noticing that

$$(\boldsymbol{K}_A - \boldsymbol{K}_B)\cdot\boldsymbol{r}_i = 2\pi n_1 + \pi n_2 \tag{2.38}$$

for any $\boldsymbol{r}_i = n_1\boldsymbol{R}_1 + n_2\boldsymbol{R}_2$, one can easily check that in the groundstate the contribution of the NN hopping term vanishes in the thermodynamic limit:

$$\sum_{\langle i,j\rangle} a_i^\dagger b_j \propto \sum_i \left(e^{-i\boldsymbol{K}_B\cdot\mathbf{r}_i}\sum_{j=1}^{3} e^{-i\boldsymbol{K}_B\cdot\mathbf{u}_j}a_i^\dagger b_{\boldsymbol{K}_B}\right) = \sum_i e^{i(\boldsymbol{K}_A-\boldsymbol{K}_B)\cdot\boldsymbol{r}_i}a_{\boldsymbol{K}_A}^\dagger b_{\boldsymbol{K}_B} = 0\,. \tag{2.39}$$

Hence, we deduce that in the regime $t_2 \gg t_2^c$, within the mean-field approximation the Hamiltonian simplifies into

$$H \approx (\epsilon_0 - 4t_2 - U/2)\left(a^\dagger_{\boldsymbol{K}_A} a_{\boldsymbol{K}_A} + b^\dagger_{\boldsymbol{K}_B} b_{\boldsymbol{K}_B}\right) + \frac{U}{N_s}\left[\left(a^\dagger_{\boldsymbol{K}_A} a_{\boldsymbol{K}_A}\right)^2 + \left(b^\dagger_{\boldsymbol{K}_B} b_{\boldsymbol{K}_B}\right)^2\right] , \quad (2.40)$$

so that the groundstate energy reads

$$\epsilon_{GS} = N_s\left[(\epsilon_0 - 4t_2 - U/2)\, n + U\left(n_A^2 + n_B^2\right)/4\right] . \quad (2.41)$$

As the two sublattices are completely decoupled, both phases θ_A and θ_B become independent parameters, which corresponds to the presence of two Goldstone modes.

The phase difference $\theta_- = \theta_A - \theta_B$ can be fixed if a coherent coupling between the two wells is generated. Such effect can be induced, for example, by adding impurities to the model or, in the thermodynamic limit, by taking into account quantum fluctuations via the so called "order by disorder" mechanism [163]. In this case we obtain the following expression of NN current expectation values

$$\begin{aligned}
J_{AB,\boldsymbol{u}_1}(t_2 \gg t_2^c) &= \quad 2\sqrt{n_A n_B} t_1 \cos\left[(\boldsymbol{K}_A - \boldsymbol{K}_B)\cdot \boldsymbol{r}_i - \theta_-\right] = \pm 2\sqrt{n_A n_B} t_1 \cos(\theta_-) , \\
J_{AB,\boldsymbol{u}_2}(t_2 \gg t_2^c) &= -2\sqrt{n_A n_B} t_1 \cos\left[(\boldsymbol{K}_A - \boldsymbol{K}_B)\cdot \boldsymbol{r}_i - \theta_-\right] = \mp 2\sqrt{n_A n_B} t_1 \cos(\theta_-) , \\
J_{AB,\boldsymbol{u}_3}(t_2 \gg t_2^c) &= -2\sqrt{n_A n_B} t_1 \sin\left[(\boldsymbol{K}_A - \boldsymbol{K}_B)\cdot \boldsymbol{r}_i - \theta_-\right] = \pm 2\sqrt{n_A n_B} t_1 \sin(\theta_-) .
\end{aligned} \quad (2.42)$$

When moving along the vectors $\boldsymbol{R}_1$ or $\boldsymbol{R}_2$ of the Bravais lattice, the currents periodically change sign, implying the spontaneous breaking of translation symmetry. Such oscillations originate from Eq. (2.35). In numerical simulations with PBC, we do not observe the coherent coupling between sublattices. In particular, NN currents J_{AB} calculated in the groundstate using ED are always exactly zero. As a consequence, in the following we will refer to the relatively simple case of two condensates at $\boldsymbol{K}_A$ and $\boldsymbol{K}_B$, that are completely decoupled. Independently on this assumption, we deduce that NNN currents are exactly zero in the limit $t_2 \gg t_2^c$

$$J_{AA,\boldsymbol{v}_1} = J_{AA,\boldsymbol{v}_2} = 2\mathfrak{Im}\left(-t_2 n\right) = 0 . \quad (2.43)$$

(ii) Intermediate regime. We now consider the more realistic scenario where t_2 becomes of the order of t_1, still remaining in the $t_2 > t_2^c$ regime. We define $\alpha_{\boldsymbol{k}}$ and $\beta_{\boldsymbol{k}}$ as the annihilation operators in the lower and upper energy bands of the single-particle Hamiltonian. At each point of the BZ these operators are related to $a_{\boldsymbol{k}}$ and $b_{\boldsymbol{k}}$ through the unitary transformation:

$$a_{\boldsymbol{k}} = \mu(\boldsymbol{k})\alpha_{\boldsymbol{k}} + \nu(\boldsymbol{k})\beta_{\boldsymbol{k}} , \quad b_{\boldsymbol{k}} = e^{i\phi(\boldsymbol{k})}\left[-\nu^*(\boldsymbol{k})\alpha_{\boldsymbol{k}} + \mu^*(\boldsymbol{k})\beta_{\boldsymbol{k}}\right] , \quad (2.44)$$

with $|\mu(\boldsymbol{k})|^2 + |\nu(\boldsymbol{k})|^2 = 1$. In the low temperature limit, bosons condense at points $\pm\boldsymbol{K}_c = \pm\left(z_c \pi/\sqrt{3}a\right)\boldsymbol{e}_x$ (we recall that by our definition $z_c > 0$) so that $\langle \alpha_{\pm\boldsymbol{K}_c}\rangle \sim \sqrt{N}$ and $\langle \beta_{\pm\boldsymbol{K}_c}\rangle = 0$. Thus, annihilation (and creation) operators in real space are approximated by

$$a_i \approx \frac{e^{-i\boldsymbol{K}_c\boldsymbol{r}_i} a_{\boldsymbol{K}_c} + e^{i\boldsymbol{K}_c\boldsymbol{r}_i} a_{-\boldsymbol{K}_c}}{\sqrt{N_c}} , \quad b_i \approx \frac{e^{-i\boldsymbol{K}_c\boldsymbol{r}_i} b_{\boldsymbol{K}_c} + e^{i\boldsymbol{K}_c\boldsymbol{r}_i} b_{-\boldsymbol{K}_c}}{\sqrt{N_c}} . \quad (2.45)$$

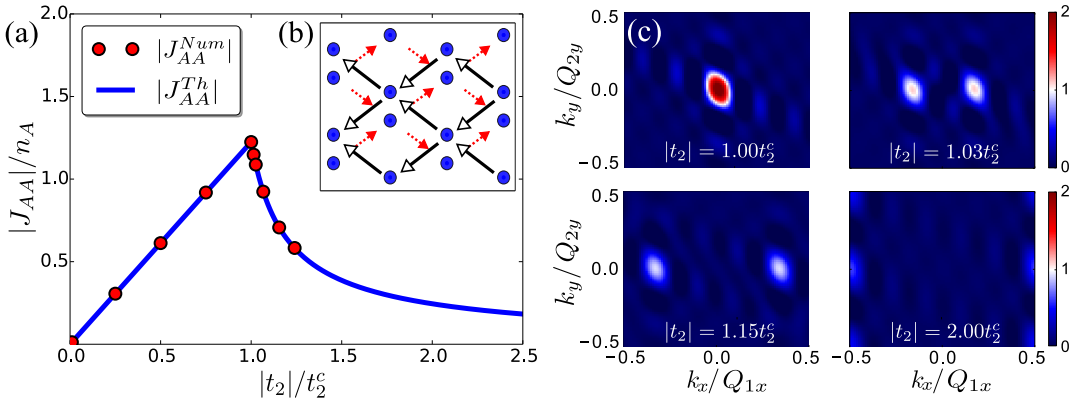

FIGURE 2.6: **(a)** Variation of the second neighbour current J_{AA} with t_2. Qualitative change of behaviour can be seen when crossing the critical value $t_2^c = \sqrt{3/8}t_1$. In the figure analytical prediction (blue line) is compared with the results of ED (red circles). **(b)** Result of ED showing patterns of currents J_{AA}. Closed loops of chiral currents involve lozenge geometries. Different types of arrows correspond to different sublattices. **(c)** Momentum distribution $n(\boldsymbol{k})$ at the transition in the *FMSF* phase in the bosonic many-body ground-state. Structure of the ED cluster is 6×4 cells (48 sites) with tilt $t_h = -2$. Parameters of simulations: $N = 2$, $U = 0$. Finite size effects result in a tilt of the maxima of $n(\boldsymbol{k})$ and its non-physical oscillations.

We then introduce the averages

$$\langle a_{\pm \boldsymbol{K}_c} \rangle = \sqrt{N_{A,\pm}} e^{i\theta_{A,\pm}}, \qquad \langle b_{\pm \boldsymbol{K}_c} \rangle = \sqrt{N_{B,\pm}} e^{i\theta_{B,\pm}} , \tag{2.46}$$

such that $N_{A,+} + N_{A,-} = N_A$, $N_{B,+} + N_{B,-} = N_B$, $N_{A,\pm} + N_{B,\pm} = N_\pm$ and $N_A + N_B = N_+ + N_- = N$. The approximation (2.45) can be used to find a more general form of the GS Hamiltonian and GS energy in the *FMSF* phase (see Appendix D for their complete expressions). Moreover, we observe that phases $\theta_{A,\pm}$ and $\theta_{B,\pm}$ are pinned pairwise, that corresponds to the presence of two Goldstone modes. We also get the expression of currents valid in both regimes of t_2

$$J_{AA,v_1} = J_{AA,v_2} = -\, t_2 \frac{N_A}{N_c} \cos\left(z_c \frac{\pi}{2}\right) , \quad J_{AA,v_3} = 0 . \tag{2.47}$$

The evolution of the currents J_{AA} with t_2 is shown on Fig. 2.6(a-b), where the analytical prediction is compared to the ED results in a weakly interacting regime. Another way to perform a numerical verification of the behavior of the system in the *FMSF* regime is to look at the momentum distribution $n(\boldsymbol{k})$. In Fig. 2.6(c), we give some results of ED showing how the momentum distribution in the many-body GS in the $\mathbf{k} = \mathbf{\Gamma}$ sector evolves when changing t_2 above the critical value t_2^c. We effectively observe the splitting of the condensation point into two points and their further displacement along the $k_y = 0$ line.

The continuous variation of currents suggests that the *ZMSF–FMSF* transition in the anisotropic Haldane model is of the second order. In order to justify this point, we first write explicitly the unitary transformation of Eq. (2.44) at momentum $\pm \boldsymbol{K}_c$

in terms of z_c:

$$a_{\pm\boldsymbol{K}_c} = -\sqrt{\frac{\sqrt{X^2(z_c)+Y^2(z_c)}\pm Y(z_c)}{2\sqrt{X^2(z_c)+Y^2(z_c)}}}\alpha_{\pm\boldsymbol{K}_c} + \sqrt{\frac{\sqrt{X^2(z_c)+Y^2(z_c)}\mp Y(z_c)}{2\sqrt{X^2(z_c)+Y^2(z_c)}}}\beta_{\pm\boldsymbol{K}_c}\ ,$$
$$b_{\pm\boldsymbol{K}_c} = -\sqrt{\frac{\sqrt{X^2(z_c)+Y^2(z_c)}\mp Y(z_c)}{2\sqrt{X^2(z_c)+Y^2(z_c)}}}\alpha_{\pm\boldsymbol{K}_c} - \sqrt{\frac{\sqrt{X^2(z_c)+Y^2(z_c)}\pm Y(z_c)}{2\sqrt{X^2(z_c)+Y^2(z_c)}}}\beta_{\pm\boldsymbol{K}_c}\ , \tag{2.48}$$

where $X(z_c)$ and $Y(z_c)$ are defined as follows:

$$X(z_c) = t_1\left[1+2\cos\left(z_c\frac{\pi}{2}\right)\right]\ ,\quad Y(z_c) = 4t_2\sin\left(z_c\frac{\pi}{2}\right)\ . \tag{2.49}$$

One notices that N_+ and N_-, corresponding to the number of particles in the wells at $\pm\boldsymbol{K}_c$, and z_c are the only parameters of the problem. In Eq. (D.6), we express the GS energy in terms of these quantities. Close to the *ZMSF–FMSF* phase transition, we expand the GS energy in powers of z_c. By doing this calculation in the non-interacting case we obtain

$$\epsilon_{GS} \underset{z_c\to 0}{=} \text{cst} - t_1 N\left[\frac{8}{3}\left(\frac{t_2}{t_1}\right)^2 - 1\right]\left(\frac{\pi z_c}{2}\right)^2 + \frac{N}{108t_1^3}\left(128t_2^4 - 9t_1^4\right)\left(\frac{\pi z_c}{2}\right)^4 + \dots \tag{2.50}$$

The sign change of the first term, proportional to z_c^2, occurs at the value $t_2^c = \sqrt{3/8}t_1$, in agreement with our previous estimations. Moreover, the sign of the second term, proportional to z_c^4, is always positive in the *FMSF* phase. Thus, we clearly see that the transition in the anisotropic Haldane model is second order. This is different from the case of the isotropic Haldane model [153, 164], where the transition is first order, since three wells are simultaneously present at the transition.

D. Interaction effects

In order to study more precisely the effect of interactions on the *ZMSF – FMSF* phase transition, we repeat the previous analysis and write down the contribution to the GS energy in powers of z_c associated with the interaction term only. This calculation is based on the ansatz (2.45). Thus, we must assume that interactions are weak enough so that they do not affect the double-well structure of the system in the *FMSF* phase. The result of such a calculation is given in Eq. (D.6) of Appendix D.

First, we see that in the *FMSF* phase interactions impose constraints onto N_+ and N_- – the numbers of particles in each well, and remove the degeneracy that was present in the non-interacting system. However, contrary to the most intuitive guess, there are two groundstates that minimize the energy in two distinct sub-regimes of the *FMSF* phase: for $t_2^c < t_2 < \sqrt{(17+\sqrt{97})/24}\ t_2^c$ interactions favor particles in one particular well, such that either N_+ or N_- becomes precisely equal to N. When $t_2 > \sqrt{(17+\sqrt{97})/24}\ t_2^c$ the uniform distribution of particles $N_+ = N_- = N/2$ is preferred. The second effect of weak interactions consists in moving the position of minima away from $\pm\boldsymbol{K}_c$. In particular, to the lowest order in z_c, the contribution of

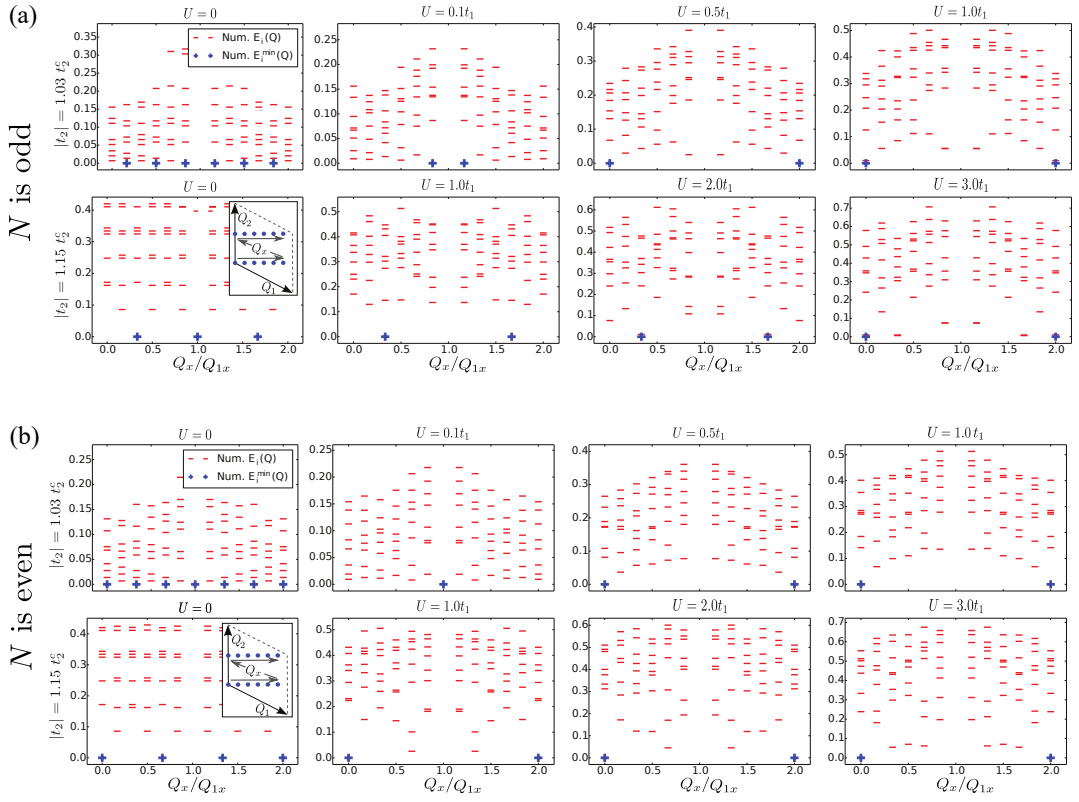

FIGURE 2.7: Many-body energy levels (cut along the $k_y = 0$ line in the BZ). ED cluster: 6×2 cells (24 sites) with tilt $t_h = -5$. Position in the BZ of quantum number associated to this precise cluster are shown in a corner of the leftmost plot. Different columns correspond to different values of U. Different rows correspond to different values of t_2. Parameters: **(a)** $N = 5$ particles; **(b)** $N = 6$ particles

interactions to the GS energy at the *ZMSF–FMSF* transition is

$$\Delta\epsilon'_{GS} = NUn\frac{8t_2^2}{9t_1^2}\left(z_c\frac{\pi}{2}\right)^2 . \tag{2.51}$$

This leads to the increase of the critical NNN coupling amplitude t_2^c. If particles are not located all in one well, there appears an additional contribution

$$\Delta\epsilon''_{GS} = -\frac{16U}{3}\frac{N_+\left(N-N_+\right)}{N_s}\left(\frac{t_2}{t_1}\right)^2\left(z_c\frac{\pi}{2}\right)^2 , \tag{2.52}$$

that, on the opposite, tends to decrease t_2^c. The second contribution $\Delta E''_{GS}$ dominates when $N_+ = N_- = N/2$, resulting in the generation of an effective repulsion between the two wells (see also Appendix D for a more detailed analysis).

In order to check our theoretical predictions, we perform ED calculations. Details on the implementation of numerical algorithms used in this section are presented in Appendix A. We plot the many-body energy levels $\epsilon_i(k_x) - \epsilon_0$ for different values of the total momentum $\boldsymbol{k}$ (here ϵ_0 denotes the lowest energy over all momentum sectors). Simulation results are shown in Figs. 2.7(a) for an odd number of particles and 2.7(b) for an even number of particles. Without interactions, we observe a high degeneracy of the many-body groundstate due to the fact that all bosons condense independently in one of the two wells. If one increases the interaction strength, this degeneracy is lifted. We observe that, close to the transition ($t_2 \approx t_2^c$) to the *FMSF*

phase, the most energetically favored groundstate of the weakly interacting regime corresponds to the state with all particles condensed in the same well. This is not the case for higher values of t_2. If t_2 increases, the groundstate becomes, as expected, the state with all particles uniformly distributed over two wells (with $N_+ - N_- = \pm 1$ if N is odd). The value at which this transition occurs agrees well with the analytical prediction $t_2 = \sqrt{(17+\sqrt{97})/24}\, t_2^c$, with some imprecision coming from finite size effects.

When U increases, the groundstate changes into a more complicated many-body state with $n(\boldsymbol{k})$ having a non-zero contribution at the $\boldsymbol{\Gamma}$ point. This transition is accompanied by the change of the location of the minimum in momentum space. In this regime the perturbation due to interactions cannot be interpreted as small in terms of other parameters of our problem. The effect of interactions in this non-perturbative regime will not be considered in this work. In simulations we do not observe the displacement of the condensation point due to interactions. This is explained by the fact that for weak interactions this effect is not noticeable enough to be observed because of the finite sizes of ED clusters, whereas in the regime of stronger interactions other effects occur earlier.

2.2.3 Excitation properties

In this subsection we use the Bogoliubov transformation to study excitations above the groundstate, according to the formalism presented in Section 1.2. If the system is in the *ZMSF* phase, at low temperature T, one can suppose that the groundstate at $\boldsymbol{k} = \boldsymbol{\Gamma}$ will be still macroscopically occupied by a population of $N_0 = n_0 N_s$ bosons (with filling n_0). Small fluctuations can be described by operators $z_{c,\boldsymbol{k}}$ with $c = A$ or B, depending on the sublattice. The total number of particles is thus

$$N = N_0 + \sum_{\substack{\boldsymbol{k}\in \mathrm{BZ},\\ \boldsymbol{k}\neq\boldsymbol{\Gamma},c}} z^\dagger_{\nu,\boldsymbol{k}} z_{c,\boldsymbol{k}} \,. \tag{2.53}$$

We are interested in writing the Hamiltonian H in powers of $z_{c,\boldsymbol{k}}$. For convenience we also prefer to express H in the grand canonical ensemble, by introducing the chemical potential μ. To zero order in the perturbation we recognize the expression for the groundstate energy $E_{GS} - \mu N_0$. The term linear in the fluctuations vanishes for a particular value of the chemical potential, which is:

$$\mu = -3t_1 + Un_0 \,. \tag{2.54}$$

To second order in perturbation we obtain:

$$\begin{aligned} H_2 = &\sum_{\substack{\boldsymbol{k}\in \mathrm{BZ},\\ \boldsymbol{k}\neq 0}} \begin{pmatrix} z^\dagger_{A,\boldsymbol{k}} \\ z^\dagger_{B,\boldsymbol{k}} \end{pmatrix}^t \cdot \left[-d_\nu(\boldsymbol{k})\sigma^\nu - \mu I_2\right] \cdot \begin{pmatrix} z_{A,\boldsymbol{k}} \\ z_{B,\boldsymbol{k}} \end{pmatrix} \\ &+ \frac{Un_0}{2} \sum_{\substack{\boldsymbol{k}\in \mathcal{BZ},\\ \boldsymbol{k}\neq 0,c}} \left(z^\dagger_{c,\boldsymbol{k}} z^\dagger_{c,-\boldsymbol{k}} + z_{c,\boldsymbol{k}} z_{c,-\boldsymbol{k}} + 4 z^\dagger_{c,\boldsymbol{k}} z_{c,\boldsymbol{k}} \right) \,, \end{aligned} \tag{2.55}$$

where functions $d_\nu(\boldsymbol{k})$ are defined as in Eq. (2.17). The resulting Hamiltonian can now be rewritten (up to some constant term E_0) as

$$H_2 = -\frac{1}{2} \sum_{\boldsymbol{k}} Z^\dagger_{\boldsymbol{k}} \cdot \mathcal{H}_{\mathrm{PH}}(\boldsymbol{k}) \cdot Z_{\boldsymbol{k}} \,, \tag{2.56}$$

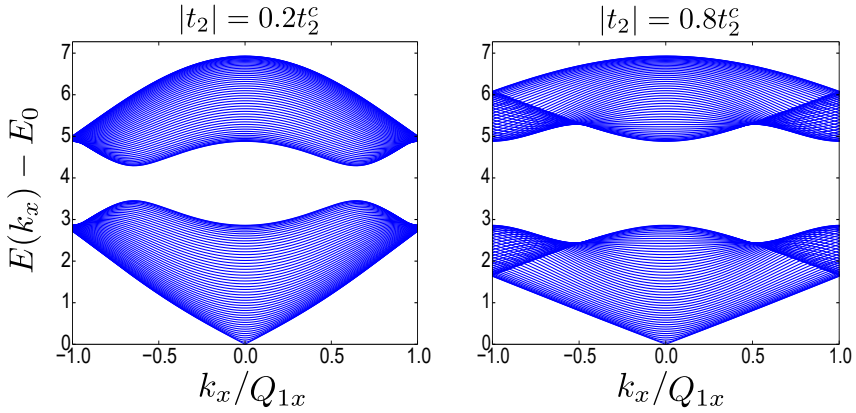

FIGURE 2.8: Dispersion relation of excitations in the *ZMSF* phase of the anisotropic Haldane model, showing the linear Bogoliubov dispersion relation around the point $\mathbf{\Gamma}$ in the BZ. Both figures were taken for $t_1 = 1$ and $Un_0 = 1$.

where $Z_{\boldsymbol{k}}$ and $\mathcal{H}_{\mathrm{PH}}(\boldsymbol{k})$ are defined as follows:

$$Z_{\boldsymbol{k}}^{\dagger} = \left(z_{A,\boldsymbol{k}}^{\dagger}, z_{B,\boldsymbol{k}}^{\dagger}, z_{A,-\boldsymbol{k}}, z_{B,-\boldsymbol{k}}\right) , \tag{2.57}$$

$$\mathcal{H}_{\mathrm{PH}}(\boldsymbol{k}) = \begin{pmatrix} \mu + d_z(\boldsymbol{k}) - 2Un_0 & d_x(\boldsymbol{k}) - d_y(\boldsymbol{k})i & -Un_0 & 0 \\ d_x(\boldsymbol{k}) + d_y(\boldsymbol{k})i & \mu - d_z(\boldsymbol{k}) - 2Un_0 & 0 & -Un_0 \\ -Un_0 & 0 & \mu - d_z(\boldsymbol{k}) - 2Un_0 & d_x(\boldsymbol{k}) + d_y(\boldsymbol{k})i \\ 0 & -Un_0 & d_x(\boldsymbol{k}) - d_y(\boldsymbol{k})i & \mu + d_z(\boldsymbol{k}) - 2Un_0 \end{pmatrix} . \tag{2.58}$$

This Hamiltonian can be diagonalized by using the Bogoliubov transformation. In Fig. 2.8 we show the corresponding solution at the value of the interaction such that $n_0U = t_1 = 1$. The dispersion relation is linear around the point $\boldsymbol{k} = \mathbf{\Gamma}$. We remark that in the anisotropic case the velocity of the "sound" mode depends on t_2, whereas in the isotropic case it was completely independent of t_2. In Ref. [165] it was shown for the case of the isotropic Haldane model, that the topological properties of Bloch bands present in the non-interacting case are smoothly carried over to Bogoliubov excitation bands. We expect the same formalism to be applicable to the case of the anisotropic Haldane model.

If the system is in the *FMSF* phase, two wells at $\boldsymbol{k} = \pm\boldsymbol{K}_c$ are macroscopically occupied at low temperature, according to the ansatz of Eq. (2.45). In addition to the effects presented in Section 2.2.2, and similarly to the *ZMSF* case, the interaction term H_{BH} couples different $\boldsymbol{k}$-modes. However, now a greater number of modes at $\boldsymbol{k}$, $-\boldsymbol{k}$, $\boldsymbol{k} \pm 2\boldsymbol{K}_c$, and $-\boldsymbol{k} \pm 2\boldsymbol{K}_c$ become coupled. Hence, the matrix one should diagonalize using the Bogoliubov transformation has the size 12×12 instead of 4×4. In this case we naturally expect to observe the presence of two Goldstone modes, with linear dispersion relations around two points $\pm\boldsymbol{K}_c$. Since the gap does not close at the transition, we expect that the topological properties of Bogoliubov excitations remain unaffected when going through the *ZMSF–FMSF* phase transition.

2.2.4 Mott insulator phase

When the interaction strength U becomes very strong compared to the hopping amplitudes t_1 and t_2, the system develops a Mott insulator phase. It is associated with

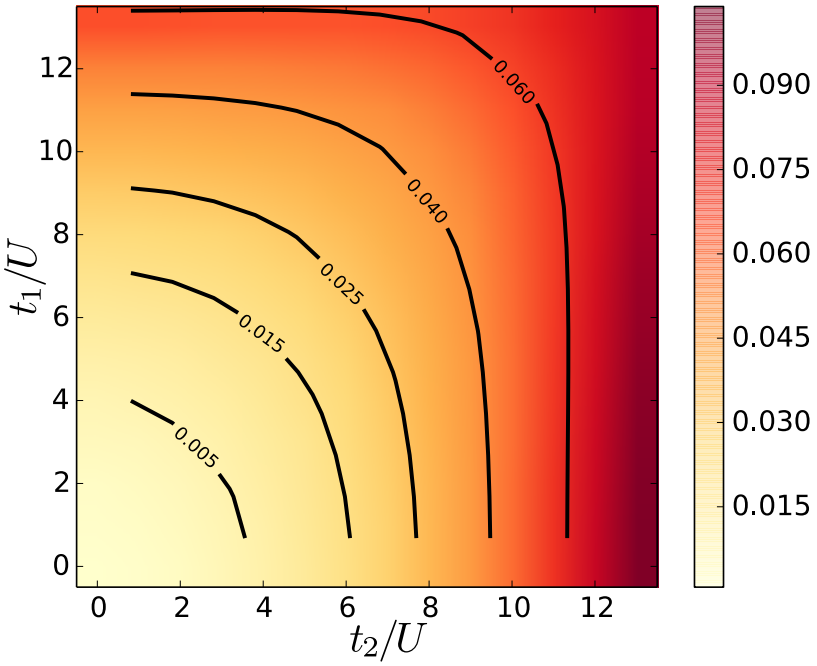

FIGURE 2.9: ED calculation of the averaged boson number fluctuation defined in Eq. (2.59), as a function of the ratios t_1/U and t_2/U. We observe the formation of the Mott insulator phase where the number fluctuation vanishes for $t_i/U \sim 10$. Simulations are performed on a lattice of 3×3 unit cells with no tilt. The maximum number of bosons per site is fixed to 2.

the vanishing value of the order parameters $\langle a_i \rangle$ and $\langle b_i \rangle$. Ground-state properties in the Mott insulator phase of the isotropic Haldane model for bosons have already been addressed in Ref. [153]. In this subsection we perform numerical ED calculation of the phase diagram of the anisotropic Haldane model for strong interactions.

Because the local bosonic Hilbert space is infinite, we truncate it so that the maximum number of bosons per site cannot be bigger than 2. We consider the ED cluster of 3×3 unit cells (18 sites) with no tilt. This lattice is poorly suited to study the anisotropic version of the Haldane model where the condensation point moves with the ratio t_2/t_1, however bigger lattices are hardly achievable in numerical simulations. Since the total number of bosons is conserved in our simulations, we cannot probe the change in the order parameters $\langle a_i \rangle$ and $\langle b_i \rangle$. The Mott insulator – superfluid phase transition is captured by looking at the boson number fluctuation

$$\frac{1}{N_c} \sum_i \left(\langle n_{A,i}^2 + n_{B,i}^2 \rangle - \langle n_{A,i} \rangle^2 - \langle n_{B,i} \rangle^2 \right) . \tag{2.59}$$

Here we average the observable over all the cells of the cluster. Results of such simulation are shown in Fig. 2.9. We observe that the Mott insulator phase is described by a vanishing boson number fluctuation, as opposed to the superfluid phases when it acquires a finite value. The phase transition occurs for significantly large values of U/t_i of the order of 10. We notice however that the exact point of the phase transition and the details related to the *ZMSF – FMSF* are unlikely to be reproduced correctly on the lattice of such a small size. In particular, we do not recover the lobe observed in the isotropic version of the Haldane model, signifying that when $t_2 \sim t_1$, the competing effect of two hopping amplitudes makes the Mott insulator phase more

favorable (higher values of amplitudes t_i are required to go to the superfluid phases).

2.3 Interacting bosons on brickwall ladder geometry

In Sections 2.1 and 2.2 we have observed that the Haldane model on the honeycomb lattice hosts rich phase diagrams both for fermions and for bosons. However, addressing the interacting problem in 2D geometries is often a very challenging task. If exact solutions do not exist, field theories could be used, but the quantum fluctuations cannot be neglected in these cases and mean-field solutions are not trustful. In particular, we are not able to calculate analytically the relevant properties of the Haldane model, when both t_1 and t_2 terms are large, and the interactions are not perturbative. Moreover, in the following chapter (Chapter 3) we will see that this regime allows one to probe the physics of exotic frustrated spin models in the spinful counterpart of the Haldane model – the Kane-Mele model for quantum spin Hall effect [46, 47].

From the other side, many theoretical and experimental works were performed during last decades using the quasi one-dimensional geometries, such as chains, two or multi-leg ladders. Efficient and very powerful analytical tool that can be employed in this case is called bosonization [166–169]. In particular, in bosonic systems, questions related to the Mott insulator – superfluid phase transition, effects induced by the magnetic field, such as Meissner effect and apparition of one dimensional equivalent of a vortex lattice were addressed [170–178]. In the context of topological states of matter, low-dimensional systems attract attention because of the possibility to create bosonic SPT order and valence bond solids [82, 87, 179] – topologically nontrivial bosonic states of matter we discussed in Section 1.5. The famous example of such states is the one found by Affleck, Kennedy, Lieb and Tasaki [81]. Experimental realizations of bosonic chains and ladders, giving opportunity to study the rich and profound physics of such systems, have already been done recently using ultra-cold atom setups [142–144].

Motivated by such theoretical and experimental context, we consider in this section a ladder version of the anisotropic Haldane model introduced previously in Section 2.2. We break the translation invariance along the vector $\boldsymbol{R}_2$, but the system is still invariant under the translations along $\boldsymbol{R}_1$. Hence, the relevant vectors in the first BZ live on a circle. Moreover, for a better visibility we also replace the honeycombs by the rectangles of the brick-wall lattice. The model constructed in such a way is shown in Fig. 2.10(a). The unit cell of the ladder is formed by 4 distinct sites, that we will distinguish by chain index $\nu \in \{0, 1\}$ and by sublattice index $c \in \{A, B\}$, with the convention that the operator $c_{\nu,i}$ is either $a_{\nu,i}$ or $b_{\nu,i}$, reminiscent of the 2D formulation of the problem. The corresponding Hamiltonian can be conveniently written in terms of 4 distinct terms

$$H = \sum_{\nu,c} H^{\mathrm{BH}}_{\nu,c} + \sum_{\nu} H^{\parallel}_{\nu} + \sum_{c} H^{t_2}_{c} + H^{\perp} \tag{2.60}$$

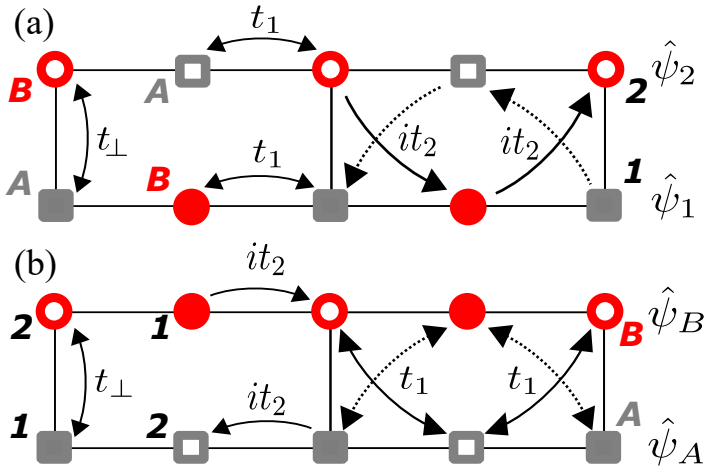

FIGURE 2.10: Strip (ladder) geometry consisting of two coupled chains. Each site of the unit cell of this ladder is characterized by the chain index 1 or 2 (represented in the picture by the fact that the figure is either filled or not) and the sublattice index A or B (represented by the color and the shape of the figure). In the continuum limit, depending on the ratio t_1/t_2 we would prefer either to describe the system in terms of **(a)** operators ψ_1 and ψ_2 if $t_1 \gg t_2$, or **(b)** operators ψ_A and ψ_B if $t_1 \ll t_2$.

expressed as follows:

$$
\begin{aligned}
H_\nu^{\parallel} &= -t_1 \sum_i \left(a^\dagger_{\nu,2i} b_{\nu,2i+1} + a^\dagger_{\nu,2i} b_{\nu,2i-1} + \text{h.c.} \right) , \\
H_c^{t_2} &= -it_2 \sum_i \left(c^\dagger_{1,2i} c_{2,2i+1} + c^\dagger_{2,2i-1} c_{1,2i} - \text{h.c.} \right) , \\
H^{\perp} &= -t_\perp \sum_i \left(a^\dagger_{1,2i} b_{2,2i} + b^\dagger_{2,2i} a_{1,2i} \right) , \\
H_{\nu,c}^{\text{BH}} &= \frac{U}{2} \sum_i c^\dagger_{\nu,i} c_{\nu,i} \left(c^\dagger_{\nu,i} c_{\nu,i} - 1 \right) .
\end{aligned}
\tag{2.61}
$$

Here the spatial index i runs over $\{1, 2, \ldots, N_c\}$. We keep the same notation and denote by N_c the total number of unit cells. Thus, the number of sites in each chain is $2N_c$, and the total number of sites is $N_s = 4N_c$. If we denote by a the distance between NN sites, the total length of the ladder in the x direction will be $L = 2N_c a$. Terms $H_\nu^{\parallel}$, $H^{\perp}$ and $H_c^{t_2}$ in the Hamiltonian are usual NN and NNN hopping terms. However, we distinguish $H_\nu^{\parallel}$, that couples bosons on the same chain, from $H^{\perp}$, that couples bosons at the same position in the x direction (and at the same coordinate i), but on two different chains. If we compare the strip geometry to the 2D geometry, we should consider $t_\perp = t_1$. Yet, we will study a more general case with arbitrary hopping $t_\perp$. Term $H_c^{t_2}$ couples different chains at different spatial positions (but not necessarily at different coordinates i), which belong to the same sublattice $c \in A$ or B. The last term, $H_{\nu,c}^{\text{BH}}$ is the local Bose-Hubbard interaction between bosons at the same site of the ladder.

2.3.1 Band structure in free case

We first calculate the band structure $\epsilon_0(k)$ of the non-interacting system by going to the momentum space. The Hamiltonian is rewritten in terms of 4×4 matrices $\mathcal{H}(k)$

as follows: $H = -\sum_k \psi_k^\dagger \cdot \mathcal{H}(k) \cdot \psi_k$, where $k \in \left[-\frac{\pi}{2a}, \frac{\pi}{2a}\right]$ is the vector in the 1D first BZ, $\psi_k = (a_{1,k}, b_{1,k}, a_{2,k}, b_{2,k})^t$ and

$$\mathcal{H}(k) = \begin{pmatrix} 0 & 2t_1\cos(ak) & -2t_2\sin(ak) & t_\perp \\ 2t_1\cos(ak) & 0 & 0 & 2t_2\sin(ak) \\ -2t_2\sin(ak) & 0 & 0 & 2t_1\cos(ak) \\ t_\perp & 2t_2\sin(ak) & 2t_1\cos(ak) & 0 \end{pmatrix} \tag{2.62}$$

In Fig. 2.11, we show the spectrum $\epsilon_0(k)$ for various t_2. If we consider for instance $t_2 = 0$, we find that the spectrum is

$$\epsilon_0(k) = \pm\frac{1}{2}\left[t_\perp \pm \sqrt{t_\perp^2 + 16t_1^2\cos^2(ak)}\right] , \tag{2.63}$$

to be compared to the standard ladder (*i.e.* a two-leg square ladder with no t_2 terms) bands $\epsilon_0(k) = \pm t_\perp - 2t_1\cos(ak)$. In the general case, the four eigenvalues of $\mathcal{H}(k)$ are

$$\epsilon_0(k) = \pm\frac{1}{2}\left[t_\perp \pm \sqrt{t_\perp^2 + 16t_1^2\cos^2(ak) + 16t_2^2\sin^2(ak)}\right] . \tag{2.64}$$

From this equation and Fig. 2.11, we observe that there is a transition at $t_1 = t_2$, separating the situation $t_2 < t_1$, in which the minimum of the lowest band is located at $k = 0$, from the situation $t_2 > t_1$, where the minimum of the lowest band is $k = \pi/2a$ (up to a reciprocal lattice vector). This is thus analogous to the *ZMSF–FMSF* transition of the 2D version of the model, except that the minimum at $k = \pi/2a$ does not move when changing t_2. This transition is actually related to the duality in the model, appearing in Fig 2.10(b), in which $t_1 \leftrightarrow it_2$ and two sites in the middle of each rectangular "brick" are interchanged. This duality maps local kinetic energy of each chain onto current operators. It is lastly important to notice that, at this very transition point $t_1 = t_2$, the model displays flat bands since the four energies become

$$\epsilon_0(k) = \pm\frac{1}{2}\left[t_\perp \pm \sqrt{t_\perp^2 + 16t_1^2}\right] , \tag{2.65}$$

and are thus independent of k. Such peculiar band structure makes it difficult to analyze the effect of interactions on the model at the phase transition, but is promising in the search for Laughlin states [180–182] – the celebrated example of the intrinsic topological order.

2.3.2 Interactions and bosonization

In order to describe the behavior of the interacting system in *ZMSF* and *FMSF* phases, far from the regime of flat bands at $t_1 \sim t_2$, we write Hamiltonian (2.61) in the continuum limit. If one considers only one chain for instance, its low-energy description falls into the universality class of Tomonaga-Luttinger liquids. Excitations are collective sound modes with linear dispersion and are described using the "harmonic fluid approach" also known as "bosonization" [166–169]. The Hamiltonian describing such kind of systems in the continuum limit can be expressed in terms of real bosonic fields ϕ and θ in the following way

$$H_\nu = v\int \frac{\mathrm{d}x}{2\pi}\left(K\left|\partial_x\theta(x)\right|^2 + \frac{1}{K}\left|\partial_x\phi(x)\right|^2\right) . \tag{2.66}$$

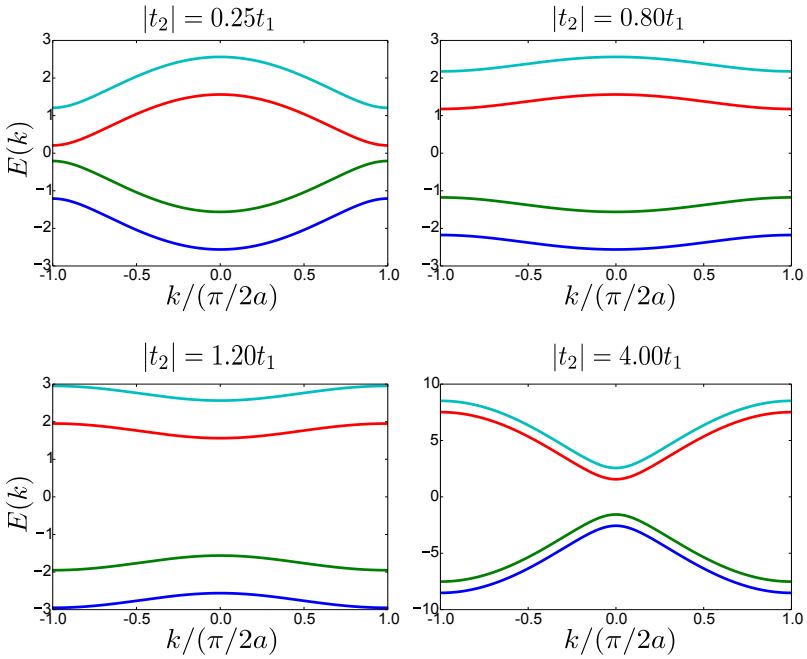

FIGURE 2.11: Single particle spectra of the ladder model ($U = 0$). All figures have parameters $t_1 = t_\perp = 1$. We see that as t_2 increases, the minima of the bands moves from $k = 0$ to $k = \pm\frac{\pi}{2a}$. The gap between middle bands closes at $t_2 = 0$.

Here v is the speed of sound and K is the Luttinger parameter that quantifies the strength of the interactions. We have $K > 1$ for finite repulsive short-range interactions, $K = 1$ in the hard core limit, and $K \to \infty$ in the limit of free bosons. Bosonic fields $\theta(x)$ and $\phi(x)$ are conjugate and satisfy the following commutation relations:

$$[\phi(x), \theta(x')] = i\frac{\pi}{2}\,\mathrm{Sign}(x - x')\,, \quad [\phi(x), \phi(x')] = [\theta(x), \theta(x')] = 0\,. \tag{2.67}$$

In order to go to the continuum limit of the lattice model, we set $x = ja$ with a – the lattice spacing. In our particular case, we have the freedom to define either the set of operators

$$\psi_{1(2)}(x) = c_{1(2),j}/\sqrt{a}\,, \tag{2.68}$$

corresponding to the lower/upper chain prescription, or the operators

$$\psi_{A(B)}(x) = a(b)_j/\sqrt{a}\,, \tag{2.69}$$

that correspond to the sublattice prescription. This choice of prescription is schematically represented in Fig. 2.10. Bosonic creation operators $\psi_\nu^\dagger(x)$ are then written in terms of bosonic fields $\theta_\nu(x)$ and $\phi_\nu(x)$ via the following relation:

$$\psi_\nu^\dagger(x) = \left(\rho_0 - \frac{1}{\pi}\partial_x\phi_\nu(x)\right)^{1/2} \sum_p \exp\left[i2p\left(\pi\rho_0 x - \phi_\nu(x)\right)\right] \exp\left[-i\theta_\nu(x)\right]\,. \tag{2.70}$$

The $\theta_\nu(x)$ is a phase field and the $\phi_\nu(x)$ is the long wavelength density excitation

$$\partial_x\phi_\nu(x) = -\pi\left(\rho_\nu(x) - \rho_0\right) \tag{2.71}$$

Here $\rho_\nu(x)$ is the density operator and ρ_0 is its mean value in the groundstate. If the

system is translation invariant, $\rho_0 = n/a$ with $n = N/N_s$ – the filling. The oscillating contribution in Eq. (2.70) reflects the ordering in the lattice description of the model (particles tend to develop a crystal-like structure). If one averages the density over the distances large compared to a, only the $p = 0$ term will remain. This is the simplification that we will consider in the following.

A. Strong t_1 phase

When NNN hopping amplitude t_2 is small compared to t_1, the lower/upper chain prescription is well suited. One can thus express the Hamiltonians

$$H_\nu = H_\nu^{\parallel} + H_{\nu,A}^{\mathrm{BH}} + H_{\nu,B}^{\mathrm{BH}} \,, \tag{2.72}$$

which separately describe two chains, in the following way:

$$H_\nu = \int \frac{\mathrm{d}x}{2\pi} \left(vK \left|\partial_x \theta_\nu(x)\right|^2 + \frac{v}{K} \left|\partial_x \phi_\nu(x)\right|^2 \right) \,. \tag{2.73}$$

In the limit of weakly interacting chains, the speed of sound v and the Luttinger parameter K are identified as $v = \rho_0 \sqrt{t_1 U}$ and $K = \sqrt{t_1/U}$. The two chains are coupled by the two sine-Gordon terms. The first term is

$$H^\perp = -\rho_0 t_\perp \int \mathrm{d}x \cos\left[\theta_1(x) - \theta_2(x)\right] \,, \tag{2.74}$$

and it couples phase fields at the same site. The second term is

$$\begin{aligned} H_A^{t_2} + H_B^{t_2} = \rho_0 t_2 \int \mathrm{d}x \Big(& \sin\left[\theta_2(x+a) - \theta_1(x)\right] + \sin\left[\theta_1(x) - \theta_2(x-a)\right] \\ & + \sin\left[\theta_2(x) - \theta_1(x+a)\right] + \sin\left[\theta_1(x-a) - \theta_2(x)\right] \Big) \,. \end{aligned} \tag{2.75}$$

If $t_\perp$ is strong (compared to t_1), phases $\theta_\mu(x)$ will be pinned by the term $H^\perp$ in such a way that $\langle \theta_1(x) \rangle = \langle \theta_2(x) \rangle = \text{const}$, where $\langle . \rangle$ is taken in the groundstate. In this case the system becomes gapped, as can be shown following the renormalization group procedure, with the gap Δ being of the order of

$$\Delta \sim \left(\frac{v}{a}\right) t_\perp^{\frac{2K}{4K-1}} \,. \tag{2.76}$$

Such configuration also implies that $\langle H_c^{t_2} \rangle = 0$ and bosons on two chains form a quasi-condensate at the point $k = 0$ in the BZ. The groundstate energy of the system is thus

$$E_{GS} = -\rho_0 L t_\perp \tag{2.77}$$

The expectation value of $\theta_\nu(x+a) - \theta_\nu(x)$ and $\theta_2(x+a) - \theta_1(x)$ is related to the value of densities of local currents between respectively NN and NNN sites. One can deduce in particular that to the lowest order in a all currents that flow in the right direction (with increasing x) can be expressed as

$$\begin{aligned} J_{AB,r}^{\parallel,1} &= -J_{AB,r}^{\parallel,2} = -2\rho_0 \mathfrak{Im} \left[t_1 \left\langle e^{i(\theta_1(x) - \theta_1(x+a))} \right\rangle \right] = 0 \,, \\ J_{AA,r} &= -J_{BB,r} = -2\rho_0 \mathfrak{Im} \left[i t_2 \left\langle e^{i(\theta_1(x) - \theta_2(x+a))} \right\rangle \right] = -2\rho_0 t_2 \,. \end{aligned} \tag{2.78}$$

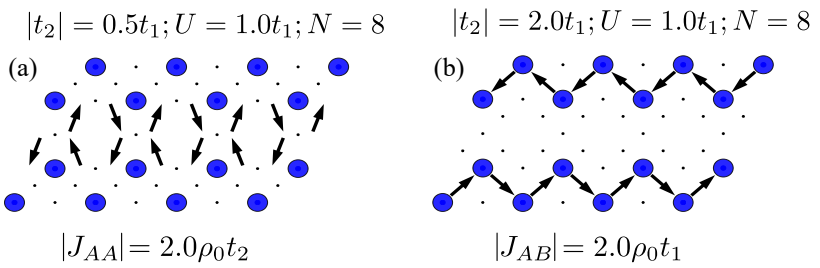

FIGURE 2.12: Numerical simulations showing the local density of states $\left\langle c^{\dagger}_{\nu,i} c_{\nu,i} \right\rangle$ (via scaling of blue circles) and the lattice current density J_{ij} (black arrows) in the groundstate of the system in ladder geometry with 8×2 sites. **(a)** The phase $t_1 > t_2$ is characterized by $|J^{\parallel}_{AB}| = 0$ and $|J_{AA}| \approx 2\rho_0 t_2$. **(b)** The phase $t_1 < t_2$ is characterized by $|J^{\parallel}_{AB}| \approx 2\rho_0 t_1$ and $|J_{AA}| = 0$. All simulations were performed in the system with PBC along the x axis for $t_{\perp} = t_1$ and $N = 8$.

Indices AB and AA correspond respectively to NN and NNN currents, 1 and 2 are chain indices and r refers to the right direction. Interchain NN currents are zero everywhere:

$$J^{\perp}_{AB} = -2\rho_0 \mathfrak{Im} \left[t_1 \left\langle e^{i(\theta_2(x) - \theta_1(x))} \right\rangle \right] = 0, \tag{2.79}$$

which is a property related to the Meissner phase in bosonic ladders, observed in particular in the experimental realization reported in Ref. [144]. We illustrate this scenario by ED calculations using hard-core bosons (strongly interacting regime). The numerical results are shown in Fig. 2.12(a) and display the expected current pattern for $t_2 = t_1/2$.

B. Strong t_2 phase

In the opposite limit, when t_2 is strong, terms $H^{t_2}_A$ and $H^{t_2}_B$ favor the generation of two decoupled intercrossing chains characterized by

$$\langle \theta_2(x+a) - \theta_1(x) \rangle = \langle \theta_1(x) - \theta_2(x-a) \rangle = -\pi/2 \,, \tag{2.80}$$

which means that the phase decreases with x, and

$$\langle \theta_1(x+a) - \theta_2(x) \rangle = \langle \theta_2(x) - \theta_1(x-a) \rangle = \pi/2 \,, \tag{2.81}$$

which signifies that the phase increases with x for all $x = 2ja$. In order to simply describe this phase, we use the sublattice prescription and consider operators $\theta_{A/B}(x)$ and $\phi_{A/B}(x)$. We also perform the gauge transformation:

$$\theta_{A/B}(x) \to \theta'_{A/B}(x) = \theta_{A/B}(x) \pm \pi x/2a \,. \tag{2.82}$$

This allows us to simply write the Hamiltonian for two newly generated chains

$$H_c = H^{t_2}_c + H^{\mathrm{BH}}_{1,c} + H^{\mathrm{BH}}_{2,c} \tag{2.83}$$

as

$$H_c = \int \frac{\mathrm{d}x}{2\pi} \left(vK \left| \partial_x \theta'_c(x) \right|^2 + \frac{v}{K} \left| \partial_x \phi_c(x) \right|^2 \right) . \tag{2.84}$$

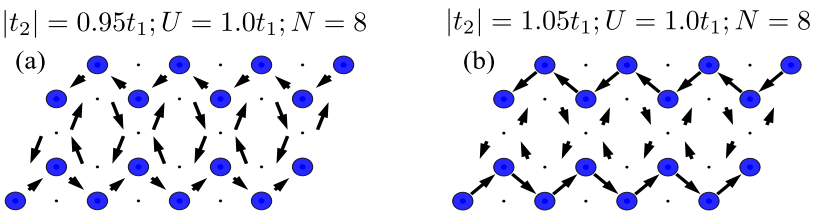

FIGURE 2.13: Numerical simulations showing the local density of states $\left\langle c^{\dagger}_{\nu,i} c_{\nu,i} \right\rangle$ (via scaling of blue circles) and the lattice current density J_{ij} (black arrows) in the groundstate of the system in ladder geometry with 8×2 sites close to the transition point of the single-particle spectrum at $t_1 = t_2$. We observe that both NN and NNN currents coexist. All simulations were performed in the system with PBC along the x axis for $t_\perp = t_1$ and $N = 8$.

The new speed of sound v and Luttinger parameter K are identified as $v = \rho_0 \sqrt{t_2 U}$ and $K = \sqrt{t_2/U}$. The two chains are coupled by t_1 and $t_\perp$ terms in the following way:

$$H^{\perp} = -t_\perp \rho_0 \int \mathrm{d}x \cos\left[\theta_A(x) - \theta_B(x)\right] \,, \tag{2.85}$$

and

$$H_1^{\parallel} + H_2^{\parallel} = -t_1 \rho_0 \int \mathrm{d}x \Big(\cos\left[\theta_B(x+a) - \theta_A(x)\right] + \cos\left[\theta_A(x) - \theta_B(x-a)\right] + \cos\left[\theta_B(x) - \theta_A(x-a)\right] + \cos\left[\theta_A(x+a) - \theta_B(x)\right] \Big) \,. \tag{2.86}$$

The groundstate in the strong t_2 limit corresponds to the quasi-condensation of bosons at the point $k = \pm\pi/(2a)$ (defined up to a reciprocal lattice vector π/a) in the BZ. The effect of the $t_\perp$ coupling consists in pinning the phases of the two chains. One remarks that, according to the duality, t_1 plays the same role as t_2 in the strong t_1 phase. We are also interested in how expectation values of the local current are modified. Straightforward calculations imply that in the strong t_2 phase currents (expressed in the same way as previously) become

$$\begin{aligned} J^{\parallel,1}_{AB,r} &= -J^{\parallel,2}_{AB,r} = -2\rho_0 \mathfrak{Im}\left[t_1 \left\langle e^{i(\theta_1(x) - \theta_1(x+a))} \right\rangle \right] = 2\rho_0 t_1 \,, \\ J_{AA,r} &= -J_{BB,r} = -2\rho_0 \mathfrak{Im}\left[i t_2 \left\langle e^{i(\theta_1(x) - \theta_2(x+a))} \right\rangle \right] = 0 \,, \\ J^{\perp}_{AB} &= -2\rho_0 \mathfrak{Im}\left[t_1 \left\langle e^{i(\theta_2(x) - \theta_1(x))} \right\rangle \right] = 0 \,. \end{aligned} \tag{2.87}$$

These analytical predictions are also illustrated by ED simulations gathered in Fig. 2.12(b).

2.3.3 Perspectives

In this section we did not have the opportunity to study in details the effect of interlattice coupling term $H^{\perp}$. The renormalization group analyze indicates that far away from the transition point of the single-particle spectrum at $t_1 = t_2$, two phases should exist: one where the sine-Gordon term is irrelevant and the bare interaction strength $t_\perp$ renormalizes to zero, and another one where the sine-Gordon term is relevant and the interaction strength $t_\perp$ renormalizes to $+\infty$. The bosons are then

gapped in the second case and the associated fields are pinned to a particular value. However, because of the non-trivial competition between t_1 and t_2-terms, additional effects could appear close to the transition point. A simple bosonization approach we used in this section is not suitable to analyze the flat band region that forms for $t_1 \sim t_2$. By doing numerical simulations in this case, we see that our predictions of the form of currents become wrong close to the transition point. As we show in Fig. 2.13, both NN and NNN currents coexist close to the transition point.

Recent theoretical works suggest that the formation of a precursor of bosonic and fermionic Laughlin states [56] could happen in ladder geometries under artificial gauge fields [180–182]. Such states represent an interest because they have an intrinsic topological order with long-range entanglement, as opposed to short-range entangled SPT states. By analogy with the Landau levels, flat band models are best candidates to study such states. In flat bands the kinetic energy term is suppressed, implying that the ground-state properties are fully determined by interactions. Such systems were intensively explored in 2D [79, 132–141] leading to the establishment of a novel notion of fractional Chern insulators. It was proposed to generate such states using the coupled wire construction [183–186], but the possibility to achieve similar phenomenology in lower dimensions despite the direct interaction between two edges implying the presence of backscattering for chiral edge states is still unclear. However, the possibility to explore two-dimensional strongly interacting systems in quasi one-dimensional geometries, opens new perspectives in the context of possible experimental protocols and addresses new questions and challenges related to the observation of even more exotic non-abelian states of matter.

Chapter 3

Phases of the bosonic Kane-Mele Hubbard model

This chapter is dedicated to the study of the celebrated Kane-Mele model, well known to have a non-trivial topological description at the single-particle level. The topological description of this model is however more subtle than in the case of the Haldane model presented in Chapter 2, and involves a $\mathbb{Z}_2$ topological invariant, rather than the first Chern number $Ch_1 \in \mathbb{Z}$. After making a short introduction to the topology of the Kane-Mele model and describing the nature of this $\mathbb{Z}_2$ topological invariant in Section 3.1, we address the question of interactions. In Section 3.2 we present our study of the bosonic Kane-Mele-Hubbard model. While the properties to the superfluid phases and phase transitions are similar to the previously explored case of the Haldane model, the physics of the strongly-interacting regime and the Mott insulator phase is very different. In particular, we find that the problem in this regime can be mapped to an effective frustrated spin-1/2 XY model. This model is studied in more details in Section 3.3. We show a numerical evidence for the formation of a disordered spin state. This frustrated magnetic model has already been considered in a different context and it was suggested that the disordered spin state could be a spin liquid ground-state, described by a spontaneous breaking of time-reversal and parity symmetries. In Section 3.4 we verify these predictions both analytically and numerically. Finally, in Section 3.4.4 we test the topological properties of the disordered spin state.

Starting from Section 3.2, the work presented in this chapter has been performed in a collaborative project with Dr. Ivana Vasic, Dr. Alexandru Petrescu, Rajbir Nirwan, and Prof. Walter Hofstetter. Our results are divided on both analytical and numerical contributions. Numerical techniques we used in this work comprise the bosonic dynamical mean-field theory (B-DMFT) simulations of the bosonic Kane-Mele-Hubbard model, and exact diagonalization (ED) calculations of the frustrated spin-1/2 XY model. The B-DMFT simulations were performed by Dr. Ivana Vasic, while we contributed to the ED part. This work has also already been reported in Ref. [2].

Contents of the chapter

3.1 Kane-Mele model and topological insulators . . . 82
3.1.1 Introduction to the model and symmetries . . . 83
3.1.2 $\mathbb{Z}_2$ topological invariant . . . 85
3.1.3 Interactions in the Kane-Mele model . . . 87
3.2 Bosonic Kane-Mele-Hubbard model . . . 88
3.2.1 Overview of the problem . . . 89
3.2.2 Mott – superfluid phase transitions . . . 90

3.2.3 Mott phase and emergent magnetism . . . 91
3.3 Effective frustrated spin-1/2 XY model . . . 93
3.3.1 Classical phase diagram . . . 94
3.3.2 Magnetically ordered states . . . 95
A. Fidelity metric . . . 96
B. Static structure factors . . . 96
3.4 Disordered spin state . . . 99
3.4.1 Chiral spin liquids . . . 99
3.4.2 Chern-Simons field theory arguments . . . 100
A. Jordan-Wigner transformation in 2D . . . 100
B. Free fermionic problem . . . 102
C. Physical interpretation . . . 105
D. Explicitly broken symmetries . . . 105
3.4.3 Chiral spin state . . . 106
3.4.4 Laughlin's pump and topological order . . . 109
A. Ground-state degeneracy . . . 109
B. Twisted boundary conditions . . . 110
C. Berry curvature and first Chern number . . . 111

3.1 Kane-Mele model and topological insulators

Theoretical [46–48] and experimental [49] discovery of the quantum spin Hall effect played a crucial role in revolutionizing the current understanding of the condensed matter physics. It followed the discovery of the quantum Hall effect [11, 35] and Haldane's proposal of the Chern insulator [32] by almost two decades, showing a significant jump in the ideas and the conceptual development of new approaches to study condensed matter systems. Similarly to quantum Hall states and Chern insulators, quantum spin Hall states are non-interacting states of matter that have bands described by topological numbers. Hence, according to the bulk-boundary correspondence, they should have quantized edge modes on a geometry with open boundary conditions. However, unlike quantum Hall states and Chern insulators quantum spin Hall states do not require any magnetic field [1]. As it naturally appears in their name, quantum spin Hall states acquire the topological description through the spin-orbit coupling between different spin components. As a consequence, such systems are time-reversal symmetric, which forces the first Chern number associated with different bands to vanish exactly, and forbids the presence of a matter current along the edges (*i.e.* chiral edge modes). Instead, their topology is described by $\mathbb{Z}_2$ topological invariants and boundaries host **helical edge modes**, which correspond to spin-filtered counter-propagating pairs of chiral edge modes. Such systems are called **topological insulators** [46–49, 113–116, 122].

From the historical perspective, the concept of the quantum spin Hall effect and topological insulators made a big step towards the topological description of non-interacting states of matter we discussed in Section 1.4.4. The purpose of this section is to introduce the Kane-Mele model [46, 47] – the seminal model of a topological insulator, which belongs to the *AII* Altland-Zirnbauer symmetry class. We will describe in greater details the impact of the time-reversal symmetry, and define the

[1] We notice that in the Haldane model the external magnetic field is also zero. However, this model has a particular configuration of staggered magnetic fluxes that sum up to zero inside the unit cell. More generally, quantum Hall states and Chern insulators can exist only when the time-reversal symmetry is broken (only in this case the Berry curvature does not vanish).

$\mathbb{Z}_2$ topological invariant characterizing new phases as a bulk property, in a manner analogous to the previous description of Chern insulators.

3.1.1 Introduction to the model and symmetries

As we have seen previously in Section 1.4.4, the time-reversal transformation T is an antiunitary one. If we consider a system with translation invariance, it can be diagonalized in momentum space using the approach described in Section 1.2. In this context, the time-reversal symmetry relates Bloch states at $\boldsymbol{k}$ and $-\boldsymbol{k}$ through the following relation

$$\mathcal{H}(-\boldsymbol{k}) = T\mathcal{H}(\boldsymbol{k})T^{-1} \,. \tag{3.1}$$

The relation means that if $|\phi\rangle$ is an eigenstate of the Bloch Hamiltonian $\mathcal{H}(\boldsymbol{k})$, $|T\phi\rangle$ is another eigenstate of the Hamiltonian $\mathcal{H}(-\boldsymbol{k})$ with exactly the same energy. Particular high-symmetry points $\boldsymbol{k}_{\text{hs}}$ of the BZ, verifying

$$\boldsymbol{k}_{\text{hs}} = -\boldsymbol{k}_{\text{hs}} + \boldsymbol{Q}_i \,, \tag{3.2}$$

where $\boldsymbol{Q}_i$ is the reciprocal lattice vector, play an important role in time-reversal invariant systems.

When spin degrees of freedom are included into the problem, the time-reversal transformation has to inverse the spin operators. The usual representation of such transformation is

$$T = \exp\left(-i\pi S_y\right) K \,, \tag{3.3}$$

where K is the complex conjugation operator and S_y is the y-component of the spin. We notice in particular that in the case of half-integer spin operators, such transformation squares to $-I$. This plays a crucial role in the topological classification we presented in Section 1.4.4 and results in the so-called Kramers degeneracy. Kramers theorem states that all energy levels of time-reversal systems are doubly degenerate: states $|\phi\rangle$ and $|T\phi\rangle$, which are eigenstates with the same eigenvalue, have to be orthogonal

$$\langle T\phi, \phi\rangle = \left\langle T\phi, T^2\phi\right\rangle = -\langle T\phi, \phi\rangle = 0 \,. \tag{3.4}$$

It is also straightforward to check that if the relation (3.1) holds true, the Berry curvature $\mathcal{B}^n_{xy}(\boldsymbol{k})$ integrated over the entire BZ has to sum up to zero, since

$$\mathcal{B}^n_{xy}(\boldsymbol{k}) = -\mathcal{B}^n_{xy}(-\boldsymbol{k}) \,. \tag{3.5}$$

Hence, time-reversal invariant systems cannot be Chern insulators and their boundaries do not support chiral edge modes.

Let us now turn to the Hamiltonian of the quantum spin Hall effect. Kane and Mele first proposed a generalization of the spinless Haldane model, by considering its spinful counterpart and taking into account the spin-orbit interactions. They predicted that it leads to the emergence of the quantum spin Hall effect. The Kane-Mele model [46, 47] is described by the following Hamiltonian

$$\begin{aligned} H = &- t_1 \sum_{\langle i,j\rangle,\sigma} c^\dagger_{\sigma,i} c_{\sigma,j} + it_2 \sum_{\langle\langle i,j\rangle\rangle,\alpha,\beta} c^\dagger_{\alpha,i} \nu_{ij} \sigma^z_{\alpha\beta} c_{\beta,j} \\ &+ i\lambda_R \sum_{\langle i,j\rangle,\alpha,\beta} c^\dagger_{\alpha,i} \left(\boldsymbol{\sigma}_{\alpha\beta} \times \boldsymbol{d}\right)_z c_{\beta,j} + \sum_{i,\sigma} (-1)^i M c^\dagger_{\sigma,i} c_{\sigma,i} \,. \end{aligned} \tag{3.6}$$

d_1	$t_1(1+2\cos x\cos y)$	d_{12}	$-2t_1\cos x\sin y$
d_2	M	d_{15}	$t_2(2\sin 2x-4\sin x\cos y)$
d_3	$\lambda_R(1-\cos x\cos y)$	d_{23}	$-\lambda_R\cos x\sin y$
d_4	$-\sqrt{3}\lambda_R\sin x\sin y$	d_{24}	$\sqrt{3}\lambda_R\sin x\cos y$

TABLE 3.1: The nonzero coefficients in Eq. (3.7), when the convention of the original work by Kane and Mele [47] is used. Here x and y are shorthand notations $x = k_x a/2$ and $y = \sqrt{3}k_y a/2$.

Here t_1 is the NN hopping amplitude, t_2 is the strength of the intrinsic spin-orbit coupling, which involves spin-dependent second neighbor hoppings, λ_R is the amplitude of the Rashba spin-orbit coupling, and M is the Semenoff mass term describing the staggered chemical potential. Coefficients ν_{ij} are equal to ± 1 depending on whether the particle traversing from i to j makes a right (corresponding to $\nu_{ij} = +1$) or a left turn (corresponding to $\nu_{ij} = -1$) exactly as in the Haldane model. The vector $\boldsymbol{d}$ points from site i to site j and corresponds to three NN vectors $\boldsymbol{u}_i$, the same as in Fig. 2.1. Three Pauli matrices σ_μ correspond to the spin degree of freedom, and their indices are denoted by letters α and β. The intrinsic spin-orbit coupling term breaks the $SU(2)$ symmetry down to $U(1)$. The remaining symmetry corresponds to the spin rotations around the z-axis. The Rashba term further breaks the $U(1)$ symmetry down to $\mathbb{Z}_2$. It also breaks the $z \to -z$ reflection symmetry.

By going to the momentum space, one can rewrite the Hamiltonian (3.6) using the following general 4×4 matrix form

$$\mathcal{H}(k) = d_0(\boldsymbol{k})I_4 + \sum_{i=1}^{5} d_i(\boldsymbol{k})\Gamma_i + \sum_{j>i} d_{ij}(\boldsymbol{k})\Gamma_{ij} \,. \tag{3.7}$$

Here Γ_i are 5 gamma matrices obeying the Clifford algebra and $\Gamma_{ij} = (2i)^{-1}\left[\Gamma_i, \Gamma_j\right]$ are their commutators, ten of which are independent. The gamma matrices are constructed as tensor products of Pauli matrices that represent the two-level systems associated with the sublattice degree of freedom ν_μ and the spin degree of freedom σ_μ. The tensor product of the sublattice and spin basis provides the total basis

$$\{A, B\} \otimes \{\uparrow, \downarrow\} \,. \tag{3.8}$$

The time-reversal operator T acts in such basis as

$$T = i\left(I_2 \otimes \sigma_y\right) K \,, \tag{3.9}$$

and the gamma matrices can be defined as

$$\Gamma_{(1,2,3,4,5)} = \left(\nu_x \otimes I_2, \nu_z \otimes I_2, \nu_y \otimes \sigma_x, \nu_y \otimes \sigma_y, \nu_y \otimes \sigma_z\right) \,, \tag{3.10}$$

Several conventions are possible for the gamma matrices, and here we used the convention of the original work by Kane and Mele [47]. The explicit expression of corresponding functions $d_i(\boldsymbol{k})$ and $d_{ij}(\boldsymbol{k})$ is shown in Table 3.1. One can also use the convenient form proposed by Fu and Kane [187], forcing all the functions $d_{ij}(\boldsymbol{k})$ to vanish exactly, but valid only if the parity symmetry R (*i.e.* a symmetry $y \to -y$, that maps the sublattice A onto the sublattice B) is present in the problem.

In the absence of the Rashba coupling, $\lambda_R = 0$, the Kane-Mele model can be simply thought as two copies of the Haldane model, with an opposite choice of the Haldane phases and opposite directions of the magnetic fields. In particular, the

Bloch Hamiltonian $\mathcal{H}(k)$ can be written as

$$\mathcal{H}(k) = \begin{pmatrix} \mathcal{H}_\uparrow(k) & 0 \\ 0 & \mathcal{H}_\downarrow(k) \end{pmatrix} . \tag{3.11}$$

Each component $\mathcal{H}_\mu(k)$ describes a two-band Chern insulator characterized by the first Chern number $Ch_{1,\mu}$. Each band of such topological insulator is double degenerate: spin-up and spin-down states have exactly the same energy. Since the total Chern number has to be zero, $Ch_{1,\uparrow} = -Ch_{1,\downarrow}$. It is thus possible to define a new topological invariant – the spin Chern number

$$Ch_{1,\text{spin}} = \left(Ch_{1,\uparrow} - Ch_{1,\downarrow}\right)/2 . \tag{3.12}$$

In the general case, however, the Rashba coupling is non-zero and the two spin degrees of freedom are mixed up, which invalidates the definition of the spin Chern number. Nevertheless, there exists a more universal $\mathbb{Z}_2$ topological invariant for the quantum spin Hall effect. In the following section we will describe the mathematical definition and the physical interpretation of such invariant.

3.1.2 $\mathbb{Z}_2$ topological invariant

Similarly to Chern insulators with their first Chern number description (see Section 1.4.2), there exist several expressions of the $\mathbb{Z}_2$ topological invariant, which have different physical interpretations. Historically, the first expression of this topological invariant was obtained by Kane and Mele [47] in terms of a Pfaffian invariant. In order to understand the emergence of such invariant, let us first formulate the problem of topological classification in the mathematical language.

Consider a Bloch bundle of occupied bands. At each momentum $\boldsymbol{k}$ of the first BZ, the fibre is a vector space (it is thus a vector bundle) generated by vectors $\{|e_i(\boldsymbol{k})\rangle\}$. In our case, there are two such states [2]. Because of the time-reversal symmetry, there is a redundancy in the description of the system over the whole BZ. One can get rid of this redundancy by deciding to work on the two times smaller effective BZ, by keeping only one term of each Kramers pair $(\boldsymbol{k}, -\boldsymbol{k})$. One can foresee the non-trivial topology of such fibre bundle by looking at the action of the time-reversal transformation T on the states of the fibre $|e_i(-\boldsymbol{k})\rangle = |Te_i(\boldsymbol{k})\rangle$. Since $T^2 = -1$, T has a period 4, so that the bundle is twisted. One can develop these arguments by looking at the matrix elements of the time-reversal operator

$$M_{ij}(\boldsymbol{k}) = \left\langle e_i(\boldsymbol{k}), Te_j(\boldsymbol{k})\right\rangle . \tag{3.13}$$

The matrix M is not unitary, but it is antisymmetric. As the number of filled bands is even, the Pfaffian $\text{Pf}(M)$ is well defined:

$$\text{Pf}(M) = \frac{1}{2^n n!} \sum_{\mathcal{P}} \text{sign}(\mathcal{P}) \prod_{i=1}^{n} M_{\mathcal{P}(2i-1)\mathcal{P}(2i)} , \tag{3.14}$$

where $2n$ is the number of the elements of the matrix (number of filled bands), and the summation is performed over all the permutations $\mathcal{P}$ of its indices. It is exactly this Pfaffian, that reveals the $\mathbb{Z}_2$ topological properties of the model. To show this,

[2] Notice why the problem is more complicated in the current situation: the fibre bundle is not a relatively simple $U(1)$-principal bundle anymore, as was the case *e.g.* in Sections 1.4.1 and 1.4.2, or in Chapter 2.

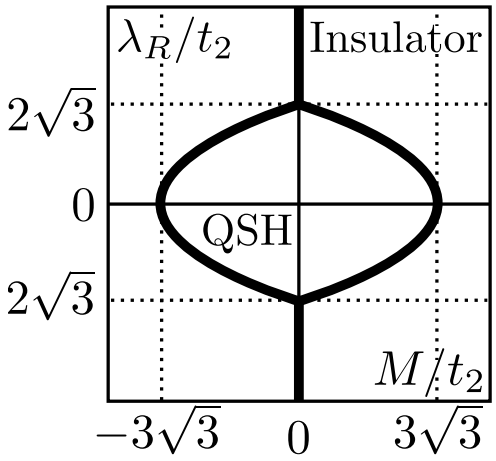

FIGURE 3.1: Phase diagram of the Kane-Mele model, showing the $\mathbb{Z}_2$ topological invariant as a function of the ratios M/t_2 and λ_R/t_2 in the regime $0 < t_2 \ll t_1$. The topological invariant vanishes in the insulator regime and becomes equal to 1 in the quantum spin Hall (QSH) regime.

assume that it has first order zeros, *i.e.* phase vortices with a winding number ± 1. Because of Eq. (3.1), such vortices always come in Kramers pairs $(\boldsymbol{k}, -\boldsymbol{k})$, and have opposite winding numbers. If there is an even number of pairs of vortices, one can always remove them through a simple pairwise merging. However, if there is only one pair of vortices, it is impossible to remove it by applying a continuous transformation. The reason is that at high-symmetry points $\boldsymbol{k}_{\text{hs}}$ of the BZ, states $|Te_i(\boldsymbol{k}_{\text{hs}})\rangle$ and $|e_i(\boldsymbol{k}_{\text{hs}})\rangle$ are related through a $U(2)$ rotation, and the Pfaffian has necessarily to have unit modulus: $|\text{Pf}\,[M(\boldsymbol{k}_{\text{hs}})]| = 1$. Hence, one cannot move two vortices of a single pair to such high-symmetry point, and there is no other points when the vortices can be merged. The procedure described above means that the $\mathbb{Z}_2$ topological invariant ν is identified with the parity of the number of pairs of vortices of the Pfaffian. It can be determined by counting the number of pairs of complex zeros of $\text{Pf}(M)$, equal to the winding of the phase of the Pfaffian around a loop $\mathcal{C}$ enclosing the effective BZ (half of the entire BZ)

$$\nu = \frac{1}{2\pi i} \oint_{\mathcal{C}} \mathrm{d}\boldsymbol{k} \cdot \partial_{\boldsymbol{k}} \ln \text{Pf}\,[M(\boldsymbol{k})] \mod 2 \,. \tag{3.15}$$

Fig. 3.1 illustrates the result of a calculation of the $\mathbb{Z}_2$ topological invariant in the Kane-Mele model. We observe an emergence of the quantum spin Hall regime when $|M/t_2| \leq 3\sqrt{3}$ and $|\lambda_R/t_2| \leq 2\sqrt{3}$.

Another expression of the $\mathbb{Z}_2$ topological invariant was proposed by Fu and Kane [188]. It is based on the usage of the "sewing matrix" W defined as

$$W_{ij}(\boldsymbol{k}) = \langle e_i(-\boldsymbol{k}), Te_j(\boldsymbol{k}) \rangle \,. \tag{3.16}$$

As opposed to the matrix M, the sewing matrix is unitary. It is also antisymmetric at high-symmetry points $\boldsymbol{k}_{\text{hs}}$. Fu and Kane have shown that the topological invariant ν can be expressed as

$$(-1)^{\nu} = \prod_{\{\boldsymbol{k}_{\text{hs}}\}} \frac{\text{Pf}\,[W(\boldsymbol{k}_{\text{hs}})]}{\sqrt{\det\,[W(\boldsymbol{k}_{\text{hs}})]}} \,. \tag{3.17}$$

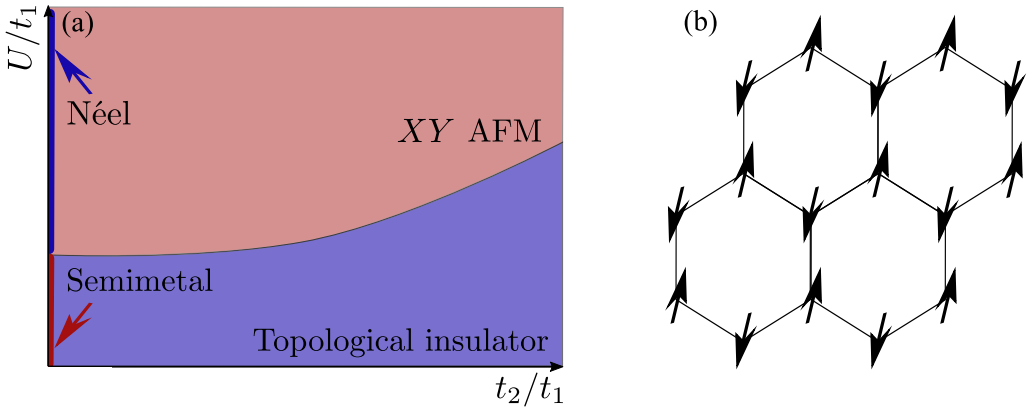

FIGURE 3.2: **(a)** Phase diagram of the Kane-Mele-Hubbard model (figure is reproduced from Ref. [193]). At weak interactions the non-interacting picture is recovered: at $t_2 = 0$ the system is in a semimetal phase, at finite t_2 a topological insulator phase is formed. When the interactions become strong ($U \sim t_1$) the system displays an antiferromagnetic order. **(b)** Antiferromagnetic alignment of spins.

The advantage of the formula (3.17) also consists in the possibility to generalize it to three dimensions [113, 117].

Similarly to the case of the Chern number, the $\mathbb{Z}_2$ topological invariant can also be seen as an obstruction to smoothly define the wavefunction throughout the effective BZ [188]. This implies an impossibility to choose a continuous basis $\{|e_i(\boldsymbol{k})\rangle\}$ such that $|Te_{2i}(\boldsymbol{k})\rangle = |e_{2i-1}(-\boldsymbol{k})\rangle$. The resulting expression is

$$\nu = \frac{1}{2\pi}\left(\oint\limits_{\delta\text{EBZ}} \mathcal{A} - \int\limits_{\text{EBZ}} \mathcal{B}\right) \mod 2\,, \tag{3.18}$$

where $\mathcal{A}$ and $\mathcal{B}$ are respectively the sums of the Berry's connection and the Berry's curvature of all filled bands, EBZ denotes the effective BZ, and δEBZ – its boundary. The obstruction associated to a $\mathbb{Z}_2$ invariant is of the $SU(2)$ type, while the one associated to the integer first Chern number is $U(1)$ [189].

3.1.3 Interactions in the Kane-Mele model

Now, when the topological nature of the Kane-Mele model is well understood, an important question one could ask is what will happen to the system, when interactions are taken into account. In this context, the simplest model to study is the Kane-Mele-Hubbard model described by the following Hamiltonian

$$H = -t_1 \sum_{\langle i,j\rangle,\sigma} c^\dagger_{\sigma,i} c_{\sigma,j} + it_2 \sum_{\langle\langle i,j\rangle\rangle,\alpha,\beta} c^\dagger_{\alpha,i} \nu_{ij} \sigma^z_{\alpha\beta} c_{\beta,j} + U \sum_i c^\dagger_{\uparrow,i} c_{\uparrow,i} c^\dagger_{\downarrow,i} c_{\downarrow,i}\,.$$

Here U is the strength of the on-site Hubbard interaction. For simplicity, we assume that the Rashba term and the Semenoff staggered chemical potential term are equal to zero. This model was extensively studied both analytically [190, 191] and numerically [192–196] (see also Ref. [79] for an excellent review), and its phase diagram is schematically presented in Fig. 3.2(a).

For weak enough interactions, the Kane-Mele-Hubbard model preserves the topological nature associated with the $\mathbb{Z}_2$ topological invariant. In the strong interacting regime, the Kane-Mele-Hubbard model can be mapped onto an Heisenberg model

using the Schrieffer-Wolff transformation [197, 198] [3]

$$H = \frac{4t_1^2}{U} \sum_{\langle i,j \rangle} \boldsymbol{S}_i \cdot \boldsymbol{S}_j + \frac{4t_2^2}{U} \sum_{\langle\langle i,j \rangle\rangle} \left(-S_i^x S_j^x - S_i^y S_j^y + S_i^z S_j^z \right) . \tag{3.19}$$

In this magnetic model, the XY term favors a translation-invariant antiferromagnetic ordering, as shown in Fig. 3.2(b). The NN and NNN Ising interactions are competing, that leads to the frustration. Nevertheless, quantum fluctuations do not allow for a quantum spin liquid behavior, and the resulting state keeps the antiferromagnetic ordering up to a critical value of the interaction strength, where the transition to the topological insulator phase occurs.

3.2 Bosonic Kane-Mele-Hubbard model

As we have seen previously (see Section 3.1.3), the seminal model for topological insulators – the Kane-Mele model, under the effect of Hubbard interactions is subjected to a single phase transition from the topologically non-trivial phase described by a finite value of the $\mathbb{Z}_2$ topological invariant, to a trivial (from the topological side) magnetically ordered antiferromagnetic state. In this section, we are interested in investigating the ground-state properties of its bosonic counterpart – the bosonic Kane-Mele-Hubbard (BKMH) model. To our knowledge, despite an intensive study of the fermionic model, its bosonic version has not yet been considered.

We will show using both theoretical and numerical arguments, that the phase diagram of the BKMH model, and in particular in the strongly interacting regime and the Mott insulator phase, is very rich. We will also outline the connection between the strongly interacting regime of the BKMH model at unit filling and the frustrated XY model on the honeycomb lattice. This model has been studied recently, and its ground-state phase diagram is still debated: some of the works show that the ground-state in the intermediate frustration regime could be a spin liquid [199–204], while others identify it with a topologically trivial long-range ordered Néel state [205–207]. This magnetic model will be treated separately later, in Section 3.3.

In order to study this model numerically, we use the bosonic dynamical mean-field theory (B-DMFT). The essence of DMFT consists in mapping the full lattice model onto a set of local models whose parameters are determined through a self-consistency condition. This is achieved by attaching at each site i a bath described by orbital degrees of freedom, so that the effective local Hamiltonian is given by a bosonic Anderson impurity model. The self-consistency is imposed on the level of single–particle Green's functions, and the approximation is such that local correlations are fully taken into account, while non-local correlations are treated at the mean-field level. This method is thus perfectly suited to study the superfluid and the classical Mott insulator phases. However, because of the local mapping one could encounter difficulties in situations, when the ground-state is expected to have some non-local entanglement. The numerical results presented in this section were obtained in a collaborative project with Dr. Ivana Vasic, Dr. Alexandru Petrescu, Rajbir Nirwan, and Prof. Walter Hofstetter. The B-DMFT simulations were run by Dr. Ivana Vasic.

[3] We will describe a similar mapping in more details in Section 3.2.3. Notice that in the Heisenberg model we obtain here Ising interactions are not tunable, *i.e.* they are always equal in amplitude to the XY terms. The model we will propose next will allow for an additional tuning of the XY and Ising interactions through an additional term of the model.

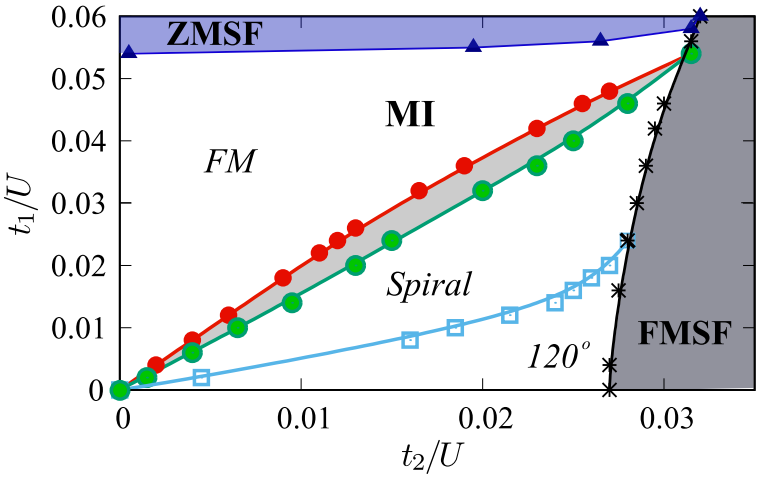

FIGURE 3.3: Phase diagram of the BKMH model obtained using B-DMFT for parameters $U_{\uparrow\downarrow}/U = 0.5$, $\mu/U = 0.25$, on a lattice of 96 sites. It comprises a Mott insulator phase (*MI*, shown in white), a zero-momentum BEC (*ZMSF*, shown in blue) and a finite-momentum BEC (*FMSF*, shown in gray). Based on the coplanar magnetic ordering of the state, the *MI* phase is further divided onto several regimes, marked in italic. The physical nature of these regions will be discussed, and the names will be justified in Section 3.3. The central gray region corresponds to the states with no coplanar order. The numerical simulations have been done by Dr. Ivana Vasic and presented in Ref. [2].

3.2.1 Overview of the problem

Let us consider the BKMH model described by the following Hamiltonian

$$H = -t_1 \sum_{\langle i,j\rangle,\sigma} c^\dagger_{\sigma,i} c_{\sigma,j} + it_2 \sum_{\langle\langle i,j\rangle\rangle,\alpha,\beta} c^\dagger_{\alpha,i} \nu_{ij} \sigma^z_{\alpha\beta} c_{\beta,j} + \mu \sum_{i,\sigma} c^\dagger_{\sigma,i} c_{\sigma,i} + \frac{U}{2} \sum_{i,\sigma} c^\dagger_{\sigma,i} c_{\sigma,i} \left(c^\dagger_{\sigma,i} c_{\sigma,i} - 1 \right) + U_{\uparrow\downarrow} \sum_i c^\dagger_{\uparrow,i} c_{\uparrow,i} c^\dagger_{\downarrow,i} c_{\downarrow,i} \,. \tag{3.20}$$

Here the degrees of freedom denoted by the index σ correspond to two different species of bosons, instead of real spins. For simplicity we will keep the notation $\sigma \in \{\uparrow,\downarrow\}$ to distinguish the two species. The spin-orbit coupling of the BKMH model is not real, and the time-reversal symmetry is not restored, as in the fermionic version of the Kane-Mele model, because reversing the time cannot interchange two species of bosons. However, keeping the time-reversal symmetry is not crucial for our future consideration. In addition to intra-species Bose-Hubbard interactions with the amplitude U, we also consider local inter-species interactions with the amplitude $U_{\uparrow\downarrow}$. Finally, μ is the chemical potential term. We notice that different experimental protocols could be employed to realize such system in practice. Two-dimensional spin-orbit models have been proposed and experimentally achieved in optical lattices setups [208–217] and with photons [3, 218–220].

The ground-state phase diagram of the BKMH model obtained from B-DMFT is shown in Fig. 3.3, as a function of the hopping amplitudes t_1 and t_2 versus the interaction strength $U = 2U_{\uparrow,\downarrow}$, at a fixed value of the chemical potential $\mu = 0.25U$, such that there is an average of $n = \left\langle c^\dagger_{\sigma,i} c_{\sigma,i} \right\rangle = 1$ bosons per each site of the lattice. Similarly to the bosonic Haldane model at the same filling (see Section 2.2 and Ref. [153]

for more details), we observe that three phases are competing: a zero-momentum BEC (*ZMSF*, also called a uniform superfluid), a finite-momentum BEC (*FMSF*, also called chiral superfluid) and a Mott insulator (*MI*).

3.2.2 Mott – superfluid phase transitions

When the interactions are weak, as compared to the hopping terms t_1 and t_2, the superfluid phases are formed. A *ZMSF* phase appears, when t_1 is big. In the opposite limit, when t_2 is big, the *FMSF* is formed. The critical value at which the transition occurs is $t_2/t_1 = 1/\sqrt{3}$. We notice, that in the isotropic Haldane model, because of the C_3 point-wise group symmetry, in the *FMSF* phase the condensation occurs exactly at two Dirac points, independently of the ratio of t_2/t_1, and the transition is of the first order. If the C_3 symmetry is broken, the position of the condensation points depends on the exact value of t_2/t_1, and the transition is second order.

In addition to the numerical probes mentioned previously in Section 2.2, such as the density distribution in the momentum space

$$n_\sigma(\boldsymbol{k}) = \left\langle a^\dagger_{\sigma,k} a_{\sigma,k} \right\rangle + \left\langle b^\dagger_{\sigma,k} b_{\sigma,k} \right\rangle \ , \tag{3.21}$$

and the bond current expectation value

$$J_{\sigma,ik} = -2\mathfrak{Im}\left(t_{ik} \left\langle c^\dagger_{\sigma,i} c_{\sigma,k} \right\rangle \right) \ , \tag{3.22}$$

the B-DMFT allows us to probe directly the condensate order parameters

$$\phi_{\sigma,i} = \langle c_{\sigma,i} \rangle \ . \tag{3.23}$$

Finite values of $\phi_{\sigma,i}$ mark a superfluid phase, while vanishing values correspond to a *MI* state. In the *ZMSF* the order parameters of the two species $\uparrow$ and $\downarrow$ on both sublattices are aligned. In the *FMSF*, we observe a $2\pi/3$ winding of the order parameters. For the parameters studied in the paper, we find that the absolute values of the order parameters are the same for the two species on all lattice sites, yet for *FMSF* state winding directions are opposite for the two species on the two sublattices. Moreover, in *FMSF* phase condensate order parameters on the two sublattices and for the two species are determined only up to a relative phase. This behavior is shown in Fig. 3.4(a-b).

In Fig. 3.4(c) we plot absolute values of the order parameters $\phi_{\sigma,i}$ as functions of t_2/U for several values of t_1/U. Since the ground-state is translation invariant, the order parameter is uniform throughout the lattice and we omit writing the spatial index i. For the case of $t_1/U = 0$, we find a transition from the *MI* into the *FMSF* phase at $t_2/U \approx 0.027$. At $t_1/U = 0.03$, the transition sets in at a slightly higher value $t_2/U \approx 0.0285$. The most interesting behavior is found for $t_1/U = 0.056$, where for small values of t_2 we find a *ZMSF* state. With an increase in t_2, at $t_2/U \approx 0.0265$ the *MI* state is reached due to competing effects of t_1 and t_2, and finally at $t_2/U \approx 0.0315$ the system becomes *FMSF*.

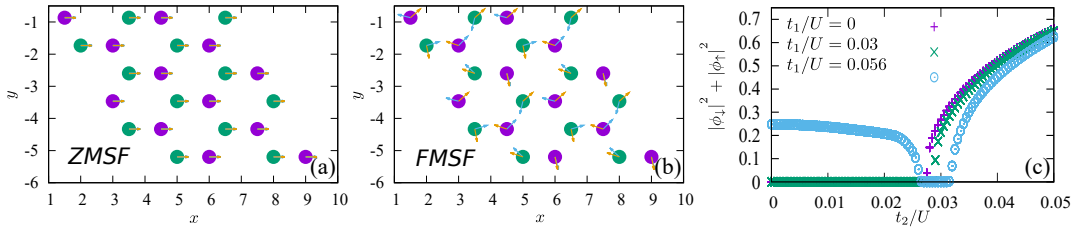

FIGURE 3.4: Real-space distribution of condensate order parameters of the two bosonic species **(a)** in the *ZMSF* phase for $t_1/U = 0.056, t_2/U = 0.005$, and **(b)** in the *FMSF* phase for $t_1/U = 0.018, t_2/U = 0.032$. Local condensate order parameters are aligned in the *ZMSF*. In contrast, they exhibit a $2\pi/3$ winding in the *FMSF*. The "winding direction" is opposite for the two species and for the two sublattices, implying that for each sublattice the two species condense exactly in the two different Dirac points. The choice of the Dirac points is opposite for the two sublattices. **(c)** The condensate order parameters as a function of t_2/U for several values of t_1/U. All the simulations were performed at $U_{\uparrow\downarrow}/U = 0.5, \mu/U = 0.25$.
The numerical simulations have been done by Dr. Ivana Vasic and presented in Ref. [2].

3.2.3 Mott phase and emergent magnetism

In the *MI* regime of the BKMH model, when interactions are very strong ($U, U_{\uparrow\downarrow} \to \infty$), all the states such that any site i on a lattice has a multiple occupation

$$\left\langle c^\dagger_{\uparrow,i} c_{\uparrow,i} \right\rangle + \left\langle c^\dagger_{\downarrow,i} c_{\downarrow,i} \right\rangle \geq 2 \,, \tag{3.24}$$

lie much higher in energy than the ground-state. At total unit filling the dynamics of the system is dominated by the virtual processes, where one of such states becomes excited only for a short amount of time. The system is thus described by an effective Hamiltonian acting on an effective Hilbert space, which excludes all the high-energy states. The effective Hamiltonian can be deduced using the Schrieffer-Wolf transformation [197, 198] and calculated perturbatively in powers of $t_{1(2)}/U_{(\uparrow\downarrow)}$ [157, 221]. In this subsection we will represent the way to make this calculation.

We first decompose the Hamiltonian into two parts: the non-interacting Kane-Mele term, which is equal to the total Hamiltonian, when the interactions are zero $H_{\mathrm{KM}} = H(U, U_{\uparrow,\downarrow} = 0)$, and the interaction term, which is equal to the total Hamiltonian, when the hopping terms and the chemical potential are all zeros $H_{\mathrm{BH}} = H(t_1, t_2, \mu = 0)$. We treat the first term as a perturbation. The effective Hilbert space is composed of states

$$|\alpha_{\mathrm{eff}}\rangle = \left|\sigma_1, \ldots, \sigma_i, \ldots \sigma_j, \ldots \sigma_{N_s}\right\rangle \,, \tag{3.25}$$

were N_s is the total number of sites of the lattice. Each site i is singly occupied by the boson of species $\sigma_i \in \{\uparrow, \downarrow\}$. At the second order in perturbation theory, the only relevant virtual excited states are the ones, which have one of the sites doubly occupied (denoted as $\sigma_i \cdot \sigma_j$), and another – empty (denoted as 0):

$$|\gamma_{\mathrm{exc}}\rangle = \left|\sigma_1, \ldots, 0, \ldots \sigma_i \cdot \sigma_j, \ldots \sigma_{N_s}\right\rangle \,. \tag{3.26}$$

This construction is schematically presented in Fig. 3.5. The effective Hamiltonian H_{eff} can then be constructed using the matrix elements of the original Hamiltonian assignments

$$[H_{\mathrm{eff}}]_{\alpha\beta} = -\sum_\gamma \frac{[H_{\mathrm{KM}}]_{\alpha\gamma} [H_{\mathrm{KM}}]_{\gamma\beta}}{\epsilon_\gamma - (\epsilon_\alpha + \epsilon_\beta)/2} \,. \tag{3.27}$$

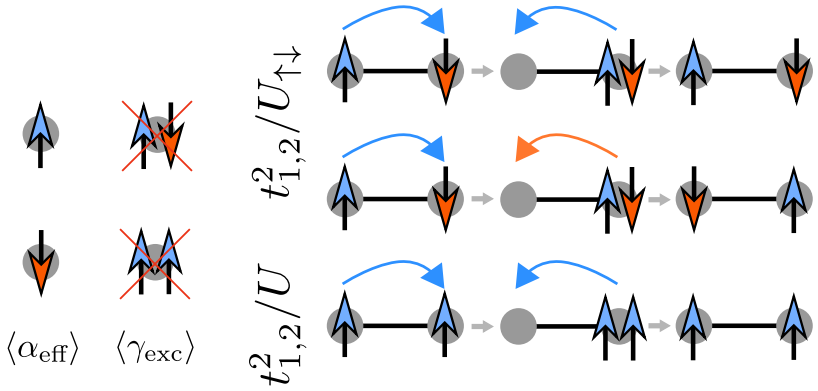

FIGURE 3.5: Schematic representation of the effective low-energy physics of the BKMH model in the *MI* phase. All the states, which have an occupation of any site of the lattice, bigger than one, are highly excited and serve only as intermediate steps in virtual processes.

Here α and β label states $|\alpha_{\rm eff}\rangle$ in the effective Hilbert space, γ labels excited states $|\gamma_{\rm exc}\rangle$, and $\epsilon_\phi = [H_{\rm BH}]_{\phi\phi}$ is the energy of state $|\phi\rangle$ in the unperturbed Hamiltonian $H_{\rm BH}$.

States $|\alpha_{\rm eff}\rangle$ of the effective Hilbert space form a basis of an effective spin model. Original bosons provide a Schwinger boson representation of spins-1/2:

$$\begin{aligned} S^x_j &= \frac{S^+_j + S^-_j}{2} = c^\dagger_{\uparrow,j}c_{\downarrow,j} + c^\dagger_{\downarrow,j}c_{\uparrow,j}\,, \\ S^y_j &= \frac{S^+_j - S^-_j}{2i} = -i\left(c^\dagger_{\uparrow,j}c_{\downarrow,j} - c^\dagger_{\downarrow,j}c_{\uparrow,j}\right)\,, \\ S^z_j &= \left(c^\dagger_{\uparrow,j}c_{\uparrow,j} - c^\dagger_{\downarrow,j}c_{\downarrow,j}\right)/2\,. \end{aligned} \tag{3.28}$$

The effective Hamiltonian can be written in terms of the spin-1/2 operators as

$$H = -\sum_{\langle i,j\rangle}\left[J_1\left(S^+_iS^-_j + \text{h.c.}\right) - K_1S^z_iS^z_j\right] + \sum_{\langle\langle i,k\rangle\rangle}\left[J_2\left(S^+_iS^-_k + \text{h.c.}\right) + K_2S^z_iS^z_k\right]\,, \tag{3.29}$$

where the coupling terms in the new Hamitlonian are identified as

$$J_i = t_i^2/U_{\uparrow\downarrow}, \quad K_i = t_i^2\left(1/U_{\uparrow\downarrow} - 2/U\right)\,. \tag{3.30}$$

The resulting Hamiltonian comprises several terms: the XY hopping interactions between NN and NNN spins with amplitudes respectively equal to J_1 and J_2, and the Ising interactions with the amplitudes K_1 and K_2. It also conserves the total magnetization $S^z_{\rm tot}$, and the total filling equal to one corresponds to $S^z_{\rm tot} = 0$. We stress that the Ising interactions are tunable in this model, as compared to the fermionic case (see Eq. (3.19)). In particular, by carefully choosing the value of the interactions, so that $U = 2U_{\uparrow,\downarrow}$, we can make the Ising term vanish exactly. This can be achieved with ultra-cold atoms using the Feshbach resonance technique. In the following we will consider the particular case, when K_1 and K_2 are both equal to zero, so that the

resulting Hamiltonian is simply

$$H = -J_1 \sum_{\langle i,j \rangle} \left(S_i^+ S_j^- + \text{h.c.} \right) + J_2 \sum_{\langle\langle i,k \rangle\rangle} \left(S_i^+ S_k^- + \text{h.c.} \right) \ . \tag{3.31}$$

In this case the properties of the effective XY model depend only on the ratio of two coupling strengths, which is related to the parameters of the BKMH model via $J_2/J_1 = (t_2/t_1)^2$.

By comparing Eqs. (3.29) and (3.31) with Eq. (3.19), we observe that two XY terms are now competing: the NN term is ferromagnetic and tends to align neighboring spins, while NNN term is antiferromagnetic [4] and favors the antiferromagnetic order breaking the translation symmetry. Moreover, since NNN term couples spins on the same triangular Bravais lattices, this term is frustrated by itself: we encounter the same difficulty as shown in Fig. 1.9(a). We expect thus that the phase diagram associated with the strongly interacting regime of the BKMH is much richer than for the fermionic version of the model. A more detailed study of this regime will be performed in the following section.

3.3 Effective frustrated spin-1/2 XY model

Studying frustrated models for spin-1/2 particles is exciting, because strong quantum fluctuations combined with frustration make such systems the best candidates for hosting quantum spin liquid ground-states, as we already mentioned in Section 1.5.3. In this context and motivated by the recent experimental development concerning quantum magnets [222], the frustrated Heisenberg model on the honeycomb lattice have been recently explored [223–236]. In parallel, some materials were found to realize the XXZ version of this model [237], and theoretical and numerical studies suggested that the XY version possibly hosted a spin liquid state, with seemingly contradictory results [199–202, 204–207].

As suggested in Ref. [203], in the intermediate frustration regime of the frustrated spin-1/2 XY model, the ground-state physics at zero total magnetization could be mapped onto a fermionic Haldane model at the mean-field level, using the Chern-Simons (ChS) field theory considerations and the 2D Jordan-Wigner transformation [60, 238–241]. The resulting Haldane model is situated in the topological regime, and is described by a non-zero value of the first Chern number (see Section 2.1 for more details on the Haldane model). However, the topological nature of this spin state is still elusive.

In this section, we will show our contribution to the exploration of the ground-state properties of the frustrated spin-1/2 XY model. As in the previous section we have seen that this spin model is effectively generated in the Mott insulator phase of the BKMH model at unit filling, we can still continue using B-DMFT to understand the magnetic properties of the ground-state of the bosonic model. However, in order to have an alternative view on the problem and overcome possible limitations of B-DMFT in treating the non-local entanglement, we will also employ the exact

[4] The positive sign of the J_2-term combines the sign of the bosonic exchange and the phase of π accumulated in the hoppings between second neighbors.

diagonalization (ED) method for the spin model [5]. Details on the implementation of numerical algorithms used in this (and the following) section are presented in Appendix A. We will combine these results with the analytic treatment of the problem at, or close to the classical level. This approach is not well suited in the intermediate frustration regime, where the spin liquid state is expected. Finally, in order to better understand the ground-state for the associated set of parameters, we will use the ChS field theory, and perform numerical verification of the topological properties associated with the ground-state.

3.3.1 Classical phase diagram

In order to show the rich properties of the frustrated spin-1/2 XY model defined by Eq. (3.31), we first calculate its classical solution. Since the Hamiltonian of the model is composed of purely in-plane XY interaction terms, the natural choice of the classical ground-state ansatz [223, 242] can be expressed as

$$\boldsymbol{S}_i = S \begin{pmatrix} \cos\left(\phi_{\mu,i}\right) \\ \sin\left(\phi_{\mu,i}\right) \\ 0 \end{pmatrix} . \tag{3.32}$$

Here the actual value of S is $1/2$, but the classical solution is equivalent to taking the limit $S \to \infty$. The variables $\phi_{A,i} = \boldsymbol{q} \cdot \boldsymbol{R}_i$ and $\phi_{B,i} = \boldsymbol{q} \cdot \boldsymbol{R}_i + \eta$ describe the orientation of the spin at the site i of the lattice. $\boldsymbol{q}$ is the spiral wave-vector, that determines, how much the spin is rotated by going from one unit cell to another. The angular parameter η describes the relative orientation of spins on the sublattices A and B at the same unit cell. We assumed that all the spins lie completely in the xy plane. A generalized ansatz is studied in Appendix E.

Classical solution is obtained by minimizing the expectation value of the ground-state energy in the ansatz (3.32). By substituting (3.32) into Eq. (3.31), we obtain the following expression of the energy per spin

$$\begin{aligned} \epsilon = &- J_1 S^2 \left[\cos\eta + \cos\left(\eta - Q_1\right) + \cos\left(\eta + Q_2\right)\right] \\ &+ 2J_2 S^2 \left[\cos Q_1 + \cos Q_2 + \cos\left(Q_1 + Q_2\right)\right] . \end{aligned} \tag{3.33}$$

Here for simplicity we defined $Q_i = \boldsymbol{q} \cdot \boldsymbol{v}_i$ with $\boldsymbol{v}_i$ – 3 NNN vectors from Fig. 2.1. Clearly, only two of such vectors are independent, it is why we use only Q_1 and Q_2 at the end. The minimization condition implies

$$\begin{aligned} \cos\eta &= \frac{2J_2}{J_1}\left(1 + \cos Q_1 + \cos Q_2\right) , \\ \sin\eta &= \frac{2J_2}{J_1}\left(\sin Q_1 - \sin Q_2\right) , \\ \cos Q_1 + \cos Q_2 + \cos\left(Q_1 + Q_2\right) &= \frac{1}{2}\left(\frac{J_1^2}{4J_2^2} - 3\right) . \end{aligned} \tag{3.34}$$

Solving this system of three equations allows us to deduce the solution $\boldsymbol{q}_{\mathrm{cl}}$, η_{cl} as a function of the ratio J_2/J_1. This solution is shown in Fig. 3.6. In particular, when

[5] The method of exact diagonalization is completely inapplicable for the BKMH model written in the form of Eq. (3.20). One can only consider very small lattices of less than 9 unit cells (18 sites), with no more than 1 boson of any species per site (that is equivalent to consider the limit $U \to \infty$). For the spin model, one can use an effective mapping to the hard-core bosons, and the Hilbert space is significantly smaller, so that bigger lattices can be considered.

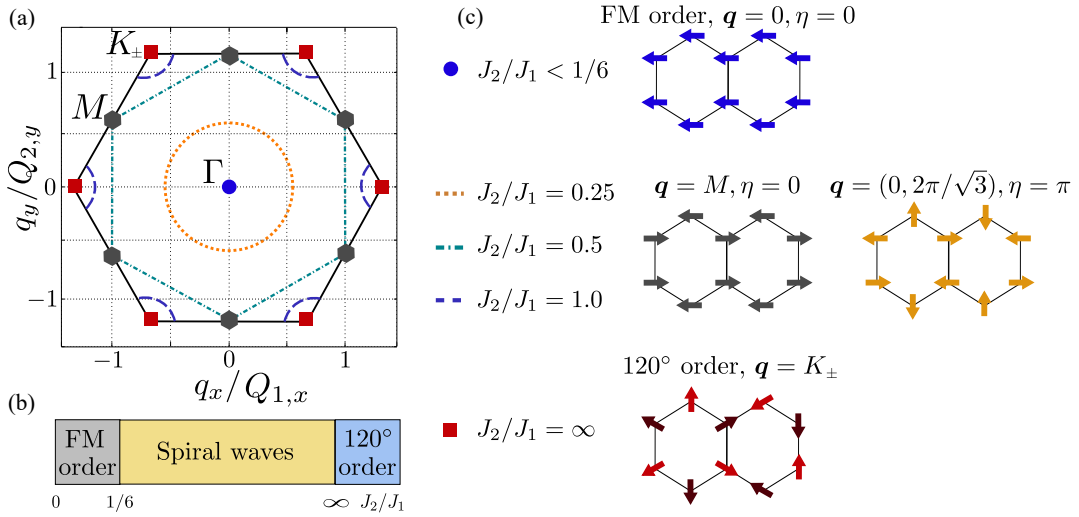

FIGURE 3.6: **(a)** Classical solution $\boldsymbol{q}_{\text{cl}}$ shown for several values of J_2/J_1. When $J_2/J_1 \leq 1/6$, the solution is a single point in the center of the first BZ $\boldsymbol{\Gamma}$, and when $J_2/J_1 \to \infty$ it corresponds to two Dirac points $\boldsymbol{K}_\pm$. In all the remaining cases the continuum of degenerate solutions is formed instead. **(b)** Classical phase diagram of the frustrated spin-1/2 XY model. **(c)** Magnetic orientation of spins for several classical solutions from (a).

$J_2/J_1 \leq 1/6$, we recover the uniform solution corresponding to the ferromagnetic (*FM*) ordering, with $\boldsymbol{q}_{\text{cl}} = \boldsymbol{\Gamma} = 0$ and $\eta_{\text{cl}} = 0$. When J_2/J_1 becomes bigger than $1/6$, the results become less trivial, and we observe the formation of a continuum of spiral solutions around the point $\boldsymbol{\Gamma}$, breaking the translation symmetry. We recover one of the usual properties of the frustrated spin problems: a very high degeneracy of the classical ground-state. By further increasing the ratio J_2/J_1, we see that the diameter of the circle increases, until it transforms into a hexagon at the value $J_2/J_1 = 1/2$. Beyond this point we observe the formation of a continuum of degenerate solutions forming circles around two Dirac points. Only in the limit $J_2/J_1 \to \infty$ we observe again a commensurate solution at exactly two Dirac points $\boldsymbol{K}_\pm$. This solution still breaks the translation symmetry, and is called a *120° order*.

3.3.2 Magnetically ordered states

Since the actual value of the spin S in our problem is equal to $1/2$, we expect the quantum fluctuations to be strong. In particular, they could easily destroy the classical solution. One expects that for the classical solution of the form described by Eq. (3.34), the quantum fluctuation would lead to the selection of a particular solution from the continuously degenerate manifold via the phenomenon called an order by disorder [163]. This effect was studied in the case of the Heisenberg model in Ref. [225] using the Holstein-Primakoff transformation and the $1/S$ power expansion. The result is that to the first order in $1/S$, in the regime $J_2/J_1 < 1/2$, the particular states selected via the order by disorder mechanism lie on the intersection of the manifold of degenerate solutions and the line that connects the points $\boldsymbol{\Gamma}$ and $\boldsymbol{M}$ in the first BZ. When $J_2/J_1 > 1/2$, these points lie on the edge of the first BZ. Higher order terms could further constrain the set of accessible solutions.

In order to verify these predictions, we perform numerical calculations with ED. We notice that from the point of view of a numerical implementation, it is easier to

think of spins-1/2 as of hard-core bosons defined via the following mapping

$$S_i^+ = b_i^\dagger, \quad S_i^- = b_i, \quad S_i^z = b_i^\dagger b_i - 1/2\,. \tag{3.35}$$

Here $b_i^\dagger(b_i)$ are bosonic creation (annihilation) operators. The hard-core constraint implies $\langle b_i^\dagger b_i \rangle \leq 1$. Zero total magnetization corresponds to the system of hard-core bosons at half-filling. This interpretation allows for a more intuitive binary representation of states in the Hilbert space.

A. Fidelity metric

First, we deduce the boundaries between different phases by calculating the fidelity metric g, defined as

$$g(\lambda, \delta\lambda) = \frac{2}{N_c} \frac{1 - F(\lambda, \delta\lambda)}{\delta\lambda^2}\,, \quad \text{where } F(\lambda, \delta\lambda) = |\langle \Phi(\lambda) \,|\, \Phi(\lambda + \delta\lambda)\rangle|\,. \tag{3.36}$$

Here λ corresponds to the parameter J_2/J_1 and $\delta\lambda$ – its small variation. N_c is the total number of unit cells of the lattice and $|\Phi(\lambda)\rangle$ – the many-body ground-state wavefunction. As the size of the system increases, the overlap between two many-body ground-states at λ and $\lambda + \delta\lambda$ goes to zero, even if $\delta\lambda$ is very small. This phenomenon is known as the Anderson orthogonality catastrophe [243]. It was shown however that close to the critical regimes the scaling of the overlap $F(\lambda, \delta\lambda)$ is much more pronounced, as a consequence of the quantitative, structural difference between two ground-states [244]. One can thus probe the phase transitions by studying the asymptotic behavior of this quantity [245, 246]. The expression of the fidelity metric g is obtained by normalizing the overlap $F(\lambda, \delta\lambda)$ in a particular manner [6]. We extract the zeroth order in the expansion in powers of $\delta\lambda$, which is simply equal to 1. Because of the normalization condition we expect that the first order contribution vanishes exactly. The second order contribution is then renormalized by $\delta\lambda^2$. We show the measurement of the metric fidelity $g(\lambda, \delta\lambda)$ for $\delta\lambda \sim 0.01$ in Fig. 3.7. In our ED simulations we used clusters of 6×2 unit cells with tilt $t_h = -4$, 4×3 with no tilt, and 4×4 with no tilt. We remind the reader that our convention for labeling the clusters is presented in Section A.1.5 of Appendix A. We observe the presence of three phase transitions on the clusters 6×2 and 4×3. On the 4×4 cluster we observe only two phase transitions. As we will see in the following, this is due to the geometry of the cluster and particular points that are missing in the reciprocal lattice. By using the 6×2 cluster as a reference, we deduce the presence of three phase transitions at $J_2/J_1 \approx 0.21, 0.36$ and 1.32.

B. Static structure factors

The measurement of the overlap between ground-states $F(\lambda, \delta\lambda)$ and the fidelity metric $g(\lambda, \delta\lambda)$ does not allow us to study the structure and understand the magnetic ordering of the obtained ground-state. This goal can be achieved by looking at the spin-spin correlation functions $\langle S_i^\mu S_j^\nu \rangle$ and their Fourier transform – the structure factors

$$S_{\mu\nu}(\boldsymbol{q}) = \frac{1}{N_c} \sum_\rho \sum_{i,j \in \rho} e^{i\boldsymbol{q}\cdot(\boldsymbol{r}_i - \boldsymbol{r}_j)} \langle S_i^\mu S_j^\nu \rangle\,. \tag{3.37}$$

[6] The "metric" characteristics of the fidelity g originates from the situation when the parameter space is multi-dimensional. Then, one should rather define a matrix $g_{\mu\nu}$, where μ and ν denote different components of the parameter λ.

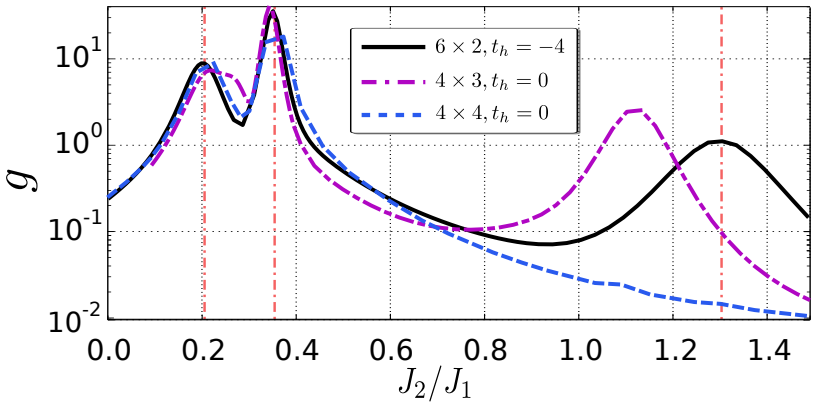

FIGURE 3.7: ED calculation of the fidelity metric g as a function of J_2/J_1 on different clusters. Cluster are labeled according to the notation of Section A.1.5. For the clusters of 4×3 and 6×2 unit cells we observe three critical values of J_2/J_1, for which the scaling of the fidelity metric is more pronounced, meaning that four different phases are expected to be present in the model. For the cluster of 4×4 unit cells we do not observe the third phase transition due to the peculiarity of the cluster geometry.

Here the summation over i is performed over the sites of the same sublattice $\rho \in \{A, B\}$. Notice that the hard-core boson picture provides an alternative point of view on the structure factors. If we limit ourselves to one particular sector of the conserved total magnetization (conserved total number of bosons), we obtain the following identity

$$S_{xx}(\boldsymbol{q}) = S_{yy}(\boldsymbol{q}) = n(\boldsymbol{k}) = \left\langle a_k^\dagger a_k \right\rangle + \left\langle b_k^\dagger b_k \right\rangle . \tag{3.38}$$

Here $n(\boldsymbol{k})$ is the single-particle occupation number of hard-core bosons in the momentum space. The plots of the planar static structure factor $S_{xx}(\boldsymbol{q})$ are shown in Fig. 3.8. On the panel (a) the structure factor is varied as a function of the ratio J_2/J_1 for several values of the momentum $\boldsymbol{q}$, where it has maxima. On the panel (b) we show the structure factor as a function of $\boldsymbol{q}$ for several values of J_2/J_1. We recover four phases, three of which correspond to magnetically ordered spin states.

(i) In the region $J_2/J_1 \lesssim 0.21$ we observe the formation of a *FM* order since $S_{xx}(\boldsymbol{q})$ has a peak at $\boldsymbol{q} = \boldsymbol{\Gamma}$. The exact point of the phase transition is shifted compared to the classical case.

(ii) The phase in range $0.36 \lesssim J_2/J_1 \lesssim 1.32$ corresponds to a spiral wave with *collinear order*. The structure factor has maxima at three inequivalent $\boldsymbol{M}$ points. This is expected from the order by disorder mechanism – the continuum degeneracy of the ground-state is lifted and one particular spiral state is selected because of the effect of quantum fluctuations.

(iii) When $1.32 \lesssim J_2/J_1$ the ground-state is the *120° order* spiral wave. The planar structure factor has a peak at two Dirac points $\boldsymbol{K}_\pm$. We remind the reader that according to the classical solution this phase should be stable only in the limit $J_2/J_1 \to \infty$. Quantum fluctuations act thus positively and stabilize the *120° order*.

(iv) Most surprisingly, in the intermediate frustration regime $0.21 \lesssim J_2/J_1 \lesssim 0.36$, we observe that the structure factor $S_{xx}(\boldsymbol{q})$ seems flat in the reciprocal space. The resulting state could be described by a more complicated magnetic order or have no long-range order at all. The second scenario is the most interesting for us, because

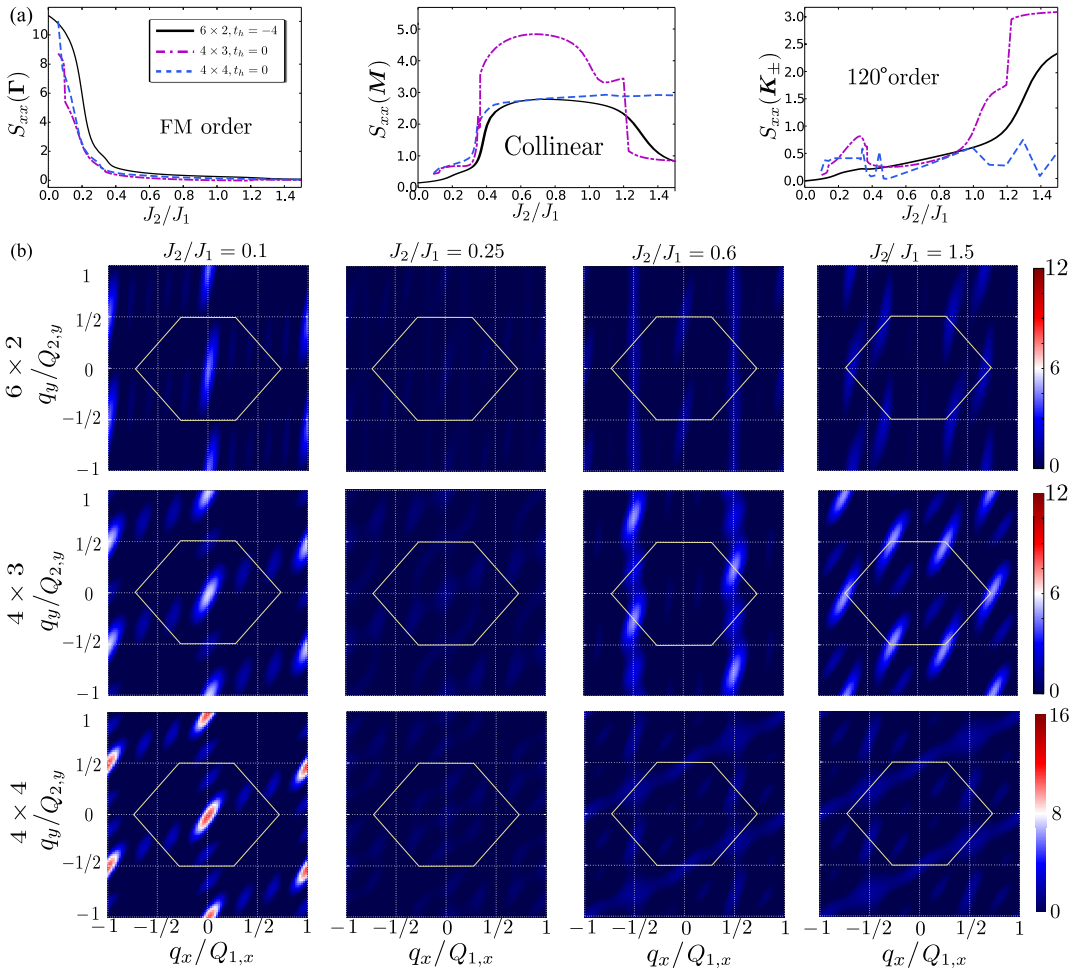

FIGURE 3.8: **(a)** ED calculation of the planar static structure factor $S_{xx}(\boldsymbol{q})$ as a function of the ratio J_2/J_1 for 3 particular points in the first BZ. Maximum of the structure factor at particular value of the momentum $\boldsymbol{q}$ is associated with the presence of a magnetically ordered spin state at the same wave-vector. **(b)** Plot of the structure factor $S_{xx}(\boldsymbol{q})$ in the momentum space at 4 typical values of the ratio $J_2/J_1 \in \{0.1, 0.25, 0.6, 1.5\}$ in 4 phases (different columns). Different ED clusters are shown at different rows. The yellow hexagon represents the boundary of the first BZ, shown for convenience. Vectors $\boldsymbol{Q}_1$ and $\boldsymbol{Q}_2$ are defined as in Fig. 2.1(b). In the *FM* phase ($J_2/J_1 = 0.1$ column) the planar structure factor has a peak at $\boldsymbol{q} = \boldsymbol{\Gamma}$. In the intermediate frustration regime ($J_2/J_1 = 0.25$ column) the system seems to be disordered in the xy plane. For $J_2/J_1 = 0.6$, we observe the formation of the *collinear order*, where the maximum of $S_{xx}(\boldsymbol{q})$ occurs at the $\boldsymbol{M}$ points of the first BZ. We notice however the significant difference of the result on the lattice 4×3. This is explained by the fact that this lattice does not contain all the $\boldsymbol{M}$ points in the reciprocal space. In the case $J_2/J_1 = 1.5$, the system develops a *120° order*. We notice that, similarly to the previous case, the lattice 4×4 does not contain Dirac points $\boldsymbol{K}_\pm$ in the reciprocal space, that results in the impossibility to recover correctly the *120° order* phase: two rightmost figures in the bottom line look very similar to each other.

this is a strong indication that the magnetic state is a spin liquid (see Section 1.5.3 for more details). In the following, we will pay particular attention to this seemingly disordered spin state and uncover its true nature.

We notice that exact positions of the phase transitions, especially the transition between the *collinear order* and the *120° order*, is sensitive to the choice of the finite size clusters. Small clusters available with ED do not allow to analyze deeply the transitions between the spiral states at momenta $\boldsymbol{q}$ comparable with the inverse total size of the lattice. In this case, one needs to carefully choose the lattice, so that all the relevant momenta are contained in the BZ. In Fig. 3.8(b) we observe that the 4×4 ED cluster does not allow us to probe the *120° order*, since its reciprocal lattice does not contain any Dirac point. On the other side, the ED cluster of 4×3 unit cells does not contain all the $\boldsymbol{M}$ points.

3.4 Disordered spin state

In the previous section, we observed that the intermediate regime of the frustrated J_1–J_2 spin-1/2 XY model on the honeycomb lattice does not have a well defined maxima structure of the planar static structure factor $S_{xx}(\boldsymbol{q})$, that gives a strong indication that this state is disordered in the xy plane and could be a quantum spin liquid (see Section 1.5.3). It was suggested [203] that this state could in fact be a chiral spin liquid (CSL) state. In this section we will first remind briefly the properties of the chiral spin liquids. We will then show and complete the arguments of Ref. [203] based on the application of the ChS field theory at the mean-field level, that supports the above mentioned proposition. We will perform a numerical test of this analytical prediction. We will focus on two discrete symmetries, which are expected to be spontaneously broken in chiral spin liquids, and the topological properties of the ground-state. We will show that while the state at the intermediate frustration is indeed described by an order parameter of chiral spin liquids, it is not topologically ordered, since it has a vanishing first Chern number associated with the degenerate ground-state manifold.

3.4.1 Chiral spin liquids

CSLs were proposed for the first time by Kalmeyer and Laughlin [97] soon after the seminal work by Anderson [96]. As other spin liquids, CSLs describe spin states that defy the Landau-Ginzburg description in terms of broken symmetries and local order parameters because they do not have any long-range order even at zero temperature. These spin liquids are however described by two broken discrete symmetries – the time-reversal symmetry T and the lattice parity symmetry R. The parity symmetry corresponds to the reflection which maps sublattice A onto sublattice B, and it is not anti-unitary. Symmetry breaking could be both explicit or spontaneous, as a result of the many-body interactions. As a consequence, CSLs have to be described by a non-trivial value of the spatial order parameter – the scalar spin chirality

$$\chi_{ijk} = \left\langle \boldsymbol{S}_i \cdot \left(\boldsymbol{S}_j \times \boldsymbol{S}_k \right) \right\rangle \ . \tag{3.39}$$

CSLs are topologically ordered, *i.e.* they exhibit topological ground state degeneracy per chirality sector equal to 2^g in the thermodynamic limit on a compact space with genus g [80, 98]. Moreover, field theory considerations allow to describe them using the ChS field theory [60, 73, 74] – in the same way as the FQH states. It allows to recover at the mean-field level the main peculiarity of the FQH states, which

consists in the formation of composite particles – real particles with an attachment of several quanta of magnetic fluxes. In particular, the Kalmeyer and Laughlin CSL is equivalent to an incompressible Laughlin's state for interacting bosons at filling $\nu = 1/2$. We notice however that the subtleties arise, when one tries to map a discretized lattice problem onto a continuous ChS field theory problem [238–241]. This construction was effectively performed on a square [238] and kagome [247] planar lattices. However, the question of generalizing this procedure on a more quantitative level for more generic lattices, including the honeycomb one, and the non-planar lattices, still remains unresolved. We discuss some of these subtleties in Appendix B.

3.4.2 Chern-Simons field theory arguments

Now, we would like to describe how the problem (3.31) can be simplified using the ChS field theory approach. This calculation is based on the fermionic representation of spins. Similarly to the Jordan-Wigner transformation in 1D [248], spins-1/2 can be mapped onto fermions using the following transformation

$$S_j^+ = c_j^\dagger e^{i\alpha_j}, \quad S_j^- = c_j e^{-i\alpha_j}, \quad n_j = c_j^\dagger c_j = S_j^z + 1/2\,. \tag{3.40}$$

Here $c_j^\dagger(c_j)$ are fermionic creation (annihilation) operators, and $n_j = c_j^\dagger c_j$ is the number operator. Spins do not verify the correct commutation relations at different positions. Thus, the phase factor α_j is required to enforce the fermionic commutation relation. It can be written in the following way

$$\alpha_j = \sum_{k\neq j} B_{jk} n_k\,. \tag{3.41}$$

Several choices of B_{jk} can be used. In the 1D XY model, a particularly convenient choice is

$$B_{jk} = \sum_{k<j} n_j\,. \tag{3.42}$$

It allows one to map an interacting spin problem onto a free fermion problem, if only NN interactions are present. Difficulties start to arise when higher-range interactions are considered. This transformation also becomes less helpful in 2D, when there is no possibility to order the sites in such a way, that local interactions in the spin language remain also local in the fermionic one. This difficulty is schematically presented in Fig. 3.9.

A. Jordan-Wigner transformation in 2D

The Jordan-Wigner transformation in 2D is largely used in the context of the FQHE and quantum spin liquid problems. Similarly to the FQH cases, one could use the following convention for defining the phases in the Jordan-Wigner transformation:

$$B_{jk} = \arg\left(\tau_k - \tau_j\right) = \mathfrak{Im}\,\ln\left(\tau_k - \tau_j\right)\,. \tag{3.43}$$

Here $\tau_j = x_j + iy_j$ is the complex number associated to each point j of the lattice, situated at $\boldsymbol{r}_j = x_j\boldsymbol{e}_x + y_j\boldsymbol{e}_y$. The complex number B_{jk} corresponds to an angle that the vector $\boldsymbol{r}_k - \boldsymbol{r}_j$ forms with the x-axis. Following Ref. [203], the Hamiltonian (3.31)

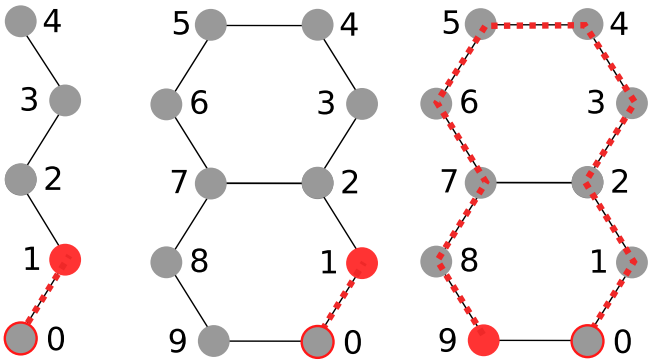

FIGURE 3.9: Jordan-Wigner transformation can be used to map a spin-1/2 degrees of freedom onto fermionic degrees of freedom. This mapping is very convenient in **(a)** 1D case with NN interactions, when the local spin problem is mapped onto a local fermionic problem. Difficulties arise however, when the problem has longer range interactions, or is defined in higher dimensions. 2D scenario is shown in **(b)** and **(c)**. While some interactions remain local in the originally local problem, some of them become highly non-local, leading to the emergence of so-called Jordan-Wigner strings (represented by a dotted line in the figure).

can now be rewritten as

$$H = -J_1 \sum_{\langle i,j \rangle} c_i^\dagger e^{i(\alpha_i - \alpha_j)} c_j + J_2 \sum_{\langle\langle i,j \rangle\rangle} c_i^\dagger e^{i(\alpha_i - \alpha_j)} c_j + \text{h.c.} \,. \tag{3.44}$$

The complicated many-body nature of the problem is hidden in the phases α_j. In order to simplify this expression, we introduce a vector field $\boldsymbol{\mathcal{A}}_i$ as

$$\alpha_j - \alpha_k = \int_{\boldsymbol{r}_k}^{\boldsymbol{r}_j} \mathrm{d}\boldsymbol{r}_i \cdot \boldsymbol{\mathcal{A}}_i \,, \tag{3.45}$$

such that

$$\boldsymbol{\mathcal{A}}_i = \sum_{j \neq i} n_j \frac{\boldsymbol{e}_z \times (\boldsymbol{r}_j - \boldsymbol{r}_i)}{(\boldsymbol{r}_j - \boldsymbol{r}_i)^2} = \sum_{j \neq i} n_j \frac{(\boldsymbol{r}_j - \boldsymbol{r}_i)_\perp}{(\boldsymbol{r}_j - \boldsymbol{r}_i)^2} \,. \tag{3.46}$$

Here we denote by $(\boldsymbol{r_j} - \boldsymbol{r_i})_\perp$ the vector perpendicular to $\boldsymbol{r_j} - \boldsymbol{r_i}$ (rotated by a $\pi/2$ angle in the counter-clockwise direction). We also define a statistical magnetic field $\boldsymbol{\mathcal{B}}_i = \mathcal{B}_i \boldsymbol{e}_z$:

$$\mathcal{B}_i = \mathrm{curl} \boldsymbol{\mathcal{A}}_i = 2\pi \sum_{j \neq i} n_j \delta(\boldsymbol{r}_j - \boldsymbol{r}_i) \,. \tag{3.47}$$

We can then introduce a mean magnetic field $\mathcal{B}(\boldsymbol{r}_i)$ by taking the expectation value of the number operators $\langle n_i \rangle$ and interpreting the resulting sum as the local density $n(\boldsymbol{r}_i)$ at position $\boldsymbol{r}_i$:

$$\mathcal{B}(\boldsymbol{r}_i) = \langle \mathcal{B}_i \rangle = 2\pi n(\boldsymbol{r}_i) \,. \tag{3.48}$$

This allows us to make the following interpretation of the problem: at the mean-field level each fermionic particle sees a point-vortex of flux $2\pi n(\boldsymbol{r}_i)$ attached to each other particle. This formulates exactly the idea of a composite particle with a magnetic flux attachment, and allows us to interpret $\mathcal{B}(\boldsymbol{r}_i)$ as ChS magnetic field. Remarkably, the resulting problem becomes a problem of non-interacting fermions. Notice however

the complicated spatial dependency of the magnetic fields, implying high inhomogeneity of the resulting fermion model.

Finally, we remove exponential string operators by introducing the δ-function that imposes a constraint on $\mathcal{B}(\boldsymbol{r}_i)$ through the Lagrange multiplier $\mathcal{A}^0(\boldsymbol{r}_i)$:

$$2\pi\delta\left(\mathcal{B}(\boldsymbol{r}_i)/(2\pi) - n(\boldsymbol{r}_i)\right) = \int \mathrm{d}\mathcal{A}^0(\boldsymbol{r}_i) e^{i\mathcal{A}^0(\boldsymbol{r}_i)[\mathcal{B}(\boldsymbol{r}_i)/(2\pi) - n(\boldsymbol{r}_i)]} \,. \tag{3.49}$$

The Lagrange multiplier plays the role of a scalar ChS potential. We can now write down the resulting Lagrangian

$$\begin{aligned}\mathcal{L} =& \sum_i \bar{\psi}(\boldsymbol{r}_i)\left(i\partial_t - \mathcal{A}^0(\boldsymbol{r}_i)\right)\psi(\boldsymbol{r}_i) + \frac{1}{2\pi}\sum_i \mathcal{A}^0(\boldsymbol{r}_i)\mathcal{B}(\boldsymbol{r}_i) \\ &+ J_1 \sum_{\langle i,j\rangle} \bar{\psi}(\boldsymbol{r}_i)\psi(\boldsymbol{r}_j) e^{i\left(\alpha_i - \alpha_j\right)} - J_2 \sum_{\langle\langle i,j\rangle\rangle} \bar{\psi}(\boldsymbol{r}_i)\psi(\boldsymbol{r}_j) e^{i\left(\alpha_i - \alpha_j\right)} + \text{h.c.}\end{aligned} \tag{3.50}$$

Here $\bar{\psi}(\boldsymbol{r}_i)$ and $\psi(\boldsymbol{r}_i)$ are two Grassman variables associated with the fermionic creation and annihilation operators. The partition function and the observables are calculated, as usual, after taking the functional integration with respect to the ChS magnetic field $\mathcal{B}(\boldsymbol{r}_i)$, the Lagrange multiplier $\mathcal{A}^0(\boldsymbol{r}_i)$, and the Grassman variables.

B. Free fermionic problem

One can easily integrate out the Grassmann variables in Eq. (3.50), since the problem in the fermionic language is free (the Lagrangian is quadratic in fermionic fields). The resulting effective Lagrangian can be written as

$$\mathcal{L}_{\text{eff}}\left(\left\{\mathcal{A}^0(\boldsymbol{r}_i), \mathcal{B}(\boldsymbol{r}_i)\right\}\right) = W\left(\left\{\mathcal{A}^0(\boldsymbol{r}_i), \mathcal{B}(\boldsymbol{r}_i)\right\}\right) + \frac{1}{2\pi}\sum_i \mathcal{A}^0(\boldsymbol{r}_i)\mathcal{B}(\boldsymbol{r}_i) \,. \tag{3.51}$$

The fermionic free energy functional $W(\{\mathcal{A}^0(\boldsymbol{r}_i), \mathcal{B}(\boldsymbol{r}_i)\})$ is calculated as the sum over eigenvalues ϵ_k of the single-particle fermionic problem up to some chemical potential ϵ_F

$$W(\{\mathcal{A}^0(\boldsymbol{r}_i), \mathcal{B}(\boldsymbol{r}_i)\}) = \sum_k \epsilon_k\left(\{\mathcal{A}^0(\boldsymbol{r}_i), \mathcal{B}(\boldsymbol{r}_i)\}\right)\Theta(\epsilon_k - \epsilon_F) \,. \tag{3.52}$$

Here Θ is the Heaviside step function. Exact value of the chemical potential ϵ_F is obtained by recalling that the total filling of fermions has to be equal to $1/2$

$$\sum_k \Theta(\epsilon_k - \epsilon_F) = N_s/2 \,, \tag{3.53}$$

with N_s – the total number of states in the system. In a lattice problem it will be equal to the total number of sites. In order to perform the calculation, we need however to solve the high inhomogeneity of the fermionic problem. To do so, we suppose that the solution is translation invariant, but we allow for a breaking of the symmetry between two sublattices. The only remaining independent variables can be denoted as n_A and n_B – the density on respectively sublattice A and B. The half-filling constraint implies

$$n_A + n_B = 1 \,. \tag{3.54}$$

The NN hopping terms are sensitive only to the total flux through the unit cell $\mathcal{B}_{\text{tot}} = 2\pi$, since each unit cell contains precisely one A and one B-site. The average

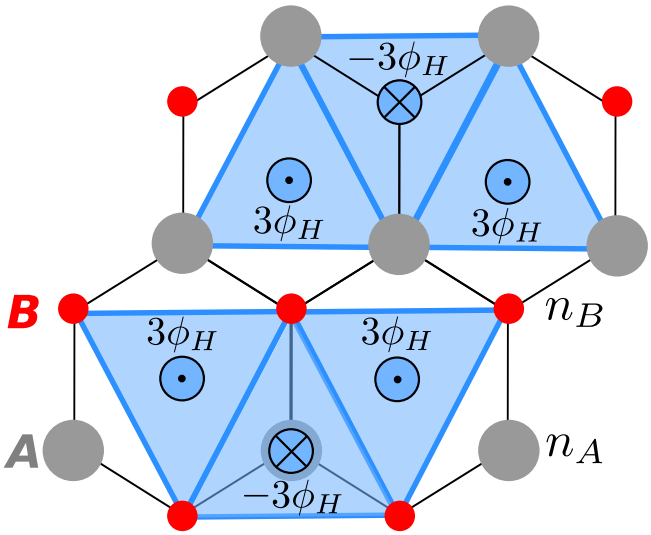

FIGURE 3.10: Schematic representation of the mean-field fermionic solution. n_A and n_B are the densities on respectively sublattices A and B. Imbalance of the densities leads to the emergence of a staggered magnetic field, described by the Haldane phase ϕ_H, piercing the lattice.

magnetic field has thus to be equal to 2π, gauge-equivalent to zero, and is not relevant for our future considerations. Let us now focus on the big triangles defined by vectors $\boldsymbol{i}$ connecting NNN sites (See Figs. 2.1 and 3.10). If we go in the anti-clockwise direction on the big triangle on the A sublattice, that encloses a site of the B sublattice, we see that a non-trivial phase $2\pi n_B$ is accumulated in average. The flux piercing the neighboring triangle on the A sublattice has thus to be equal to

$$-2\pi n_B = 2\pi n_A \bmod 2\pi \,. \tag{3.55}$$

Similarly, on the B sublattice the magnetic fluxes $2\pi n_B$ and $2\pi n_A$ emerge. We then denote by $\mathcal{B}_A$ and $\mathcal{B}_B$ the magnetic fields attached to the sites on the sublattices A and B

$$\mathcal{B}_A = 2\pi n_A, \quad \mathcal{B}_B = 2\pi n_B \,. \tag{3.56}$$

We observe that NNN hoppings exhibit the modulation of the fields $\mathcal{B}_A$ and $\mathcal{B}_B$, similar to the phases of the Haldane model (see Section 2.1 for details on the Haldane model). In order to see it more clearly, we separate symmetric and antisymmetric components of the scalar potential and the magnetic field on two sublattices:

$$\mathcal{B}_\pm = \mathcal{B}_A \pm \mathcal{B}_B, \quad \mathcal{A}^0_\pm = \mathcal{A}^0_A \pm \mathcal{A}^0_B \,. \tag{3.57}$$

The flux configuration originating from the symmetric component is also gauge equivalent to zero for NNN links, since $\mathcal{B}_A + \mathcal{B}_B = 2\pi$. We see thus that the only non-trivial contribution originates from the antisymmetric component. It allows us to identify

$$\mathcal{B}_- = 2\pi\,(n_A - n_B) = 4\pi n_A \bmod 2\pi = -4\pi n_B \bmod 2\pi \,. \tag{3.58}$$

We introduce the phase ϕ_H accumulated for each hopping along the NNN link in the anti-clockwise direction, equivalently to the Haldane phase of the (isotropic)

Haldane model, as shown in Fig. 3.10. The antisymmetric magnetic field is thus equal to

$$\mathcal{B}_- = 4\pi n_A = -4\pi n_B = 6\phi_H \,. \tag{3.59}$$

Finally, the expression of the resulting effective Lagrangian for the ChS magnetic field and scalar potential simplifies to

$$\mathcal{L}_{\text{eff}}(\mathcal{A}^0_-, \phi_H) = W(\mathcal{A}^0_-, \phi_H) + \frac{3}{2\pi}\mathcal{A}^0_-\phi_H N_c \,, \tag{3.60}$$

where $N_c = N_s/2$ is the total number of unit cells in the lattice. In the above expression the initial factor 6 is divided by 2, because of the recombination of $\mathcal{B}_{A(B)}$ and $\mathcal{A}^0_{A(B)}$ into $\mathcal{B}_-$ and $\mathcal{A}^0_-$. The spectrum of free fermions is the one of the Haldane model:

$$\epsilon_{\boldsymbol{k},\pm}(\mathcal{A}^0_-, \phi_H) = d_0(\boldsymbol{k}) \pm |\boldsymbol{d}(\boldsymbol{k})| = d_0(\boldsymbol{k}) \pm \sqrt{d_x^2(\boldsymbol{k}) + d_y^2(\boldsymbol{k}) + d_z^2(\boldsymbol{k})} \,, \tag{3.61}$$

with functions $d_\mu(\boldsymbol{k})$ defined exactly as in Eq. (2.17). One only needs to make a substitution $t_i = J_i$ and $M = \mathcal{A}^0_-/2$. Notice however that ϕ_H is not necessarily equal to $\pi/2$ and could still lead to the emergence of an additional chemical potential term.

We use the saddle-point approximation to find the values of $\mathcal{A}^0_-$ and ϕ_H extremizing the effective action

$$S_{\text{eff}} = \int \mathrm{d}t \mathcal{L}_{\text{eff}}(\mathcal{A}^0_-, \phi_H) \,, \tag{3.62}$$

and solving the equations of motion

$$\delta_{\mathcal{A}^0_-} S_{\text{eff}} = 0, \quad \delta_{\phi_H} S_{\text{eff}} = 0 \,. \tag{3.63}$$

The first equation gives

$$\frac{3}{2\pi}\phi_H = \frac{1}{2N_c}\sum_k (-1)^\mu \frac{d_z(\boldsymbol{k})}{|\boldsymbol{d}(\boldsymbol{k})|}\Theta(\epsilon_k - \epsilon_F) \,, \tag{3.64}$$

where $\mu \in \{1, 2\}$ is the lower/upper band index. The second equation leads to

$$\frac{3}{2\pi}\mathcal{A}^0_- = \frac{1}{N_c}\sum_k X_k(\mathcal{A}^0_-, \phi_H)\Theta(\epsilon_k - \epsilon_F) \,, \tag{3.65}$$

with

$$X_k(\mathcal{A}^0_-, \phi_H) = 2J_2\left(\sin(\phi_H)\sum_i \cos(\boldsymbol{k}\cdot\boldsymbol{v}_i) - (-1)^\mu \cos(\phi_H)\frac{d_z(\boldsymbol{k})}{|\boldsymbol{d}(\boldsymbol{k})|}\sum_i \sin(\boldsymbol{k}\cdot\boldsymbol{v}_i)\right) \,. \tag{3.66}$$

By calculating the functional $\mathcal{L}_{\text{eff}}$ and solving the two equations of motions for different values of the ratio J_2/J_1, we deduce three different regimes in the phase diagram.

(i) In the region $J_2/J_1 \lesssim 0.2$ the functional $\mathcal{L}_{\text{eff}}$ has only one point where both equations are verified, which is the saddle point at $\mathcal{A}^0_- = 0$, $\phi_H = 0$ (see Fig. 3.11(a)). This is clearly the trivial phase of the effective fermionic Haldane model, which is of little interest to us.

(ii) In the region $0.2 \lesssim J_2/J_1 \lesssim 0.36$ there are three solutions of the extremization equations. The solution at $\mathcal{A}^0_- = 0$, $\phi_H = 0$ corresponds to a local maximum of the functional $\mathcal{L}_{\text{eff}}$, whereas two symmetric solutions (for positive and negative values of ϕ_H and $\mathcal{A}^0_-$) not located at zero become new saddle point solutions (see

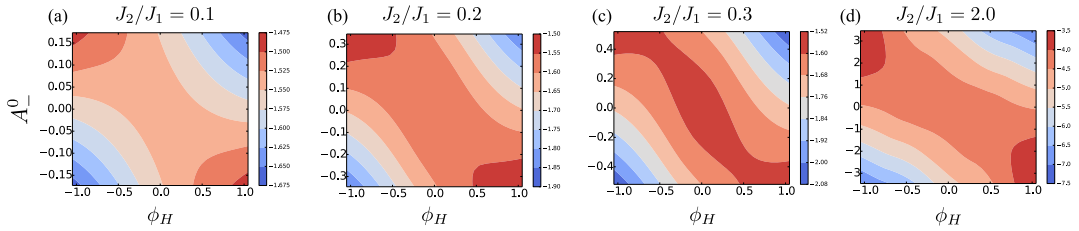

FIGURE 3.11: The functional $\mathcal{L}_{\text{eff}}(\phi_H, \mathcal{A}^0_-)$ shown for different values of J_2/J_1. **(a)** When $J_2/J_1 \lessapprox 0.21$ the only solution of Eqs. (3.65) and (3.66) corresponds to $\mathcal{A}^0_- = 0$, $\phi_H = 0$. **(b-c)** In the region $0.21 \lessapprox J_2/J_1 \lessapprox 0.36$ two symmetric saddle-point solutions non located at zero appear. **(d)** For $0.36 \lessapprox J_2/J_1$ the only solution extremizing $\mathcal{L}_{\text{eff}}$ is the local maximum $\mathcal{A}^0_- = 0, \phi_H = 0$.

Figs. 3.11(b-c)). We notice that the Haldane model is situated in the topological phase $\mathcal{A}^0_-/J_2 < 6\sqrt{3}\sin(\phi_H)$ at saddle points inside the entire region. Moreover, since the local minimum at zero transforms into a local maximum, we assume that the first *trivial*↔*non-trivial* phase transition is of the second order.

(iii) In the region $0.36 \lesssim J_2/J_1$ the solution minimizing $\mathcal{L}_{\text{eff}}$ becomes again $\mathcal{A}^0_- = 0$, $\phi_H = 0$ (see Fig. 3.11(d)). Very close to the transition point however we observe, that the local minima at finite values of $\mathcal{A}^0_-$ and ϕ_H still keep being another solution, lying higher in energy. This indicates that the second *non-trivial*↔*trivial* phase transition may be of the first order.

C. Physical interpretation

Finite values of the phase ϕ_H correspond to the breaking of two discrete symmetries. The presence of a staggered Haldane magnetic flux clearly implies the breaking of the time-reversal symmetry T. We also know that because of the ChS flux attachment, the magnetic flux through the triangular loops of the honeycomb lattices is related to the imbalance of the magnetization of spins, or densities of fermions, between two sublattices

$$\mathcal{B}_A - \mathcal{B}_B = 2\pi\,(n_A - n_B) = 2\pi\,\langle S^z_A - S^z_B\rangle = 6\phi_H\,. \tag{3.67}$$

This implies the breaking of the parity symmetry of the lattice and formation of an Ising antiferromagnetic order. The apparition of this order, coming out of the plane, is surprising in itself in the XY model, which has purely in-plane interactions. Moreover, the mean-field free fermion description formulated in terms of an effective Haldane model suggests the presence of gapless excitations along the edges in a system with open boundary conditions. Because of the non-local nature of the Jordan-Wigner transformation and based on the field theory arguments (see Appendix B), one may suggest that these states correspond to spinon excitations with fractional statistics equal to half of the fermionic one. The resulting state could thus describe a topologically ordered CSL of Kalmeyer and Laughlin. In the following subsections we will verify these predictions numerically.

D. Explicitly broken symmetries

By adding a staggered external magnetic field along the z direction

$$H_z = h_z \sum_j (-1)^j S^z_j\,, \tag{3.68}$$

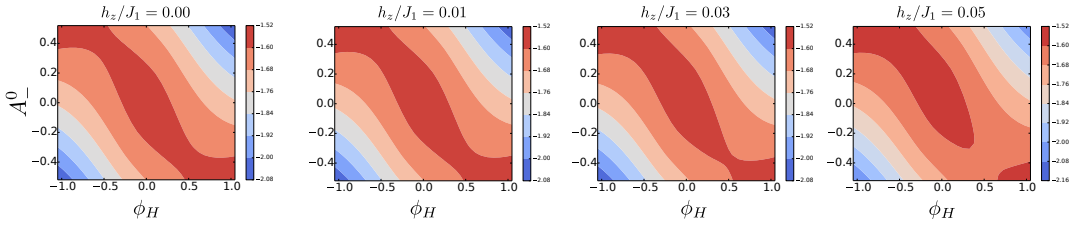

FIGURE 3.12: The effect of the parity symmetry breaking term h_z on the functional $\mathcal{L}_{\text{eff}}(\phi_H, \mathcal{A}^0_-)$ for a fixed value $J_2/J_1 = 0.3$, compared to the $h_z = 0$ case. We can see that one of the non-trivial minima shifts in energy with respect to the other one, explicitly breaking the symmetry between two degenerate solutions.

we can break explicitly the symmetry between two non-trivial solutions in the regime $0.2 \lesssim J_2/J_1 \lesssim 0.36$. The effect of such perturbation to the mean-field solution presented in the subsections above, is shown in Fig. 3.12. We observe that one of the two degenerate solutions for positive and negative values of ϕ_H and $\mathcal{A}^0_-$ increases in energy with respect to the other, depending on the sign of the perturbation. We notice, that in the hard-core boson and fermion language this term corresponds to the Semenoff staggered chemical potential term, while in the language of bosons of the initial BKMH model it is

$$H_z = h_z \sum_j \frac{(-1)^j}{2} \left(c^\dagger_{\uparrow,j} c_{\uparrow,j} - c^\dagger_{\downarrow,j} c_{\downarrow,j} \right) . \tag{3.69}$$

This perturbation will be crucial for the analysis presented in the following section. In Section E.2 of Appendix E we also study this perturbation in the context of the classical solution of the spin problem. We find that the effect of such term cannot be understood by means of the linear response theory. This further outlines the exotic nature of the disordered spin state we observe.

3.4.3 Chiral spin state

We complete the numerical study of the effective frustrated XY model using ED and new probes such as the responses to T and R breaking perturbations. We are particularly interested in checking the analytical predictions based on the ChS field theory arguments, presented previously in this section. We are interested in the relative magnetization between the two sublattices

$$m = \langle m_{\boldsymbol{r}_i} \rangle = \left\langle S^z_{\boldsymbol{r}_i} - S^z_{\boldsymbol{r}_i + \boldsymbol{u}_3} \right\rangle , \tag{3.70}$$

revealing the antiferromagnetic Ising order, as well as the scalar spin chirality

$$\chi = \langle \boldsymbol{S}_{\boldsymbol{r}_i} \cdot (\boldsymbol{S}_{\boldsymbol{r}_i + \boldsymbol{u}_1} \times \boldsymbol{S}_{\boldsymbol{r}_i + \boldsymbol{u}_2}) \rangle . \tag{3.71}$$

Here we altered the definition of the chirality in order to outline the choice of three sites i, j and k we considered. We assume that the site i belongs to sublattice A, while j and k – to sublattice B, and they are connected by vectors $\boldsymbol{u}_i$ between first neighbors. This describes the smallest triangular loop on the honeycomb lattice.

Using ED we cannot probe spontaneously broken symmetries [7]. The way to

[7] The ground-state we deduce numerically with ED has the same symmetries as the Hamiltonian and corresponds to a superposition of states with broken symmetries. The expectation value of the order parameter calculated in such state vanishes.

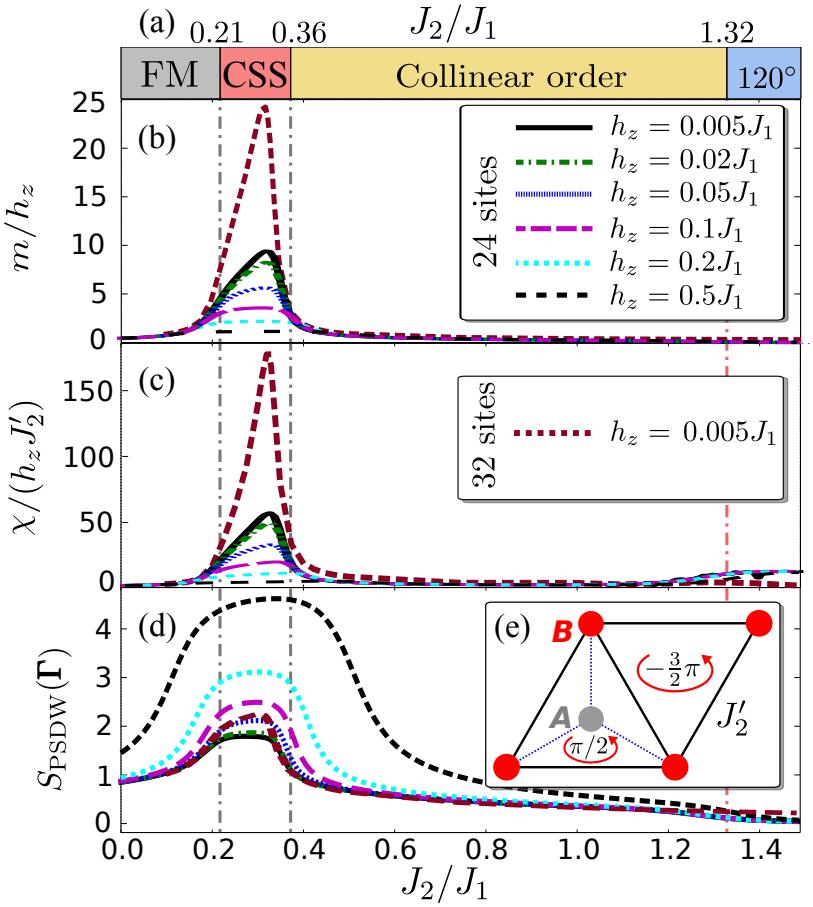

FIGURE 3.13: ED results showing the response functions after applying the symmetry-breaking perturbation (3.68) and (3.72). **(a)** Phase diagram of the frustrated XY model. **(b-d)** Variation of the observables with the dimensionless parameter J_2/J_1 for different values of h_z, with $J_2' = 0.01J_1$, on a lattice of 6×2 unit cells. **(b)** Difference of the average Ising magnetization on two sublattices m. **(c)** Scalar spin chirality χ. **(d)** Pseudo-spin density wave structure factor $S_{\mathrm{PSDW}}(\mathbf{\Gamma})$. **(e)** Schematic representation of the perturbation term $H_{J_2'}$.

probe m and χ could be achieved only after breaking the symmetries explicitly. In order to do this, we add a staggered chemical potential / magnetic field along the z axis, corresponding to the term H_z from Eq. (3.68). However, this perturbation does not break the time-reversal symmetry, the value of χ will thus still be zero. When calculating the chirality χ, we add a perturbation corresponding to the second-neighbor hopping of the Haldane model, of amplitude J_2' and phase $\pi/2$, as shown in Fig. 3.13(e)

$$H_{J_2'} = J_2' \sum_{\langle\langle i,k \rangle\rangle} \left(e^{\pm i\pi/2} S_i^+ S_k^- + \text{h.c.} \right) . \tag{3.72}$$

We are interested in the limit $h_z, J_2' \ll J_1$. Results of the ED calculations are presented in Figs. 3.13(b-c). We observe that the only state showing a non-trivial response to the perturbation is the disordered spin state in the intermediate frustration regime $0.21 \lesssim J_2/J_1 \lesssim 0.36$. This state reveals itself by sharp responses to such external fields. Moreover, the scaled quantities m/h_z and $\chi/(h_z J_2')$ tend to diverge when $h_z, J_2' \to 0$, giving a strong indication for spontaneous symmetry breaking. This is the reason, why we called this state a **chiral spin state**, abbreviated to *CSS*. This finalizes the shape of the total phase diagram of the frustrated spin-1/2 XY model, as presented in Fig. 3.13(a). One can also probe the antiferromagnetic Ising ordering without breaking R and T by calculating the **pseudo-spin density wave** (PSDW) structure factor [199, 200]:

$$S_{\text{PSDW}}(\boldsymbol{q}) = \sum_{i,j} e^{i\boldsymbol{q}\cdot(\boldsymbol{r}_i - \boldsymbol{r}_j)} \left\langle m_{\boldsymbol{r}_i} m_{\boldsymbol{r}_j} \right\rangle . \tag{3.73}$$

We observe in Fig. 3.13(d) that $S_{\text{PSDW}}(\boldsymbol{q})$ has a peak at $\boldsymbol{q} = \boldsymbol{\Gamma}$ in the intermediate frustration regime.

We remind the reader that the properties of the *CSS*, predicted both theoretically and numerically, can also be tested experimentally in the strongly interacting regime (Mott phase) of the BKMH model. This model could be constructed in optical lattices setups [209–211] and with photons [3, 218–220]. From the point of view of experimental probes, one could track the on-site populations of bosons $n_{\sigma,i} = \left\langle c_{\sigma,i}^\dagger c_{\sigma,i} \right\rangle$ in order to verify whether the parity symmetry R is broken. In the bosonic language, the finite value of the relative magnetization and the emergence of the antiferromagnetic Ising order have to be related to the imbalance of the densities of two species of bosons

$$2\left\langle S_A^z - S_B^z \right\rangle = \left(n_{\uparrow,A} - n_{\downarrow,A} \right) - \left(n_{\uparrow,B} - n_{\downarrow,B} \right) . \tag{3.74}$$

In addition, one could probe the breaking of the time-reversal symmetry by looking at the current expectation values. In fact, the chirality is equal to the antisymmetric combination of terms $\left\langle S_i^z S_j^+ S_k^- \right\rangle$, that could be approximated by

$$\left\langle S_i^z \right\rangle \left(\left\langle S_j^+ S_k^- \right\rangle - \left\langle S_k^+ S_j^- \right\rangle \right) \sim m J_{jk} , \tag{3.75}$$

since the expectation value of $\langle S_i^z \rangle$ is finite and the expectation value of $\langle S_i^\pm \rangle$ is zero in the ground-state. The currents

$$J_{jk} = \mathfrak{Im} \left\langle S_j^+ S_k^- \right\rangle \tag{3.76}$$

that appear in the equation above are spin currents of the frustrated spin model. In

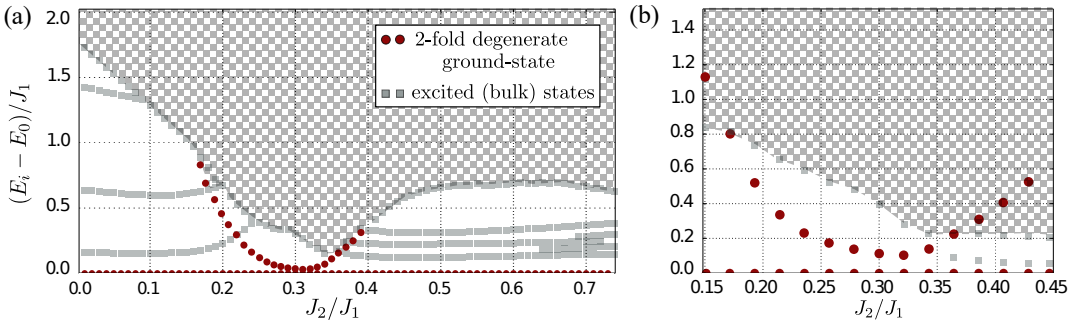

FIGURE 3.14: ED calculations of the low energy spectra as a function of J_2/J_1 showing (using red circles) the formation of a quasi-degenerate two-fold ground-state manifold **(a)** on a lattice of 4×3 unit cells for various values of the total magnetization S^z_{Tot}; **(b)** on a lattice of 4×4 unit cells in the $S^z_{\text{Tot}} = 0$ sector only.

the BKMH model they correspond to a difference of currents of two bosonic species ($\uparrow$ and $\downarrow$):

$$J^{\sigma}_{jk} = \mathfrak{Im} \left\langle b^{\dagger}_{\sigma,k} b_{\sigma,k} \right\rangle \ . \tag{3.77}$$

These currents should be tracked individually in the experiment. The technique reported in Ref. [144] made feasible the proposed observation.

3.4.4 Laughlin's pump and topological order

The numerical observations described previously agree well with the properties of the CSL. Nevertheless, we have not yet done a direct verification, whether the *CSS* is indeed a CSL, or not. This subsection is dedicated to the verification of topological properties of the ground-state in the intermediate frustration regime of the frustrated XY model.

A. Ground-state degeneracy

We know that chiral spin liquids are characterized by a topological degeneracy in the thermodynamic limit on base manifolds with non-trivial topology. In our numerical simulations with periodic boundary conditions, the base manifold is the torus and has the genus $g = 1$. The Kalmeyer and Laughlin CSL state should thus be described by a topological degeneracy equal to $2^g = 2$. Since in the initial spin problem the symmetries R and T are not broken, we expect to observe the total number of 4 degenerate ground-states, with two degeneracies per chirality sector. Still, because of finite size effects, one only expects an approximate degeneracy in simulations.

In Fig. 3.14 we show the low-energy spectrum as a function of J_2/J_1. The ground-state always belongs to the sector $\boldsymbol{Q} = \boldsymbol{\Gamma}$. In the intermediate frustration regime, we observe the onset of a gapped doubly-degenerate ground-state manifold. The first excited state has the same momentum $\boldsymbol{Q} = \boldsymbol{\Gamma}$, but lies in the opposite sector of $\mathcal{R}$ [8]. This is different from the predictions for the CSL state, but it is unclear whether some degenerate states are mixed with the bulk or not. The first excited state also moves away in energy when the perturbations H_z and $H_{J_2'}$ are switched on, but for weak perturbations this is not noticeable.

[8] In numerical simulations for some particular ED clusters (*e.g.* the cluster of 4×4 unit cells with tilt $t_h = -1$) we can use the lattice reflection symmetry to perform an additional block-diagonalization of the Hamiltonian. In this case we observe two ground-states belong to different sectors of the symmetry.

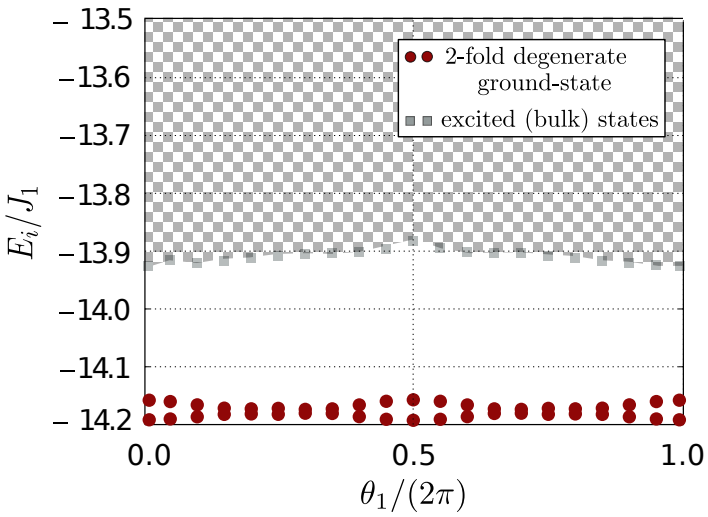

FIGURE 3.15: ED calculation of the low energy spectra as a function of the twist angle θ_1 for $J_2/J_1 = 0.3$ and $\theta_2 = 0$ on a lattice of 4×3 unit cells with no tilt. Parameters are for $J_2/J_1 = 0.3$, $h_z/J_1 = J_2'/J_1 = 0.02$.

B. Twisted boundary conditions

In order to have an unambiguous verification of the topological properties of the ground-state manifold we perform a measurement of the Berry curvature and the first Chern number. We first probe the robustness of the low energy quasi-degenerate state sector by performing Laughlin's Gedanken experiment [14, 56, 249] (see also Section 1.1). Numerically, this is achieved through the implementation of twisted boundary conditions defined as

$$\Phi\left(\boldsymbol{r} + L_1\boldsymbol{R}_1\right) = e^{i\theta_1}\Phi\left(\boldsymbol{r}\right), \quad \Phi\left(\boldsymbol{r} + L_2\boldsymbol{R}_2\right) = e^{i\theta_2}\Phi\left(\boldsymbol{r}\right) \ . \tag{3.78}$$

Here $\Phi\left(\boldsymbol{r}\right) = \langle \boldsymbol{r} \,|\, \Phi \rangle$ is the many-body ground-state wavefunction at the position $\boldsymbol{r}$. L_1 and L_2 are linear sizes of the cluster in the directions determined respectively by vectors $\boldsymbol{R}_1$ and $\boldsymbol{R}_2$. Angular parameters θ_1 and θ_2 are the phases of twisted boundary conditions. Physically, this corresponds to an insertion of two fluxes θ_1 and θ_2 through two topologically distinct loops of the torus [9]. Using the tight-binding language, this can be accomplished by replacing the hopping interactions of the Hamiltonian. One could replace all the hoppings from one cluster to another by the hoppings with the same amplitudes, but multiplied by an additional phase factor, that depends on θ_1 and θ_2 and verifies Eq. (3.78). For example the NNN hopping interaction of the XY model would be modified as

$$J_2 S^+_{L_1\boldsymbol{R}_1+v_3} S^-_{L_1\boldsymbol{R}_1} \rightarrow e^{i\theta_1} J_2 S^+_{L_1\boldsymbol{R}_1+v_3} S^-_{L_1\boldsymbol{R}_1} \ . \tag{3.79}$$

We want however to keep the translation invariance of the system. Hence, we redistribute these phases over all the hoppings in the translation symmetry preserving manner. In order to do this we introduce the vector $\boldsymbol{\theta}$ defined as

$$\boldsymbol{\theta} = \frac{1}{2\pi}\left(\frac{\theta_1}{L_1}\boldsymbol{Q}_1 + \frac{\theta_2}{L_2}\boldsymbol{Q}_2\right) \ , \tag{3.80}$$

[9] Clearly, inserting one flux quantum $\theta_i = 2\pi$ should not affect the physical properties of the system. The spectrum at $\theta_i = 2\pi$ should thus be identical to the spectrum at $\theta_i = 0$.

with $\boldsymbol{Q}_i$ – the reciprocal lattice vectors. Clearly, $L_i\boldsymbol{\theta}\cdot\boldsymbol{R}_i = \theta_i$, as required by Eq. (3.78). The terms of the Hamiltonian are transformed as

$$J_1 S^+_{\boldsymbol{r}_i+\boldsymbol{u}_i} S^-_{\boldsymbol{r}_i} \to e^{i\boldsymbol{\theta}\cdot\boldsymbol{u}_i} J_1 S^+_{\boldsymbol{r}_i+\boldsymbol{u}_i} S^-_{\boldsymbol{r}_i} \tag{3.81}$$

and

$$J_2 S^+_{\boldsymbol{r}_i+\boldsymbol{v}_i} S^-_{\boldsymbol{r}_i} \to e^{i\boldsymbol{\theta}\cdot\boldsymbol{v}_i} J_2 S^+_{\boldsymbol{r}_i+\boldsymbol{v}_i} S^-_{\boldsymbol{r}_i} \ . \tag{3.82}$$

The results of such flux insertion procedure in the *CSS* are showed in Fig. 3.15. We observe that the same states in the sector $\boldsymbol{Q} = \boldsymbol{\Gamma}$ are non-trivially gapped for all twists. For the pumping of a single flux quantum we could not observe a spectral flow in the ground-state manifold. This however does not imply that the manifold is topologically trivial, since both states are situated in the same symmetry sector [135, 250, 251].

We notice that two phases θ_i ($i = 1,2$) introduced in the spin language would correspond to four phases θ_i^σ in the language of bosons of the BKMH model, for which the spin component $\theta_i^\uparrow - \theta_i^\downarrow = \theta_i$ is fixed and the $U(1)$ component $\theta_i^\uparrow + \theta_i^\downarrow$ is free. This is also in agreement with the arguments of Fu and Kane [188], describing the presence of two possible flux insertion procedures in the Kane-Mele model: the one that couples to the spin degree of freedom, and the other one that is coupled to the density degree of freedom. Only the first one presents the interest to us.

C. Berry curvature and first Chern number

The topological nature of the ground-state manifold is unambiguously determined by calculating the Chern number [36, 252–254] defined as

$$Ch_1 = \frac{1}{2\pi}\int_0^{2\pi}\int_0^{2\pi} \mathcal{B}(\theta_1,\theta_2)\mathrm{d}\theta_1\mathrm{d}\theta_2 \ . \tag{3.83}$$

Here $B(\theta_1,\theta_2)$ is the Berry curvature [23] associated with the many-body wavefunction. Since the two quasi-degenerate ground-states lie in the same symmetry sector and cannot be separated unless twists are trivial (the reflection symmetry of the lattice can be used only when the twisted boundary condition phases θ_i are real), we cannot employ a simple formula of the Berry curvature introduced, for example, in Eq. (1.85). We need to compute the Berry curvature associated with the entire doubly-degenerate ground-state manifold. This can be done using the gauge-invariant non-abelian formulation [251, 255, 256]:

$$\mathcal{B}(\theta_1,\theta_2)\delta\theta_1\delta\theta_2 = \mathfrak{Im}\ln\mathfrak{Det}\left(\mathcal{M}(\theta_1,\theta_2)\right) \ , \tag{3.84}$$

where elements of the matrix $\mathcal{M}$ are obtained as follows:

$$\begin{aligned}\mathcal{M}_{ij}(\theta_1,\theta_2) = &\left\langle \Phi_i(\theta_1,\theta_2)\,\middle|\,\Phi_{\mu_1}(\theta_1+\delta\theta_1,\theta_2)\right\rangle\\ &\times\left\langle \Phi_{\mu_1}(\theta_1+\delta\theta_1,\theta_2)\,\middle|\,\Phi_{\mu_2}(\theta_1+\delta\theta_1,\theta_2+\delta\theta_2)\right\rangle\\ &\times\left\langle \Phi_{\mu_2}(\theta_1+\delta\theta_1,\theta_2+\delta\theta_2)\,\middle|\,\Phi_{\mu_3}(\theta_1,\theta_2+\delta\theta_2)\right\rangle\\ &\times\left\langle \Phi_{\mu_3}(\theta_1,\theta_2+\delta\theta_2)\,\middle|\,\Phi_j(\theta_1,\theta_2)\right\rangle \ .\end{aligned} \tag{3.85}$$

Here $\delta\theta_1$ and $\delta\theta_2$ refer to the numerical mesh along the θ_1 and θ_2. $i,j,\mu_i = 1,2$ are indices of states $|\Phi_1\rangle$ and $|\Phi_2\rangle$ in the ground-state manifold and the summation over μ_i is implicit.

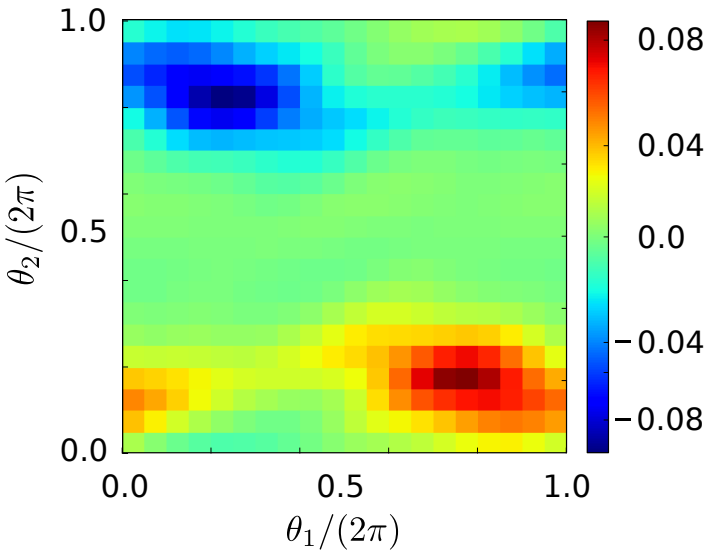

FIGURE 3.16: ED calculation of the Berry curvature associated with the degenerate ground-state manifold. The calculation is performed using the non-abelian formalism and results in a vanishing first Chern number. The parameters are $J_2/J_1 = 0.3$, $h_z/J_1 = J_2'/J_1 = 0.02$, and the ED cluster is 4×3, with no tilt.

In Fig. 3.16, we show a typical shape of the Berry curvature. We find that the first Chern number is zero in the intermediate frustration regime. As a result of the explicit time-reversal symmetry breaking, the Berry curvature is non-zero, but it vanishes in average over the first BZ. The points, where the variation of the Berry curvature is the most significant correspond to the values of θ_i, for which two states of the ground-state manifold are very close to each other energetically. This result suggests that the intermediate phase in the frustrated XY model is most likely to be a *CSS* with no topological order, as suggested in Refs. [205–207], and not the Kalmeyer-Laughlin state, with gauge fluctuations beyond the mean-field solution making the phase topologically trivial as in the fermionic Kane-Mele model [79, 190–196]. We notice however that the nature of the *CSS* is still unexpected and has no classical counterpart: we observe two spontaneously broken symmetry and a formation of the Ising antiferromagnetic order.

Chapter 4

Quantum simulator engineering and probing exotic states of matter

One of the main goals of this last chapter is to provide the reader with more details on quantum simulator realizations of the models we have already mentioned in Chapters 2 and 3. As an introduction, in Section 4.1 we give a short overview of the current development in the domain of quantum simulators. Then, we address in greater details the Floquet engineering concept. It unifies several ideas related to the effective generation of desired models, based on the application of periodic time-dependent protocols and a theory to solve the associated problems, called Floquet theory. In Section 4.2 we show how a general time-dependent problem can be simplified using Floquet theory and how Floquet engineering can be performed based on the high-frequency expansion. Then, in Section 4.3 we describe how periodic time-dependent perturbations can be used to engineer artificial gauge fields, required to observe the exotic phenomena we studied in Chapters 2 and 3. We consider two particular examples of quantum simulators – ultra-cold atoms in optical lattices and photonic circuits. The protocol for the photonic lattices is based on our work, that has already been reported in Ref. [1].

Finally, in the last two sections of this chapter we describe our proposals of two particular protocols that could be employed to study quantum systems experimentally. In Section 4.4 we show, how one could realize the Su-Schrieffer-Heeger model with *LC* circuits, and how out-of equilibrium probes can be used to explore its topological properties. The results of this section are based on Ref. [4]. In Section 4.5 we propose a novel protocol to explore the spectral properties of quantum systems based on the purification idea. This protocol could be employed both in quantum simulators and in numerical simulations, and the main results have been presented in Ref. [5].

Contents of the chapter

4.1 Quantum simulators . . . 114
A. Ultra-cold atoms . . . 115
B. Photonic circuits . . . 115
4.2 Periodically driven systems . . . 116
4.2.1 Floquet theory . . . 116
A. Floquet Hamiltonian . . . 117
B. Effective Hamiltonian . . . 118
4.2.2 High-frequency approximations . . . 119
A. Magnus expansion . . . 120
B. Degenerate perturbative expansion . . . 120

4.2.3 The role of interactions . . . 121
4.3 Floquet engineering of artificial gauge fields . . . 121
4.3.1 Ultra-cold atoms . . . 122
4.3.2 Photonic lattices . . . 124
A. Magnetic fields under a resonance condition . . . 124
B. NNN hoppings using Floquet theory . . . 125
C. Higher order terms . . . 126
4.3.3 Numerical verification . . . 127
4.4 Dynamical probe of the Zak phase in the photonic SSH model . . . 131
4.4.1 SSH model . . . 131
4.4.2 Circuit model . . . 132
4.4.3 Measuring the Zak phase . . . 134
4.5 Purification spectroscopy protocol . . . 137
4.5.1 Purification spectroscopy . . . 137
A. Numerical simulations at finite temperature . . . 137
B. Purification spectroscopy . . . 138
C. Numerical verification . . . 139
4.5.2 Experimental proposal . . . 139
4.5.3 Fock state spectroscopy and many-body localization . . . 141

4.1 Quantum simulators

Understanding and exploring quantum systems is known to be a hard problem, both from the theoretical and numerical sides. One of the main reasons of such complexity originates from the size of the Hilbert space, that increases exponentially with the system size. Moreover, in the regime of strong interactions, when no small parameters are available to perform perturbative calculations, the models with no exact solutions require inventing sophisticated analytical and numerical techniques, and the obtained results are often disputable. In the domain of condensed matter, the phenomena related to the presence of strong interactions are in the process of an active exploration at the current moment. For example, the physics of high-temperature superconductors [95] is still unclear. From another perspective, new exotic phenomena related to the inability of some interacting disordered quantum states to thermalize, were discovered under the name of a many-body localization [257–259]. Recently, a lot of attention has also been dedicated to exploring the effect of interactions on topological states of matter, whose properties are protected by symmetries (SPT states) or an intrinsic structure of the system (topologically ordered states) [77, 78]. The latter category includes the FQH states and some quantum spin liquids.

In the context described above, an important role is played by the experimental verification of predicted analytical and numerical results. Finding and making real materials or composite structures that have desired properties or are expected to describe a particular model of interests is one of the most important goals of the modern condensed matter physics. However, conventional solid-state protocols suffer from a limited number of possible experimental probes: one usually cannot do more than calculating the response functions to some external perturbations and thermodynamic properties, or performing scattering and spectroscopy measurements (to determine, for example, the lattice structure or the energy and momentum of electronic excitations of a material). Moreover, solid-state systems are often not controllable enough: each complicated experimental measurement corresponds to a single

point / line in the phase diagram [1]. Hence, in order to explore the rest one should make a new material. It is thus crucial to have an alternative tool to probe the physics of quantum systems, that does not suffer from the above limitations. Such a tool is provided by means of quantum simulators.

Quantum simulator is a problem-specific version of a quantum computer proposed by Feynman in 1982 [260] [2]. They are intended to mimic the evolution of other quantum systems and allow for more advanced experimental probes, with a significantly improved degree of control and high-resolution detection techniques. Such systems are also highly tunable. Several physical platforms can be used for these goals. In particular, quantum simulators based on ultra-cold atoms in optical lattices [261–264], Rydberg atoms [265], trapped ions [266], polar molecules [267], photonic lattices [3, 268–270] have been proposed and constructed in practice. We invite the readers interested in this topic to look at the following excellent review articles [271, 272].

The quantum simulator setups we have been paying a particular attention to in this work, are photonic circuits and ultra-cold atoms. In the last part of this introductory section we will describe in more details these two approaches for quantum simulations.

A. Ultra-cold atoms

In ultra-cold atom setups, neutral atoms are cooled down and trapped in periodic potentials created by interfering laser beams [261–264]. Atoms in such optical lattices are simulating the behavior of electrons in solid crystals. These systems are however even more advantageous, since the atoms charged into the lattice can be either fermionic or bosonic. Various geometries and dimensionalities of the lattices can be realized by changing the shape of optical potentials. The tunability of the lattice also allows to change the kinetic potential by adapting the lattice depth, and the interaction strength via Feshbach resonances [273]. Moreover, recent developments in the domain even allow for a single-site and single-atom resolved measurements and control [274].

B. Photonic circuits

Photonic systems can be realized using arrays (circuits) of coupled cavities [3, 268–270]. As compared to ultra-cold atom setups, the excitations in such systems are bosonic circuit excitations rather than real particles, and are sometimes referred to as "photons". The physical realization of the cavities is achieved using Josephson junction based superconducting qubits, or even simple RLC resonators. The coupling between different cavities is realized between neighbors using mutual capacitance, inductance or Josephson junctions, or at long distances by means of a finite-section transmission line playing the role of a Fabry-Perot cavity. When the coupling between cavities is much smaller than their internal frequencies, the problem is simplified. An effective description in terms of hopping terms of photons between different sites can then be used. The coupling strength between cavities can be tuned

[1] With few exceptions, when the pressure or magnetic field can be used to affect the relevant degrees of freedom.

[2] This type of simulations is called analog quantum simulation, as opposed to the more universal digital quantum computing. Digital quantum simulators however also have some disadvantages, such as a smaller tolerance to errors and the necessity to apply a time-ordered sequence of single and two-qubit gates. This implies that the number of Hamiltonians which can be made using a digital simulator is limited.

by adjusting some external parameters, such as the magnetic field. Moreover, non-linearity of the cavities (*e.g.* due to the qubit confining potential) could be used to generate interaction between photons. We also notice that such systems usually work in the dissipative–driven regime and allow to study non-equilibrium steady states rather than equilibrium properties.

4.2 Periodically driven systems

As we have seen previously in Chapters 2 and 3, engineering gauge fields in quantum simulators allows for the exploration of the interplay between topology and strong interactions. In particular, one could effectively realize models for quantum Hall effects. In the bosonic version of the Haldane model such protocols would also allow to probe the physics of finite-momentum BECs. In the strong interaction regime of the bosonic version of the Kane-Mele model one could study effectively the physics of the frustrated spin-1/2 XY model on the honeycomb lattice. However, photonic systems and optical lattices are based on neutral particles, which do not feel the Lorentz force. Gauge fields in such systems have thus to be generated artificially.

Numerous experimental realizations of artificial gauge fields or effective interactions in quantum simulator setups are based on the application of external periodic time-dependent perturbations. While in general time-dependent problems are impossible to solve exactly, the periodicity of the time-dependency leads to significant simplifications. In particular, Floquet theory [275–277] can be used to solve this type of problems. According to Floquet theory, the dynamics of periodically driven systems can be decomposed into two different contributions corresponding to a "slow" and "fast" time-evolution. This rapidity should be compared to the frequency of the perturbation. The slow part of the dynamics is simply described in terms of a time-independent effective (Floquet) Hamiltonian, while the fast contribution can be sometimes completely neglected. Generally, an exact expression of the Floquet Hamiltonian is however not accessible and one should rely on approximations. Under the assumption of very fast perturbation (as compared to all other energy scales of the problem), high-frequency expansions can be considered. Different high-frequency approximations include the Magnus expansion [278–280] and alternative approaches [281–284] (see also Refs. [285–288] for a general review).

In this section we want to make a short overview of the quantum-mechanical re-interpretation of Floquet theory. First, we will show the Floquet solution of a periodic time-dependent problem, and an alternative approach, that can be used to map the initial dynamical problem onto a static problem on an enlarged Hilbert space. This second approach also provides an intuitive physical picture of the matter coupled to an effective photon-like mode. Next, we will describe how one can use high-frequency approximations to solve both initial time-dependent and effective static problems. Finally, we will discuss the validity of the high-frequency approximations and the main difficulties that arise when the many-body effects are taken into account.

4.2.1 Floquet theory

First, we will explain the basic ideas of the Floquet theory. Let us start by considering a quantum system described by a periodic time-dependent Hamiltonian

$$H(t) = H_0 + V(t), \quad V(t) = V(t+T)\,. \tag{4.1}$$

This Hamiltonian comprises a constant term H_0 and a periodical drive term $V(t)$, with $T = 2\pi/\omega$ – the period of the driving cycle. In the following it will be convenient to use the Fourier decomposition of $V(t)$:

$$V(t) = \sum_j V^{(j)} e^{-ij\omega t} \ . \tag{4.2}$$

According to Floquet's theorem, the quantum-mechanical system described by Eq. (4.1) possesses solutions $|\psi_n(t)\rangle$ of the form

$$|\psi_n(t)\rangle = e^{-i\epsilon_n t} |u_n(t)\rangle \ . \tag{4.3}$$

Such states $|\psi_n(t)\rangle$ are called Floquet states, and $\epsilon_n \in \mathbb{R}$ are associated static quasienergies. The states $|u_n(t)\rangle$ are called Floquet modes. In the same way Bloch waves are periodic in real space, Floquet modes are periodic in time [275]:

$$|u_n(t)\rangle = |u_n(t+T)\rangle \ . \tag{4.4}$$

One could then rewrite the Schroedinger equation using Floquet modes in the following manner

$$Q(t) |u_n(t)\rangle = (H(t) - i\mathrm{d}_t) |u_n(t)\rangle = \epsilon_n |u_n(t)\rangle \ . \tag{4.5}$$

The operator $Q(t)$ appearing in the expression above is called a **quasienergy operator** and will play an important role in the following.

A. Floquet Hamiltonian

At any time t the Floquet states $|\psi_n(t)\rangle$ can be set to form a complete orthonormal basis. Thus, the time-evolution operator $U(t,t')$ can be written as

$$U(t,t') = \sum_n e^{-i\epsilon_n(t'-t)} \left|u_n(t')\right\rangle \langle u_n(t)| \ . \tag{4.6}$$

We notice that the above expression becomes simpler when we are interested in the stroboscopic evolution only (*i.e.* when $t' = t + mT$ for some $m \in \mathbb{Z}$):

$$U(t,t+mT) = \sum_n e^{-i\epsilon_n mT} |u_n(t)\rangle \langle u_n(t)| \ . \tag{4.7}$$

This makes explicit one of the key properties of periodically driven systems, which is the separation of the dynamics onto two contributions: a "fast" (as compared to the driving period T) micro-motion described by operator

$$K(t,t') = \sum_n \left|u_n(t')\right\rangle \langle u_n(t)| \ , \tag{4.8}$$

and "slow" long-time dynamics described by quasienergies ϵ_n. This second contribution is often interpreted in terms of an evolution under a static Floquet Hamiltonian $H_F[t_0]$:

$$H_F[t_0] = \sum_n \epsilon_n |u_n(t_0)\rangle \langle u_n(t_0)| \ . \tag{4.9}$$

If we are interested in the long-time or stroboscopic dynamics only, the knowledge of the Floquet Hamiltonian provides all the required information. Thus, the problem

simplifies to finding quasienergies ϵ_n and the set of Floquet modes $|u_n(t_0)\rangle$ for a particular time t_0. This could be done, for example, by diagonalizing the time-evolution operator from Eq. (4.6) over one driving period. We will show how such calculation is achieved using the high-frequency expansion in Section 4.2.2. We also notice the dependency of the Floquet Hamiltonian on the time t_0. This parameter should be understood as the time when the evolution started. Performing the change $t_0 \to t_1$ in the Floquet Hamiltonian is achieved by multiplying $H_F[t_0]$ by two micro-motion operators $K(t_0, t_1)$ and $K(t_1, t_0)$.

B. Effective Hamiltonian

Inspired by Refs. [286, 288] (for more detailed calculations and some proofs, please see these very good reviews as well as [285] and [287]) we want to make an alternative re-formulation of the Floquet problem in quantum mechanics, provided with a clear physical interpretation. In order to proceed, we notice that adding an additional term $\omega = 2\pi/T$ to the quasienergy ϵ_n leaves unchanged the phase factor $\exp(-i\epsilon_n mT)$, that describes the time evolution over an integer number of periods. Hence, quasienergies ϵ_n and Floquet modes $|u_n(t)\rangle$ are not uniquely defined. One can resolve this ambiguity by imposing quasienergies to lie in the Floquet Brillouin zone: $-\omega/2 < \epsilon_n \leq \omega/2$. Then, one can label all other possible choices by introducing an additional index m:

$$\epsilon_{nm} = \epsilon_n + m\omega, \quad |u_{nm}(t)\rangle = e^{im\omega t} |u_n(t)\rangle \ . \tag{4.10}$$

The stationary solutions are invariant under such transformation:

$$|\psi_n(t)\rangle = e^{-i\epsilon_n t} |u_n(t)\rangle = e^{-i\epsilon_{nm} t} |u_{nm}(t)\rangle \ . \tag{4.11}$$

We use this rewriting to interpret the out-of-equilibrium problem we had initially as a new static eigenvalue problem in an extended Floquet Hilbert space defined as a direct product

$$\mathcal{FS} = \mathcal{HS} \bigotimes \mathcal{L}_T \ . \tag{4.12}$$

Here $\mathcal{HS}$ is the original quantum Hilbert space, and $\mathcal{L}_T$ – the space of square-integrable T-periodic time-dependent functions. A complete orthonormal basis $\{|\alpha; m\rangle\rangle\}$ of states of $\mathcal{FS}$ can be constructed by combining a basis $\{|\alpha\rangle\}$ of $\mathcal{HS}$ and a basis of T-periodic time-dependent functions $e^{im\omega t}$ labeled by the index m:

$$|\alpha; m\rangle\rangle = e^{im\omega t} |\alpha\rangle \ . \tag{4.13}$$

The scalar product in the extended Hilbert space is defined as

$$\langle\langle \alpha; m \,|\, \alpha'; m' \rangle\rangle = \frac{1}{T} \int_0^T \mathrm{d}t \, \langle \alpha \,|\, \alpha' \rangle \, e^{i(m'-m)\omega t} = \langle \alpha \,|\, \alpha' \rangle \, \delta_{m,m'} \ . \tag{4.14}$$

The quasienergy operator Q expressed in this basis has a block structure:

$$\langle\langle \alpha; m \,|\, Q \,|\, \alpha'; m' \rangle\rangle = m\omega \delta_{m,m'} \delta_{\alpha,\alpha'} + \langle \alpha \,|\, H_0 \,|\, \alpha' \rangle \, \delta_{m,m'} + \left\langle \alpha \,\middle|\, V^{(m-m')} \,\middle|\, \alpha' \right\rangle \ . \tag{4.15}$$

The resulting problem is equivalent to a problem of the matter coupled to a single photonic mode. The photon sectors are labeled by the index m and located around the energy levels $\{m\omega\}$. The width of each sector is determined by H_0, and different

sectors m and m' are coupled via the $V^{(m-m')}$ terms. The overall structure of the operator Q in the basis of states $\{|\alpha; m\rangle\rangle\}$ is shown in the equation below

$$Q = \left(\begin{array}{c|c|c|c|c|c} \ddots & & & & & \\ \hline & H_0 - 2\omega I & V^{(1)} & V^{(2)} & V^{(3)} & \\ \hline & V^{(-1)} & H_0 - \omega I & V^{(1)} & V^{(2)} & \\ \hline & V^{(-2)} & V^{(-1)} & H_0 & V^{(1)} & \\ \hline & V^{(-3)} & V^{(-2)} & V^{(-1)} & H_0 + \omega I & \\ \hline & & & & & \ddots \end{array}\right) . \tag{4.16}$$

The problem of finding an effective time-independent Hamiltonian H_{eff} describing the long-time dynamics of the system transforms into a problem of block-diagonalizing the quasienergy operator Q, *i.e.* rewriting Eq. (4.16) in the following form

$$Q_{\text{eff}} = \left(\begin{array}{c|c|c|c|c|c} \ddots & & & & & \\ \hline & H_{\text{eff}} - 2\omega I & & & & \\ \hline & & H_{\text{eff}} - \omega I & & & \\ \hline & & & H_{\text{eff}} & & \\ \hline & & & & H_{\text{eff}} + \omega I & \\ \hline & & & & & \ddots \end{array}\right) , \tag{4.17}$$

by applying a unitary transformation

$$Q_{\text{eff}} = U_{\text{eff}}^{\dagger} Q U_{\text{eff}} . \tag{4.18}$$

Solving the eigenvalue problem then results in finding quasienergies ϵ_{nm} and Floquet modes $|u_{nm}(t)\rangle = |u_n; m\rangle\rangle$. We notice that this approach also allows to get rid of the dependency of the Floquet Hamiltonian $H_F[t_0]$ on the launching time t_0 (the time variable appears nowhere in the eigenvalue problem (4.15)). The Floquet Hamiltonian $H_F[t_0]$ is related to the effective Hamiltonian H_{eff} by means of another unitary transformation $U_F(t_0)$:

$$H_F[t_0] = U_F(t_0) H_{\text{eff}} U_F^{\dagger}(t_0) . \tag{4.19}$$

As a consequence, the spectrum of the two Hamiltonians has to be identical. This transformation is also used to calculate the micro-motion operator:

$$K(t, t') = U_F(t) U_F^{\dagger}(t') . \tag{4.20}$$

4.2.2 High-frequency approximations

Calculating the Floquet Hamiltonian $H_F[t_0]$ or the effective Hamiltonian H_{eff} is a challenging task and in majority of cases can not be performed exactly. As a consequence, approximated calculations have to be employed. One possibility consists in using the high-frequency expansion (HFE). In this approximation we suppose that the frequency ω is the biggest energy scale of the system and we use the $1/\omega$ power expansion.

A. Magnus expansion

The HFE used to get the Floquet Hamiltonian is known as the Magnus expansion [278, 279]. The Floquet theorem allows us to write exactly

$$U(t_0, t_0+T) = \mathcal{T}\exp\left(-i\int_{t_0}^{t_0+T} H(t)\mathrm{d}t\right) = \exp\left(-iTH_F[t_0]\right) \ . \tag{4.21}$$

Here $\mathcal{T}$ denotes the time ordering, and in the middle expression we recover the general form of the time-evolution operator under any arbitrary time-dependent Hamiltonian. We then perform the expansion of the Floquet Hamiltonian in powers of $1/\omega$

$$H_F[t_0] = H_0 + \sum_{n=1}^{\infty} \frac{1}{\omega^n} H_F^{(n)}[t_0] \ . \tag{4.22}$$

By performing the same power expansion for the middle expression of Eq. (4.21) and taking the *log*, we write the identity term by term. This allows us to deduce each of the terms $H_F^{(n)}[t_0]$ separately. The first two terms in the expansion are written in the following way

$$\begin{aligned} H_F^{(1)}[t_0] &= -\frac{i}{2}\frac{2\pi}{T}\int_{t_0}^{t_0+T}\int_{t_0}^{t_1}[H(t_1), H(t_2)]\,\mathrm{d}t_1\mathrm{d}t_2 \\ H_F^{(2)}[t_0] &= -\frac{1}{6}\left(\frac{2\pi}{T}\right)^2\int_{t_0}^{t_0+T}\int_{t_0}^{t_1}\int_{t_0}^{t_2}\Big([H(t_1),[H(t_2),H(t_3)]]+[H(t_3),[H(t_2),H(t_1)]]\Big)\mathrm{d}t_1\mathrm{d}t_2\mathrm{d}t_3 \ . \end{aligned} \tag{4.23}$$

B. Degenerate perturbative expansion

In a similar manner, the perturbative expansion can be used to calculate the effective Hamiltonian [280–286]. In the photon picture, this approximation can be understood in the following way: each photon sector is separated from others via a spectral gap of the order of ω. This spectral gap is supposed to be much larger than the inter-sector couplings described by terms $V^{(m-m')}$, and the spectral width of each sector described by H_0. Then, the degenerate perturbative expansion can be used to diagonalize the quasienergy operator in Eq. (4.15) leading to

$$H_{\text{eff}} = H_0 + \sum_{n=1}^{\infty}\frac{1}{\omega^n}H_{\text{eff}}^{(n)} \ . \tag{4.24}$$

The leading terms in the HFE are expressed as follows:

$$\begin{aligned} H_{\text{eff}}^{(1)} =& \frac{1}{\omega}\sum_{j=1}^{\infty}\frac{1}{j}\left[V^{(j)}, V^{(-j)}\right] \ , \\ H_{\text{eff}}^{(2)} =& \frac{1}{2\omega^2}\sum_{j=1}^{\infty}\frac{1}{j^2}\left(\left[\left[V^{(j)}, H_0\right], V^{(-j)}\right] + \text{h.c.}\right) + \\ &+\frac{1}{3\omega^2}\sum_{j,l=1}^{\infty}\frac{1}{jl}\left(\left[V^{(j)}, \left[V^{(l)}, V^{(-j-l)}\right]\right] - 2\left[V^{(j)}, \left[V^{(-l)}, V^{(-j+l)}\right]\right] + \text{h.c.}\right) \ . \end{aligned} \tag{4.25}$$

The spectrum of the two Hamiltonians is identical up to a next order term in the HFE, *i.e.* for the calculation at the order n the error will be of the order $\mathcal{O}(1/\omega^{n+1})$.

4.2.3 The role of interactions

The situation described above becomes more complicated when interactions are taken into account. The difficulties arise even if the width of the single-particle spectrum and the energy scales associated with the parameters of the unperturbed Hamiltonian H_0 are small compared to the periodic driving frequency ω [285–288]. The main reason is that the spectral width associated with the unperturbed Hamiltonian could be macroscopically big as a result of the collective many-body excitations. Hence, the main argument supporting the validity of the high-frequency expansion does not hold, since ω is not the largest energy scale of the system anymore.

In general, it is not known whether the perturbative high-frequency expansions are asymptotic or have a finite radius of convergence. The question on the convergence of the series and, as a result, the existence of the effective and Floquet Hamiltonians, is also intrinsically related to the problem of heating in periodically driven systems [289–294]. Clearly, during the periodic drive the energy of the system is not conserved. A system will thus absorb the energy and, if this process is not bounded, heat up to an infinite temperature [3]. The existence of the Floquet Hamiltonian corresponds to a localization process and the presence of a bound to the energy absorption. The exact behavior of a system depends strongly on its other properties. For example, exactly solvable and integrable systems have been shown to have a finite radius of convergence for high-frequency expansions [295–297]. Many-body localized systems are also good candidates to overcome the problem of heating [298–301].

Hopefully, even if the actual series is diverging, when the energy scales associated with the parameters of the unperturbed Hamiltonian are small, the probability to create high-energy many-body excitations has to be small as well. Hence, the heating will occur at time long enough, so that the truncation of the high-frequency expansion to a given order will still be suitable to describe the short-time dynamics of the system. In this context, the important question is whether there exists an emergent time-scale, that separates the desired dynamics described by an effective / Floquet Hamiltonian, from the region of an undesired heating. While this question still remains open, some recent works suggest that such a region of pre-thermalization exists and could be employed in practice [281, 302–307].

Finally, an alternative way to solve the problem of heating is to consider an open Floquet system. The main idea consists in forcing the state at long time to reach a stationary non-equilibrium steady state by coupling the systems to a thermal bath [308–312].

4.3 Floquet engineering of artificial gauge fields

In the previous section, we have briefly presented Floquet theory and the associated HFE, as well as the idea of how they can be used to solve the periodic time-dependent quantum-mechanical problems. Today a lot of interest is dedicated to "Floquet engineering" [285–288, 313]. It consists in generating an effective / Floquet

[3] We suppose for instance that the system is isolated, *i.e.* not coupled to a bath. We notice also that the spectrum width of finite size systems is always bounded. Thus, the corresponding final state will not be an infinite-temperature state, but a high-energy steady state.

Hamiltonian with desired properties, starting from a more trivial one, by superimposing a periodic time-dependent perturbation. Using these approaches as well as a particularly chosen geometry allows one to design targeted Hamiltonians. In particular, many theoretical studies were done in order to investigate the possibility to obtain a Floquet topological (Chern) insulator from irradiated graphene structures [314–322], that was recently observed experimentally [323]. Similarly, even more exotic Floquet fractional Chern insulators have been proposed [324]. Driven superconducting wires were considered in order to observe Floquet Majorana zero modes [325–330]. More elaborated quantum wire protocols also suggest a possible generation of even more exotic parafermions [331] in 1D, and topological insulators in integer and fractional regimes in higher dimensions [332]. In ultra-cold atoms, a significant progress has been achieved with the experimental realization of the Haldane model [126] and a direct measurement of the Berry curvature in the graphene system [333]. The Haldane model was also realized experimentally in an array of coupled photonic waveguides [334].

In line with these references and as promised previously, in this section we describe in more details how one could perform "Floquet engineering" of artificial gauge fields for ultra-cold atoms and excitations in photonic lattices. These magnetic fields are one of key ingredients to create exotic states, such as finite-momentum BECs, or topological states. We first briefly discuss protocols to implement gauge fields in shaken optical lattices. Second, we propose an approach to perform an analogous procedure for excitations in photonic lattices. Because of the significant difference in physical realizations, two ways of generating gauge fields are not compatible. The two approaches that we discuss are also based on the application of the HFE. As we mentioned previously, this perturbative expansion is subtle, and its convergence is not always ensured. Hence, we present our numerical verification of the validity of the proposed protocol.

4.3.1 Ultra-cold atoms

In this subsection, we explain how artificial gauge fields have been realized experimentally with ultra-cold atoms in shaken optical lattices [126]. The effective static model realized in this way is the celebrated Haldane model [32], presented previously in Section 2.1 of this thesis. We start by considering the following time-dependent Hamiltonian defined on the honeycomb lattice

$$H = H_0 + V(t) = -t_1 \sum_{\langle i,j \rangle} c_i^\dagger c_j + \sum_i (\boldsymbol{F}(t) \cdot \boldsymbol{r}_i)\, c_i^\dagger c_i \,. \tag{4.26}$$

Here $c_i^\dagger (c_i)$ are creation (annihilation) operators at site i. The Hamiltonian comprises the term of NN hoppings with the amplitude t_1 and the modulated chemical potential describing the shaking of the lattice with the period $T = 2\pi/\omega$. The vector $\boldsymbol{F}(t) = -m\mathrm{d}^2\boldsymbol{R}(t)/\mathrm{d}t^2$ is an inertial force originating from the movement of the lattice along the periodic trajectory $\boldsymbol{R}(t)$. In the co-moving frame, *i.e.* under a unitary transformation

$$U = \exp\left(i \int_0^t V(\tau)\mathrm{d}\tau \right) = \exp\left(\sum_n i\,[\boldsymbol{q}(t) \cdot \boldsymbol{r}_n]\, c_n^\dagger c_n \right) \tag{4.27}$$

the Hamiltonian becomes

$$H' = UHU^\dagger + iU^\dagger \frac{\partial U}{\partial t} = -t_1 \sum_{\langle i,j \rangle} e^{i\boldsymbol{q}(t)\cdot(\boldsymbol{r}_i - \boldsymbol{r}_j)} c_i^\dagger c_j \,, \tag{4.28}$$

where $\boldsymbol{q}(t) = -m\mathrm{d}\boldsymbol{R}(t)/\mathrm{d}t$. We notice that the Hamiltonian (4.28) differs from the unperturbed one only by a renormalization factor of the hopping rates $\exp\left[i\boldsymbol{q}(t)\cdot(\boldsymbol{r}_i - \boldsymbol{r}_j)\right]$. The phases appearing in this factor are local: $\boldsymbol{r}_i - \boldsymbol{r}_j$ run over vectors $\boldsymbol{u}_j$ between three NN sites. As a consequence, H' has the same spatial periodicity as H_0.

Now, according to the notation of [126], we consider that the lattice is moving along the following elliptic trajectory:

$$\boldsymbol{R}(t) = -R\left[\cos(\omega t)\boldsymbol{e}_x + \cos(\omega t - \phi)\boldsymbol{e}_y\right] \,. \tag{4.29}$$

Here R describes the amplitude of the modulation, and ϕ is a phase factor. We define

$$\rho_{ij} e^{i\theta_{ij}} = (\boldsymbol{r}_i - \boldsymbol{r}_j)\cdot(\boldsymbol{e}_x + \boldsymbol{e}_y e^{-i\phi}), \quad z_{ij} = m\omega R \rho_{ij} \,. \tag{4.30}$$

This will lead to the following re-expression of the Hamiltonian

$$H' = -t_1 \sum_{\langle i,j \rangle} e^{iz_{ij}\sin(\omega t + \theta_{ij})} c_i^\dagger c_j \,. \tag{4.31}$$

We can then use the Jacobi–Anger expansion to expand the exponentials in series

$$e^{iz\sin(\theta)} = \sum_{n=-\infty}^{\infty} \mathcal{J}_n(z) e^{in\theta} \,, \tag{4.32}$$

so that the Hamiltonian can be simply written in terms of its Fourier modes

$$H'^{(n)} = -t_1 \sum_{\langle i,j \rangle} \mathcal{J}_n(z_{ij}) e^{in\theta_{ij}} c_i^\dagger c_j \,. \tag{4.33}$$

Here $\mathcal{J}_n$ is the n^{th}-order Bessel function of the first kind. Each harmonic of the modulated Hamiltonian can be diagonalized in $\boldsymbol{k}$-space. It can be simply expressed as

$$H'^{(n)} = d_\mu^{(n)}(\boldsymbol{k})\sigma^\mu \tag{4.34}$$

since the translation invariance is preserved and the Hamiltonian still describes a two-band system. Scalar terms $d_\mu^{(n)}(\boldsymbol{k})$ will however depend on the renormalized and dephased hopping amplitudes.

Finally, we assume that the HFE conditions are verified and that ω is the biggest energy scale of the problem. One can then use Eq. (4.25) to express the effective Hamiltonian H_{eff} and the effective functions $d_\mu^{\text{eff}}(\boldsymbol{k})$ at different orders of the perturbative expansion in powers of $1/\omega$. At the lowest order the effect of the modulation consists only in a renormalization of NN couplings according to the zeroth order Bessel functions. The first order contribution will generate new NNN couplings by adding a purely imaginary part to the hopping amplitudes, as required for the generation of an effective Haldane model. Interestingly, this effective model corresponds to an anisotropic version we considered in Sections 2.1.3 and 2.2, rather than the isotropic one. By choosing ω big enough, we can limit ourselves to this first order only. The goal of realizing an effective Haldane model is thus successfully accomplished.

4.3.2 Photonic lattices

Now, we will explain how a generation of artificial gauge fields can be accomplished using photonic circuit setups. We consider the system described by the Hamiltonian $H(t) = H_0 + V(t)$, defined on a bipartite lattice, with two sublattices labeled by A and B (we have in mind the honeycomb lattice, but everything could be generalized to an arbitrary bipartite lattice). The two terms of the Hamiltonian read

$$\begin{aligned} H_0 &= \omega_A \sum_{i\in A} a_i^\dagger a_i + \omega_B \sum_{j\in B} b_j^\dagger b_j - t_1 \sum_{\langle i,j\rangle} \left(a_i^\dagger b_j + b_j^\dagger a_i \right) , \\ V(t) &= V \sum_{\langle i,j\rangle} \cos(\omega t + \theta_{ij}) \left(a_i^\dagger b_j + b_j^\dagger a_i \right) . \end{aligned} \tag{4.35}$$

Here $a_i(b_j)$ are annihilation operators on site $i(j)$ of sublattice $A(B)$. $\omega_A(\omega_B)$ is an associated frequency of a photon (internal frequency of the cavity in the photonic lattice), playing the role of a chemical potential. Sublattices are coupled through a constant tunneling term t_1 and a time-dependent term V (which is periodic in time with period $T = 2\pi/\omega$) coupling nearest neighbors. In photonic systems, this consists in coupling the cavities with a DC and AC terms assuming that each of them has approximately the same length. $\theta_{ij} = -\theta_{ji}$ are scalar phases associated to each oriented link between sites i and j.

The laboratory frame realization of such Hamiltonian in the context of photonic lattices was proposed in Refs. [335, 336] based on classical RLC resonators or photonic crystals. It was also successfully implemented using superconducting qubits arranged in a triangular loop with pairwise couplings [337], based on earlier theoretical suggestions [338]. While the first setup can be implemented at room temperatures, the second one is perfectly suited to go further and explore the quantum many-body effects.

A. Magnetic fields under a resonance condition

First, let us explain how using the Hamiltonian (4.35) one can effectively generate artificial gauge fields based on the resonant condition. This approach does not allow to change the structure of the problem, *i.e.* add new terms to the effective Hamiltonian. In this particular case we consider the same method as the one proposed in Refs. [335–337]. In order to solve the Hamiltonian, we switch to the interaction picture defined by $U = \exp(iH_0 t)$, under which the Hamiltonian takes the following form:

$$H' = V \sum_{\langle i,j\rangle} \cos\left(\omega t + \theta_{ij}\right) \left(e^{i(\omega_A - \omega_B)t} a_i^\dagger b_j + e^{i(\omega_B - \omega_A)t} a_i b_j^\dagger \right) . \tag{4.36}$$

We suppose that the system is at resonance, meaning that $\omega = \omega_B - \omega_A$. We perform the rotating wave approximation (RWA) by claiming that the contribution of highly oscillating terms is averaged to zero. Hence, only the constant term remains:

$$H' = \frac{V}{2} \sum_{\langle i,j\rangle} \left(e^{-i\theta_{ij}} a_i b_j^\dagger + e^{i\theta_{ij}} a_i^\dagger b_j \right) . \tag{4.37}$$

In the last expression we recognize the tight-binding Hamiltonian for a system under an applied external magnetic field. All the hoppings have been renormalized by a phase factor. By carefully choosing the phases θ_{ij}, the exact form of the magnetic

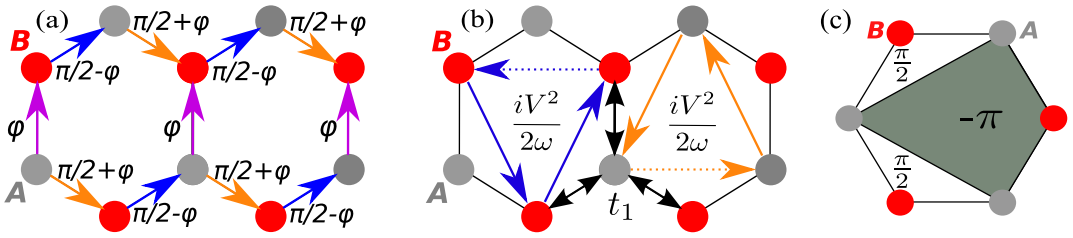

FIGURE 4.1: **(a)** Distribution of phases θ_{ij} on the NN bonds in the time-dependent Hamiltonian (4.35) required to generate an effective anisotropic Haldane model. The phase φ is a free parameter. We notice that the phases θ_{ij} only change the value of the NNN hopping amplitude and have no effect on the Haldane phase ϕ_H, that is always equal to $\pi/2$. **(b)** Anisotropic Haldane model. Colored bold lines represent NNN hoppings with amplitude modulus $V^2/(2\omega)$ assigning a phase $\pm\pi/2$ if they are made in the anticlockwise (clockwise) direction. Dotted lines correspond to the hopping absent in the model. **(c)** Magnetic flux distribution in the anisotropic Haldane model. The total magnetic flux through the unit cell sums up to zero, with closed loops of vector potentials involving kite geometries rather than triangles as in the isotropic case.

field can be tuned. However, as we said previously, the structure of the hoppings remains exactly the same.

B. NNN hoppings using Floquet theory

Second, we show how the system described by the Hamiltonian (4.35) can be used to generate an effective photonic Haldane model, similarly to Section 4.3.1. This approach is based on a different frequency regime of the photonic system: instead of having a resonance condition $\omega = \omega_B - \omega_A$, we require the system to be in the high-frequency regime $\omega \gg \omega_A, \omega_B, t_1$. Then, we apply the power expansion of Eq. (4.25) and write down the effective Hamiltonian H_{eff} in powers of $1/\omega$. The zero order contribution reads: $H_{\text{eff}}^{(0)} = H_0$. At order one, we obtain:

$$H_{\text{eff}}^{(1)} = \frac{iV^2}{2\omega} \sum_{\langle\langle i,k \rangle\rangle} \sin(\Theta_{ik}) \left(a_i^\dagger a_k - a_k^\dagger a_i \right) - \frac{iV^2}{2\omega} \sum_{\langle\langle j,l \rangle\rangle} \sin(\Theta_{jl}) \left(b_j^\dagger b_l - b_l^\dagger b_j \right) . \quad (4.38)$$

Here we have defined $\Theta_{ik} = \theta_{ij} + \theta_{jk}$ for each couple of NNN sites i and k, sharing both the same NN with the index j.

We see that terms in $H_{\text{eff}}^{(1)}$ are purely imaginary NNN hoppings whose amplitude $t_{2,ik}$ depends on the phases θ_{ij} and θ_{jk} on corresponding links:

$$t_{2,ik} = -\frac{V^2}{2\omega} \sin(\Theta_{ik}) . \quad (4.39)$$

The structure of hopping terms is changed, as compared to the Hamiltonin (4.37). The physical interpretation of this effect can be seen as follows: when the hopping mediated by the time-driving term is performed, the particle acquires an energy ω (particle absorbs the virtual "photon" using the picture from Section 4.2.1). Since this energy is huge, the corresponding state is highly unstable and the particle is forced to perform the conjugated NN hopping and re-emits the energy ω (re-emits the virtual photon), in agreement with the degenerate perturbative expansion. Since these hoppings are dephased in our model, this leads to the apparition of the effective phase acquired by the particle, resulting in the generation of an artificial gauge field.

In order to be able to solve the problem, one should consider a particular choice of the lattice geometry and of the phases θ_{ij}. By having in mind the idea of obtaining a topologically non-trivial model with non zero Chern number, we decided to explore the possibility of generating an effective Haldane model [32]. We thus consider the problem defined on the honeycomb lattice. Fig. 4.1(a) represents a possible choice of phases θ_{ij} that fulfills our requirement. The resulting term in the effective Hamiltonian corresponds to the anisotropic Haldane model with absent horizontal NNN hoppings and of amplitude $t_2 = V^2/2\omega$ for the four leftover NNN hoppings at each unit cell:

$$H_{\text{eff}}^{(1)} = -t_2\Big(\sum_{\langle\langle i,k\rangle\rangle}^{\text{anis}} e^{\pm i\pi/2} a_i^\dagger a_k + \sum_{\langle\langle j,l\rangle\rangle}^{\text{anis}} e^{\pm i\pi/2} b_j^\dagger b_l + \text{h.c.}\Big) \,. \tag{4.40}$$

In the above equation, we denoted the presence of the anisotropy by the label *anis* above the summation sign. The configuration of hopping amplitudes in the anisotropic model is also displayed on Fig. 4.1(b). The total magnetic flux through the unit cell of the lattice sums up to zero, so that Landau levels do not appear in the problem. However, the closed loops of vector potentials in this model involve kite geometries rather than triangles, as in the isotropic case (see Fig. 4.1(c)). We outline that phases θ_{ij} modify only the value of NNN hopping amplitudes and have no effect on the Haldane phase ϕ_H, that is always equal to $\pi/2$. We notice that this is exactly the model we considered in Sections 2.1.3 and 2.2. This is also similar in the ultra-cold atom protocol reported in Ref. [126], that we discussed in Section 4.3.1.

C. Higher order terms

In order to establish the condition on the HFE stability one needs to calculate the higher-order terms in the power expansion. This is the goal of this subsection. As before, using Eq. (4.25) we evaluate the second order contribution $H_{\text{eff}}^{(2)}$. It is easier to interpret separately different terms coming from two different components of H_0. We denote these terms as follows

$$H_{\text{eff}}^{(2)}\left[\omega_A,\omega_B\right] = \frac{1}{2\omega^2}\left[\left[V^{(1)},\omega_A\sum_i a_i^\dagger a_i + \omega_B\sum_j b_j^\dagger b_j\right],V^{(-1)}\right] + \text{h.c.} \tag{4.41}$$

$$H_{\text{eff}}^{(2)}\left[t_1\right] = -\frac{t_1}{2\omega^2}\left[\left[V^{(1)},\sum_{\langle i,j\rangle}\left(a_i^\dagger b_j + b_j^\dagger a_i\right)\right],V^{(-1)}\right] + \text{h.c.} \tag{4.42}$$

A straightforward calculation leads to

$$H_{\text{eff}}^{(2)}\left[\omega_A,\omega_B\right] = \frac{V^2}{2\omega}\left(\frac{\omega_B-\omega_A}{\omega}\right)\left[\sum_{\langle\langle i,k\rangle\rangle}\cos(\Theta_{ik})a_i^\dagger a_k - \sum_{\langle\langle j,l\rangle\rangle}\cos(\Theta_{jl})b_j^\dagger b_l + \text{h.c.}\right] . \tag{4.43}$$

In a similar way, we deduce that the second term is expressed as

$$H_{\text{eff}}^{(2)}\left[t_1\right] = \frac{V^2}{2\omega}\left(\frac{t_1}{\omega}\right)\left[3^{\text{rd}}\text{ order hoppings: NN and NNNN with complex amplitudes}\right] . \tag{4.44}$$

If we consider the phase choice depicted in Fig. 4.1(a), $H_{\text{eff}}^{(2)}\left[\omega_A,\omega_B\right]$ generates a Semenov mass term, while $H_{\text{eff}}^{(2)}\left[t_1\right]$ renormalizes the NN and generates new next-next nearest neighbor (NNNN) hopping terms. Such higher order hoppings can

be used to obtain a Chern insulator with the first Chern number greater than 1. The terms involving the perturbation strength V do not appear, since the time-dependent Hamiltonian (4.35) comprises only two different harmonics.

The second order terms in $H_{\text{eff}}^{(2)}$ can be neglected with respect to the first order contribution $H_{\text{eff}}^{(1)}$ in the limit $\omega \gg t_1, |\omega_B - \omega_A|, V$. We notice however, that the gap between two bands of the Haldane model is of the order of $|t_2| = V^2/(2\omega)$. In order to be able to observe the edge modes experimentally, this energy gap should be as big as possible. Hence, we would like to impose the value of the gap to be of the order of t_1

$$|t_2| = V^2/(2\omega) \sim t_1 \,. \tag{4.45}$$

This implies that the coupling strength V scales as $V \sim \sqrt{\omega t_1}$. The second order terms scale respectively as $(\omega_B - \omega_A)/\omega$ and t_1/ω. By further continuing this analysis, we deduce that higher order terms (we do not want to provide their exact expression because of its complexity) are expected to scale as

$$\frac{V^{2n-m_1-m_2}\left(\omega_A-\omega_B\right)^{m_1} t_1^{m_2}}{\omega^{2n-1}} \sim \frac{\left(\omega_A-\omega_B\right)^{m_1} t_1^{n+(m_2-m_1)/2}}{\omega^{n-1+(m_1+m_2)/2}} \,. \tag{4.46}$$

at odd orders of $1/\omega$, with $n \in [2,3,\dots]$, $m_1, m_2 \in \mathbb{N}$, and $m_1 + m_2$ necessarily even. For even orders of $1/\omega$ the expression is changed to

$$\frac{V^{2n+1-m_1-m_2}\left(\omega_A-\omega_B\right)^{m_1} t_1^{m_2}}{\omega^{2n}} \sim \frac{\left(\omega_A-\omega_B\right)^{m_1} t_1^{n+(m_2-m_1-1)/2}}{\omega^{n+(m_1+m_2-1)/2}} \,, \tag{4.47}$$

with $m_1 + m_2$ necessarily odd. In both cases the scaling factor is at worst $1/\omega$, and increases rapidly with n, *i.e.* for higher orders in the HFE [4]. All the corresponding terms thus go to zero when $\omega \to \infty$.

4.3.3 Numerical verification

As we have seen previously, the HFE is not ensured to converge even in relatively simple non-interacting cases. When interactions are taken into account, the situation usually becomes worse and the system heats up. The perturbative expansion is expected to be controllable for the approach proposed in Section 4.3.2, because all the higher order terms scale as $1/\omega$ or better. This remains valid even in the regime of a strong coupling strength V scaling as $V \sim \sqrt{\omega t_1}$. Nevertheless, in this subsection we want to estimate more quantitatively, which values of the modulation frequency ω are big enough, compared to t_1, so that we can neglect all second order contributions in the HFE. For clarity, we consider the case of $\omega_A = \omega_B$, such that the term $H_{\text{eff}}^{(2)}[\omega_A, \omega_B]$ is exactly zero.

We perform numerical simulations of the exact time-evolution in the model described by the Hamiltonian (4.35). We initially prepare the system in the state

$$|\Psi(t=0)\rangle = |\Psi_0\rangle \,, \tag{4.48}$$

and we use exact diagonalization (ED) to calculate states $|\Psi(t)\rangle$ and $|\Psi_{\text{eff}}(t)\rangle$ at time t, evolved with $H(t)$ and H_{eff} respectively. The latter Hamiltonian is calculated up to the first order in the HFE and thus corresponds to the Hamiltonian of the anisotropic

[4] In addition to two cases that we considered previously and that we dropped from the generalization **(i)** $n = 1$, $m_1 = 1$, $m_2 = 0$, **(ii)** $n = 1$, $m_1 = 0$, $m_2 = 1$, the scaling $1/\omega$ occurs only for **(iii)** $n = 2$, $m_1 = 0$, $m_2 = 0$.

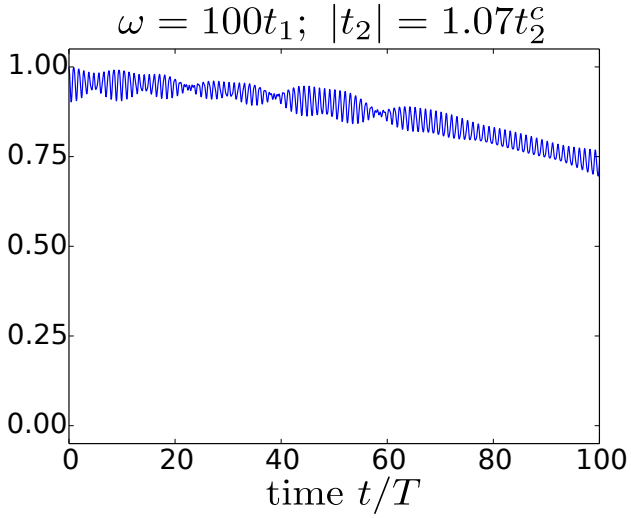

FIGURE 4.2: Numerical measurement of the fidelity $F(t) = |\langle\Psi(t)\,|\,\Psi_{\text{eff}}(t)\rangle|$ for the time evolution over 100 periods. Exact time-dependent evolution is performed for $V = \sqrt{2\omega t_2}$.

Haldane model. As long as two states propagate in time, they deviate one from the other. This deviation is captured by the "fidelity" $F(t)$ defined as the absolute value of the overlap between two states:

$$F(t) = |\langle\Psi(t)\,|\,\Psi_{\text{eff}}(t)\rangle| \ . \tag{4.49}$$

From the results of Sec. 2.2 in Chapter 4, we learned a particular value of the NNN hopping amplitude t_2, required to observe the *ZMSF–FMSF* phase transition. This value is

$$t_2^c = \sqrt{3/8}t_1 \ . \tag{4.50}$$

We can also calculate the critical value of the modulation amplitude V_c required to reach the transition at fixed frequency $\omega = 60t_1$. It is equal to $V_c \approx 8.57t_1$. To start with the calculations, we show in Fig. 4.2 the typical shape of the fidelity for the time evolution over 100 periods. The first important observation is related to the fast oscillation of $F(t)$, forming an envelop for its propagation in time. These oscillations are due to intra-periodic submotions of the system, not captured by H_{eff}, but described by micro-motion operators $K(t,t')$ (see for example Eq. (4.8)).

We observe that during the time evolution over an integer number of periods, the value of intra-periodic maxima of $F(t)$ decreases. This effect originates from higher order terms in the HFE. Errors due to neglected terms are accumulated during each period, leading to an exponential decrease of $F(t)$ with time. The total error becomes smaller when we increase the ratio ω/t_1 or decrease t_2/t_1. This effect is observed more quantitatively in Fig. 4.3(a-b), where we plot the fidelity for different values of parameters ω and t_2. For clarity, we do not show the entire time-evolution, but only the value of $F(t)$ at few stroboscopic times. In Fig. 4.3(c), we also plot the diagram of minima and local intra-periodic maxima of the fidelity, corresponding to the lowest position of the "envelop" of $F(t)$.

Another important point, not captured by Floquet theory and the HFE, which appears in simulations, is the fact that the time evolution with both effective and exact Hamiltonians depends on the initial state $|\Psi_0\rangle$. In our numerical simulations we consider three different types of initial states: the groundstate of the effective

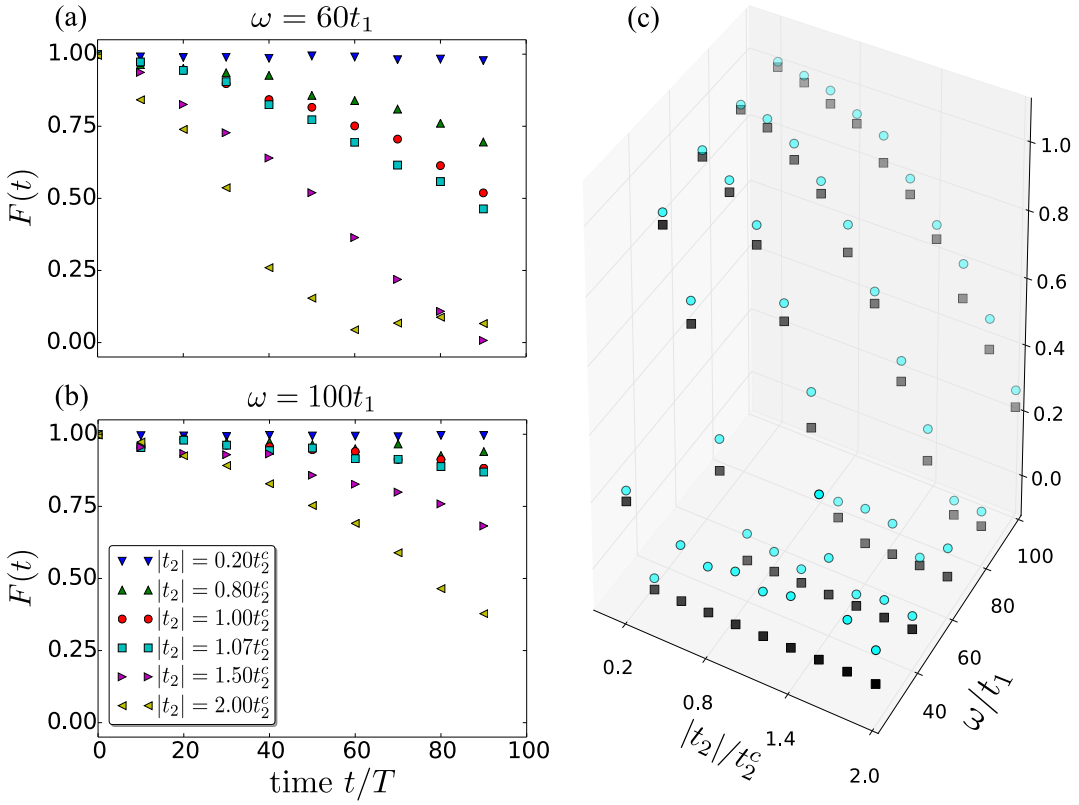

FIGURE 4.3: **(a-b)** Fidelity $F(t)$ shown for the time evolution over $T = 100$ periods for different values of t_2. **(c)** Diagram showing minima (black squares) and local maxima (blues circles) of $F(t)$ for different values of t_2 and ω. All simulations are performed with a randomly distributed initial state $|\Psi_{\text{rand}}\rangle$.

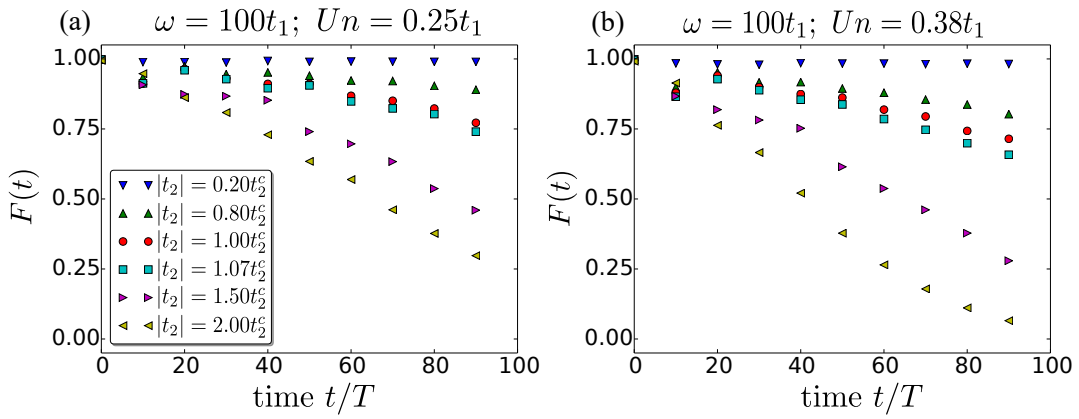

FIGURE 4.4: Fidelity $F(t)$ shown for the time evolution over $T = 100$ periods in the many-body case for several values of t_2. Parameters are $\omega = 100t_1$ and **(a)** $Un = 0.25t_1$, **(b)** $Un = 0.38t_1$, with n – the density of bosons.

Hamiltonian $|\mathrm{GS}_{\mathrm{eff}}\rangle$, the groundstate of the unperturbed Hamiltonian $|\mathrm{GS}_0\rangle$ and a state $|\Psi_{\mathrm{rand}}\rangle$ with a random wavefunction. All properties related to the fidelity, described above, are observed in the case of the state $|\Psi_{\mathrm{rand}}\rangle$. If we consider the state $|\mathrm{GS}_0\rangle$ instead, we do not observe any noticeable time-evolution. In the case of the state $|\mathrm{GS}_{\mathrm{eff}}\rangle$ in the regime when the minimum of the lowest band is not localized at point $\mathbf{\Gamma}$, we clearly observe intra-periodic sub-motions of the system. However, the envelop of $F(t)$ is located close to the maximum and does not decay with time. This can be interpreted in terms of the symmetry of these states with respect to Hamiltonians. For example, if the initial state is one of two eigenstates at momentum $\boldsymbol{k} = \mathbf{\Gamma}$, it will always stay an eigenstate of both effective, exact time-dependent and unperturbed Hamiltonians. Thus, we will not observe any evolution of the fidelity. This problem can be solved by adiabatically switching on the perturbation or considering more advanced and better optimized time-dependent protocols.

In Section 2.2 we have seen that the effect of interactions in the bosonic Haldane model can lead to some non-trivial physics. Motivated by these results, and in order to explore in more details the problems that arise in periodically modulated many-body systems, discussed in Section 4.2.3, we perform similar numerical tests for fidelities of the HFE in the interacting bosonic case. We consider an additional term of the Bose-Hubbard type

$$H_{\mathrm{BH}} = \frac{U}{2}\sum_i \left[a_i^\dagger a_i \left(a_i^\dagger a_i - 1\right) + b_i^\dagger b_i \left(b_i^\dagger b_i - 1\right)\right] . \tag{4.51}$$

We are particularly interested in how the convergence of the HFE is modified by such Bose-Hubbard interactions. In Fig. 4.4 we plot $F(t)$ for two different values of Un, with $n = N/N_s$ – the density of bosons. Here N is the total number of particles, and N_s – the total number of sites. We restrict the maximal number of bosons per site to 2, and we work on a lattice of 6×2 unit cells (24 sites) with tilt $t_h = -5$. We see that the effect of U leads to a faster decay of the fidelity. However, we still observe that at times short enough the perturbative expansion remains valid.

4.4 Dynamical probe of the Zak phase in the photonic SSH model

Previously in this chapter we have seen, how one could use time-dependent perturbations to generate exotic states of matter, based in particular on the implementation of artificial gauge fields in ultra-cold atoms and photonic circuit setups. In this section we want to make a step aside and consider in greater details a particular quantum circuit setup. The idea of this setup is to realize a Su-Schrieffer-Heeger (SSH) model [27, 28] with *LC* circuits. The SSH model is one of the simplest models to understand the topological phase transitions in 1D. Hence, its experimental realization is the first step to explore more elaborated topological states of matter. However, in the following we will be particularly interested in studying the strong-coupling limit of this model. The strong-coupling regime leads to the breaking of the particle number conservation symmetry as a result of the emergence of pairing terms. We will show however that the topological description is smoothly carried from usual particles to Bogoliubov excitations. Finally, we will describe a way to probe the topology of the system, defined in terms of the winding of the Berry's connection (see Section 1.4.1 for more details on the definition of the Berry's connection) across the BZ, using a reflection measurement of (microwave) light. The results presented in this section have already been reported in Ref. [4].

4.4.1 SSH model

Su-Schrieffer-Heeger (SSH) model, also known as a model for polyacetylene, is a 1D model defined by the following Hamiltonian [27, 28]

$$H = \sum_i \left(v a_i^\dagger b_i + w b_i^\dagger a_{i+1} + \text{h.c.} \right) \ . \tag{4.52}$$

It describes electrons (spinless fermions) on a lattice with staggered hopping amplitudes v and w, composed of two sublattices, that we will label as usual by indices A and B. $a_i(b_i)$ are annihilation operators on the sublattice $A(B)$ at unit cell i. The schematic representation of this model is shown in Fig. 4.5(a). The SSH model belongs to the *BDI* class of the topological classification we presented in Section 1.4.4. It clearly has a time-reversal symmetry T, since no magnetic fields are present in the model. T squares to 1 because the fermions are spinless. The chiral symmetry C defined in this particular case by

$$C a_j C^{-1} = a_j^\dagger \ , \quad C b_j C^{-1} = -b_j^\dagger \ , \quad C i C^{-1} = i \tag{4.53}$$

is present in the model as long as no hoppings inside the same sublattice are allowed. Finally, since both T and C are symmetries, the particle-hole symmetry P is also a symmetry of the problem.

The SSH model is described by a $\mathbb{Z}$ topological invariant equal to the Zak phase $\gamma_{\text{Zak}}^{\pm}$, that we discussed in details in Section 1.4.1. Zak phase is associated with two eigenstates $|\pm; k\rangle$ of the Hamiltonian (4.52), and can be calculated as an integral of the Berry's connection over the first BZ

$$\gamma_{\text{Zak}}^{\pm} = i \oint_{\text{BZ}} \mathrm{d}k \, \langle \pm; k | \, \partial_k \, | \pm; k \rangle \ . \tag{4.54}$$

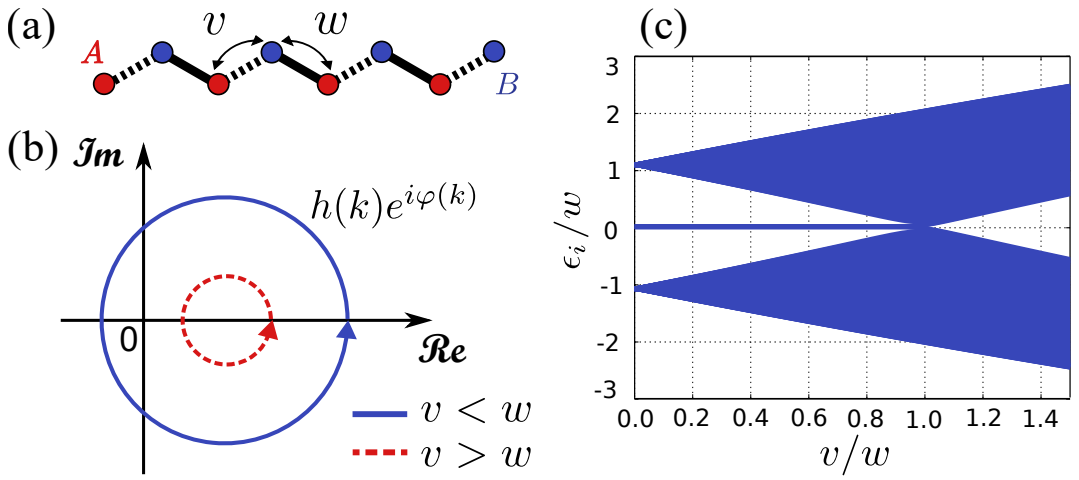

FIGURE 4.5: **(a)** Schematic presentation of the SSH model. **(b)** Function $h(k)e^{i\varphi(k)}$ shown for two different values of the ratio v/w. In the topological phase $v < w$ this function winds once around the origin, while in the topologically trivial phase $v > w$ the winding number is equal to zero. **(c)** Energy spectrum $\{\epsilon_i\}$ of the SSH model in a geometry with open boundary conditions. In the region $v < w$ we see the emergence of two zero-energy states. In the region $v > w$ these states move away from zero in energy.

By re-writing the Hamiltonian (4.52) in the momentum space we obtain that

$$\mathcal{H}(k) = d_x(k)\sigma^x + d_y(k)\sigma^y, \quad h(k)e^{i\varphi(k)} = d_x(k) + id_y(k) = v + we^{-ika}\,, \tag{4.55}$$

where a is the size of the unit cell of the lattice. The Zak phase can be simply re-expressed using Eq. (1.83) as the winding number of the curve defined by $h(k)e^{i\varphi(k)}$ (or equivalently the vector $\boldsymbol{d}(k)$) around the origin

$$\gamma^{\pm}_{\text{Zak}} = \frac{1}{2}\oint_{\text{BZ}} \mathrm{d}k \frac{\mathrm{d}\varphi(k)}{\mathrm{d}k}\,. \tag{4.56}$$

We observe that in the topological phase $v < w$ the curve winds around the origin once, while for $v > w$ the winding number is equal to zero, as shown in Fig. 4.5(b). The action of the chiral symmetry C on the Bloch Hamiltonian $\mathcal{H}(k)$ is described in terms of a Pauli matrix σ_z. It forbids the vector $\boldsymbol{d}(k)$ to get out of the plane. The winding number description is thus valid thanks to the presence of the C symmetry.

According to the bulk-boundary correspondence, the topological description of the bulk is related to the presence of edge modes at the boundary, if open boundary conditions are considered. There are no exceptions in the rules in the case of the SSH model. In Fig. 4.5(c) we show the energy structure of the SSH model as a function of the ratio v/w on a lattice of 100 unit cells (200 sites). We observe first of all that the spectrum is symmetric with respect to zero, as a result of the chiral symmetry. Second, we see that for $v < w$ two zero-energy modes are present. They disappear in the opposite regime $v > w$, when the phase becomes topologically trivial.

4.4.2 Circuit model

An experimental realization of the SSH model can be performed using a chain of LC resonators with alternating capacitive couplings, as shown in Fig. 4.6. In the following we will refer to this model as the circuit model. The capacitive coupling between resonators i and $i+1$ can be expressed as Q_iQ_{i+1}, leading to the following

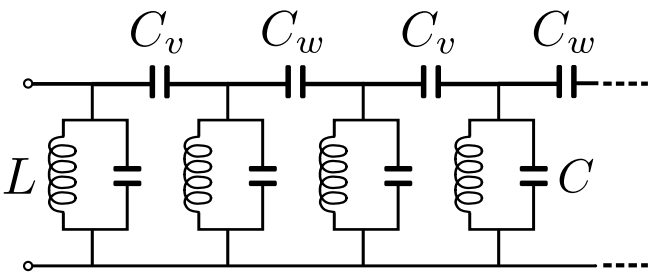

FIGURE 4.6: Schematic representation of the chain of LC resonators with alternating capacitive couplings described by the Hamiltonian (4.57).

Hamiltonian

$$H = \epsilon_0 \sum_i \left(a_i^\dagger a_i + b_i^\dagger b_i \right) + v \sum_i \left(a_i + a_i^\dagger \right) \left(b_i + b_i^\dagger \right) + w \sum_i \left(a_{i+1} + a_{i+1}^\dagger \right) \left(b_i + b_i^\dagger \right) . \tag{4.57}$$

Here operators $a_i(b_i)$ originate from the quantization of the charge on the capacitors of quantum LC resonators [339]. Notice that they describe photon excitations, which are bosonic. The chemical potential

$$\epsilon_0 = \sqrt{\frac{1}{LC}} \sqrt{\frac{C + C_v + C_w}{C}} \tag{4.58}$$

corresponds to the frequency of the resonators. The hopping terms v and w can be expressed in terms of parameters of the resonators as

$$v, w = \epsilon_0 \sqrt{\frac{C_{v,w}}{C + C_v + C_w}} . \tag{4.59}$$

The inductance L and capacitances C, C_v and C_w are defined as in Fig. 4.6. We notice that similar systems have been achieved experimentally [340] and some topological aspects can already be measured in the classical limit (without quantification of the phase and charge in the circuit) [341–344].

In the interaction picture, the pairing terms $a^\dagger b^\dagger$ and ab oscillate at twice the resonator frequency $2\epsilon_0$. In the weak coupling limit this frequency is much larger than the hopping amplitudes $\epsilon_0 \gg (v, w)$. Hence, the rotating wave approximation (RWA) allows to neglect the fast rotating terms, and the Hamiltonian acquires exactly the same form as in Eq. (4.52), up to a chemical potential term that does not affect the topological description. In the strong coupling regime the hopping amplitudes are of the same order of magnitude as the resonator frequency $\epsilon_0 \sim (v, w)$, and the RWA breaks down. As a result, the contribution of the pairing terms $a^\dagger b^\dagger$ and ab must be incorporated. In this case the Hamiltonian (4.57) can be diagonalized using the Bogoliubov transformation as

$$H = \sum_{k \in \mathrm{BZ}} \left[\epsilon_+(k) \gamma_k^{+\dagger} \gamma_k^+ + \epsilon_-(k) \gamma_k^{-\dagger} \gamma_k^- \right] , \tag{4.60}$$

where two eigenenergies $\epsilon_\pm(k)$ correspond to two doubly degenerate bands. They are equal to

$$\epsilon_\pm(k) = \sqrt{\epsilon_0^2 \pm 2\epsilon_0 h(k)}. \tag{4.61}$$

The Bogoliubov quasi-particle operators are given by

$$\begin{aligned}\gamma_k^{\pm} &= \psi_k^{\pm} \cdot (a_k, a_{-k}^{\dagger}, b_k, b_{-k}^{\dagger}) \ , \\ \psi_k^{\pm} &= \frac{1}{\sqrt{2}} \left(\pm e^{i\varphi(k)} \boldsymbol{v}_k^{\pm}, \boldsymbol{v}_k^{\pm} \right) \ , \\ \boldsymbol{v}_k^{\pm} &= (\cosh \eta_k^{\pm}, \sinh \eta_k^{\pm}) \ , \end{aligned} \tag{4.62}$$

and the Bogoliubov rotation $\eta_k^{\pm}$ is defined as

$$\tanh 2\eta_k^{\pm} = \pm h(k) / \left(\epsilon_0 \pm h(k) \right) \ . \tag{4.63}$$

The topological description of the model is unaffected by the introduction of pairing terms. In fact, one can re-express the Berry's connection using the wavefunctions $\psi_k^{\pm}$ (instead of $|\pm; k\rangle$) that are the vectors of size 4. Since the Bogoliubov transformation for boson is symplectic rather than unitary as for fermions (see Section 1.2 for more details), the scalar product has to be modified. The symbol $*$ denotes the new definition

$$\psi^{\dagger} * \psi = \psi^{\dagger} \cdot \mathcal{D} \cdot \psi \ . \tag{4.64}$$

For the choice of the basis shown in Eq. (4.62), the diagonal matrix $\mathcal{D}$ has to take the form $\mathcal{D} = \mathrm{diag}(1, -1, 1, -1)$. The Zak phase obtained in this way is identical to (4.54). We recover that the regime $v < w$ is topological with $\gamma_{\mathrm{Zak}}^{\pm} = \pi \bmod 2\pi$, while the regime $v > w$ is topologically trivial with $\gamma_{\mathrm{Zak}}^{\pm} = 0$.

We verify that the topological phase transition is unaffected in the circuit model, by performing a numerical calculation in a geometry with open boundary conditions. We diagonalize the Hamiltonian (4.57) in real space using the Bogoliubov transformation. This approach is equivalent to the one described in Section 1.2, except that we skip the step of a block-diagonalization in momentum space, since the translation symmetry is broken. In Fig. 4.7 we draw the resulting energy spectrum associated with Bogoliubov excitations. We observe that the spectrum is not symmetric with respect to the resonators frequency ϵ_0. This originates from the fact that unlike the SSH model, the chiral symmetry is explicitly broken in the circuit model by the on-site energy term ϵ_0 and the pairing terms. The difference between two bandwidths $\mathcal{W}^{\pm}$, to lowest order in v and w, is equal to

$$\mathcal{W}^{-} - \mathcal{W}^{+} = \frac{4wv}{\epsilon_0} \ . \tag{4.65}$$

Nevertheless, the sublattice symmetry still remains the symmetry of the problem, since no terms connecting the sites of the same sublattices are present in the Hamiltonian. Hence, the value of the Zak phase remains unaffected. Moreover, we notice that identically to Fig. 4.5(c), two mid-gap edge modes are present in the regime $v < w$ (topological phase) and vanish in the regime $v > w$ (topologically trivial phase).

4.4.3 Measuring the Zak phase

Finally, we propose an experimental protocol to measure the Zak phase in the circuit model (4.57). Our protocol consists in probing the winding of the phase $\varphi(k)$ from Eqs. (4.55) and (4.62), based on the measurement of the correlation function

$$\chi_n(t) = -i\Theta(t) \left\langle [q_n(t), q_n(0)] \right\rangle \ . \tag{4.66}$$

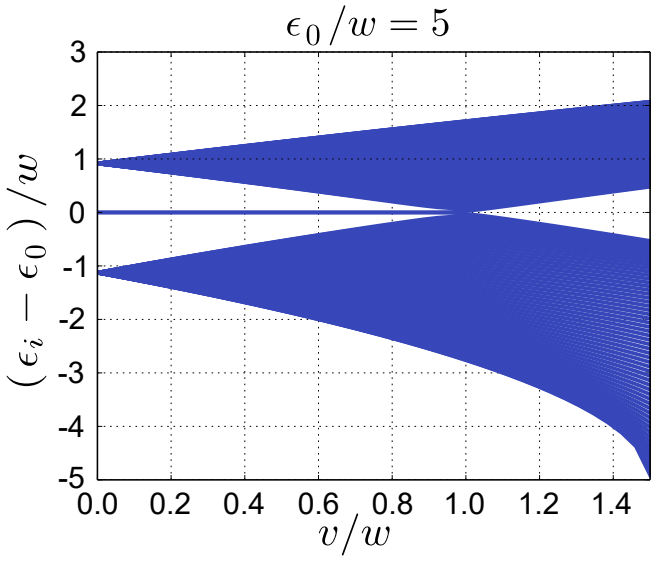

FIGURE 4.7: Energy spectrum $\{\epsilon_i\}$ of the model (4.57) describing a chain of coupled LC resonators, with the frequency of resonators ϵ_0 subtracted. Calculations are performed in the geometry with open boundary conditions. Because of the pairing terms, the spectrum is not symmetric with respect to ϵ_0, as compared to Fig. 4.5(c). The topological phase transition and the presence of edge modes in the region $v < w$ remain unaffected.

Here q_n is defined as a single cell (charge) operator $q_n = a_n^\dagger + a_n + b_n^\dagger + b_n$. This correlation function can be probed by measuring the reflection coefficient of a transmission line (capacitively) coupled to a single cell in the chain, given by

$$r(\omega) = 1 + \lambda^2 \chi_n(\omega) \, . \tag{4.67}$$

Here λ is the coupling constant between the transmission line and the chain, which is supposed to be small. In the periodic boundary condition case $\chi_n(t)$ does not depend on n. The Fourier transform of the correlation function yields

$$\begin{aligned} \chi_n(\omega) = & \frac{1}{N_c} \sum_k (1 + \cos\varphi(k)) \frac{\epsilon_0}{\epsilon_+(k)} \frac{1}{\omega - \epsilon_+(k) + i0^+} \\ & + \frac{1}{N_c} \sum_k (1 - \cos\varphi(k)) \frac{\epsilon_0}{\epsilon_-(k)} \frac{1}{\omega - \epsilon_-(k) + i0^+}, \end{aligned} \tag{4.68}$$

where N_c denotes the total number of unit cells.

The imaginary part of $\chi_n(\omega)$ exhibits resonances at the eigenenergies $\epsilon_\pm(k)$, thus revealing the band structure of the chain. The envelope of the resonances reflects the winding of the phase $\varphi(k)$ through the terms $1 \mp \cos\varphi(k)$. In order to see it more clearly, let us consider the envelope function of the first band $1 - \cos\varphi(k)$. The bottom of the first band is at $k = 0$ where $\varphi(0) = 0$ and its top is at $ka = \pi$ where $\varphi(\pi) = 0$ in the trivial phase and $\varphi(\pi) = \pi$ in the topological phase. Therefore, in the topological phase the envelope function of the first band is a monotonically increasing function whereas in the trivial phase it starts and ends at zero. The behaviour of the envelope of the second band resonances can be understood in the same way, noticing that the bottom of the second band is at $ka = \pi$ and its top is at $k = 0$. The general behaviour of the envelope function is similar in the weak and strong coupling regimes. Numerical verification of this behaviour is shown in Fig. 4.8(a-b).

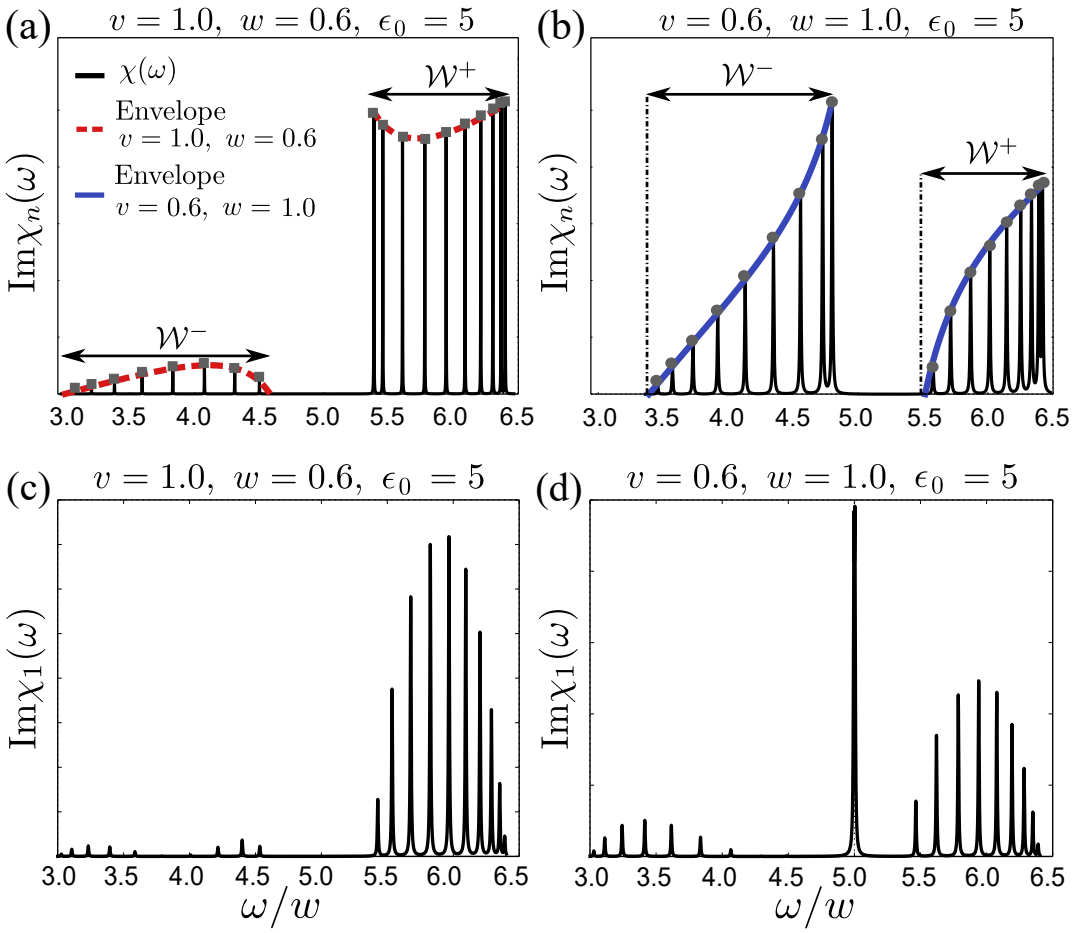

FIGURE 4.8: **(a-b)** The correlation function $\chi_n(\omega)$ from Eq. (4.68) in a geometry with periodic boundary conditions. The envelope of the resonances starts and ends at zero in the trivial phase ($v > w$) **(a)** whereas it is a monotonically increasing function in the topological phase ($v < w$) **(b)**. **(c-d)** The correlation function $\chi_{n=1}(\omega)$ in a geometry with open boundary conditions. The midgap states are absent in the topologically trivial phase ($v > w$) **(c)**, but in the topological phase ($v < w$) we observe a peak showing the presence of edge modes **(d)**. All the simulations were performed on a system of 20 unit cells.

The midgap edge state can also be observed in the correlation $\chi_{n=1}$ for a system with open boundary conditions. In Fig. 4.8(c-d) we show the imaginary part of $\chi_{n=1}$ for an open system with $N = 20$ unit cells. The midgap states appear only in the topological phase ($v < w$). Note that the envelope of the bulk resonances in $\chi_{n=1}$ differs from the periodic boundary condition case due to boundary effects.

4.5 Purification spectroscopy protocol

In this final section of the final chapter we would like to describe another protocol that has a promising application in the context of quantum simulator setups. This protocol allows to study bulk spectral properties of quantum systems. It is based on the purification concept [345] and the ancilla method [346–349], consisting in doubling the size of the initial system by making two copies of it. One can then prepare a particular maximally-entangled infinite temperature initial state and measure the Loschmidt echo associated with the time-evolution of only one half (one copy) of the purified system. We notice that this method can be applied not only experimentally, but also numerically, in particular in the cases when sufficiently large system sizes can be afforded. In this section we will first describe in greater details the idea of the purification protocol. We will show, how it can be used to measure the eigenenergies of quantum systems through the above mentioned quench dynamics. We will then perform a numerical verification of the analytical predictions. Finally, we will also propose a protocol to verify the properties of many-body localized systems.

4.5.1 Purification spectroscopy

Let us consider a quantum system $\mathcal{S}$, describing a model with a Hamiltonian H defined on a lattice $\mathcal{L}$. According to the purification concept [345], any density operator ρ in $\mathcal{S}$ can be represented in terms of some pure state $|\psi\rangle$ in an enlarged Hilbert space. This enlarged Hilbert space is constructed by combining $\mathcal{S}$ and some ancillary system $\mathcal{A}$, which is taken to be the copy of $\mathcal{S}$. The density matrix ρ can be deduced by simply tracing out $\mathcal{A}$

$$\rho = \mathrm{tr}_{\mathcal{A}} \left(|\psi\rangle \langle\psi| \right) \ . \tag{4.69}$$

The state $|\psi\rangle$ is then called a purification of ρ. Notice that $|\psi\rangle$ is not usually uniquely defined.

A. Numerical simulations at finite temperature

The ancilla method is based on the purification concept. It has been introduced to perform the density matrix generalization group simulations [350–352] at finite temperature [346–349]. In this case, the density matrix of interests is the thermal density operator $\rho_\beta = \exp(-\beta H)$, with β – the inverse temperature. Let us denote by $|\psi_\beta\rangle$ a purification associated to ρ_β. At $\beta = 0$ (infinite-temperature state) this purification can be constructed as

$$|\psi_0\rangle = \frac{1}{\sqrt{D}} \prod_{j \in \mathcal{L}} \sum_{\sigma_j} |\sigma_j\rangle_{\mathcal{S}} \otimes |\sigma_j\rangle_{\mathcal{A}} = \frac{1}{\sqrt{D}} \sum_{\sigma} |\sigma\rangle_{\mathcal{S}} \otimes |\sigma\rangle_{\mathcal{A}} \ . \tag{4.70}$$

Here the product is taken over all the sites of the lattice $\mathcal{L}$. At each site j the local physical Hilbert space is described by the set of states $\{|\sigma_j\rangle_{\mathcal{S}}\}$. Similarly $\{|\sigma_j\rangle_{\mathcal{A}}\}$ are local states of the ancillary system. The states $|\sigma_j\rangle$ in the middle expression of

Eq. (4.70) are however identical for both $\mathcal{S}$ and $\mathcal{A}$. The last expression of Eq. (4.70) is a shorthand notation, with $|\sigma\rangle = |\sigma_1; \ldots; \sigma_{N_s}\rangle$ describing many-body states. N_s is the total number of sites in the lattice. The total size of the Hilbert space is equal to D, so that the state $|\psi_0\rangle$ is correctly normalized.

Any general finite temperature states can be obtained by simply evolving the state $|\psi_0\rangle$ in imaginary time, with the Hamiltonian H acting on the physical system $\mathcal{S}$ only

$$|\psi_\beta\rangle = e^{-\beta H/2}|\psi_0\rangle = \frac{1}{\sqrt{D}}\sum_\sigma \left(e^{-\beta H/2}|\sigma\rangle_{\mathcal{S}}\right)\otimes|\sigma\rangle_{\mathcal{A}} \ . \tag{4.71}$$

The thermal density operator ρ_β is then calculated using Eq. (4.69), while the thermodynamic averages $\langle O\rangle_\beta$ of any observable O can be simply calculated as

$$\langle O\rangle_\beta = \frac{\langle\psi_\beta \,|\, O \,|\, \psi_\beta\rangle}{\langle\psi_\beta \,|\, \psi_\beta\rangle} \ . \tag{4.72}$$

B. Purification spectroscopy

In order to probe the spectral properties of the system, we calculate the real time evolution of the infinite temperature state $|\psi_0\rangle$. We still assume that the state evolves with the Hamiltonian H acting on the physical system S only

$$|\psi(t)\rangle = e^{-itH}|\psi_0\rangle = \frac{1}{\sqrt{D}}\sum_\sigma \left(e^{-itH}|\sigma\rangle_{\mathcal{S}}\right)\otimes|\sigma\rangle_{\mathcal{A}} \ . \tag{4.73}$$

We are particularly interested in evaluating the Loschmidt echo [353, 354]

$$L(t) = |G(t)|^2 \ , \tag{4.74}$$

and the Loschmidt amplitude $G(t)$ defined as

$$G(t) = \left\langle\psi_0\left|e^{-itH}\right|\psi_0\right\rangle = \langle\psi_0\,|\,\psi(t)\rangle \ . \tag{4.75}$$

We notice that for the evolution of the infinite temperature state this expression acquires a particularly simple and recognizable form

$$G(t) = \frac{1}{D}\sum_{\sigma,\sigma'}\langle\sigma'|\,e^{-itH}\,|\sigma\rangle_{\mathcal{S}}\times\langle\sigma'\,|\,\sigma\rangle_{\mathcal{A}} = \frac{1}{D}\mathrm{tr}(e^{-itH}) = \frac{Z(it)}{D} \ . \tag{4.76}$$

We observe that the Loschmidt echo is equal to the partition function $Z(it)$ extended to the complex plane and evaluated along the imaginary axis.

By definition, the partition function $Z(it)$ is the Fourier transform of the density of states

$$\rho(\epsilon) = \sum_n \delta(\epsilon - \epsilon_n) \ . \tag{4.77}$$

Here the summation is performed over all eigenvalues ϵ_n of the Hamiltonian H. Hence, measuring $G(t)$ up to some finite time T allows one to construct the coarse-grained function

$$\rho_c(\epsilon, T) = \int_0^T \frac{\mathrm{d}t}{\pi}\mathfrak{Re}\left(Z(it)e^{it\epsilon}\right) = \sum_n \delta_T(\epsilon - \epsilon_n) \underset{T\to\infty}{\longrightarrow} \rho(\epsilon) \ , \tag{4.78}$$

where

$$\delta_T(\epsilon) = \frac{\sin[T\epsilon]}{\pi\epsilon} . \tag{4.79}$$

The resolution of the coarse-grained spectral function is increased with T. We expect thus that there exists some critical value T_c, above which the coarse-grained spectral function will allow to resolve each peak of the energy structure. Clearly, in the bulk, because of the high density of states, T_c should scale exponentially with the size of the system. However, we expect that at the edge of the spectrum T_c scales polynomially, or is finite, depending on whether the system is gapless or gaped.

In a similar way, one could perform the spectroscopy of observables. Indeed, if we apply an observable O to the state $|\psi(t)\rangle$ at the end of the time evolution, we obtain

$$\langle\psi_0 \,|\, O \,|\, \psi(t)\rangle = \frac{1}{D}\mathrm{tr}\left(Oe^{-itH}\right) = \frac{1}{D}\sum_n O_n e^{-it\epsilon_n} , \tag{4.80}$$

where $O_n = \langle n \,|\, O \,|\, n\rangle$, and $|n\rangle$ are eigenstates of the Hamiltonian H associated to eigenvalues ϵ_n. We call

$$O(t) = \mathrm{tr}\left(Oe^{-itH}\right) , \tag{4.81}$$

so that the coarse-grained estimation of the observable can be expressed as

$$O_c(\epsilon, T) = \frac{1}{\rho_c(\epsilon, T)}\int_0^T \frac{\mathrm{d}t}{\pi}\mathfrak{Re}\left(O(t)e^{it\epsilon}\right) \underset{\substack{T\to\infty \\ \epsilon\to\epsilon_n}}{\longrightarrow} O_n . \tag{4.82}$$

C. Numerical verification

Now we would like to show results of a numerical verification of the purification protocol. We will pay particular attention to verify the Eq. (4.78). A more detailed analysis is presented in Ref. [5]. In order to do the verification we perform ED simulations of the 1D Ising spin chain, described by the following Hamiltonian

$$H = -J_z\sum_i S_i^z S_{i+1}^z - h_x\sum_i S_i^x - h_z\sum_i S_i^z . \tag{4.83}$$

The Hamiltonian comprises the term of Ising interactions with the strength J_z, and two terms describing the effect of magnetic fields h_x and h_z applied respectively along the axis x and z.

In Fig. 4.9 we show ED results performed on a small system of 8 sites. After expressing $|\psi(t)\rangle$ and the Loschmidt amplitude $\langle\psi_0 \,|\, \psi(t)\rangle$, we calculate the discrete Fourier transform from Eq. (4.78) to get the coarse-grained spectral function $\rho_c(\epsilon, T)$. The calculation is done for several values of the time-evolution interval T. We observe that when T is big, we can resolve all the eigenvalues close to the boundary of the spectrum and some eigenvalues at the bulk. When T decreases, the distribution becomes smooth but still allows to resolve separate peaks. We notice also that the discretization step Δt plays an important role in the calculation: in order to obtain reasonable results one should have the energy scale $1/\Delta t$ bigger than the spectral width of the problem.

4.5.2 Experimental proposal

In this subsection we describe an experimental protocol to make the purification measurement proposed previously. The main difficulty of the protocol resides in the measurement of the Loschmidt amplitude $\langle\psi_0 \,|\, \psi(t)\rangle$. This measurement can be

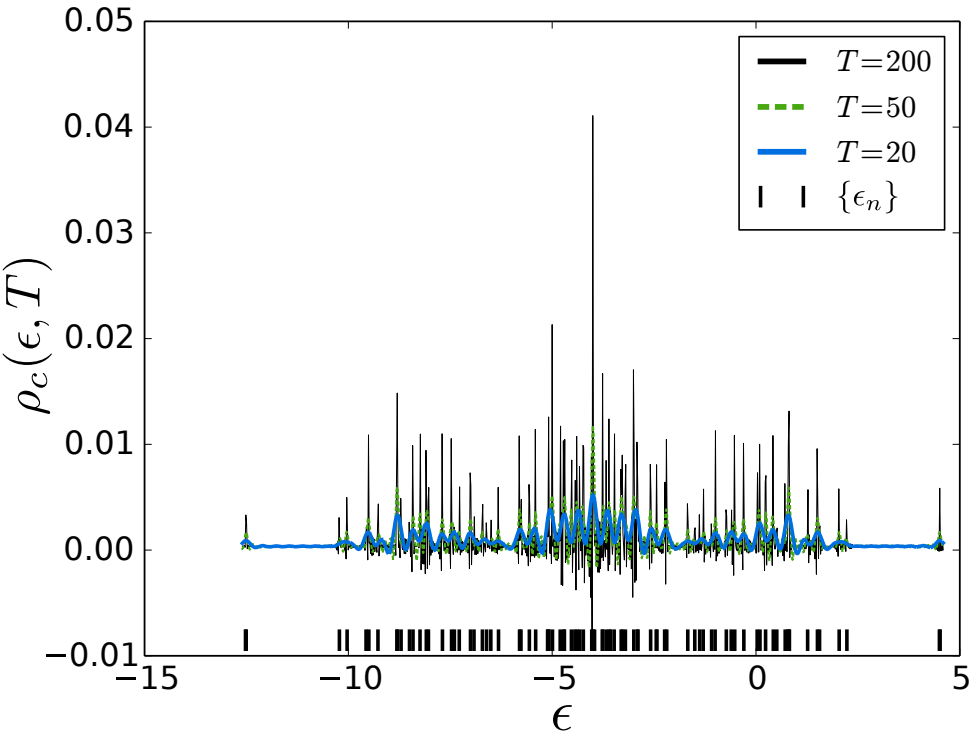

FIGURE 4.9: Illustration of the coarse-grained spectral function $\rho_c(\epsilon, T)$ of the Hamiltonian (4.83) for several values of T. Black lines at the bottom show the exact positions of the eigenvalues ϵ_n along the axis of ω. We observe that even relatively small values of the time-evolution interval $T \sim 50$ are sufficient to resolve the energy levels situated close to each other. Parameters of the simulation are $J_z = 1.0$, $h_x = 1.0$, $h_z = 0.001$. ϵ and T are given in units of J_z. Size of the lattice is $N_s = 8$.

achieved using a probe qubit approach, by performing an interferometric measurement between the initial state $|\psi_0\rangle$ and the time-evolved state $|\psi(t)\rangle$ [355–358]. More precisely, let us consider a system of $\mathcal{S}$ and $\mathcal{A}$ coupled additionally to a qubit degree of freedom denoted by $|q\rangle_{\mathrm{p}}$. We assume that the system is initially prepared in the state $|\psi_0\rangle \otimes |0\rangle_{\mathrm{p}}$. First, we rotate the probe state to

$$\frac{1}{\sqrt{2}}(|\psi_0\rangle \otimes |0\rangle_{\mathrm{p}} + |\psi_0\rangle \otimes |1\rangle_{\mathrm{p}}) \,. \tag{4.84}$$

The resulting state can then be evolved through a control-U gate [355–358], that applies the time-evolution operator $\exp(-itH)$ conditionally on the $|1\rangle_{\mathrm{p}}$ state and leaves the $|0\rangle_{\mathrm{p}}$ state unchanged. After time t the state becomes

$$\frac{1}{\sqrt{2}}(|\psi_0\rangle \otimes |0\rangle_{\mathrm{p}} + |\psi(t)\rangle \otimes |1\rangle_{\mathrm{p}}) \,. \tag{4.85}$$

Last, we measure the real and imaginary parts of $\langle\psi_0 \,|\, \psi(t)\rangle$ through the expectation values of Pauli matrices $\langle\sigma_x\rangle_{\mathrm{p}}$ and $\langle\sigma_y\rangle_{\mathrm{p}}$, computed in the reduced density matrix of the probe. An alternative approach can also be achieved using the single-site-resolved control of ultracold bosonic atoms in optical lattices [359].

4.5.3 Fock state spectroscopy and many-body localization

Finally, we would like to mention another possible protocol to probe many-body localization (MBL) [257–259]. This phenomenon is strongly related to the notion of thermalization and the eigenstate thermalization hypothesis (ETH) [360, 361]. According to the ETH, eigenstates close in energy are expected to have similar expectation values of few-body observables, and their time-dynamics should lead to the same "thermal" states at long times. Localized states break the ETH picture: they do not thermalize, and even at the same energy density they have a very different structure. The main ingredient to have such exotic behaviour is the disorder, and the current problem consists in understanding the interplay of disorder and interactions, leading to the formation of MBL states.

Similarly to Eq. (4.78), one can use the measurement of

$$G_\sigma(t) = \langle\sigma|\, e^{-itH}\, |\sigma\rangle = \sum_n |\langle\sigma \,|\, n\rangle|^2 e^{-it\epsilon_n} \tag{4.86}$$

to access the distribution of the weights $|\langle\sigma \,|\, n\rangle|^2$ describing how the state $|\sigma\rangle$ is spread over the eigenstates. In order to show this, let us introduce the matrix M with entries $M_{\sigma n} = |\langle\sigma \,|\, n\rangle|^2$. This matrix is real positive, bistochastic and non-symmetric. The Fourier transform of $G_\sigma(t)$ is

$$\rho_\sigma(\epsilon) = \frac{\pi}{T}\sum_n M_{\sigma n}\delta(\epsilon - \epsilon_n) \,. \tag{4.87}$$

At finite time T, the measurement of $G_\sigma(t)$ provides a coarse-grained reconstruction of the weights distribution

$$\rho_\sigma(\epsilon, T) = \frac{\pi}{T}\sum_n M_{\sigma n}\delta_T(\epsilon - \epsilon_n) \tag{4.88}$$

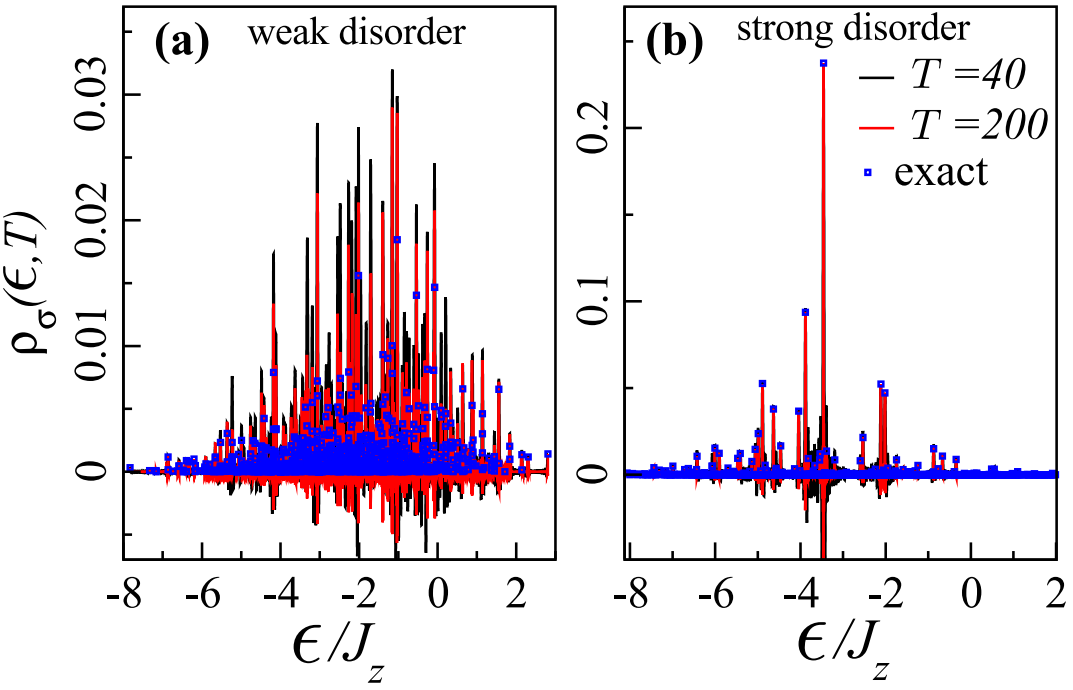

FIGURE 4.10: **(a-b)** Illustration of (bulk) Fock state energy distribution $\rho_\sigma(\epsilon, T)$ with $|\sigma\rangle = |\uparrow\uparrow\downarrow\downarrow\uparrow\uparrow\downarrow\downarrow\uparrow\uparrow\rangle$, starting from the paramagnetic regime $J_z = 1.0$, $h_x = 1.0$. The energy localization is seen at large disorder $r_z = 5.0$ **(b)** while energy delocalization is found at low disorder $r_z = 0.1$ **(a)**. r_z, ϵ and T are given in units of J_z. Size of the lattice is $N_s = 10$.

of the Fock state energy distribution. We notice also that this measurement is simpler to perform experimentally, since there is no need to employ the ancilla method. In Fig. 4.10 we show the typical behavior of $\rho_\sigma(\epsilon, T)$ in the situation of many-body localization. We use the Hamiltonian (4.83) with an additional disorder term

$$H_{\text{disorder}} = \sum_i h_i S_i^z \,, \tag{4.89}$$

where h_i are random longitudinal fields uniformly distributed in the range $[-r_z/2, r_z/2]$. Starting from the paramagnetic phase at $J_z = 1.0$, $h_x = 1.0$ in which a typical bulk Fock state is naturally delocalized over the eigenstates (Fig. 4.10(a)), increasing the disorder makes the Fock state closer and closer to an exact eigenstate, building a localized energy distribution (Fig. 4.10(b)). This behavior is indeed expected for MBL states.

Conclusion and perspectives

In this thesis we treated different problems in one and two dimensions. We were particularly interested in investigating rich properties of systems related to the questions of topology and many-body phenomena.

In Chapter 2 we studied the bosonic Haldane model. In Section 2.2 we explored the superfluid phase transitions between Bose-Einstein condensates at zero and finite momenta, and studied the effect of the anisotropy and interactions. We observed that the transition is of second order in the anisotropic model, and that interactions have an impact on the phase transition even in the weak interaction strength limit. While the topological properties associated with the ground-state are trivial in this case, the Bogoliubov excitations still feel the non-trivial topology of the bands. In a ladder version of the model, we recover a similar phase transition, but of first order. The Luttinger liquid theory allowed us to obtain analytical predictions even in the limit of strong interactions, almost in all regions of the phase diagram, as presented in Section 2.3. However, when two hopping amplitudes of the Haldane model become very close, we observe the emergence of flat bands, non-treatable with bosonization.

The flat-band region of the Haldane ladder model seems a very promising direction for more advanced numerical and analytical studies. In particular, one could expect that the emergence of flat bands combined with the reminiscence of the topology from the two-dimensional case would lead to new phenomena as exciting as the formation of fractional quantum Hall states. Such states have already been proposed in similar ladder geometries [181, 182]. However the question on how much of the physics of two-dimensional states will remain in this case is still open.

As a straightforward continuation of the work presented in Chapter 2, Chapter 3 analyzes the bosonic counterpart of the Kane-Mele model, known as a model for topological insulators. We also considered the effect of strong interactions in this system. Unlike the fermionic Kane-Mele model with Hubbard interactions already explored previously, we found that the Mott insulator physics of the bosonic Kane-Mele-Hubbard model is much richer and is related to the emergence of an effective frustrated spin-1/2 XY model. This model has a very diversified phase diagram with a variety of symmetry broken spin states, one of which has been a candidate for the chiral spin liquid of Kalmeyer and Laughlin. In Section 3.4 we confirmed numerically the main predictions from the previous analytical work, such as the spontaneous breaking of the time-reversal and parity symmetries. Nevertheless, we also showed that the corresponding state does not have a topological order and thus cannot be a chiral spin liquid. Its exotic nature gives strong motivation to explore experimentally the predicted results.

In Chapter 4 we discussed one of the main ingredients required to perform an experimental observation proposed in Chapters 2 and 3. This key ingredient is artificial gauge fields. In Section 4.3.2 we proposed an experimental protocol to generate

such artificial gauge fields in photonic lattices, that can be either classical (*e.g. RLC* circuits) or quantum (*e.g.* superconducting circuits). While the first protocol would allow to achieve the results at room temperature, the second one opens roads to the exploration of many-body phenomena. The approach we proposed is based on the application of periodic time-dependent perturbations and a high-frequency expansion. In Section 4.3.3 we verified numerically the validity of the proposed Floquet protocol. We observed that the exact time evolution agrees well with the first order terms in the high frequency expansion even for long times and for reasonably high frequency of the perturbation.

In the following, it would be very interesting to explore further the Floquet engineering procedure for more intriguing phases originating from strong interaction effects. In particular, a very promising idea is to use such out-of-equilibrium protocols to realize topologically ordered states and quasi-particles with fractional statistics. However, while Floquet engineering is relatively well understood in the case of non-interacting systems, it addresses a lot of open questions related to the problem of decoherence and heating, once interactions are taken into account. Hence, the question on how these negative side effects can be removed or weakened is another extremely important direction to investigate in more details.

Recently, a completely new point of view on Floquet engineering has also been developed, thanks to the discovery of novel Floquet topological insulators [362–366]. Such systems have no analogs among the equilibrium states of matter, since their existence relies on the peculiar periodicity of Floquet states (or, more precisely, associated Floquet quasienergies) in energy space. This paves the way for new possible discoveries and applications in the domain of quantum information.

In the last two sections of Chapter 4 we also studied in more details few particular quantum simulator protocols. In Section 4.4 we proposed a way to design the Su-Schrieffer-Heeger model with quantum circuits, by paying particular attention to its strong coupling regime. We showed that the topology of the model remains unaffected despite the emergence of pairing terms, and proposed a way to probe the winding of the Zak phase via a scattering measurement. By developing these ideas, it could be interesting to work on possible generalizations of this protocol and apply them to probe more exotic topological insulators or topologically ordered states.

In Section 4.5.1 we proposed a way to measure the bulk spectral properties of arbitrary lattice quantum simulator systems using a purification idea. This approach seems to be very promising not only from the experimental side, but also for possible numerical applications. This could be particularly useful in the context of density-matrix renormalization group (or, more generally, matrix product states) methods.

Appendix A

Numerical methods

Numerical simulations play a crucial role in the domain of condensed matter physics, and, more precisely, in the study of strongly correlated quantum systems. The reason for it is that corresponding problems are hard to solve, especially in two dimensions. One often does not have any small parameter to perform perturbative calculations. An integrability of the system can be helpful, but such situations occur rarely. Numerical methods are thus used to make a first impression of the model, or to perform more detailed studies and verify analytical predictions.

This supplemental chapter is dedicated to presenting numerical tools we used in this thesis, or in current projects and ongoing works. We consider a generic many-body condensed matter system defined on a lattice. We do not describe algorithms to simulate infinite-size systems, hence, we consider a model defined on a finite-size cluster. We assume that it is described by a Hamiltonian $\mathcal{H}$ acting on a Hilbert space $\mathcal{HS}$. For a future (numerical) convenience, it is better to imagine $\mathcal{H}$ written in the matrix form with elements

$$\mathcal{H}_{ij} = \langle c_i \,|\, \mathcal{H} \,|\, c_j \rangle \ , \tag{A.1}$$

where states $\{|c_i\rangle\}$ form a basis of the $\mathcal{HS}$. The numerical problem one needs to solve is the time-independent Schrödinger equation

$$\mathcal{H} \,|\Psi_n\rangle = \epsilon_n \,|\Psi_n\rangle \ . \tag{A.2}$$

Here $\{|\Psi_n\rangle\}$ are eigenstates of the Hamiltonian matrix $\mathcal{H}$, and $\{\epsilon_n\}$ are associated eigenenergies. One clearly sees why this problem is complicated. With the dimension of the Hilbert space $\mathcal{HS}$ growing exponentially with the system size, it is impossible to get the exact solution in a reasonable time even for relatively small clusters. If we take as an example the Heisenberg model for spins-1/2, the $\mathcal{HS}$ dimension grows as 2^{N_s}, with N_s – the total number of sites in the cluster. For $N_s = 16$ it becomes equal to 65536. The memory required to save the corresponding matrix $\mathcal{H}$ (in a dense format) is 8×4^{N_s} bytes, equal to 32 Gigabytes. Moreover, each matrix multiplication, based on the basic algorithms, takes $\mathcal{O}(4^{N_s})$ operations. Such sizes and time scales are expensive in practice. Hence, it is necessary to address the numerical problems differently and find solutions smarter than brute-force calculations.

There exist a variety of computational techniques to solve many-body condensed matter problems. Each of these methods has its advantages and drawbacks. In this chapter we focus on two particular methods, based on a variational solution of Eq. (A.2). First, in Section A.1 we consider exact diagonalization (ED). It is an iterative method, that allows to get very efficiently and precisely several most relevant eigenvalues and eigenvectors of $\mathcal{H}$. However, this method still suffers from the exponential increase of the $\mathcal{HS}$, and only small systems are tractable with it. Second, in Section A.2 we describe the density matrix renormalization group (DMRG). We consider its modern interpretation in terms of matrix product states (MPS) and tensor

networks. It is based on a particular way to restrict the total Hilbert space based on the entanglement properties of the physical problem, and allows to consider much larger cluster sizes. Nevertheless, it works best for one-dimensional systems.

A.1 Exact diagonalization

Very often, when studying condensed matter problems, we are interested only in the properties of the ground-state $|\Psi_0\rangle$ and several low-energy excited states of the system. If moreover, the model has no long-range interactions, so that the Hamiltonian matrix is sparse, the matrix-vector multiplication can be performed relatively fast and at a low memory cost. Hence, iterative methods can be used efficiently.

The simplest power algorithm consists in a consecutive application of the Hamiltonian $\mathcal{H}$: the state $|m\rangle$ at step m is obtained recursively as

$$|m\rangle = \frac{\mathcal{H}\,|m-1\rangle}{||\mathcal{H}\,|m-1\rangle||}\,. \tag{A.3}$$

In the limit $m \to \infty$ the state $|m\rangle$ converges to the eigenstate of the Hamiltonian with the greatest (in absolute value) eigenvalue [1]. By subtracting a constant to the Hamiltonian, we can make the algorithm converge to the ground-state $|\Psi_0\rangle$. In order for the sequence $\{|m\rangle\}$ to converge, we should also ensure that the initial state $|0\rangle$ has a finite overlap with the ground-state $|\Psi_0\rangle$. Usually, this state is taken to be close to the ground-state, or chosen at random.

A huge default of the approach described above is its slow convergence time. Moreover, we notice that at each iteration m the power algorithm uses only one input, which is the result of the previous iteration. An idea to improve this approach consists in following a particular direction which maximizes the convergence rate. One way to do such calculation consists in finding a stationary point of the so-called **Rayleigh quotient**

$$r(\Phi) = \frac{\langle\Phi\,|\,\mathcal{H}\,|\,\Phi\rangle}{\langle\Phi\,|\,\Phi\rangle}\,. \tag{A.4}$$

Starting from an arbitrary state (or a candidate for the ground-state $|\Psi_0\rangle$), the optimal way to proceed consists in following the derivative of $r(\Phi)$, which is equal to

$$\nabla r(\Phi) = \frac{2}{\langle\Phi\,|\,\Phi\rangle}\left(\mathcal{H}\,|\Phi\rangle - r(\Phi)\,|\Phi\rangle\right)\,. \tag{A.5}$$

We are thus interested in minimizing the Rayleigh quotient in the subspace of the total Hilbert space generated by the states $\{|0\rangle, \mathcal{H}\,|0\rangle\}$. By continuing further this approach, at step m we create the subspace generated by states

$$\{|0\rangle, \mathcal{H}\,|0\rangle, \mathcal{H}^2\,|0\rangle, \ldots, \mathcal{H}^m\,|0\rangle\}\,, \tag{A.6}$$

called the **Krylov subspace**. The ground-state is obtained by performing an optimization in the Krylov subspace.

A.1.1 Lanczos algorithm

The basis states of the Krylov subspace from Eq. (A.6) are not convenient to work with, since by construction all the states are meant to converge to the same state,

[1] This eigenvalue is also assumed to be unique.

which is the ground-state of the Hamiltonian, and thus are not orthogonal. This problem can be avoided by combing the construction of the Krylov subspace with the Gram–Schmidt orthonormalization procedure. This leads to the formulation of the Lanczos algorithm [367], defined as follows

1. Choose an arbitrary normalized starting state $|0\rangle$.

2. Construct the second state, orthogonal to the first one, as

$$\left|1'\right\rangle = \mathcal{H}\left|0\right\rangle - a_0\left|0\right\rangle \ , \tag{A.7}$$

   with $a_0 = \langle 0 \,|\, \mathcal{H} \,|\, 0\rangle$. Normalize this state, by defining $b_1^2 = \langle 1' \,|\, 1'\rangle$ and $|1\rangle = \left|1'\right\rangle / b_1$.

3. Recursively construct a set of Lanczos states $|m\rangle$, $m \in [1, \ldots, M]$ using the relations

$$\begin{aligned} \left|(m+1)'\right\rangle &= H\left|m\right\rangle - a_m\left|m\right\rangle - b_m\left|m-1\right\rangle \ , \\ \left|m+1\right\rangle &= \left|(m+1)'\right\rangle / b_{m+1} \ . \end{aligned} \tag{A.8}$$

   The coefficients a_m and b_m must be calculated at the preceding step as

$$a_m = \langle m \,|\, \mathcal{H} \,|\, m\rangle \ , \quad b_m^2 = \left\langle m' \,\middle|\, m'\right\rangle \ . \tag{A.9}$$

   Each state $|m+1\rangle$ constructed in such a way is orthogonal to all previous Lanczos vectors.

4. The representation of the Hamiltonian $\mathcal{H}$ in the basis of the states $|m\rangle$, $m \in [1, \ldots, M]$ is given by a tridiagonal matrix $\mathcal{H}_M$

$$\mathcal{H}_M = \begin{pmatrix} a_0 & b_1 & 0 & \ldots & 0 \\ b_1 & a_1 & b_2 & \ldots & 0 \\ 0 & b_2 & \ddots & \ddots & \vdots \\ \vdots & \vdots & \ddots & a_{M-1} & b_M \\ 0 & 0 & \ldots & b_M & a_M \end{pmatrix} . \tag{A.10}$$

   Diagonalization of the tridiagonal matrix $\mathcal{H}_M$ provides an approximation for the lowest eigenenergies of $\mathcal{H}$.

In order to calculate the tridiagonal matrix $\mathcal{H}_M$ and deduce the low-energy spectrum of $\mathcal{H}$ one only needs to keep track of all the coefficients a_m and b_m calculated at steps $[1, \ldots, M]$. In a similar way, to calculate the ground-state one needs to know the exact expression of all the states $|m\rangle$ in the original (Fock) basis $\{|c_i\rangle\}$. The ground-state can then be obtained as

$$\left|\Psi_0^M\right\rangle = \sum_{m=1}^{M} U_{1m}^M \left|m\right\rangle \ , \tag{A.11}$$

where we denoted by U_{1m}^M the unitary matrix that diagonalizes $\mathcal{H}_M$ in the basis of states $\{|m\rangle\}$, sorted by ascending eigenvalues. We notice however that if the Hilbert space is big enough, it would be costly to keep track of all intermediate states $|m\rangle$. Hence, in order to calculate the ground-state $\left|\Psi_0^M\right\rangle$, once the main loop is terminated, one needs to make an additional loop, defined as follows

1. Start from the same initial state $|0\rangle$. Initialize $\left|\Psi_0^M\right\rangle$ to be zero.

2. Repeat the Lanczos construction of the state $|m+1\rangle$ from $|m\rangle$ and $|m-1\rangle$. Modify $\left|\Psi_0^M\right\rangle$ as
$$\left|\Psi_0^M\right\rangle \rightarrow \left|\Psi_0^M\right\rangle + U_{1m}^M |m\rangle \ . \tag{A.12}$$

3. Normalize $\left|\Psi_0^M\right\rangle$.

In a similar way one can calculate the second-lowest energy states $\left|\Psi_1^M\right\rangle$ etc.

A.1.2 Davidson algorithm

Usually, having $M \sim 100$ Lanczos iterations is enough to obtain faithfully the ground-state and the associated eigenvalue. Moreover, one is usually able to deduce several eigenenergies above the ground-state. We notice however that the Lanczos algorithm suffers from the orthogonality problem. Because of small numerical errors accumulated during the calculation, the orthogonality of the states $|m\rangle$ can be lost, leading to the apparition of "ghost" eigenstates and non-physical degeneracies of the eigenvalues. This problem can be solved, by re-orthogonalizing the subspace $\{|m\rangle\}$ at each iteration. Below we will present the main idea of this improved algorithm, called the Davidson algorithm [368].

In the Lanczos algorithm, at the m-th iteration, we calculate an approximate ground-state $|\Psi_0^m\rangle$ and its associated eigenenergy ϵ_0^m. If we compare it to the true ground-state $|\Psi_0\rangle$, we can express the true residual state (up to a normalization factor) as
$$|R^m\rangle = |\Psi_0\rangle - |\Psi_0^m\rangle \ . \tag{A.13}$$
The residual state estimated by the Lanczos algorithm writes however as
$$|R_L^m\rangle = \mathcal{H} |\Psi_0^m\rangle - \epsilon_0^m |\Psi_0^m\rangle \ , \tag{A.14}$$
and the Krylov space is expanded along this state. The idea of Davidson was to construct a better residual state. One can verify that if the energy ϵ_0^m is close to the true ground-state energy ϵ_0, the two residual states are related through the following identity
$$(\mathcal{H} - \epsilon_0^m) |R^m\rangle = - |R_L^m\rangle \ . \tag{A.15}$$
In order to obtain $|R^m\rangle$, knowing $|R_L^m\rangle$, one needs to inverse the relation (A.15). However, the Hamiltonian is usually very hard to inverse. The solution consists then in using only the diagonal part $\mathcal{D}$ of the Hamiltonian:
$$\left|R'^m\right\rangle = - (\mathcal{D} - \epsilon_m)^{-1} |R_L^m\rangle \ . \tag{A.16}$$
It finally allows us to express the Davidson algorithm for finding k low-energy eigenstates of the Hamiltonian.

1. Choose a set of $m \geq k$ othonormal states $\{|1\rangle, |2\rangle \ldots, |m\rangle\}$. Construct the matrix B which has these vectors as its columns. Construct the matrix H which has as columns the vectors $\{\mathcal{H}|1\rangle, \mathcal{H}|2\rangle \ldots, \mathcal{H}|m\rangle\}$.

2. Diagonalize the Hamiltonian $\mathcal{H}$ in the basis of states $\{|m\rangle\}$. Determine its k-th eigenvalue ϵ_k^m and the associated eigenstate $\left|\Psi_k^m\right\rangle$, expressed in this basis.

3. Verify the convergence by calculating the norm of the vector

$$|\epsilon^m\rangle = (H - \epsilon_k^m B)\,|\Psi_k^m\rangle \ . \tag{A.17}$$

   If the norm is smaller than some fixed small number, the calculation is terminated, and the states $|\Psi_k^m\rangle$ are kept (expressed in the original basis $\{|c_i\rangle\}$).

4. If the condition on the state $|\epsilon^m\rangle$ is not verified, the basis $\{|m\rangle\}$ is expanded. A new state added is taken as a residual state

$$|R^m\rangle = (\mathcal{D} - \epsilon_k^m)^{-1}\,|\Psi_k^m\rangle \ , \tag{A.18}$$

   orthonormalized with respect to the rest of the basis $\{|m\rangle\}$.

5. In order to keep low the memory usage, this process is restarted if the number of iterations reaches some critical value, while the convergence condition is still unsatisfied. In this case we start however with the states obtained in the last iteration of the previous calculation.

We notice that the Davidson method is very successful in finding lowest eigenenergies of the Hamiltonians with dominant diagonal terms (such as Bose-Hubbard interactions). More generally, it solves successfully the problem of ghost eigenstates, but requires more memory to keep track of all the vectors $\{|m\rangle\}$ used in the algorithm.

A.1.3 Basis states

For instance we have not discussed, what is the most suitable choice of the basis of the $\mathcal{HS}$ one should consider. In ED, in order to have an efficient numerical calculation, it is crucial that the basis states $\{|c_i\rangle\}$ have a convenient binary representation. If we consider a particular example of spin-1/2 systems, the most intuitive choice is

$$|c\rangle = |\sigma_1, \sigma_2, \ldots, \sigma_{N_s}\rangle \ , \quad c = \mathrm{bin}(|c\rangle) = \sum_{s=1}^{N_s} c_s 2^{s-1} \ , \quad c_s \in \{0(\downarrow), 1(\uparrow)\} \ . \tag{A.19}$$

Here we denote by c the binary representation associated to the vector $|c\rangle$. This construction can be easily generalized to the situations, when the local Hilbert spaces have more than two states, by allocating more bits to each site.

A.1.4 Symmetries

Taking into account the symmetries of the problem greatly simplifies the complexity of the numerical task to solve, and allows to consider bigger cluster sizes. As already briefly discussed in Section 1.4.4, the presence of a unitary symmetry implies that the Hamiltonian should be diagonalizable by blocks. Each block corresponds to a particular value of the quantum number, associated to a conserved quantity of the system. The approach described in Sections A.1.1 and A.1.2 can thus be applied to each symmetry block separately. Moreover, each ground-state calculated in different symmetry sectors will be unaffected by the Lanczos ghost eigenstate problem, and the sector dependency of a given observable provides some useful information by itself.

Several symmetries can be used in the problem, and several symmetries have been used throughout this work. The most straightforward ones to implement are

the global $U(1)$ symmetries, associated, for example, with the conservation of the total number of particles (has been used in Sections 2.2 and 2.3), or the total magnetization along the z axis (has been used in Sections 3.3 and 3.4). They are taken into account on the level of the construction of the Hilbert space. More interesting to implement are the spatial symmetries, which permute sites of the cluster, so that the Hamiltonian remains invariant. Such symmetries comprise lattice translations, rotations and reflections. In the following we will present a general approach to handle these symmetries. We will not discuss more complicated non-abelian cases here (such as the global $SU(2)$ symmetry of the Heisenberg model) [2].

Consider an action of the symmetry group G. The symmetry group acts within the subspace of the total Hilbert space $\mathcal{HS}$, by forming a reducible representation $\Gamma(G)$. This reducible representation $\Gamma(G)$ can be decomposed into irreducible representations $\Gamma_\alpha(G)$. Here α is the index of the representation, associated to a particular value of the conserved quantity. For each $g \in G$ they act on the state of the Hilbert space as

$$\Gamma_\alpha(g)\,|c_i\rangle = \Gamma^{ij}_\alpha(g)\,|c_j\rangle \ . \tag{A.20}$$

In practice, one prefers to work with one-dimensional representations only. In this case the above equation can be rewritten as

$$\Gamma_\alpha(g)\,|c\rangle = |g\cdot c\rangle \ , \tag{A.21}$$

where $|g\cdot c\rangle$ denotes an action of the group element g on the state $|c\rangle$. The resulting state necessarily belongs to the $\mathcal{HS}$, and the set of states $\{|g\cdot c\rangle\,, g\in G\}$ is called an orbit associated with $|c\rangle$. One can write projectors onto different representations as

$$P_\alpha = \frac{1}{|G|}\sum_g \chi_\alpha(g)\Gamma_\alpha(g) \ . \tag{A.22}$$

Here $\chi_\alpha(g) = \text{tr}\ \Gamma_\alpha(g)$ is the character of the group element g in the irreducible representation α, and $|G|$ is the number of elements in the group. This also allows us to construct the symmetrized state $|s_\alpha(c)\rangle$ as

$$|s_\alpha(c)\rangle = \frac{1}{\mathcal{N}_\alpha(c)}\sum_g \chi_\alpha(g)\,|g\cdot c\rangle \ . \tag{A.23}$$

Here $\mathcal{N}_\alpha(c)$ is a renormalization coefficient, that is not necessarily equal to $|G|$. The reason is that the action of certain elements $g \in G$ on some states is equivalent to the identity operation, and some symmetrized states can even vanish. It is useless to keep these vanishing states since it will lead to zero elements of the Hamiltonian matrix, and the renormalization factor for the remaining states is

$$\mathcal{N}_\alpha(c) = \sqrt{|G|\,d_\alpha(c)}\,, \tag{A.24}$$

with

$$d_\alpha(c) = \sum_{g\in G:\ |g\cdot c\rangle = |c\rangle} \chi_\alpha(g) \ . \tag{A.25}$$

[2] In order to take into account the non-abelian symmetries, one needs to consider the irreducible representations of the group with dimensions greater than one, which makes more complicated the construction of the symmetrized Hilbert space.

The symmetrized state is either zero or unique for a given orbit of G. For each such state we can thus select a representative $|r\rangle$ in the orbit. Usually, the state with the smallest binary representation is chosen. The action of the Hamiltonian $\mathcal{H}$ on such state generates a new configuration $|c'\rangle$ [3]. Such state has no reason to be a representative. Hence, we denote by $|r'\rangle$ the representative of this new state, and by g' the group element connecting them $|r'\rangle = |g' \cdot c'\rangle$. The associated symmetrized state is $|s_\alpha(r')\rangle$. This construction allows to deduce the matrix elements of the Hamiltonian $\mathcal{H}$ in the symmetry sector α as

$$\langle s_\alpha(r') \,|\, \mathcal{H} \,|\, s_\alpha(r)\rangle = \sqrt{\frac{d_{\alpha(r')}}{d_{\alpha(r)}}}\chi_\alpha(g') \,\langle c' \,|\, \mathcal{H} \,|\, r\rangle \ . \tag{A.26}$$

The ED problem is thus greatly simplified, since much smaller symmetrized Hilbert spaces are considered. We notice however that one still needs to solve in an efficient manner the problem of looking for a couple $(|r'\rangle, \chi_\alpha(g'))$ for a given state $|c'\rangle$. This can be accomplished using a hash table which maps a binary representation of the state $|c'\rangle$ onto its index, and a lookup list of the size of the total (non-symmetrized) Hilbert space, which allows to access $(|r'\rangle, \chi_\alpha(g'))$ by knowing the index of the state $|c'\rangle$. For big systems the search in the hash-table is costly. In this case, a two sublattice approach can be employed.

A.1.5 Simple way to sample clusters

In this last subsection we want to describe a convenient way to represent different clusters used in this thesis for ED simulations with periodic boundary conditions. We suppose that the model is defined on a 2D Bravais lattice generated by a couple of primitive vectors $\boldsymbol{R}_1$ and $\boldsymbol{R}_2$, connecting different unit cells of the lattice. We define the ED cluster by specifying the length (the number of unit cells) L_1 required to move along the direction $\boldsymbol{R}_1$ before encountering the periodic boundary condition wall. In this way we fix the size of a permutation group associated to the translation along the vector $\boldsymbol{R}_1$. The length of the cluster in the second direction L_2 is trivially deduced as the total number of unit cells divided by L_1. Then, we have several choices to connect different clusters in the lattice, corresponding to a different length of the permutation group associated to the translation along $\boldsymbol{R}_2$. We can list all such choices, by defining the horizontal tilt t_h. This tilt describes, by how much the cluster just above is shifted in the direction $\boldsymbol{R}_1$ with respect to the cluster under consideration. The total lattice is thus spanned by translating the cluster with vectors $L_1\boldsymbol{R}_1$ and $L_2\boldsymbol{R}_2 - t_h\boldsymbol{R}_1$. In this thesis we use a notation

$$(L_1 \times L_2,\ t_h) \tag{A.27}$$

in order to label such clusters. We notice that an alternative construction can be performed by first fixing L_2, and then defining the vertical tilt, describing by how much the cluster to the left side of the cluster in consideration is shifted up or down.

In Fig. A.1(a) we show a practical example of the above construction in a particular case of the honeycomb lattice considered in Chapters 2 and 3. By changing L_1 and t_h, we change the points in the first BZ, associated to different irreducible representations of the translation symmetry group. For a particular value of the tilt $t_h = 1 - L_1$ with L_1 being even, we obtain the discretization of the BZ shown in

[3] In practice, there could be not one, but several configurations. It is however always possible to decompose the Hamiltonian into terms that generate only one such term.

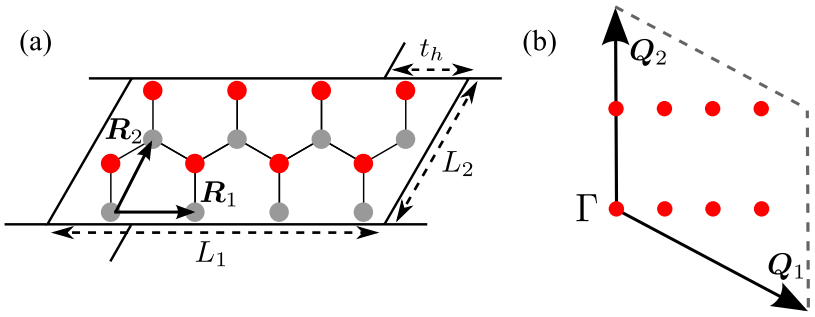

FIGURE A.1: **(a)** Schematic representation of the cluster on the honeycomb lattice. Here $L_1 = 4$, $L_2 = 2$ and tilt $t_h = -3$. **(b)** The sampling of the first BZ associated to the cluster (a).

Fig. A.1(b). In this sampling all the points lie on the same horizontal line, passing through the $\boldsymbol{\Gamma}$ point. This property has been used in practice in Section 2.2 to study the *FMSF* phase of the bosonic Haldane model.

In Section 3.3 we needed to find the best lattice to study the transitions between the *CSS*, *collinear order* and *120° order* phases of the frustrated spin-1/2 *XY* model. We observed that the 4×3 cluster with zero tilt contains (approximately) the two Dirac points $\boldsymbol{K}_\pm$ of the honeycomb lattice [4], but does not contain all the $\boldsymbol{M}$ points. Another cluster we considered in this thesis – the 4×4 cluster with no tilt, contains all three $\boldsymbol{M}$ points, but does not contain any Dirac point (even approximately). The last cluster we used – the 6×2 cluster with tilt $t_h = -4$, contains (exactly) the Dirac points and the $\boldsymbol{M}$ points. This is the reason, why we considered this cluster as a reference to deduce the phase transition points.

A.2 Density matrix renormalization group

The density matrix renormalization group (DMRG) approach to study quantum many body systems was invented by White in 1992 [350, 351]. This is an iterative variational method to find many-body ground-states, based on a particular way to truncate the Hilbert space. If we are interested only in low energy properties of the system, the space of relevant states is significantly smaller than the total Hilbert space. Hence, one only needs to find an efficient method to separate such states. The DMRG keeps quantum states, that maximize the Von Neumann entanglement entropy between two different subparts of the system. We will clarify this statement in a moment.

We consider a quantum system described by a density matrix ρ. We perform a bi-partitioning of the system onto two subparts A and B. We define the entanglement entropy associated to such partitioning as

$$S_{A|B} = -\mathrm{tr}\left(\rho_A \ln \rho_A\right) = -\mathrm{tr}\left(\rho_B \ln \rho_B\right) \ , \tag{A.28}$$

where

$$\rho_{A(B)} = \mathrm{tr}_{A(B)}\left(\rho\right) \tag{A.29}$$

is the reduced density matrix of the subpart $A(B)$, obtained by integrating out the degrees of freedom associated to the other subpart. If we denote by w_a eigenvalues

[4] The 4×3 cluster in fact does not contain exactly the two Dirac points. However, the points present in the BZ are very close to them.

of the reduced density matrix ρ_A, the entanglement entropy can be simply expressed as

$$S_{A|B} = -\sum_a w_a \ln w_a \ . \tag{A.30}$$

We see thus that if we have to remove the states from the Hilbert space, we should remove the ones corresponding to the smallest eigenvalues w_a, as this will have the weakest impact on $S_{A|B}$ and keep the most of the information on the quantum entanglement between subparts A and B. This is exactly what the DMRG algorithm is doing when constructing iteratively the many-body ground-state.

The validity of the DMRG is related to the scaling of the entanglement entropy. Gapped systems with short-range interactions are expected to follow an **area low**. It means that in the thermodynamic limit, the entanglement entropy associated to A of the size L^d (d being the spatial dimension and L – the linear size of the subsystem), scales as L^{d-1} [369]. This roughly implies that for gapped 1D systems, one can keep the same amount of eigenvalues w_a independently of the size L of the system. This also explains, why DMRG becomes less powerful in higher dimensions, or for gapless systems, for which entanglement entropy increases faster with L.

The current formulation of the DMRG is often done using matrix product states (MPS) formalism. Matrix product states provide a natural way to represent many-body quantum states in 1D. This representation can be easily obtained using the so-called singular-value decomposition technique, and the DMRG algorithm has a particularly simple form in this language. In the remaining part of this section we first make a short introduction to the singular value decomposition and the matrix product states. Next, we introduce the matrix product operators and provide a simple way to construct them in practice. At the end, we describe the DMRG algorithm formulated using the MPS language. This section is highly inspired by several excellent reviews [370–372]. To readers, interested in learning more about the method, we propose to see them. We also notice that this thesis does not have results including the DMRG (or MPS) calculations. This is the reason, why only a small section is dedicated to the subject. Our current projects are however based on this method and we will try to present relevant results for the thesis defense.

A.2.1 Singular-value decomposition

Singular-value decomposition (SVD) is a method of linear algebra used to factorize rectangular matrices. More precisely, if we consider an arbitrary matrix M of dimensions $m \times n$, using the SVD we can write it in the following form

$$M = USV^\dagger \ , \tag{A.31}$$

where three resulting matrices are

- U of dimensions $m \times \min(m,n)$, such that $UU^\dagger = I$.
- $S = \mathrm{diag}(s_1, s_2, \dots, s_r, 0, \dots)$ of dimensions $\min(m,n) \times \min(m,n)$. The entries s_i of this diagonal square matrix are called **singular values**. They are strictly positive and are usually taken in the descending order $s_1 \geq s_2 \geq \cdots \geq s_r > 0$. The number r is called the Schmidt rank of M.
- $V^\dagger$ of dimensions $\min(m,n) \times n$, such that $VV^\dagger = I$.

A.2.2 Matrix product states

We now consider a many-body quantum system defined on a lattice of N_s sites. We assume that the local degree of freedom at each site i of the lattice is described by a local Hilbert space of dimension d, composed of states $\{|\sigma_i\rangle\}$, so that any (pure) quantum state can be written as

$$|\Psi\rangle = \sum_{\sigma_1,\ldots,\sigma_{N_s}} \Psi_{\sigma_1\ldots\sigma_{N_s}} |\sigma_1,\ldots,\sigma_{N_s}\rangle \ . \tag{A.32}$$

For simplicity, we consider that the dimension d does not depend on the site i, but all the arguments can be generalized to a non-homogeneous case. The wavefunction $\Psi_{\sigma_1\ldots\sigma_{N_s}}$ is a vector of size d^{N_s}. However, it can also be seen as a tensor of rank N_s or a matrix of dimensions $d \times d^{N_s-1}$. The last representation allows us to use the SVD and decompose the wavefunction as

$$\Psi_{\sigma_1(\sigma_2\ldots\sigma_{N_s})} = U_{\sigma_1 a_1} s_{a_1} V^\dagger_{a_1(\sigma_2\ldots\sigma_{N_s})} = U_{\sigma_1 a_1} \Psi_{a_1(\sigma_2\ldots\sigma_{N_s})} \ . \tag{A.33}$$

Here we used brackets to separate the indices affected by the SVD, and the remaining indices of the many-body wavefunction. The singular value coefficient s_{a_1} was absorbed into $V^\dagger$ to provide a new wavefunction $\Psi_{a_1(\sigma_2\ldots\sigma_{N_s})}$. We repeat this procedure for the second time to get

$$\Psi_{\sigma_1\sigma_2(\sigma_3\ldots\sigma_{N_s})} = U_{\sigma_1 a_1} U_{a_1\sigma_2 a_2} \Psi_{a_1 a_2(\sigma_3\ldots\sigma_{N_s})} = U^{\sigma_1}_{a_1} U^{\sigma_2}_{a_1 a_2} \Psi_{a_1 a_2(\sigma_3\ldots\sigma_{N_s})} \ . \tag{A.34}$$

We distinguish two types of indices: the physical indices σ_i associated to physical states $|\sigma_i\rangle$, and SVD indices a_i, that we will call **auxiliary** indices. At the right hand side of the above equation we raised physical indices to outline this distinction [5]. One can now iterate the calculation, to obtain

$$\Psi_{\sigma_1\ldots\sigma_{N_s}} = U^{\sigma_1}_{a_1} U^{\sigma_2}_{a_1 a_2} \ldots U^{\sigma_{N_s-1}}_{a_{N_s-2} a_{N_s-1}} U'^{\sigma_{N_s}}_{a_{N_s-1}} = U^{\sigma_1} U^{\sigma_2} \ldots U^{\sigma_{N_s-1}} U'^{\sigma_{N_s}} \ . \tag{A.35}$$

The final expression is written in a compact form, without showing explicitly auxiliary indices a_i, in order to outline the matrix product nature of the resulting wavefunction.

The matrices U^{σ_i} have no reason to be equal at each site i. In order to be more precise, one should rather write $U^{[i]\sigma_i}$. In this section we omit to write the label $[i]$, except if the matrices has to be distinguished explicitly, for the sake of clarity. Notice that we marked the last matrix in Eq. (A.35) by a back quote sign. This matrix is in fact different from all others. Remember that we have always absorbed the singular value s_{a_i}, coming from the SVD, to the matrix $V^\dagger$ to the right. For the last iteration there is no such matrix $V^\dagger$. Hence, the last matrix does not a priori verify the relation $UU^\dagger = I$. However, in order for the wavefunction to be properly normalized, this condition should be verified, and one could freely forget this subtlety in the following.

The above procedure can be compactly written using tensor networks. The key idea of this approach consists in representing rank-n tensors as nodes with n legs. Contraction over shared indices of two tensors corresponds thus to having shared legs of the corresponding nodes. The wavefunction $\Psi_{\sigma_1\ldots\sigma_{N_s}}$ can be represented in

[5] This modification does not have any other meaning, and should not be interpreted in terms of covariant and contravariant vectors.

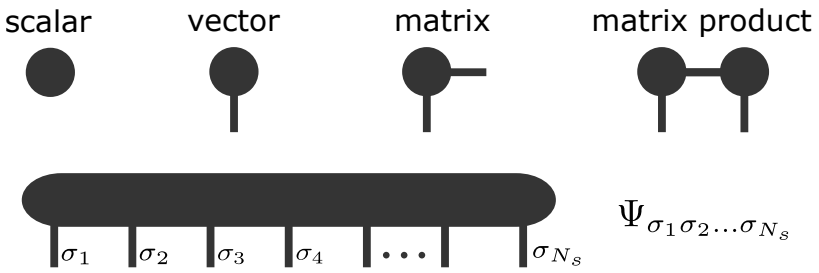

FIGURE A.2: Graphical representation of tensor networks. Each tensor is represented by a node. The rank of the tensor is equal to the number of legs of the corresponding node. Scalars correspond to a single node with no legs. Vectors have a single leg, matrices – two legs. A tensor contraction is achieved by gluing together shared legs. A wavefunction $\Psi_{\sigma_1\ldots\sigma_{N_s}}$ is represented by a single node with N_s vertical legs corresponding to physical states $\{|\sigma_i\rangle\}$.

such a way as a big node with N_s legs, labeled by physical indices σ_i. Several other simple examples of tensor networks are shown in Fig. A.2.

The tensor network representation of the MPS construction from Eqs. (A.33) and (A.35) is shown in Fig. A.3(a). First, we decompose the rank-N_s wavefunction $\Psi_{\sigma_1\ldots\sigma_{N_s}}$ onto a rank-2 tensor $U^{\sigma_1}_{a_1}$ (represented by a circle) contracted with the remaining part of the wavefunction $\Psi_{a_1(\sigma_2\ldots\sigma_{N_s})}$, which is another rank-$N_s$ tensor. However, we notice that this contracted wavefunction has one less physical index and one more auxiliary index. According to the established convention, the physical indices σ_i associated to physical states $|\sigma_i\rangle$ are represented by vertical legs. The auxiliary indices a_i are represented by horizontal legs. The dimension associated with auxiliary indices is called a **bond dimension**, denoted as D. At the last step of the construction we obtain a tensor network of connected rank-3 (in the bulk) and rank-2 (at the edges) tensors having respectively two and one auxiliary indices and one physical index each.

Because of the properties of the SVD, the bond dimension D increases from the edges to the center of the MPS. In order to be able to work efficiently with the resulting state, one has to make approximations. An approximated MPS is constructed by bounding the bond dimension D to some fixed number $D_{\max}$. This is achieved, by keeping at most $D_{\max}$ highest singular values at each SVD. This restriction is equivalent to the one based on the properties of the entanglement entropy. In fact, the eigenvalues w_i of the reduced density matrix ρ_A appearing in Eq. (A.30) are exactly the singular values one would obtain from the calculation of the corresponding SVD [6]. When the size of the system increases, one expects thus that, following the area low, for gapped 1D systems it should be enough to keep $D_{\max}$ constant.

Finally, notice that in the MPS construction we presented, the process goes from left ($i = 1$) to the right ($i = N_s$). This form of the MPS is called a left-canonical form. Similarly, one could perform a construction from right to the left to obtain the right-canonical form. One could also use a mixed-canonical form, shown schematically in Fig. A.3(b). In this case the construction starts from both sides and the last singular value is kept non-absorbed at a particular site $i \neq 1, N_s$.

[6] Such an SVD decomposition is known under the name of a Schmidt decomposition.

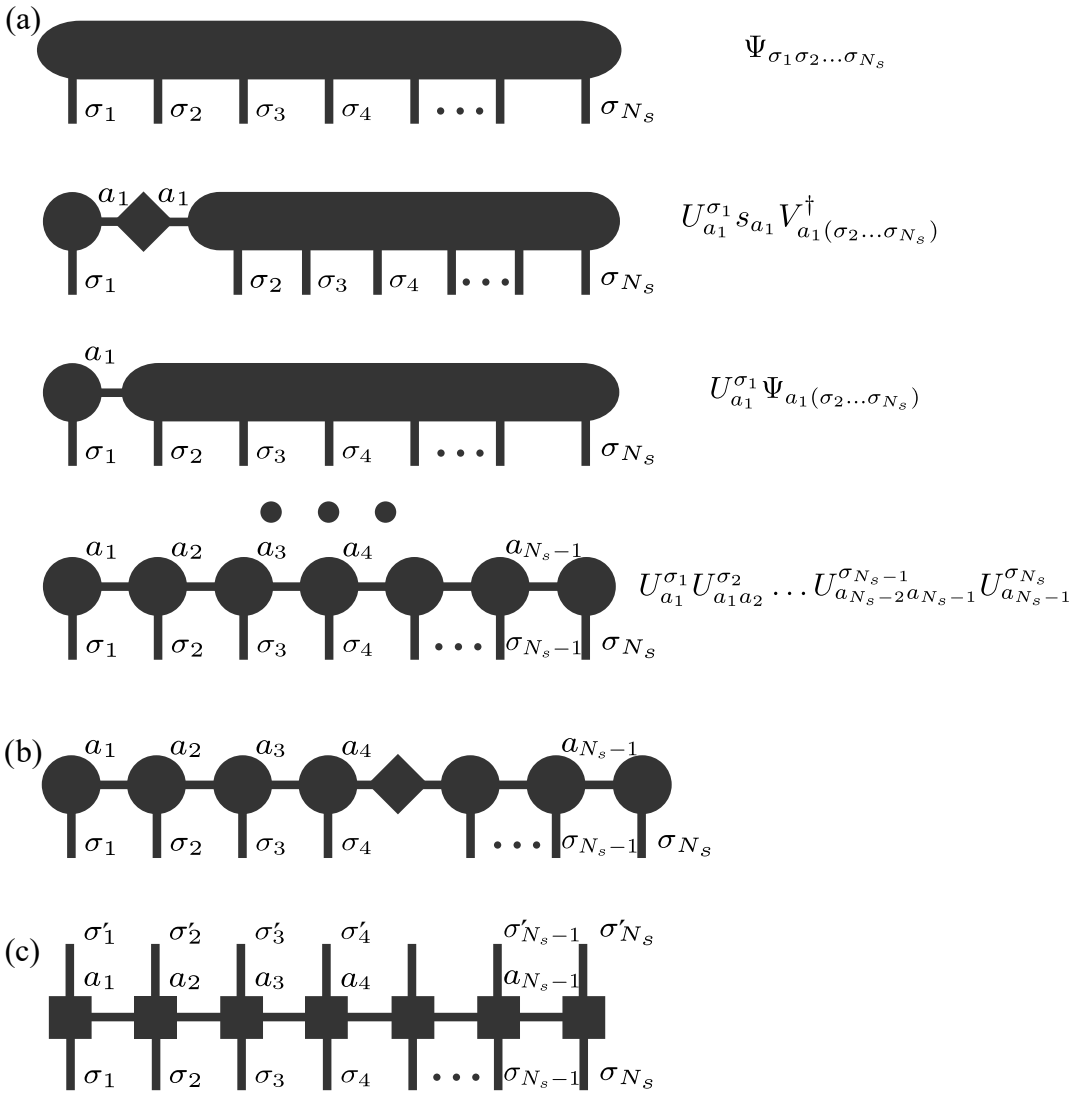

FIGURE A.3: **(a)** Graphical representation of the MPS construction, following Eqs. (A.33) and (A.35). After $N_s - 1$ iterations the resulting state corresponds to a product state of N_s tensors in the left-canonical form. Two tensors at the edges have a single auxiliary index, represented by a horizontal leg. The bulk tensors have two auxiliary indices. All tensors have a single physical index, represented by a vertical leg. **(b)** A mixed-canonical form of the MPS. The rhombus node describes a diagonal SVD matrix. **(c)** Graphical representation of an MPO. As compared to MPS, all tensors of the MPO have two physical indices σ_i and σ'_i.

A.2.3 Matrix product operators

In order to be able to work with MPS, one should have objects, which, when applied to an MPS, give as an output another MPS. Such objects are called matrix product operators (MPO). Their general expression is written as follows

$$O = W^{\sigma_1\sigma_1'} W^{\sigma_2\sigma_2'} \dots W^{\sigma_{N_s-1}\sigma_{N_s-1}'} W^{\sigma_{N_s}\sigma_{N_s}'} \ . \tag{A.36}$$

The tensor representation of MPO is shown in Fig. A.3(c). As compared to the MPS, each tensor W of an MPO has 2 physical indices σ_i and σ_i'.

It is surprisingly easy to construct a compact MPO representation for a large variety of operators. In order to show this, let us consider the following example

$$O = \sum_i \left(\alpha X_i + \beta Y_i Y_{i+1} + \gamma Z_i Z_{i+1} Z_{i+2}\right) \ . \tag{A.37}$$

We want to find an MPO representation of O. We start from the last site $i = N_s$, for which we write

$$W^{[N_s]} = \begin{pmatrix} I \\ Y_{N_s} \\ Z_{N_s} \\ 0 \\ \alpha X_{N_s} \end{pmatrix} \ , \tag{A.38}$$

where I is the identity operator on the local Hilbert space at site N_s. This vector is multiplied from the left by matrices

$$W^{[j]} = \begin{pmatrix} I & 0 & 0 & 0 & 0 \\ Y_j & 0 & 0 & 0 & 0 \\ Z_j & 0 & 0 & 0 & 0 \\ 0 & 0 & Z_j & 0 & 0 \\ \alpha X_j & \beta Y_j & 0 & \gamma Z_j & I \end{pmatrix} \ , \tag{A.39}$$

and the series is closed from the left by

$$W^{[1]} = \left(\alpha X_1, \beta Y_1, 0, \gamma Z_1, I\right) \ . \tag{A.40}$$

The operator O is obtained by multiplying all $W^{[j]}$ in the increasing order of j.

A.2.4 DMRG in the MPS language

We finally show, how MPS and MPO can be used to efficiently calculate the ground-state. This algorithm corresponds to an MPS implementation of the DMRG. It is based on a variational optimization scheme. Our goal is to find the state $|\Psi_0\rangle$ minimizing the Rayleigh quotient

$$r(\Phi) = \frac{\langle \Phi \,|\, \mathcal{H} \,|\, \Phi \rangle}{\langle \Phi \,|\, \Phi \rangle} \ . \tag{A.41}$$

This goal is achieved by introducing a Lagrange multiplier λ and extremizing the expression

$$\langle \Phi \,|\, \mathcal{H} \,|\, \Phi \rangle - \lambda \langle \Phi \,|\, \Phi \rangle \ . \tag{A.42}$$

The resulting solution $|\Psi_0\rangle$ is the ground-state, and λ – the associated eigenenergy. The calculation is performed iteratively, by modifying only one tensor $U^{[j]}$ from

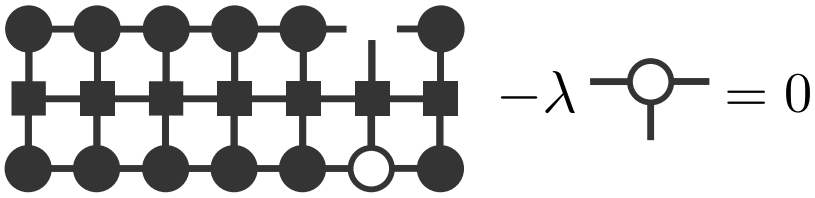

FIGURE A.4: Tensor representation of a single-site DMRG. At each iteration, a node of the MPO (denoted by an empty circle in the figure) is chosen, and the corresponding tensor is optimized.

Eq. (A.35) at a time. This optimization problem has a simple tensor representation, shown in Fig. A.4. Notice, that the most convenient form of the MPS for such an optimization, is the mixed-canonical one.

Appendix B

Chern-Simons field theory and fractional quantum Hall states

In this supplemental chapter we briefly discuss the role played by the Chern-Simons (ChS) field theory in the context of condensed matter physics. First, in Section B.1 we make a short overview of the ChS theory. Second, in Section B.2 we explain, why it is naturally used to describe the integer and fractional quantum Hall effects. Finally, in Section B.3 we discuss, how the approach should be modified in order to study lattice problems. We will explain, where lies the main difficulty, and why the quantitative results have been obtained only for the square and kagome lattices. This chapter is highly inspired by Refs. [60, 73–76].

B.1 Chern-Simons field theory

The Chern-Simons field theory is a quantum field theory in 2+1 dimensions (one time and two space dimensions) [373, 374]. The general expression of its action is

$$S = \frac{\theta}{4\pi} \int \mathrm{tr} \left(\mathcal{A} \wedge \mathrm{d}\mathcal{A} + \frac{2}{3} \mathcal{A} \wedge \mathcal{A} \wedge \mathcal{A} \right) . \tag{B.1}$$

Here $\mathcal{A} = \mathcal{A}_\mu \mathrm{d}x^\mu$ is a gauge potential defined according to the notation of Section 1.3.4, and θ is a constant, called the level of the theory. Generally, the gauge potential is a matrix-valued connection one-form. However, we will only discuss the simplest, abelian case of a one-dimensional gauge theory, which allows us to write the simplified Lagrangian density in the following way

$$\mathfrak{L} = \frac{\theta}{4\pi} \epsilon^{\mu\nu\rho} \mathcal{A}_\mu \partial_\nu \mathcal{A}_\rho \, , \tag{B.2}$$

where $\epsilon^{\mu\nu\rho}$ is an antisymmetric tensor, and $\mu, \nu, \rho = 0, 1, 2$. Notice that the Chern-Simons Lagrangian depends explicitly on the gauge potential $\mathcal{A}_\mu$, which is not gauge invariant. This is different from the case of Maxwell and Yang–Mills gauge theories, where the Lagrangian is expressed in terms of an explicitly gauge-invariant curvature two-form $\mathcal{B}$. The gauge invariance of the Chern-Simons Lagrangian is true only up to a total derivative (the action is thus invariant only up to a boundary term), and it would be impossible to write its gauge-invariant counterpart for a different number of dimensions. Finally, we notice that the Chern-Simons theory is also known as a topological field theory, since its action is invariant under coordinate transformations and, thus, independent of the metric of the base manifold.

B.2 Quantum Hall effects

B.2.1 Integer case and quantized Hall conductivity

We consider the probing ChS gauge fields $\mathcal{A}_\mu$ coupled to a dynamical (matter) degree of freedom. This coupling has to take the form

$$\mathfrak{L} = \frac{\theta}{4\pi}\epsilon^{\mu\nu\rho}\mathcal{A}_\mu\partial_\nu\mathcal{A}_\rho - J^\mu\mathcal{A}_\mu \,, \tag{B.3}$$

where the generalized current $J^\mu = (\rho, \boldsymbol{J})$ stands for both the charge density and the matter current. The gauge invariance of the action S (associated to the Lagrangian $\mathfrak{L}$) implies the conservation of the current J^μ. By calculating the variation of the action with respect to the gauge fields $\mathcal{A}_\mu$, we evaluate the response of a system in terms of such currents

$$\frac{\delta S}{\delta \mathcal{A}_\mu} = J^\mu \,. \tag{B.4}$$

By performing a rough estimation in the ChS theory case, we get two equations [1]. The first one is

$$\rho = \frac{\delta S}{\delta \mathcal{A}_0} = \frac{\theta}{2\pi}\epsilon_{ij}\partial_i\mathcal{A}_j = \frac{\theta}{2\pi}\mathcal{B} \,. \tag{B.5}$$

It describes the modification of the charge density with respect to the zero field ($\mathcal{A}_\mu = 0$) case. The second equation is

$$J^i = \frac{\delta S}{\delta \mathcal{A}_i} = -\frac{\theta}{2\pi}\epsilon^{ij}\left(\partial_0\mathcal{A}_j - \partial_j\mathcal{A}_0\right) = -\frac{\theta}{2\pi}\epsilon^{ij}E_j \,. \tag{B.6}$$

It describes the conductivity of the system. In particular, we see an apparition of a transverse conductivity component. Moreover, this conductivity is also perfectly quantized by integer numbers:

$$\frac{\hbar}{e^2}\theta = m \,, \quad \sigma_{xy} = \frac{J_x}{E_y} = -\frac{e^2}{2\pi\hbar}m \,, \quad m \in \mathbb{Z} \,. \tag{B.7}$$

This quantization originates from the compactness of the Euclidian time direction in the path-integral formulation of the quantum mechanics (the Euclidian time variable $\tau = it$ lives on a circle $[0, \beta)$, where β is the inverse temperature) [75, 76]. The theory describes thus perfectly the integer quantum Hall effect.

B.2.2 Fractional case and composite fermions

The ChS field theory provides a natural way to describe the magnetic flux attachment, exactly as required in the composite fermion formalism (see Section 1.5.1 for more details). Particle charge densities can be regarded as a set of magnetic fluxes from Eq. (B.5), while particle trajectories – as a set of currents from Eq. (B.6). This

[1] The main imprecision here consists in the fact that we do not describe the matter contribution. In particular, we assume that dynamical terms will not be affected by / affect the low-energy description. As we will see in the following, this plays a crucial role in the FQHE.

effect can be described using the following Lagrangian density

$$\mathfrak{L} = \left[\frac{\theta}{2\pi} a_0 b - \bar{\psi} e a_0 \psi\right] - \left[\frac{\theta}{4\pi}\epsilon^{ij} a_i \partial_t a_j - \bar{\psi}\frac{D_j^2}{2m}\psi\right] + \mathfrak{L}_F[\bar{\psi},\psi] \,. \tag{B.8}$$

Here a_μ are dynamical (also called **statistical**) ChS gauge fields, that should be distinguished from the external fields $\mathcal{A}_\mu$ introduced previously. b is the associated magnetic field

$$b = \epsilon_{ij}\partial_i a_j \,. \tag{B.9}$$

Fields $\bar{\psi}$ and ψ correspond to fermionic degrees of freedom. Operators $D_j = i\partial_j + e a_j$ describe the covariant derivatives. The first Lagrangian term in the square brackets provides the flux attachment

$$\langle \bar{\psi}\psi \rangle = \frac{\theta}{2\pi}\frac{b}{e} \,. \tag{B.10}$$

The second term imposes the commutation relation between gauge fields

$$[a_i(\boldsymbol{x}), a_j(\boldsymbol{y})] = i\frac{2\pi}{\theta}\epsilon_{ij}\delta(\boldsymbol{x}-\boldsymbol{y}) \,. \tag{B.11}$$

Here we made explicit the dependency of the gauge fields on the space-time coordinates, that has been omitted previously. The last term $\mathfrak{L}_F[\bar{\psi},\psi]$ describes the remaining fermionic contribution.

Integrating out the fermionic degrees of freedom leads to [75, 76]

$$\mathfrak{L} = -\frac{me^2}{4\pi\hbar}\epsilon^{\mu\nu\rho} a_\mu \partial_\nu a_\rho \,. \tag{B.12}$$

The level of the effective ChS theory must be integer, *i.e.* $m \in \mathbb{Z}$. We also consider only the leading order contribution, dominating at long wavelengths. Taking into account the coupling to the external fields $\mathcal{A}_\mu$ (as in Eq. (B.3)), the Lagrangian should be re-expressed as

$$\mathfrak{L} = \frac{e^2}{\hbar}\left(\frac{1}{2\pi}\epsilon^{\mu\nu\rho}\mathcal{A}_\mu\partial_\nu a_\rho - \frac{m}{4\pi}\epsilon^{\mu\nu\rho} a_\mu \partial_\nu a_\rho\right) \,. \tag{B.13}$$

One can now naively integrate out the fields a_μ, to see, how it will affect the probe and the measurement of the Hall conductivity. The calculation gives

$$J_i = \frac{e^2}{2\pi\hbar}\frac{1}{m}\epsilon^{ij}E_j, \quad \sigma_{xy} = \frac{e^2}{2\pi\hbar}\frac{1}{m} \,. \tag{B.14}$$

We observe that the theory provides a correct expression for the FQH conductivity associated with the Laughlin state at filling $1/m$! [2]

B.3 Lattice approach: known solutions and difficulties

The ChS theory is a continuous field theory. When considering quantum many-body problems defined on a lattice, it has to be discretized. As outlined in Ref. [241], this task is highly non-trivial and several complications arise. In this section we

[2] This calculation is known to be incorrect, following [76], since integrating out a_μ is impossible without violating the Dirac quantisation condition. The result is nevertheless known to be true. We suggest the reader to see Refs. [60, 73–76] for more advanced arguments.

discuss two main conditions that should be verified in order to keep the ChS theory consistent.

First, we notice that in a lattice problem, matter degrees of freedom $\{\bar{\psi}, \psi\}$ live on sites. The gauge fields a_μ are naturally defined on links. The magnetic fields b have thus to be defined in plaquettes of the lattice. The flux attachment procedure of the ChS theory, described by Eq. (B.10), requires to have a one-to-one correspondence between the charge densities $\langle\bar{\psi}\psi\rangle$ and the magnetic fields b. As a consequence, the lattice has to have exactly the same number of plaquettes and sites. This requirement is verified, for example, in the square lattice, studied in details in Refs. [238, 239], and in the kagome lattice, explored recently in Ref. [247]. More general situations have been addressed in Ref. [241], but, to our knowledge, no other lattice-specific study has been reported.

The second important requirement is that the constraints from Eq. (B.10) have to be independent, *i.e.* commute with each other. This is encoded more quantitatively in Eq. (B.11). This condition is naturally verified in the continuum case, because of the spatial separation: at each point in space only one gauge potential $a = a_\mu \mathrm{d}x^\mu$ is defined. The lattice problem becomes again more complicated, because the derivatives appearing in

$$b = \epsilon_{ij}\partial_i a_j \tag{B.15}$$

have to be discretized. The expression of the magnetic field in a given plaquette of the lattice involves several gauge fields defined on links composing the sides of the plaquette. The neighboring plaquettes have at least one shared link. As a consequence, the neighboring magnetic fields share the same gauge degrees of freedom. When imposing the constraint (B.10) one should thus verify that all the relations are consistent with each other and do not imply the failure of the commutation relations (B.11) between gauge fields on different links.

We notice that the the frustrated spin-1/2 model we studied in Sections 3.4 and 3.3 has been defined on the honeycomb lattice. If we exclude the NNN interactions, the corresponding geometry involves two sites per plaquette in each unit cell. One could however solve this problem in a straightforward manner, by splitting the honeycomb plaquette in two and distributing the magnetic fields attached to two densities. The real reason, why the model we considered does not allow for a proper discretization of the ChS theory, lies in the NNN hopping interactions. Such terms make the model non-planar [3]. This situation, to our knowledge, has never been discussed in literature.

[3] Planar graphs can be drawn on the plane without having their edges intersecting each other at points different from the endpoints. On the honeycomb lattice vectors connecting NNN sites intersect each other at points different from the vertices of the lattice.

Appendix C

Edge modes in Haldane Chern insulators

Our motivation in this supplemental section is to present a way to do the analytic calculation of edge modes in the Haldane model presented is Section 2.1.2 and compare it to the numerical results. We consider as a starting point the problem formulated by the Haldane Hamiltonian (2.15).

In order to perform the numerical simulation, the most convenient way is to do the partial Fourier transformation of the Hamiltonian along the x direction and to consider a finite length of the system in the y direction. Eigenvalues and eigenstate of the Hamiltonian will thus become functions of the momentum k_x and the position (layer) n along the y axis. Let us denote by

$$|\Psi(k_x, n)\rangle = \Psi(k_x, n) c^\dagger_{k_x,n} |0\rangle \tag{C.1}$$

the eigenstate on the layer n. It must verify the following equation:

$$\begin{aligned} H(k_x, n)\Psi(k_x, n) = E(k_x)\Psi(k_x, n) = \\ - \begin{pmatrix} 2t_2 \cos(\sqrt{3}ak_x + \phi_H) - (\epsilon_0 + M) & 2t_1 \cos(\frac{\sqrt{3}}{2}ak_x) \\ 2t_1 \cos(\frac{\sqrt{3}}{2}ak_x) & 2t_2 \cos(\sqrt{3}ak_x - \phi_H) - (\epsilon_0 - M) \end{pmatrix} \Psi(k_x, n) \\ - \begin{pmatrix} 2t_2 \cos(\frac{\sqrt{3}}{2}ak_x - \phi_H) & t_1 \\ 0 & 2t_2 \cos(\frac{\sqrt{3}}{2}ak_x + \phi_H) \end{pmatrix} \Psi(k_x, n+1) \\ - \begin{pmatrix} 2t_2 \cos(\frac{\sqrt{3}}{2}ak_x - \phi_H) & 0 \\ t_1 & 2t_2 \cos(\frac{\sqrt{3}}{2}ak_x + \phi_H) \end{pmatrix} \Psi(k_x, n-1) \, . \end{aligned} \tag{C.2}$$

For a finite size system different boundary conditions can be considered. In Fig. C.1 we show three different possibilities and the results of our numerical calculation of the band structure. We compare different boundary conditions with the analytical expression, obtained in Eq. (2.18).

In real space edge modes are located near the surface of the material, meaning that their local density of state exponentially decays in the bulk. In our simulations we observed these properties, as depicted on the left panel of Figure C.2. A similar analysis of edge modes can be made analytically. In order to do so let us consider an exponentially decaying Ansatz

$$\Psi(k_x, n) = \sum_i \lambda_i^n u_i(k_x) \, . \tag{C.3}$$

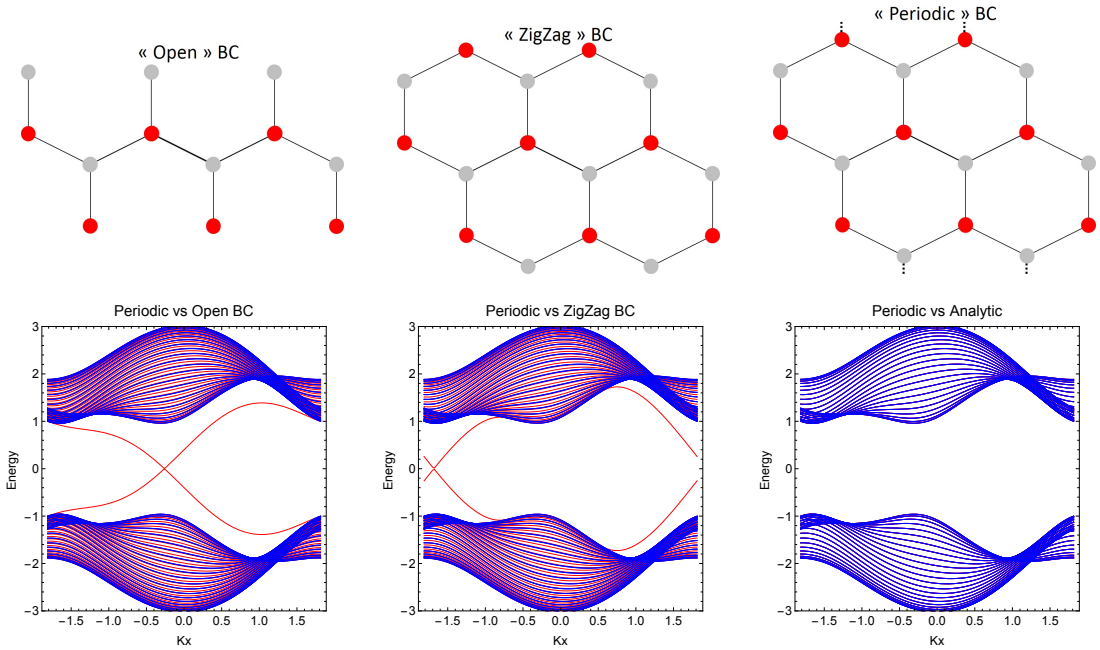

FIGURE C.1: **Top**: Three different types of boundary conditions, considered for a numerical study of the Haldane model. For the periodic case dashed lines describes the way of connecting sites at boundaries. **Bottom**: Comparison of band structure calculations for the Haldane model, based on a numerical simulation of a finite size system with different boundary conditions and an analytical calculation via Eq. 2.18. Parameters: $t_1 = 1.0, t_2 = 0.3, M = 0.4, \epsilon_0 = 0, \phi_H = \pi/2$. Results of simulation with periodic boundary condition are shown in blue.

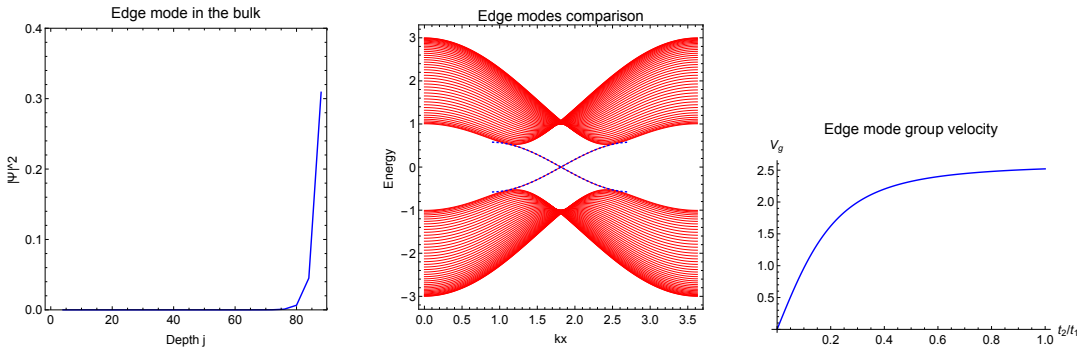

FIGURE C.2: **Left**: Exponential decrease of the chiral edge mode local density of states. **Middle**: superposition of analytical and numerical dispersion curves for edge modes. **Right**: Group velocity of edge modes at the neighborhood of the crossing point. Parameters: $t_1 = 1.0, t_2 = 0.1, M = 0, \epsilon_0 = 0, \phi_H = \pi/2$

The matrix form (C.2) gives rise to the following equation:

$$\sum_{\mu} c_{\mu}^{i}(k_x)\sigma^{\mu}u_i(k_x) = X_i(k_x)u_i(k_x) = E(k_x)u_i(k_x)\ , \tag{C.4}$$

where $X_i(k_x)$ are matrices acting on states $u_i(k_x)$ and

$$\begin{aligned}
c_0^i(k_x) =& \epsilon_0 - 2t_2\cos(\phi_H)\cos(\sqrt{3}ak_x) - 2t_2(k_x)\left(\lambda_i + \frac{1}{\lambda_i}\right)\cos(\phi_H)\cos(\frac{\sqrt{3}}{2}ak_x),\\
c_x^i(k_x) =& -2t_1\cos(\frac{\sqrt{3}}{2}ak_x) - \frac{t_1}{2}\left(\lambda_i + \frac{1}{\lambda_i}\right),\\
c_y^i(k_x) =& -\frac{it_1}{2}\left(\lambda_i - \frac{1}{\lambda_i}\right),\\
c_z^i(k_x) =& M + 2t_2\sin(\phi_H)\sin(\sqrt{3}ak_x) - 2t_2\left(\lambda_i + \frac{1}{\lambda_i}\right)\sin(\phi_H)\sin(\frac{\sqrt{3}}{2}ak_x)\ .
\end{aligned} \tag{C.5}$$

We can now diagonalize matrices X_i by squaring them (in the following we will also omit the index i). In particular, we will get

$$E(k_x) = c_0(k_x) \pm \sqrt{c_x(k_x)^2 + c_y(k_x)^2 + c_z(k_x)^2}\ . \tag{C.6}$$

We are mostly interested in the particular case with $\phi_H = \pi/2$, leading to $c_0(k_x) = 0$ everywhere in the first BZ. For the simplicity we also considered the simpler case with vanishing Semenoff mass term $M = 0$ and chemical potential $\epsilon_0 = 0$. This will lead to

$$\begin{aligned}
E^2(k_x) &= c_x^2(k_x) + c_y^2(k_x) + c_z^2(k_x)\\
&= P_0(k_x) + P_1(k_x)\left(\lambda + \frac{1}{\lambda}\right) + P_2(k_x)\left(\lambda + \frac{1}{\lambda}\right)^2\ ,
\end{aligned} \tag{C.7}$$

where

$$\begin{aligned}
P_0(k_x) &= t_1^2 + 4t_1^2\cos^2(\frac{\sqrt{3}}{2}ak_x) + 4t_2^2\sin^2(\sqrt{3}ak_x)\\
P_1(k_x) &= 2t_1^2\cos(\frac{\sqrt{3}}{2}ak_x) - 8t_2^2\sin(\sqrt{3}ak_x)\sin(\frac{\sqrt{3}}{2}ak_x)\\
P_2(k_x) &= 4t_2^2\sin^2(\frac{\sqrt{3}}{2}ak_x)\ .
\end{aligned} \tag{C.8}$$

The last expression is a second-order equation in $\tau = \lambda + 1/\lambda$. As a consequence, there exist 2 roots of τ and 4 roots of λ, and if λ_0 is a root, $1/\lambda_0$ will be another one. We can thus write the eigenfunction as a superposition of only two eigenvectors and take into account the boundary condition $u_1(k_x) + u_2(k_x) = 0$, $u_1(k_x) = -u_2(k_x) = u(k_x)$ describing the fact that the wave should vanish at the edges. This will lead to:

$$\Psi(k_x, n) = [\lambda_1^n - \lambda_2^n]\, u(k_x) \tag{C.9}$$

From the fact that matrices $E - X_1$ and $E - X_2$ share the same null eigenvector, we get

$$\begin{aligned} E^2(k_x) &= c_x^1(k_x)^2 + c_y^1(k_x)^2 + c_z^1(k_x)^2 = c_x^2(k_x)^2 + c_y^2(k_x)^2 + c_z^2(k_x)^2 = \\ &= c_x^1(k_x)c_x^2(k_x) + c_y^1(k_x)c_y^2(k_x) + c_z^1(k_x)c_z^2(k_x) \,. \end{aligned} \tag{C.10}$$

By combining these three equalities

$$\begin{aligned} 0 =& (c_x^1(k_x) - c_x^2(k_x))^2 + (c_y^1(k_x) - c_y^2(k_x))^2 + (c_z^1(k_x) - c_z^2(k_x))^2 \\ =& [\lambda_1 - \lambda_2]^2 \left[4t_2^2 \sin^2(\frac{\sqrt{3}}{2} a k_x) \left(1 - \frac{1}{\lambda_1\lambda_2}\right)^2 - \frac{t_1^2}{\lambda_1\lambda_2} \right] . \end{aligned} \tag{C.11}$$

We are not interested in a trivial solution $\lambda_1 = \lambda_2$. We want thus to find zeros of the expression at the square brackets. We define

$$L(k_x) = \frac{8t_2^2 \sin^2(\frac{\sqrt{3}}{2} a k_x) + t_1^2}{8t_2^2 \sin^2(\frac{\sqrt{3}}{2} a k_x)} \,, \tag{C.12}$$

in such a way that the condition for this expression to be vanishing gives

$$M(k_x) = \lambda_1\lambda_2 = L(k_x) \pm \sqrt{L^2(k_x) - 1} \,. \tag{C.13}$$

Independently of this result, we can use an explicit form of Eq. (C.7) to deduce that two roots of this equation should always verify

$$\left(\lambda_1 + \frac{1}{\lambda_1}\right) + \left(\lambda_2 + \frac{1}{\lambda_2}\right) = (\lambda_1 + \lambda_2)\left(1 + \frac{1}{\lambda_1\lambda_2}\right) = -\frac{P_1(k_x)}{P_2(k_x)} \,. \tag{C.14}$$

We define

$$J(k_x) = \lambda_1 + \lambda_2 = \frac{-P_1(k_x)/P_2(k_x)}{(1 + 1/\lambda_1\lambda_2)} = \frac{-P_1(k_x)/P_2(k_x)}{1 + 1/M(k_x)} \tag{C.15}$$

This new variable can now be easily calculated thanks to (C.8). At the end we can use both expressions of M and J together with Eq. (C.13) in order to deduce all roots λ_i.

$$\lambda_{1,2} = \frac{-J(k_x) \pm \sqrt{J^2(k_x) - 4M(k_x)}}{2} \tag{C.16}$$

The quadratic form of Eq. (C.7) leads to the following identity:

$$\left(\lambda_1 + \frac{1}{\lambda_1}\right)\left(\lambda_2 + \frac{1}{\lambda_2}\right) = -\frac{E^2(k_x) - P_0(k_x)}{P_2(k_x)} \tag{C.17}$$

Since an explicit expression for all roots λ_i was already found in (C.17), one can use this expression to determine finally the dispersion curve $E(k_x)$. In Fig. C.2 this result is compared to the numerical simulation output.

Appendix D

Anisotropic Haldane model for bosons: intermediate regime of the FM phase

The main goal of this supplemental section is to describe in more details the effect of the interactions on the *ZMSF – FMSF* phase transition described in Section 2.2.

We recall the approximation based on the consideration of the double-well structure, that we made in order to rewrite the Hamiltonian (2.22) in the intermediate regime of the *FM* phase:

$$\begin{aligned} a_i &\approx \frac{e^{-i\boldsymbol{K}_c\boldsymbol{r}_i}a_{\boldsymbol{K}_c} + e^{i\boldsymbol{K}_c\boldsymbol{r}_i}a_{-\boldsymbol{K}_c}}{\sqrt{N_c}} \,, \\ b_i &\approx \frac{e^{-i\boldsymbol{K}_c\boldsymbol{r}_i}b_{\boldsymbol{K}_c} + e^{i\boldsymbol{K}_c\boldsymbol{r}_i}b_{-\boldsymbol{K}_c}}{\sqrt{N_c}} \,. \end{aligned} \tag{D.1}$$

By using this, we obtain the most general approximation of the Hamiltonian:

$$\begin{aligned} H \approx& \epsilon_0 N - 4t_2 \sin\left(z_c\frac{\pi}{2}\right)\sum_{\mu=\pm}\mu\left(a^\dagger_{\mu\boldsymbol{K}_c}a_{\mu\boldsymbol{K}_c} - b^\dagger_{\mu\boldsymbol{K}_c}b_{\mu\boldsymbol{K}_c}\right) \\ &-t_1\left[2\cos\left(\frac{\pi z_c}{2}\right)+1\right]\sum_{\mu=\pm}\left(a^\dagger_{\mu\boldsymbol{K}_c}b_{\mu\boldsymbol{K}_c} + \text{h.c.}\right) \\ &+\frac{U}{2}\sum_{\mu=\pm}\left[a^\dagger_{\mu\boldsymbol{K}_c}a_{\mu\boldsymbol{K}_c}\left(\frac{a^\dagger_{\boldsymbol{K}_c}a_{\boldsymbol{K}_c}+a^\dagger_{-\boldsymbol{K}_c}a_{-\boldsymbol{K}_c}}{N_c}-1\right) + b^\dagger_{\mu\boldsymbol{K}_c}b_{\mu\boldsymbol{K}_c}\left(\frac{b^\dagger_{\boldsymbol{K}_c}b_{\boldsymbol{K}_c}+b^\dagger_{-\boldsymbol{K}_c}b_{-\boldsymbol{K}_c}}{N_c}-1\right)\right] \\ &+\frac{U}{N_s}\left[\left(a^\dagger_{\boldsymbol{K}_c}a_{-\boldsymbol{K}_c}\right)\left(a^\dagger_{-\boldsymbol{K}_c}a_{\boldsymbol{K}_c}\right) + \left(b^\dagger_{\boldsymbol{K}_c}b_{-\boldsymbol{K}_c}\right)\left(b^\dagger_{-\boldsymbol{K}_c}b_{\boldsymbol{K}_c}\right) + \text{h.c.}\right] \,. \end{aligned} \tag{D.2}$$

For the incoming purpose we define

$$\langle a_{\pm\boldsymbol{K}_c}\rangle = \sqrt{N_{A,\pm}}e^{i\theta_{A,\pm}}, \qquad \langle b_{\pm\boldsymbol{K}_c}\rangle = \sqrt{N_{B,\pm}}e^{i\theta_{B,\pm}} \,, \tag{D.3}$$

such that $N_{A,+}+N_{A,-}=N_A$, $N_{B,+}+N_{B,-}=N_B$, $N_{A,\pm}+N_{B,\pm}=N_\pm$ and $N_A+N_B = N_+ + N_- = N$. We notice that in the regime of two decoupled sublattices $t_2 \gg t_1$ one can simply write $N_{A,-} = N_{B,+} = 0$. Finally, we get the expression of the GS

energy $\epsilon_{\rm GS}$ and currents J_{AA,v_j} in terms of these new quantities:

$$\begin{aligned}\epsilon_{GS} =&\epsilon_0 N - 4t_2 \sin\left(z_c\frac{\pi}{2}\right)\sum_{\mu=\pm}\mu\left(N_{A,\mu}-N_{B,\mu}\right)\\ &-2t_1\left[2\cos\left(\frac{\pi z_c}{2}\right)+1\right]\sum_{\mu=\pm}\sqrt{N_{A,\mu}N_{B,\mu}}\cos\left(\theta_{B,\mu}-\theta_{A,\mu}\right)\\ &+\frac{U}{2}\left[N_A\left(\frac{N_A}{N_c}-1\right)+N_B\left(\frac{N_B}{N_c}-1\right)\right]+\frac{U}{N_c}\left(N_{A,+}N_{A,-}+N_{B,+}N_{B,-}\right)\ , \end{aligned} \tag{D.4}$$

$$\begin{aligned} J_{AA,v_1} = J_{AA,v_2} &= -t_2\frac{N_A}{N_c}\cos\left(z_c\frac{\pi}{2}\right)\ ,\\ J_{AA,v_3} &= 0\ . \end{aligned} \tag{D.5}$$

We see that the t_1-term pins to zero the difference between phases $\theta_{B,+}-\theta_{A,+}$ and $\theta_{B,-}-\theta_{A,-}$. However, we are still free to chose separately phases $\theta_+ = \theta_{A,+} = \theta_{B,+}$ and $\theta_- = \theta_{A,-} = \theta_{B,-}$, which corresponds again to the presence of two Goldstone modes.

We assume that the effect of interactions is weak enough so that we use the assumptions of Eq. (2.45), ie. that the double-well structure of the system is preserved. We however allow for the fact that interactions can change the value of z_c and modify the position of two minima at $\pm\boldsymbol{K}_c$. In order to study in more details this effect, we use the relations between operators $a^\dagger_{\boldsymbol{K}_c}$ and $a^\dagger_{-\boldsymbol{K}_c}$, based on properties of the unitary transformation (2.48), and write the GS energy in terms of N, N_+, $N_- = N - N_+$ and z_c only:

$$\begin{aligned}\epsilon_{GS} =&N\left\{\epsilon_0 - 4t_2\sin\left(z_c\frac{\pi}{2}\right)\frac{Y(z_c)}{\sqrt{X^2(z_c)+Y^2(z_c)}} - t_1\left[2\cos\left(z_c\frac{\pi}{2}\right)+1\right]\frac{X(z_c)}{\sqrt{X^2(z_c)+Y^2(z_c)}}\right\}\\ &+UN\left[\frac{n}{2}+\frac{Y^2(z_c)}{X^2(z_c)+Y^2(z_c)}\frac{n}{2}-\frac{1}{2}\right]+U\left[\frac{N_+\left(N-N_+\right)}{N_s}\right]\left[\frac{X^2(z_c)-2Y^2(z_c)}{X^2(z_c)+Y^2(z_c)}\right]\ , \end{aligned} \tag{D.6}$$

where $X(z_c)$ and $Y(z_c)$ are defined as follows:

$$\begin{aligned} X(z_c) &= t_1\left[1+2\cos\left(z_c\frac{\pi}{2}\right)\right]\ ,\\ Y(z_c) &= 4t_2\sin\left(z_c\frac{\pi}{2}\right)\ . \end{aligned} \tag{D.7}$$

The first effect of interactions in the *FM* consists in imposing constraints on the distribution of particles in two wells N_+ and N_-. There are two distinct sub-regimes of the *FM* phase: for $t_2^c < t_2 < \sqrt{(17+\sqrt{97})/24}\,t_2^c$ the last term in Eq. (D.6) is positive and interactions force all particles to chose one particular well, such that N_+ or N_- becomes precisely equal to N. On the other side, for $t_2 > \sqrt{(17+\sqrt{97})/24}\,t_2^c$ the last term in Eq. (D.6) is negative and the uniform distribution of particles $N_+ = N_- = N/2$ is preferred. The second effect of interactions consists in moving the position of minima at $\pm\boldsymbol{K}_c$. The contribution of interactions to the GS energy close to the

transition is

$$\Delta\epsilon'_{GS} = NUn\frac{8t_2^2}{9t_1^2}\left(z_c\frac{\pi}{2}\right)^2 + N\frac{Un}{2}\left[\frac{16}{27}\left(\frac{t_2}{t_1}\right)^2 - \frac{256}{81}\left(\frac{t_2}{t_1}\right)^4\right]\left(z_c\frac{\pi}{2}\right)^4 . \tag{D.8}$$

If particles are not all located in one well, there appears an additional contribution

$$\begin{aligned}\Delta\epsilon''_{GS} = &-\frac{16U}{3}\frac{N_+\left(N-N_+\right)}{N_s}\left(\frac{t_2}{t_1}\right)^2\left(z_c\frac{\pi}{2}\right)^2 \\ &-\frac{16U}{27}\frac{N_+\left(N-N_+\right)}{N_s}\left(\frac{3t_1^2t_2^2-16t_2^4}{t_1^4}\right)\left(z_c\frac{\pi}{2}\right)^4 .\end{aligned} \tag{D.9}$$

The second contribution $\Delta\epsilon''_{GS}$ dominates when $N_+ = N_- = N/2$, resulting in the generation of an effective repulsion between two wells.

Appendix E

Out-of plane classical solution of the frustrated spin-1/2 XY model

We consider a generalization of the ansatz (3.32) for the classical ($S \to \infty$) solution of the spin problem defined in Section 3.3. This generalized ansatz takes into account a possible out-of-plane ordering of the spin states. It is defined as follows

$$\boldsymbol{S}_i = S \begin{pmatrix} \sin\left(\theta_\mu\right)\cos\left(\phi_{\mu,i}\right) \\ \sin\left(\theta_\mu\right)\sin\left(\phi_{\mu,i}\right) \\ \cos\left(\theta_\mu\right) \end{pmatrix} . \tag{E.1}$$

Here $\mu \in [A, B]$ is the sublattice index and a free parameter θ_μ characterizes the orientation of the spin on the sublattice μ with respect to the z axis. It verifies $0 \leq \theta_\mu \leq \pi$ ($\sin\theta_\mu$ is always positive). Similarly to the Refs. [225, 242], we define phases $\phi_{A,i} = \boldsymbol{q}\cdot\boldsymbol{R}_i$ and $\phi_{B,i} = \boldsymbol{q}\cdot\boldsymbol{R}_i + \eta$, where $\boldsymbol{q}$ is the spiral wave vector and η describes the relative orientation of spins on sublattices A and B at the same unit cell. The (anti-) ferromagnetic ordering between first-neighbor sites in the xy plane is thus described by $\boldsymbol{q} = 0$, $\eta = 0(\pi)$ and $\theta_\mu = \pi/2$. The Ising antiferromagnetic ordering is defined by $\theta_A = 0, \theta_B = \pi$ and its $\mathbb{Z}_2$ symmetric solution $\theta_A = \pi, \theta_B = 0$.

E.1 Zero external magnetic field

We write the energy per spin in terms of parameters of the Hamiltonian H in Eq. (3.31) for $K_i = 0$:

$$\begin{aligned} \epsilon = &- J_1 S^2 \sin\theta_A \sin\theta_B \left[\cos\eta + \cos\left(\eta - Q_1\right) + \cos\left(\eta + Q_2\right)\right] \\ &+ J_2 S^2 \left(\sin^2\theta_A + \sin^2\theta_B\right)\left[\cos Q_1 + \cos Q_2 + \cos\left(Q_1 + Q_2\right)\right] . \end{aligned} \tag{E.2}$$

Here for simplicity we defined $Q_i = \boldsymbol{q}\cdot\boldsymbol{v}_i$ with $\boldsymbol{v}_i$ – 3 second-neighbor vectors. By minimizing the energy per spin with respect to all the parameters that we introduced, we obtain that only coplanar solutions with $\theta_\mu = \pi/2$ will survive. In this case we recover [225, 242]

$$\begin{aligned} \cos\eta &= \frac{2J_2}{J_1}\left(1 + \cos Q_1 + \cos Q_2\right) , \\ \sin\eta &= \frac{2J_2}{J_1}\left(\sin Q_1 - \sin Q_2\right) , \\ \cos Q_1 + \cos Q_2 + \cos\left(Q_1 + Q_2\right) &= \frac{1}{2}\left(\frac{J_1^2}{4J_2^2} - 3\right) . \end{aligned} \tag{E.3}$$

The uniform solution (FM order) at $\boldsymbol{q} = \boldsymbol{\Gamma}$ and $\eta = 0$ is valid until $J_2/J_1 \leq 1/6$. Spiral waves solution is valid in the regime $J_2/J_1 > 1/6$ for $J_1 \neq 0$. When two sublattices are decoupled ($J_1 = 0$), the solution corresponds to the 120° order. The energy per spin of the uniform solution is

$$\epsilon_{\text{cl}} = -3S^2 \left(J_1 - 2J_2\right) \ , \tag{E.4}$$

whereas the energy corresponding to the spiral wave state is

$$\epsilon_{\text{sp}} = -S^2 J_1 \left(\frac{J_1}{4J_2} + \frac{3J_2}{J_1}\right) \ . \tag{E.5}$$

E.2 Effect of the external magnetic field

Now we are interested in the effect of the external magnetic field h_z on the stabilization of the out-of plane (PSDW) solution. We calculate the energy per spin when the perturbation term H_z of Eq. (3.68) is added to the Hamiltonian:

$$\begin{aligned}\epsilon = &- J_1 S^2 \sin\theta_A \sin\theta_B \left[\cos\eta + \cos\left(\eta - Q_1\right) + \cos\left(\eta + Q_2\right)\right] \\ &+ J_2 S^2 \left(\sin^2\theta_A + \sin^2\theta_B\right) \left[\cos Q_1 + \cos Q_2 + \cos\left(Q_1 + Q_2\right)\right] \\ &- \frac{h_z S}{2} \left(\cos\theta_A - \cos\theta_B\right) \ .\end{aligned} \tag{E.6}$$

We suppose that the angle θ_μ is close to $\pi/2$ (the solution is almost coplanar) for small values of h_z and we perform the expansion in powers of $\tilde{\theta}_\mu = \pi/2 - \theta_\mu$. At the first order in the expansion we observe that the coplanar degree of freedom and the degree of freedom along the z axis become decoupled. Values of η, Q_1 and Q_2 correspond to the spiral wave solution (3.34) and parameters $\tilde{\theta}_A$ and $\tilde{\theta}_B$ are deduced using the following relation:

$$\begin{aligned}\tilde{\theta}_A + \tilde{\theta}_B = 0, \quad \tilde{\theta}_A - \tilde{\theta}_B = h_z \Big\{ & J_1 \left[\cos\eta + \cos\left(\eta - Q_1\right) + \cos\left(\eta + Q_2\right)\right] \\ & -2J_2 \left[\cos Q_1 + \cos Q_2 + \cos\left(Q_1 + Q_2\right)\right] \Big\}^{-1} \ .\end{aligned} \tag{E.7}$$

In the regime $J_2/J_1 \leq 1/6$ we obtain

$$\tilde{\theta}_A = -\tilde{\theta}_B = \frac{h_z}{6\left(J_1 - 2J_2\right)} \ , \tag{E.8}$$

and in the regime $J_2/J_1 > 1/6$

$$\tilde{\theta}_A = -\tilde{\theta}_B = \frac{2h_z J_2}{\left(J_1^2 + 12J_2^2\right)} \ . \tag{E.9}$$

We see thus that for the classical ansatz (3.32) the linear response of the spin to the applied magnetic field h_z is supposed to be small and of the order of h_z.

Appendix F

Résumé en français

F.1 Introduction générale

Depuis plusieurs siècles, la question fondamentale qui intéressait des générations de physiciens, était de caractériser les transitions entre les différents types de matière, telles que les changements d'état solide – liquide – gaz, le para et le ferromagnétisme, les transitions isolant – conducteur, etc. Avec le temps cette liste a été complété par des phénomènes plus abstraits et exotiques, parmi lesquelles on note la superfluidité et la supraconductivité, les isolants de Mott, les transitions vitreuses. Certaines de ces transitions nécessitent des conditions très particulières, telle que la température très basse (ou même exactement nulle) ou la pression très haute. Finalement, tous ces transitions sont très différentes. Elles correspondent à des systèmes physiques d'origine varié. Trouver la description universelle, qui permet de caractériser systématiquement les transitions des phases étaient donc un problème physique ambitieuse. Cependant, à la 2eme moitié du XX siècle, la réponse à cette question a été formulé par Ginzburg et Landau.

La description des transitions des phases proposée par Ginzburg et Landau était basé sur la considération des symétries du problème physique. En prenant comme un exemple la transition entre un liquide et un solide cristallin, on comprend intuitivement ce concept. Dans le fluide les molécules sont arrangées d'une manière homogène. L'espace des phases qui correspond à l'espace réel est occupé uniformément par le système, ce qui implique la présence de la symétrie par translation continue. Dans le cas d'un solide cristallin la situation est différente: les différentes molécules ne peuvent se trouver qu'à des coordonnés bien précis de l'espace. Ces coordonnés sont fixés par le réseau cristallin du matériel. Le réseau cristallin possède les propriétés de périodicité, ce qui implique la présence de symétrie par translation discrète. La transition entre un liquide et un solide cristallin est donc accompagné par une brisure de la symétrie par translation continue en symétrie par translation discrète.

De la même façon, en prenant comme un exemple le modèle phénoménologique de magnétisme – le modèle d'Ising, on comprend la transition de phase ferromagnétique en termes de brisure de symétrie Z_2 globale d'inversion des spins. Le modèle d'Ising est décrite par la présence des deux phases. Dans une phase tous les spins sont désordonnés – on ne verra aucune différence (à longue échelle) si on renverse tous les spins $\uparrow$ par des spins $\downarrow$. Dans la deuxième phase les domaines magnétiques se forment. Dans ce cas d'inversement des spins sera fortement visible, car la magnétisation des domaines entières sera changée lors de la transformation.

Dans certains cas, tels que, par exemple, la supraconductivité, ou la transition de Mott, les symétries en jeu peuvent être plus difficile à détecter. Cependant, l'approche de Ginzburg-Landau reste valide dans ces cas. D'une manière plus générale,

cette approche prédit que les transitions de phases nécessitent d'avoir deux phases à des symétries différentes [1]. Une phase de ces deux phases est appelée la phase ordonne, et l'autre – la phase désordonnée. La phase désordonnée a plus des symétries que la phase ordonnée: le groupe de symétrie associe aux états de basse énergie de la phase désordonnée inclus le groupe de symétrie associe a la phase ordonne. A la transition, la brisure spontanée de symétrie a lieu, et le groupe de symétrie plus grande est réduit au groupe plus petit. Cet effet se traduit par l'apparition du paramètre d'ordre – l'observable locale, qui s'annule dans la phase ordonnée et acquière la valeur finie. Le paramètre d'ordre quantifie la symétrie qui a été brisée.

Habituellement on distingue les deux types des transitions possibles: des transitions classiques, qui se passent à température finie, et des transitions quantiques, qui se passent à température nulle. Dans le deuxième cas, on peut écrire le Hamiltonien H du système comme la somme des deux termes non-commutant, comme

$$H = H_1 + pH_2, \quad [H_1, H_2] \neq 0 \,. \tag{F.1}$$

ou p est le paramètre qui interpole entre les deux termes. La transition a donc lieu, en changeant la valeur de ce paramètre. Dans le cas des transitions des phases classiques, le paramètre qu'on change a la transition affecte les fluctuations thermiques. Si les fluctuations sont suffisamment fortes, ils sont capables de détruire l'ordre macroscopique. La phase plus symétrique correspond d'habitude à la phase a haute température, tandis que la phase moins symétrique – a la phase a basse température. La physique est différente pour des transitions de phase quantiques. Dans ce cas, la transition provient des fluctuations quantiques dû au principe d'incertitude d'Heisenberg, qui sont présentes même a la température nulle. L'approche phénoménologique utilisée afin de décrire ces types de transition est cependant le même.

Malgré le fait que le paramètre d'ordre doit s'annuler dans la phase désordonné, ses fluctuations peuvent être finîtes. Lorsque le système approche le point critique, la longueur de corrélation de ces fluctuations diverge. Ceci implique l'invariance d'échelle du système et l'apparition de certaines propriétés universelles, *i.e.* des exposants critiques. Ce phénomène est connu sous le nom du phénomène critique. Les exposants critiques ne dépendent pas des détails et propriétés microscopiques du problème, mais uniquement des symétries et de la dimensionalité du modèle physique. Des systèmes d'origines très différents peuvent avoir le même ensemble d'exposants critiques, ce qui définit qualitativement le meme comportement a la transition, exprime en termes de classe d'universalité.

L'universalité de la description des transitions de phase introduite par Ginzburg et Landau est remarquable. D'autant plus remarquable était la découverte du fait que cette description n'est pas complète. La compréhension que les symétries seules ne sont pas suffisantes afin de décrire tous les phases de matière et comprendre les transitions associées, a été atteinte avec la découverte des effets de Hall quantique entier et fractionnaire. Afin de les comprendre, il faut explorer la topologie du système, et les transition de phase sont alors appelées des transitions de phase topologiques.

D'un point de vue plus pratique, les propriétés topologiques de certains matériaux et systèmes artificiels ont servi (et continuent à servir) à développer de nouvelles idées dans le contexte de l'informatique quantique. L'effet des interactions

[1] Ici on suppose qu'on change un seul paramètre à la fois. Les transitions plus compliquées avec des points triples se décomposent donc selon les transitions plus simples

fortes dans ces systèmes pourrait également conduire à des phénomènes plus exotiques tels que la formation de quasi-particules ayant une statistique anyonique et une charge fractionnaire. Ces états sont "protégés" par la topologie et peuvent servir comme blocs élémentaires d'un ordinateur quantique. À ce jour, l'influence de l'effet des interactions fortes sur la description topologique des systèmes quantiques est pourtant loin d'être maîtrisée. La réalisation expérimentale de tels systèmes est aussi difficile en pratique. Il est donc indispensable d'étudier plus en détails ces questions et d'améliorer nos protocoles de mesure afin de vérifier les prédictions théoriques.

Dans cette thèse, nous abordons les problèmes mentionnés ci-dessus. À cet égard, nous utilisons différentes méthodes analytiques et numériques. Nous proposons aussi des réalisations expérimentales des systèmes dans le contexte des simulateurs quantiques. Tout d'abord, dans le chapitre 1 nous faisons une introduction aux concepts principaux de la matière condensée topologique. Ensuite, dans les chapitres 2 et 3 nous décrivons notre travail sur l'analyse de l'effet des interactions dans des systèmes de matière condensée avec des bandes topologiques. Des problèmes liés à la réalisation expérimentale de tels systèmes sont traitées dans le chapitre 4. Ci-dessous nous fournissons une description plus détaillée du contenu de cette thèse.

F.2 Dans cette thèse

Le chapitre 1 de la thèse est dédié à l'introduction dans la topologie en mathématique et en matière condensée. En commençant par la découverte expérimentale de l'effet de Hall quantique entier, qui a conduit à la révolution dans la compréhension actuelle de la physique de matière condensée contemporaine, nous abordons d'abord le cas des systèmes non-topologiques sans interactions, ensuite des systèmes topologiques sans interactions, et enfin de la corrélation entre les propriétés topoloques et des effets des interactions fortes. Des systèmes topologiques sans interactions que nous considérons dans cette thèse correspondent à des états topologiques protégés par la symétrie. Les propriétés du volume de tels systèmes sont décrites par des invariants topologiques, tels que le nombre d'enroulement ou le nombre de Chern. En utilisant la correspondance surface – volume, la description du volume de ces systèmes est liée à la présence d'excitations de surface robustes contre le désordre. Ce propriété représente un intérêt énorme dans le domaine d'information quantique. La physique de tels états topologiques sans interactions est relativement bien comprise à nos jours. Cependant, le problème de classer des états en interactions reste largement non résolu. Ce contexte fournit donc la motivation pour la partie restante de la thèse, qui consiste à comprendre la corrélation entre l'effet des interactions et la description topologiques dans des systèmes de matière condensée.

Dans le chapitre 2, nous abordons des questions reliées aux propriétés du modèle de Haldane. C'est un modèle pour des fermions libres, définis sur le réseau en nid d'abeilles, également connu comme un modèle pour l'effet de Hall quantique anormal. Les bandes dans ce modèle sont décrites par une valeur non-nulle d'un invariant topologique $\mathbb{Z}$ – le nombre de Chern, associé à la présence de modes de bord chiraux dans un système avec des conditions au bord ouvertes. Dans la section 2.2, en suivant le travail présenté dans Réf. [1], nous présentons notre étude des propriétés du modèle de Haldane, qui se posent si au lieu des fermions nous considérons des bosons avec des interactions de Bose-Hubbard. Nous décrivons l'émergence

de phases superfluides à moment cinétique non-nul, et construisons un diagramme de phase de ce modèle. Nous considérons des géométries différentes: une géométrie habituelle en deux dimensions, mais avec une configuration anisotrope de terme des sauts, et une géométrie en échelle.

Dans le chapitre 3, nous considérons le modèle bosonique de Kane-Mele-Hubbard. Le modèle de Kane-Mele pour des fermions sans interactions est connu comme un modèle qui decrit l'effet de Hall quantique de spin. Ce modèle peut être compris comme les deux copies du modèle de Haldane bidimensionnel pour les fermions sans interactions, agencé de telle manière que l'invariant topologique $\mathbb{Z}$ est réduit à un nouveau invariant topologique $\mathbb{Z}_2$. La modification de la description du volume du système est également accompagnée par une disparition des modes de bord chiraux et l'émergence de nouveaux modes de bord hélicoïdales. Dans ce chapitre, après avoir fait un rapide introduction au cas de la particule unique, nous présentons l'exploration de l'effet des interactions. De la même façon qu'auparavant, au lieu des fermions nous considérons le système des bosons en interactions. Nous montrons que le régime de forte interactions du modèle conduit à l'émergence d'un modèle XY frustré pour des spins-1/2. Ce modèle a un très riche diagramme de phase avec une variété d'états de spins de symétrie brisée. Un des ces états de spins a été considéré comme un candidat pour le liquide de spin chiral de Kalmeyer et Laughlin, hébergeant des excitations anyoniques. En commençant par la section 3.3, nous explorons en détails des propriétés magnétiques du modèle XY frustré, en cherchant surtout des états de liquide de spin sans ordre magnétique, mais décrite par la présence de l'ordre topologique. Les résultats de ce chapitre ont déjà été présentés dans le Réf. [2].

Dans la première partie du chapitre 4 nous présentons notre travail sur des protocoles des simulateurs quantiques, qui pourraient être utilisés afin de réaliser des systèmes des chapitres 2 et 3. Ces protocoles nécessitent une génération de champs de jauge artificielle, réalisable à travers l'application de modulations périodiques dépendantes du temps. Cette procédure, connu sous le nom de l'ingénierie de Floquet, a reçu beaucoup d'attention récemment. Après avoir donné une introduction générale au domaine de l'ingénierie de Floquet et un aperçu de l'approche, qui a été appliqué récemment dans des atomes ultra-froids, nous décrivons dans Section 4.3 notre proposition d'utiliser des modulations périodiques dépendantes du temps pour générer des champs de jauge artificiels pour des excitations dans des réseaux photoniques. Cette approche a été décrite précédemment dans Refs. [1] et [3].

Dans les deux dernières sections du chapitre 4, nous considérons en détaille deux approches expérimentales qui permettent d'explorer des systèmes quantiques génériques. Tout d'abord, en suivant Réf. [4], nous proposons une approche pour réaliser le modèle de Su-Schrieffer-Heeger avec des circuits LC. Nous décrivons également un moyen de mesurer son topologie, codée dans le nombre d'enroulement associé à la phase de Berry. Ensuite, en suivant Réf. [5], nous proposons un protocole de purification qui permet de mesurer les propriétés spectrales des systèmes quantiques. Son idée principale consiste à faire deux copies du même système et mesurer le résultat d'un "quench" (c'est-à-dire une évolution du système après un changement brusque de paramètres, ou en partant d'un état initial préparé d'une manière particulière). Cette méthode a un avantage d'être applicable non seulement dans le contexte expérimental, mais aussi pour des simulations numériques, si des systèmes de taille suffisante peuvent être manipulées.

Bibliography

[1] K. Plekhanov, G. Roux, and K. Le Hur. "Floquet engineering of Haldane Chern insulators and chiral bosonic phase transitions". In: *Phys. Rev. B* 95.4, 045102 (Jan. 2017), p. 045102.

[2] K. Plekhanov et al. "Emergent Chiral Spin State in the Mott Phase of a Bosonic Kane-Mele-Hubbard Model". In: *Physical Review Letters* 120.15, 157201 (Apr. 2018), p. 157201.

[3] Karyn Le Hur et al. "Many-body quantum electrodynamics networks: Non-equilibrium condensed matter physics with light". In: *Comptes Rendus Physique* 17.8 (2016), pp. 808 –835.

[4] T. Goren et al. "Topological Zak phase in strongly coupled LC circuits". In: *Phys. Rev. B* 97.4, 041106 (Jan. 2018), p. 041106.

[5] B. Pandey, K. Plekhanov, and G. Roux. "Purification spectroscopy". In: *ArXiv e-prints* (Feb. 2018).

[6] V. L. Berezinskiĭ. "Destruction of Long-range Order in One-dimensional and Two-dimensional Systems having a Continuous Symmetry Group I. Classical Systems". In: *Soviet Journal of Experimental and Theoretical Physics* 32 (1971), p. 493.

[7] V. L. Berezinskiĭ. "Destruction of Long-range Order in One-dimensional and Two-dimensional Systems having a Continuous Symmetry Group I. Quantum Systems". In: *Soviet Journal of Experimental and Theoretical Physics* 34 (1972), p. 610.

[8] J M Kosterlitz and D J Thouless. "Ordering, metastability and phase transitions in two-dimensional systems". In: *Journal of Physics C: Solid State Physics* 6.7 (1973), p. 1181.

[9] N. D. Mermin and H. Wagner. "Absence of Ferromagnetism or Antiferromagnetism in One- or Two-Dimensional Isotropic Heisenberg Models". In: *Physical Review Letters* 17 (Nov. 1966), pp. 1133–1136.

[10] P. C. Hohenberg. "Existence of Long-Range Order in One and Two Dimensions". In: *Physical Review* 158 (June 1967), pp. 383–386.

[11] K. v. Klitzing, G. Dorda, and M. Pepper. "New Method for High-Accuracy Determination of the Fine-Structure Constant Based on Quantized Hall Resistance". In: *Phys. Rev. Lett.* 45 (6 1980), pp. 494–497.

[12] D. C. Tsui, H. L. Stormer, and A. C. Gossard. "Two-Dimensional Magnetotransport in the Extreme Quantum Limit". In: *Phys. Rev. Lett.* 48 (22 1982), pp. 1559–1562.

[13] J. P. Eisenstein and H. L. Stormer. "The Fractional Quantum Hall Effect". In: *Science* 248.4962 (1990), pp. 1510–1516.

[14] R. B. Laughlin. "Quantized Hall conductivity in two dimensions". In: *Phys. Rev. B* 23 (10 1981), pp. 5632–5633.

[15] A. Stern. "Anyons and the quantum Hall effect - A pedagogical review". In: *Annals of Physics* 323 (Jan. 2008), pp. 204–249.

[16] Leon N. Cooper. "Bound Electron Pairs in a Degenerate Fermi Gas". In: *Phys. Rev.* 104 (4 1956), pp. 1189–1190.

[17] J. Bardeen, L. N. Cooper, and J. R. Schrieffer. "Theory of Superconductivity". In: *Phys. Rev.* 108 (5 1957), pp. 1175–1204.

[18] Pierre Gilles De Gennes. *Superconductivity of Metals and Alloys*. Advanced book classics. Cambridge, MA: Perseus, 1999.

[19] Mikio Nakahara. *Geometry, topology and physics*. Graduate student series in physics. Bristol: Hilger, 1990.

[20] G.L. Naber. *Topology, Geometry and Gauge fields: Foundations*. Texts in Applied Mathematics. Springer New York, 2010.

[21] *Topological Aspects of Condensed Matter Physics: Lecture Notes of the Les Houches Summer School: Volume 103, August 2014*. Oxford: Oxford University Press, 2017, p. 704.

[22] S. Pancharatnam. "Generalized theory of interference, and its applications". In: *Proceedings of the Indian Academy of Sciences - Section A* 44.5 (1956), pp. 247–262.

[23] Berry M. V. "Quantal phase factors accompanying adiabatic changes". In: *Proceedings of the Royal Society of London A: Mathematical, Physical and Engineering Sciences* 392.1802 (1984), pp. 45–57.

[24] A. Messiah. *Quantum Mechanics*. Dover books on physics. Dover Publications, 1961.

[25] Barry Simon. "Holonomy, the Quantum Adiabatic Theorem, and Berry's Phase". In: *Phys. Rev. Lett.* 51 (24 1983), pp. 2167–2170.

[26] J. Zak. "Berry's phase for energy bands in solids". In: *Phys. Rev. Lett.* 62 (23 1989), pp. 2747–2750.

[27] W. P. Su, J. R. Schrieffer, and A. J. Heeger. "Solitons in Polyacetylene". In: *Phys. Rev. Lett.* 42 (25 1979), pp. 1698–1701.

[28] J. K. Asbóth, L. Oroszlány, and A. Pályi. "A Short Course on Topological Insulators: Band-structure topology and edge states in one and two dimensions". In: *ArXiv e-prints* (Sept. 2015).

[29] A. Y. Kitaev. "6. QUANTUM COMPUTING: Unpaired Majorana fermions in quantum wires". In: *Physics Uspekhi* 44 (Oct. 2001), p. 131.

[30] C.W.J. Beenakker. "Search for Majorana Fermions in Superconductors". In: *Annual Review of Condensed Matter Physics* 4.1 (2013), pp. 113–136.

[31] J. E. Avron, R. Seiler, and B. Simon. "Homotopy and Quantization in Condensed Matter Physics". In: *Phys. Rev. Lett.* 51 (1 1983), pp. 51–53.

[32] F. D. M. Haldane. "Model for a Quantum Hall Effect without Landau Levels: Condensed-Matter Realization of the "Parity Anomaly"". In: *Phys. Rev. Lett.* 61 (18 1988), pp. 2015–2018.

[33] G. E. Volovik. "Fermion zero modes on vortices in chiral superconductors". In: *Soviet Journal of Experimental and Theoretical Physics Letters* 70 (Nov. 1999), pp. 609–614.

[34] G.E. Volovik. *The Universe in a Helium Droplet*. International Series of Monographs on Physics. OUP Oxford, 2009.

[35] D. J. Thouless et al. "Quantized Hall Conductance in a Two-Dimensional Periodic Potential". In: *Phys. Rev. Lett.* 49 (6 1982), pp. 405–408.

[36] M. Kohmoto. "Topological invariant and the quantization of the Hall conductance". In: *Annals of Physics* 160 (Apr. 1985), pp. 343–354.

[37] R. Giles. "Reconstruction of gauge potentials from Wilson loops". In: *Phys. Rev. D* 24 (Oct. 1981), pp. 2160–2168.

[38] A. Altland and M. R. Zirnbauer. "Nonstandard symmetry classes in mesoscopic normal-superconducting hybrid structures". In: *Phys. Rev. B* 55 (Jan. 1997), pp. 1142–1161.

[39] Freeman J. Dyson. "The Threefold Way. Algebraic Structure of Symmetry Groups and Ensembles in Quantum Mechanics". In: *Journal of Mathematical Physics* 3.6 (1962), pp. 1199–1215.

[40] Alexei Kitaev. "Periodic table for topological insulators and superconductors". In: *AIP Conference Proceedings* 1134.1 (2009), pp. 22–30.

[41] Andreas P. Schnyder et al. "Classification of topological insulators and superconductors in three spatial dimensions". In: *Phys. Rev. B* 78 (19 2008), p. 195125.

[42] Andreas P. Schnyder et al. "Classification of Topological Insulators and Superconductors". In: *AIP Conference Proceedings* 1134.1 (2009), pp. 10–21.

[43] S. Ryu et al. "Topological insulators and superconductors: tenfold way and dimensional hierarchy". In: *New Journal of Physics* 12.6, 065010 (June 2010), p. 065010.

[44] A. Bernevig and T. Neupert. "Topological Superconductors and Category Theory". In: *ArXiv e-prints* (June 2015).

[45] Ching-Kai Chiu et al. "Classification of topological quantum matter with symmetries". In: *Rev. Mod. Phys.* 88 (3 2016), p. 035005.

[46] C. L. Kane and E. J. Mele. "Quantum Spin Hall Effect in Graphene". In: *Physical Review Letters* 95.22, 226801 (Nov. 2005), p. 226801.

[47] C. L. Kane and E. J. Mele. "Z_2 Topological Order and the Quantum Spin Hall Effect". In: *Phys. Rev. Lett.* 95 (14 2005), p. 146802.

[48] B. Andrei Bernevig, Taylor L. Hughes, and Shou-Cheng Zhang. "Quantum Spin Hall Effect and Topological Phase Transition in HgTe Quantum Wells". In: *Science* 314.5806 (2006), pp. 1757–1761.

[49] M. König et al. "Quantum Spin Hall Insulator State in HgTe Quantum Wells". In: *Science* 318 (Nov. 2007), p. 766.

[50] Yasuhiro Hatsugai. "Chern number and edge states in the integer quantum Hall effect". In: *Phys. Rev. Lett.* 71 (22 1993), pp. 3697–3700.

[51] Xiao-Liang Qi, Yong-Shi Wu, and Shou-Cheng Zhang. "General theorem relating the bulk topological number to edge states in two-dimensional insulators". In: *Phys. Rev. B* 74 (4 2006), p. 045125.

[52] A. M. Essin and V. Gurarie. "Bulk-boundary correspondence of topological insulators from their respective Green's functions". In: *Phys. Rev. B* 84.12, 125132 (Sept. 2011), p. 125132.

[53] G. M. Graf and M. Porta. "Bulk-Edge Correspondence for Two-Dimensional Topological Insulators". In: *Communications in Mathematical Physics* 324 (Dec. 2013), pp. 851–895.

[54] E. Prodan and H. Schulz-Baldes. "Bulk and Boundary Invariants for Complex Topological Insulators: From K-Theory to Physics". In: *ArXiv e-prints* (Oct. 2015).

[55] N. Sedlmayr et al. "Bulk boundary correspondence and the existence of Majorana bound states on the edges of 2D topological superconductors". In: *Phys. Rev. B* 96.18, 184516 (Nov. 2017), p. 184516.

[56] R. B. Laughlin. "Anomalous Quantum Hall Effect: An Incompressible Quantum Fluid with Fractionally Charged Excitations". In: *Phys. Rev. Lett.* 50 (18 1983), pp. 1395–1398.

[57] B. I. Halperin. "Statistics of Quasiparticles and the Hierarchy of Fractional Quantized Hall States". In: *Phys. Rev. Lett.* 52 (18 1984), pp. 1583–1586.

[58] Daniel Arovas, J. R. Schrieffer, and Frank Wilczek. "Fractional Statistics and the Quantum Hall Effect". In: *Phys. Rev. Lett.* 53 (7 1984), pp. 722–723.

[59] Robert B. Laughlin. "The Quantum Hall Effect". In: ed. by Richard E. Prange and Steven M. Girvin. New York, NY: Springer US, 1987. Chap. Elementary Theory: the Incompressible Quantum Fluid, pp. 233–301.

[60] Eduardo Fradkin. *Field Theories of Condensed Matter Physics*. 2nd ed. Cambridge University Press, 2013.

[61] L. Saminadayar et al. "Observation of the $e/3$ Fractionally Charged Laughlin Quasiparticle". In: *Phys. Rev. Lett.* 79 (13 1997), pp. 2526–2529.

[62] R. de-Picciotto et al. "Direct observation of a fractional charge". In: *Physica B Condensed Matter* 249 (June 1998), pp. 395–400.

[63] F. D. M. Haldane. "Fractional Quantization of the Hall Effect: A Hierarchy of Incompressible Quantum Fluid States". In: *Phys. Rev. Lett.* 51 (7 1983), pp. 605–608.

[64] J. K. Jain. "Composite-fermion approach for the fractional quantum Hall effect". In: *Phys. Rev. Lett.* 63 (2 1989), pp. 199–202.

[65] J. K. Jain. "Theory of the fractional quantum Hall effect". In: *Phys. Rev. B* 41 (11 1990), pp. 7653–7665.

[66] Jainendra K. Jain. *Composite Fermions*. Cambridge University Press, 2007.

[67] C.-C. Chang and J. K. Jain. "Microscopic Origin of the Next-Generation Fractional Quantum Hall Effect". In: *Physical Review Letters* 92.19, 196806 (May 2004), p. 196806.

[68] R. Willett et al. "Observation of an even-denominator quantum number in the fractional quantum Hall effect". In: *Physical Review Letters* 59 (Oct. 1987), pp. 1776–1779.

[69] G. Moore and N. Read. "Nonabelions in the fractional quantum hall effect". In: *Nuclear Physics B* 360 (Aug. 1991), pp. 362–396.

[70] A. Y. Kitaev. "Fault-tolerant quantum computation by anyons". In: *Annals of Physics* 303 (Jan. 2003), pp. 2–30.

[71] Chetan Nayak et al. "Non-Abelian anyons and topological quantum computation". In: *Rev. Mod. Phys.* 80 (3 2008), pp. 1083–1159.

[72] Ady Stern and Netanel H. Lindner. "Topological Quantum Computation—From Basic Concepts to First Experiments". In: *Science* 339.6124 (2013), pp. 1179–1184.

[73] Ana Lopez and Eduardo Fradkin. "Fractional quantum Hall effect and Chern-Simons gauge theories". In: *Phys. Rev. B* 44 (10 1991), pp. 5246–5262.

[74] B. I. Halperin, Patrick A. Lee, and Nicholas Read. "Theory of the half-filled Landau level". In: *Phys. Rev. B* 47 (12 1993), pp. 7312–7343.

[75] X.G. Wen. *Quantum Field Theory of Many-Body Systems: From the Origin of Sound to an Origin of Light and Electrons*. Oxford Graduate Texts. OUP Oxford, 2004.

[76] D. Tong. "Lectures on the Quantum Hall Effect". In: *ArXiv e-prints* (June 2016).

[77] X.-G. Wen. "Topological order: from long-range entangled quantum matter to an unification of light and electrons". In: *ArXiv e-prints* (Oct. 2012).

[78] T. Senthil. "Symmetry-Protected Topological Phases of Quantum Matter". In: *Annual Review of Condensed Matter Physics* 6 (Mar. 2015), pp. 299–324.

[79] S. Rachel. "Interacting Topological Insulators: a review". In: *ArXiv e-prints* (Apr. 2018).

[80] X. G. Wen. "Topological Order in Rigid States". In: *Int. J. Mod. Phys.* B4 (1990), p. 239.

[81] I. Affleck et al. "Rigorous results on valence-bond ground states in antiferromagnets". In: *Physical Review Letters* 59 (Aug. 1987), pp. 799–802.

[82] F. D. M. Haldane. "Nonlinear Field Theory of Large-Spin Heisenberg Antiferromagnets: Semiclassically Quantized Solitons of the One-Dimensional Easy-Axis Néel State". In: *Phys. Rev. Lett.* 50 (15 1983), pp. 1153–1156.

[83] F.D.M. Haldane. "Continuum dynamics of the 1-D Heisenberg antiferromagnet: Identification with the O(3) nonlinear sigma model". In: *Physics Letters A* 93.9 (1983), pp. 464 –468.

[84] I. Affleck and F. D. M. Haldane. "Critical theory of quantum spin chains". In: *Phys. Rev. B* 36 (Oct. 1987), pp. 5291–5300.

[85] I. Affleck. "REVIEW ARTICLE: Quantum spin chains and the Haldane gap". In: *Journal of Physics Condensed Matter* 1 (May 1989), pp. 3047–3072.

[86] F. Pollmann et al. "Entanglement spectrum of a topological phase in one dimension". In: *Phys. Rev. B* 81.6, 064439 (Feb. 2010), p. 064439.

[87] X. Chen, Z.-C. Gu, and X.-G. Wen. "Classification of gapped symmetric phases in one-dimensional spin systems". In: *Phys. Rev. B* 83.3, 035107 (Jan. 2011), p. 035107.

[88] Xie Chen et al. "Symmetry protected topological orders and the group cohomology of their symmetry group". In: *Phys. Rev. B* 87 (15 2013), p. 155114.

[89] G. Misguich. "Quantum spin liquids". In: *ArXiv e-prints* (Sept. 2008).

[90] Leon Balents. "Spin liquids in frustrated magnets". In: *Nature* 464 (2010), 199 EP –.

[91] C. Lacroix, P. Mendels, and F. Mila. *Introduction to Frustrated Magnetism: Materials, Experiments, Theory*. Springer Series in Solid-State Sciences. Springer Berlin Heidelberg, 2011.

[92] L. Savary and L. Balents. "Quantum spin liquids: a review". In: *Reports on Progress in Physics* 80.1, 016502 (Jan. 2017), p. 016502.

[93] Yi Zhou, Kazushi Kanoda, and Tai-Kai Ng. "Quantum spin liquid states". In: *Rev. Mod. Phys.* 89 (2 2017), p. 025003.

[94] P.W. Anderson. "Resonating valence bonds: A new kind of insulator?" In: *Materials Research Bulletin* 8.2 (1973), pp. 153 –160.

[95] J. G. Bednorz and K. A. Müller. "Possible high T_c superconductivity in the Ba-La-Cu-O system". In: *Zeitschrift fur Physik B Condensed Matter* 64 (June 1986), pp. 189–193.

[96] P. W. Anderson. "The resonating valence bond state in La2CuO4 and superconductivity". In: *Science* 235 (Mar. 1987), pp. 1196–1198.

[97] V. Kalmeyer and R. B. Laughlin. "Equivalence of the resonating-valence-bond and fractional quantum Hall states". In: *Phys. Rev. Lett.* 59 (18 1987), pp. 2095–2098.

[98] X. G. Wen, Frank Wilczek, and A. Zee. "Chiral spin states and superconductivity". In: *Phys. Rev. B* 39 (16 1989), pp. 11413–11423.

[99] X. G. Wen. "Mean-field theory of spin-liquid states with finite energy gap and topological orders". In: *Phys. Rev. B* 44 (6 1991), pp. 2664–2672.

[100] N. Read and Subir Sachdev. "Large-N expansion for frustrated quantum antiferromagnets". In: *Phys. Rev. Lett.* 66 (13 1991), pp. 1773–1776.

[101] R. Moessner and S. L. Sondhi. "Resonating Valence Bond Phase in the Triangular Lattice Quantum Dimer Model". In: *Phys. Rev. Lett.* 86 (9 2001), pp. 1881–1884.

[102] Xiao-Gang Wen. "Quantum orders and symmetric spin liquids". In: *Phys. Rev. B* 65 (16 2002), p. 165113.

[103] A. Kitaev. "Anyons in an exactly solved model and beyond". In: *Annals of Physics* 321 (Jan. 2006), pp. 2–111.

[104] Steven Weinberg. *The Quantum Theory of Fields, Volume 1: Foundations*. Cambridge University Press, 2005.

[105] "The quantum theory of the electron". In: *Proceedings of the Royal Society of London A: Mathematical, Physical and Engineering Sciences* 117.778 (1928), pp. 610–624.

[106] Hermann Weyl. "Electron and gravitation". In: *Z.Phys. 56; 330-352* (1929).

[107] E. Majorana. "Teoria simmetrica dell'elettrone e del positrone". In: *Il Nuovo Cimento* 14 (Apr. 1937), pp. 171–184.

[108] Jerome Cayssol. "Introduction to Dirac materials and topological insulators". In: *Comptes Rendus Physique, Volume 14, Issue 9, p. 760-778* (2013).

[109] T. O. Wehling, A. M. Black-Schaffer, and A. V. Balatsky. "Dirac materials". In: *Advances in Physics* 63 (Jan. 2014), pp. 1–76.

[110] P. R. Wallace. "The Band Theory of Graphite". In: *Phys. Rev.* 71 (9 1947), pp. 622–634.

[111] K. S. Novoselov et al. "Two-dimensional gas of massless Dirac fermions in graphene". In: *Nature* 438 (Nov. 2005), pp. 197–200.

[112] A. H. Castro Neto et al. "The electronic properties of graphene". In: *Rev. Mod. Phys.* 81 (1 2009), pp. 109–162.

[113] J. E. Moore and L. Balents. "Topological invariants of time-reversal-invariant band structures". In: *Phys. Rev. B* 75 (12 2007), p. 121306.

[114] M. Z. Hasan and C. L. Kane. "*Colloquium* : Topological insulators". In: *Rev. Mod. Phys.* 82 (4 2010), pp. 3045–3067.

[115] Xiao-Liang Qi and Shou-Cheng Zhang. "Topological insulators and superconductors". In: *Rev. Mod. Phys.* 83 (4 2011), pp. 1057–1110.

[116] M. Fruchart and D. Carpentier. "An introduction to topological insulators". In: *Comptes Rendus Physique* 14 (Nov. 2013), pp. 779–815.

[117] Liang Fu, C. L. Kane, and E. J. Mele. "Topological Insulators in Three Dimensions". In: *Phys. Rev. Lett.* 98 (10 2007), p. 106803.

[118] G.E. Volovik. *Exotic Properties of Superfluid 3He*. Series in modern condensed matter physics. World Scientific, 1992.

[119] Xiangang Wan et al. "Topological semimetal and Fermi-arc surface states in the electronic structure of pyrochlore iridates". In: *Phys. Rev. B* 83 (20 2011), p. 205101.

[120] S. M. Young et al. "Dirac Semimetal in Three Dimensions". In: *Phys. Rev. Lett.* 108 (14 2012), p. 140405.

[121] Lunan Huang et al. "Spectroscopic evidence for a type II Weyl semimetallic state in MoTe2". In: *Nat Mater* 15.11 (2016). Letter, pp. 1155–1160.

[122] N. P. Armitage, E. J. Mele, and A. Vishwanath. "Weyl and Dirac semimetals in three-dimensional solids". In: *Reviews of Modern Physics* 90.1, 015001 (Jan. 2018), p. 015001.

[123] Gordon W. Semenoff. "Condensed-Matter Simulation of a Three-Dimensional Anomaly". In: *Phys. Rev. Lett.* 53 (26 1984), pp. 2449–2452.

[124] Zhong Wang, Xiao-Liang Qi, and Shou-Cheng Zhang. "Equivalent topological invariants of topological insulators". In: *New Journal of Physics* 12.6 (2010), p. 065007.

[125] D. Sticlet et al. "Geometrical engineering of a two-band Chern insulator in two dimensions with arbitrary topological index". In: *Phys. Rev. B* 85.16, 165456 (Apr. 2012), p. 165456.

[126] Gregor Jotzu et al. "Experimental realization of the topological Haldane model with ultracold fermions". In: *Nature* 515.7526 (2014), pp. 237–240.

[127] N. Fläschner et al. "Experimental reconstruction of the Berry curvature in a Floquet Bloch band". In: *Science* 352.6289 (2016), pp. 1091–1094.

[128] Alexandru Petrescu, Andrew A. Houck, and Karyn Le Hur. "Anomalous Hall effects of light and chiral edge modes on the Kagome lattice". In: *Phys. Rev. A* 86 (5 2012), p. 053804.

[129] Tianhan Liu, Benoît Dou çot, and Karyn Le Hur. "Anisotropic quantum spin Hall effect, spin-orbital textures, and the Mott transition". In: *Phys. Rev. B* 88 (24 2013), p. 245119.

[130] Cristina Bena and Laurent Simon. "Dirac point metamorphosis from third-neighbor couplings in graphene and related materials". In: *Phys. Rev. B* 83 (11 2011), p. 115404.

[131] G. Montambaux et al. "A universal Hamiltonian for motion and merging of Dirac points in a two-dimensional crystal". In: *The European Physical Journal B* 72.4 (2009), p. 509.

[132] Kai Sun et al. "Nearly Flatbands with Nontrivial Topology". In: *Phys. Rev. Lett.* 106 (23 2011), p. 236803.

[133] Titus Neupert et al. "Fractional Quantum Hall States at Zero Magnetic Field". In: *Phys. Rev. Lett.* 106 (23 2011), p. 236804.

[134] D. N. Sheng et al. "Fractional quantum Hall effect in the absence of Landau levels". In: *Nature Communications* 2, 389 (July 2011), p. 389.

[135] Y.-F. Wang et al. "Fractional Quantum Hall Effect of Hard-Core Bosons in Topological Flat Bands". In: *Physical Review Letters* 107.14, 146803 (Sept. 2011), p. 146803.

[136] N. Regnault and B. A. Bernevig. "Fractional Chern Insulator". In: *Physical Review X* 1.2, 021014 (Oct. 2011), p. 021014.

[137] E. J. Bergholtz and Z. Liu. "Topological Flat Band Models and Fractional Chern Insulators". In: *International Journal of Modern Physics B* 27, 1330017 (Sept. 2013), p. 1330017.

[138] R. L. Doretto and M. O. Goerbig. "Flat-band ferromagnetism and spin waves in topological Hubbard models". In: *Phys. Rev. B* 92.24, 245124 (Dec. 2015), p. 245124.

[139] T. Neupert et al. "Fractional (Chern and topological) insulators". In: *Physica Scripta Volume T* 164.1, 014005 (Dec. 2015), p. 014005.

[140] E. M. Spanton et al. "Observation of fractional Chern insulators in a van der Waals heterostructure". In: *ArXiv e-prints* (June 2017).

[141] R. Sohal, L. H. Santos, and E. Fradkin. "Chern-Simons composite fermion theory of fractional Chern insulators". In: *Phys. Rev. B* 97.12, 125131 (Mar. 2018), p. 125131.

[142] J. Struck et al. "Tunable Gauge Potential for Neutral and Spinless Particles in Driven Optical Lattices". In: *Phys. Rev. Lett.* 108 (22 2012), p. 225304.

[143] K. Jiménez-García et al. "Peierls Substitution in an Engineered Lattice Potential". In: *Phys. Rev. Lett.* 108 (22 2012), p. 225303.

[144] M. Atala et al. "Observation of chiral currents with ultracold atoms in bosonic ladders". In: *Nature Physics* 10 (Aug. 2014), pp. 588–593.

[145] J. Struck et al. "Quantum Simulation of Frustrated Classical Magnetism in Triangular Optical Lattices". In: *Science* 333.6045 (2011), pp. 996–999.

[146] J. Struck et al. "Engineering Ising-XY spin-models in a triangular lattice using tunable artificial gauge fields". In: *Nat Phys* 9.11 (2013). Article, pp. 738–743.

[147] Colin J. Kennedy et al. "Observation of Bose-Einstein condensation in a strong synthetic magnetic field". In: *Nat Phys* 11.10 (2015), pp. 859–864.

[148] Alberto Amo et al. "Superfluidity of polaritons in semiconductor microcavities". In: *Nat Phys* 5.11 (2009), pp. 805–810.

[149] Jan Klaers et al. "Bose-Einstein condensation of photons in an optical microcavity". In: *Nature* 468.7323 (2010), pp. 545–548.

[150] Lih-King Lim, Andreas Hemmerich, and C. Morais Smith. "Artificial staggered magnetic field for ultracold atoms in optical lattices". In: *Phys. Rev. A* 81 (2 2010), p. 023404.

[151] G. Möller and N. R. Cooper. "Condensed ground states of frustrated Bose-Hubbard models". In: *Phys. Rev. A* 82 (6 2010), p. 063625.

[152] Michael P. Zaletel et al. "Chiral bosonic Mott insulator on the frustrated triangular lattice". In: *Phys. Rev. B* 89 (15 2014), p. 155142.

[153] Ivana Vasic et al. "Chiral bosonic phases on the Haldane honeycomb lattice". In: *Phys. Rev. B* 91 (9 2015), p. 094502.

[154] Peter Fulde and Richard A. Ferrell. "Superconductivity in a Strong Spin-Exchange Field". In: *Phys. Rev.* 135 (3A 1964), A550–A563.

[155] A. I. Larkin and Y. N. Ovchinnikov. "Nonuniform state of superconductors". In: *Zh. Eksp. Teor. Fiz.* 47 (1964), pp. 1136–1146.

[156] A. Isacsson and S. M. Girvin. "Multiflavor bosonic Hubbard models in the first excited Bloch band of an optical lattice". In: *Phys. Rev. A* 72 (5 2005), p. 053604.

[157] A. B. Kuklov. "Unconventional Strongly Interacting Bose-Einstein Condensates in Optical Lattices". In: *Phys. Rev. Lett.* 97 (11 2006), p. 110405.

[158] W. Vincent Liu and Congjun Wu. "Atomic matter of nonzero-momentum Bose-Einstein condensation and orbital current order". In: *Phys. Rev. A* 74 (1 2006), p. 013607.

[159] Torben Müller et al. "State Preparation and Dynamics of Ultracold Atoms in Higher Lattice Orbitals". In: *Phys. Rev. Lett.* 99 (20 2007), p. 200405.

[160] Georg Wirth, Matthias Olschlager, and Andreas Hemmerich. "Evidence for orbital superfluidity in the P-band of a bipartite optical square lattice". In: *Nat Phys* 7.2 (2011), pp. 147–153.

[161] Colin V. Parker, Li-Chung Ha, and Cheng Chin. "Direct observation of effective ferromagnetic domains of cold atoms in a shaken optical lattice". In: *Nat Phys* 9.12 (2013), pp. 769–774.

[162] M. A. Khamehchi et al. "Spin-momentum coupled Bose-Einstein condensates with lattice band pseudospins". In: *Nature Communications* 7 (2016), p. 10867.

[163] Christopher L. Henley. "Ordering due to disorder in a frustrated vector antiferromagnet". In: *Phys. Rev. Lett.* 62 (17 1989), pp. 2056–2059.

[164] Yoshihito Kuno, Takashi Nakafuji, and Ikuo Ichinose. "Phase diagrams of the Bose-Hubbard model and the Haldane-Bose-Hubbard model with complex hopping amplitudes". In: *Phys. Rev. A* 92 (6 2015), p. 063630.

[165] Shunsuke Furukawa and Masahito Ueda. "Excitation band topology and edge matter waves in Bose–Einstein condensates in optical lattices". In: *New Journal of Physics* 17.11 (2015), p. 115014.

[166] F. D. M. Haldane. "Effective Harmonic-Fluid Approach to Low-Energy Properties of One-Dimensional Quantum Fluids". In: *Phys. Rev. Lett.* 47 (25 1981), pp. 1840–1843.

[167] A.O. Gogolin, A.A. Nersesyan, and A.M. Tsvelik. *Bosonization and Strongly Correlated Systems*. Cambridge University Press, 2004.

[168] T. Giamarchi. *Quantum Physics in One Dimension*. International Series of Monographs on Physics. Clarendon Press, 2003.

[169] M. A. Cazalilla et al. "One dimensional bosons: From condensed matter systems to ultracold gases". In: *Rev. Mod. Phys.* 83 (4 2011), pp. 1405–1466.

[170] E. Orignac and T. Giamarchi. "Meissner effect in a bosonic ladder". In: *Phys. Rev. B* 64 (14 2001), p. 144515.

[171] Arya Dhar et al. "Bose-Hubbard model in a strong effective magnetic field: Emergence of a chiral Mott insulator ground state". In: *Phys. Rev. A* 85 (4 2012), p. 041602.

[172] Alexandru Petrescu and Karyn Le Hur. "Bosonic Mott Insulator with Meissner Currents". In: *Phys. Rev. Lett.* 111 (15 2013), p. 150601.

[173] Akiyuki Tokuno and Antoine Georges. "Ground states of a Bose–Hubbard ladder in an artificial magnetic field: field-theoretical approach". In: *New Journal of Physics* 16.7 (2014), p. 073005.

[174] M. Piraud et al. "Vortex and Meissner phases of strongly interacting bosons on a two-leg ladder". In: *Phys. Rev. B* 91 (14 2015), p. 140406.

[175] S. Greschner et al. "Spontaneous Increase of Magnetic Flux and Chiral-Current Reversal in Bosonic Ladders: Swimming against the Tide". In: *Phys. Rev. Lett.* 115 (19 2015), p. 190402.

[176] Ahmet Kele ş and M. Ö. Oktel. "Mott transition in a two-leg Bose-Hubbard ladder under an artificial magnetic field". In: *Phys. Rev. A* 91 (1 2015), p. 013629.

[177] E Orignac et al. "Incommensurate phases of a bosonic two-leg ladder under a flux". In: *New Journal of Physics* 18.5 (2016), p. 055017.

[178] S. Greschner and F. Heidrich-Meisner. "Quantum phases of strongly interacting bosons on a two-leg Haldane ladder". In: *Phys. Rev. A* 97.3, 033619 (Mar. 2018), p. 033619.

[179] F. Pollmann et al. "Symmetry protection of topological phases in one-dimensional quantum spin systems". In: *Phys. Rev. B* 85.7, 075125 (Feb. 2012), p. 075125.

[180] Alexandru Petrescu and Karyn Le Hur. "Chiral Mott insulators, Meissner effect, and Laughlin states in quantum ladders". In: *Phys. Rev. B* 91 (5 2015), p. 054520.

[181] A. Petrescu et al. "Precursor of the Laughlin state of hard-core bosons on a two-leg ladder". In: *Phys. Rev. B* 96.1, 014524 (July 2017), p. 014524.

[182] Marcello Calvanese Strinati et al. "Laughlin-like States in Bosonic and Fermionic Atomic Synthetic Ladders". In: *Phys. Rev. X* 7 (2 2017), p. 021033.

[183] C. L. Kane, Ranjan Mukhopadhyay, and T. C. Lubensky. "Fractional Quantum Hall Effect in an Array of Quantum Wires". In: *Phys. Rev. Lett.* 88 (3 2002), p. 036401.

[184] Jeffrey C. Y. Teo and C. L. Kane. "From Luttinger liquid to non-Abelian quantum Hall states". In: *Phys. Rev. B* 89 (8 2014), p. 085101.

[185] Titus Neupert et al. "Wire deconstructionism of two-dimensional topological phases". In: *Phys. Rev. B* 90 (20 2014), p. 205101.

[186] Po-Hao Huang et al. "Non-Abelian topological spin liquids from arrays of quantum wires or spin chains". In: *Phys. Rev. B* 93 (20 2016), p. 205123.

[187] Liang Fu and C. L. Kane. "Topological insulators with inversion symmetry". In: *Phys. Rev. B* 76 (4 2007), p. 045302.

[188] L. Fu and C. L. Kane. "Time reversal polarization and a Z_2 adiabatic spin pump". In: *Phys. Rev. B* 74.19, 195312 (Nov. 2006), p. 195312.

[189] S.-S. Lee and S. Ryu. "Many-Body Generalization of the Z_2 Topological Invariant for the Quantum Spin Hall Effect". In: *Physical Review Letters* 100.18, 186807 (May 2008), p. 186807.

[190] Stephan Rachel and Karyn Le Hur. "Topological insulators and Mott physics from the Hubbard interaction". In: *Phys. Rev. B* 82 (7 2010), p. 075106.

[191] Christian Griset and Cenke Xu. "Phase diagram of the Kane-Mele-Hubbard model". In: *Phys. Rev. B* 85 (4 2012), p. 045123.

[192] Wei Wu et al. "Quantum spin Hall insulators with interactions and lattice anisotropy". In: *Phys. Rev. B* 85 (20 2012), p. 205102.

[193] Johannes Reuther, Ronny Thomale, and Stephan Rachel. "Magnetic ordering phenomena of interacting quantum spin Hall models". In: *Phys. Rev. B* 86 (15 2012), p. 155127.

[194] M. Hohenadler et al. "Quantum phase transitions in the Kane-Mele-Hubbard model". In: *Phys. Rev. B* 85 (11 2012), p. 115132.

[195] Martin Hohenadler and Fakher F. Assaad. "Rashba coupling and magnetic order in correlated helical liquids". In: *Phys. Rev. B* 90 (24 2014), p. 245148.

[196] Manuel Laubach et al. "Rashba spin-orbit coupling in the Kane-Mele-Hubbard model". In: *Phys. Rev. B* 90 (16 2014), p. 165136.

[197] J. R. Schrieffer and P. A. Wolff. "Relation between the Anderson and Kondo Hamiltonians". In: *Physical Review* 149 (Sept. 1966), pp. 491–492.

[198] S. Bravyi, D. P. DiVincenzo, and D. Loss. "Schrieffer-Wolff transformation for quantum many-body systems". In: *Annals of Physics* 326 (Oct. 2011), pp. 2793–2826.

[199] Christopher N. Varney et al. "Kaleidoscope of Exotic Quantum Phases in a Frustrated XY Model". In: *Phys. Rev. Lett.* 107 (7 2011), p. 077201.

[200] C N Varney et al. "Quantum phases of hard-core bosons in a frustrated honeycomb lattice". In: *New Journal of Physics* 14.11 (2012), p. 115028.

[201] Juan Carrasquilla et al. "Nature of the phases in the frustrated XY model on the honeycomb lattice". In: *Phys. Rev. B* 88 (24 2013), p. 241109.

[202] Andrea Di Ciolo et al. "Spiral antiferromagnets beyond the spin-wave approximation: Frustrated XY and Heisenberg models on the honeycomb lattice". In: *Phys. Rev. B* 89 (9 2014), p. 094413.

[203] Tigran A. Sedrakyan, Leonid I. Glazman, and Alex Kamenev. "Spontaneous Formation of a Nonuniform Chiral Spin Liquid in a Moat-Band Lattice". In: *Phys. Rev. Lett.* 114 (3 2015), p. 037203.

[204] T. Nakafuji and I. Ichinose. "Phase diagrams of Bose-Hubbard model and antiferromagnetic spin-1/2 models on a honeycomb lattice". In: *Phys. Rev. A* 96.1, 013628 (July 2017), p. 013628.

[205] Zhenyue Zhu, David A. Huse, and Steven R. White. "Unexpected z-Direction Ising Antiferromagnetic Order in a Frustrated Spin-1/2 $J_1 - J_2$ XY Model on the Honeycomb Lattice". In: *Phys. Rev. Lett.* 111 (25 2013), p. 257201.

[206] Zhenyue Zhu and Steven R. White. "Quantum phases of the frustrated XY models on the honeycomb lattice". In: *Modern Physics Letters B* 28.31 (2014), p. 1430016.

[207] R. F. Bishop, P. H. Y. Li, and C. E. Campbell. "Frustrated spin-$\frac{1}{2}$ J_1–J_2 isotropic XY model on the honeycomb lattice". In: *Phys. Rev. B* 89 (21 2014), p. 214413.

[208] N. Goldman et al. "Realistic Time-Reversal Invariant Topological Insulators with Neutral Atoms". In: *Phys. Rev. Lett.* 105 (25 2010), p. 255302.

[209] Colin J. Kennedy et al. "Spin-Orbit Coupling and Quantum Spin Hall Effect for Neutral Atoms without Spin Flips". In: *Phys. Rev. Lett.* 111 (22 2013), p. 225301.

[210] J. Struck, J. Simonet, and K. Sengstock. "Spin-orbit coupling in periodically driven optical lattices". In: *Phys. Rev. A* 90 (3 2014), p. 031601.

[211] Zhongbo Yan et al. "A General Time-Periodic Driving Approach to Realize Topological Phases in Cold Atomic Systems". In: *Scientific Reports* 5 (2015), p. 16197.

[212] X.-J. Liu, K. T. Law, and T. K. Ng. "Realization of 2D Spin-Orbit Interaction and Exotic Topological Orders in Cold Atoms". In: *Physical Review Letters* 112.8, 086401 (Feb. 2014), p. 086401.

[213] Victor Galitski and Ian B. Spielman. "Spin-orbit coupling in quantum gases". In: *Nature* 494 (2013). Review Article, p. 49.

[214] N. Goldman, J. C. Budich, and P. Zoller. "Topological quantum matter with ultracold gases in optical lattices". In: *Nat Phys* 12.7 (2016), pp. 639–645.

[215] L. Zhang and X.-J. Liu. "Spin-orbit coupling and topological phases for ultracold atoms". In: *ArXiv e-prints* (June 2018).

[216] L. Huang et al. "Experimental realization of two-dimensional synthetic spin-orbit coupling in ultracold Fermi gases". In: *Nature Physics* 12 (June 2016), pp. 540–544.

[217] Z. Wu et al. "Realization of two-dimensional spin-orbit coupling for Bose-Einstein condensates". In: *Science* 354 (Oct. 2016), pp. 83–88.

[218] Mohammad Hafezi et al. "Robust optical delay lines with topological protection". In: *Nat Phys* 7.11 (2011), pp. 907–912.

[219] V. G. Sala et al. "Spin-Orbit Coupling for Photons and Polaritons in Microstructures". In: *Physical Review X* 5.1, 011034 (Jan. 2015), p. 011034.

[220] Ling Lu, John D. Joannopoulos, and Marin Soljacic. "Topological photonics". In: *Nat Photon* 8.11 (2014), pp. 821–829.

[221] A. H. MacDonald, S. M. Girvin, and D. Yoshioka. "$\frac{t}{U}$ expansion for the Hubbard model". In: *Phys. Rev. B* 37 (16 1988), pp. 9753–9756.

[222] R. Flint and P. A. Lee. "Emergent Honeycomb Lattice in $LiZn_2Mo_3O_8$". In: *Physical Review Letters* 111.21, 217201 (Nov. 2013), p. 217201.

[223] J.B. Fouet, P. Sindzingre, and C. Lhuillier. "An investigation of the quantum $J_1 - J_2 - J_3$ model on the honeycomb lattice". In: *Eur. Phys. J. B* 20.2 (2001), pp. 241–254.

[224] Fa Wang. "Schwinger boson mean field theories of spin liquid states on a honeycomb lattice: Projective symmetry group analysis and critical field theory". In: *Phys. Rev. B* 82 (2 2010), p. 024419.

[225] A. Mulder et al. "Spiral order by disorder and lattice nematic order in a frustrated Heisenberg antiferromagnet on the honeycomb lattice". In: *Phys. Rev. B* 81 (21 2010), p. 214419.

[226] B. K. Clark, D. A. Abanin, and S. L. Sondhi. "Nature of the Spin Liquid State of the Hubbard Model on a Honeycomb Lattice". In: *Phys. Rev. Lett.* 107 (8 2011), p. 087204.

[227] A. F. Albuquerque et al. "Phase diagram of a frustrated quantum antiferromagnet on the honeycomb lattice: Magnetic order versus valence-bond crystal formation". In: *Phys. Rev. B* 84 (2 2011), p. 024406.

[228] D. C. Cabra, C. A. Lamas, and H. D. Rosales. "Quantum disordered phase on the frustrated honeycomb lattice". In: *Phys. Rev. B* 83 (9 2011), p. 094506.

[229] Johannes Reuther, Dmitry A. Abanin, and Ronny Thomale. "Magnetic order and paramagnetic phases in the quantum J_1-J_2-J_3 honeycomb model". In: *Phys. Rev. B* 84 (1 2011), p. 014417.

[230] Fabio Mezzacapo and Massimo Boninsegni. "Ground-state phase diagram of the quantum $J_1 - J_2$ model on the honeycomb lattice". In: *Phys. Rev. B* 85 (6 2012), p. 060402.

[231] Hao Zhang and C. A. Lamas. "Exotic disordered phases in the quantum J_1-J_2 model on the honeycomb lattice". In: *Phys. Rev. B* 87 (2 2013), p. 024415.

[232] R. Ganesh, Jeroen van den Brink, and Satoshi Nishimoto. "Deconfined Criticality in the Frustrated Heisenberg Honeycomb Antiferromagnet". In: *Phys. Rev. Lett.* 110 (12 2013), p. 127203.

[233] Shou-Shu Gong et al. "Phase diagram of the spin-$\frac{1}{2}$ J_1-J_2 Heisenberg model on a honeycomb lattice". In: *Phys. Rev. B* 88 (16 2013), p. 165138.

[234] Zhenyue Zhu, David A. Huse, and Steven R. White. "Weak Plaquette Valence Bond Order in the S=1/2 Honeycomb J_1-J_2 Heisenberg Model". In: *Phys. Rev. Lett.* 110 (12 2013), p. 127205.

[235] Shou-Shu Gong et al. "Global phase diagram of competing ordered and quantum spin-liquid phases on the kagome lattice". In: *Phys. Rev. B* 91 (7 2015), p. 075112.

[236] F. Ferrari, S. Bieri, and F. Becca. "Competition between spin liquids and valence-bond order in the frustrated spin-1/2 Heisenberg model on the honeycomb lattice". In: *Phys. Rev. B* 96.10, 104401 (Sept. 2017), p. 104401.

[237] H. S. Nair et al. "Short range order in the quantum XXZ honeycomb lattice material BaCo_2(PO_4)_2". In: *ArXiv e-prints* (Dec. 2017).

[238] Eduardo Fradkin. "Jordan-Wigner transformation for quantum-spin systems in two dimensions and fractional statistics". In: *Phys. Rev. Lett.* 63 (3 1989), pp. 322–325.

[239] J. Ambjørn and G.W. Semenoff. "Fermionized spin systems and the boson-fermion mapping in (2+1)-dimensional gauge theory". In: *Physics Letters B* 226.1 (1989), pp. 107 –112.

[240] Ana Lopez, A. G. Rojo, and Eduardo Fradkin. "Chern-Simons theory of the anisotropic quantum Heisenberg antiferromagnet on a square lattice". In: *Phys. Rev. B* 49 (21 1994), pp. 15139–15158.

[241] Kai Sun, Krishna Kumar, and Eduardo Fradkin. "Discretized Abelian Chern-Simons gauge theory on arbitrary graphs". In: *Phys. Rev. B* 92 (11 2015), p. 115148.

[242] E. Rastelli, A. Tassi, and L. Reatto. "Non-simple magnetic order for simple Hamiltonians". In: *Physica B+C* 97.1 (1979), pp. 1 –24.

[243] P. W. Anderson. "Infrared Catastrophe in Fermi Gases with Local Scattering Potentials". In: *Phys. Rev. Lett.* 18 (24 1967), pp. 1049–1051.

[244] Paolo Zanardi and Nikola Paunković. "Ground state overlap and quantum phase transitions". In: *Phys. Rev. E* 74 (3 2006), p. 031123.

[245] S.-J. Gu. "Fidelity approach to quantum phase transitions". In: *ArXiv e-prints* (Nov. 2008).

[246] Christopher N. Varney et al. "Interaction effects and quantum phase transitions in topological insulators". In: *Phys. Rev. B* 82 (11 2010), p. 115125.

[247] K. Kumar, K. Sun, and E. Fradkin. "Chiral spin liquids on the kagome lattice". In: *Phys. Rev. B* 92.9, 094433 (Sept. 2015), p. 094433.

[248] P. Jordan and E. Wigner. "Über das Paulische Äquivalenzverbot". In: *Zeitschrift für Physik* 47.9 (1928), pp. 631–651.

[249] D. J. Thouless. "Level crossing and the fractional quantum Hall effect". In: *Phys. Rev. B* 40 (17 1989), pp. 12034–12036.

[250] Ciarán Hickey et al. "Haldane-Hubbard Mott Insulator: From Tetrahedral Spin Crystal to Chiral Spin Liquid". In: *Phys. Rev. Lett.* 116 (13 2016), p. 137202.

[251] Krishna Kumar et al. "Numerical evidence for a chiral spin liquid in the XXZ antiferromagnetic Heisenberg model on the kagome lattice at $m = \frac{2}{3}$ magnetization". In: *Phys. Rev. B* 94 (13 2016), p. 134410.

[252] Qian Niu, D. J. Thouless, and Yong-Shi Wu. "Quantized Hall conductance as a topological invariant". In: *Phys. Rev. B* 31 (6 1985), pp. 3372–3377.

[253] Yasuhiro Hatsugai. "Explicit Gauge Fixing for Degenerate Multiplets: A Generic Setup for Topological Orders". In: *Journal of the Physical Society of Japan* 73.10 (2004), pp. 2604–2607.

[254] Yasuhiro Hatsugai. "Characterization of Topological Insulators: Chern Numbers for Ground State Multiplet". In: *Journal of the Physical Society of Japan* 74.5 (2005), pp. 1374–1377.

[255] Rui Yu et al. "Equivalent expression of $\mathbb{Z}_2$ topological invariant for band insulators using the non-Abelian Berry connection". In: *Phys. Rev. B* 84 (7 2011), p. 075119.

[256] Hassan Shapourian and Bryan K. Clark. "Variational identification of a fractional Chern insulator in an extended Bose-Hubbard model". In: *Phys. Rev. B* 93 (3 2016), p. 035125.

[257] Ehud Altman and Ronen Vosk. "Universal Dynamics and Renormalization in Many-Body-Localized Systems". In: *Annual Review of Condensed Matter Physics* 6.1 (2015), pp. 383–409.

[258] Rahul Nandkishore and David A. Huse. "Many-Body Localization and Thermalization in Quantum Statistical Mechanics". In: *Annual Review of Condensed Matter Physics* 6.1 (2015), pp. 15–38.

[259] F. Alet and N. Laflorencie. "Many-body localization: an introduction and selected topics". In: *ArXiv e-prints* (Nov. 2017).

[260] Richard P. Feynman. "Simulating physics with computers". In: *International Journal of Theoretical Physics* 21.6 (1982), pp. 467–488.

[261] D. Jaksch and P. Zoller. "The cold atom Hubbard toolbox". In: *Annals of Physics* 315 (Jan. 2005), pp. 52–79.

[262] M. Lewenstein et al. "Ultracold atomic gases in optical lattices: mimicking condensed matter physics and beyond". In: *Advances in Physics* 56 (Mar. 2007), pp. 243–379.

[263] Immanuel Bloch, Jean Dalibard, and Wilhelm Zwerger. "Many-body physics with ultracold gases". In: *Rev. Mod. Phys.* 80 (3 2008), pp. 885–964.

[264] Immanuel Bloch, Jean Dalibard, and Sylvain Nascimbène. "Quantum simulations with ultracold quantum gases". In: *Nature Physics* 8 (2012). Review Article, p. 267.

[265] M. Saffman, T. G. Walker, and K. Mølmer. "Quantum information with Rydberg atoms". In: *Rev. Mod. Phys.* 82 (3 2010), pp. 2313–2363.

[266] R. Blatt and C. F. Roos. "Quantum simulations with trapped ions". In: *Nature Physics* 8 (2012). Review Article, p. 277.

[267] B. Gadway and B. Yan. "Strongly interacting ultracold polar molecules". In: *Journal of Physics B Atomic Molecular Physics* 49.15, 152002 (Aug. 2016), p. 152002.

[268] Andrew A. Houck, Hakan E. Türeci, and Jens Koch. "On-chip quantum simulation with superconducting circuits". In: *Nature Physics* 8 (2012), p. 292.

[269] Iacopo Carusotto and Cristiano Ciuti. "Quantum fluids of light". In: *Rev. Mod. Phys.* 85 (1 2013), pp. 299–366.

[270] X. Gu et al. "Microwave photonics with superconducting quantum circuits". In: *Physics Reports* 718 (Nov. 2017), pp. 1–102.

[271] Iulia Buluta and Franco Nori. "Quantum Simulators". In: *Science* 326.5949 (2009), pp. 108–111.

[272] I. M. Georgescu, S. Ashhab, and Franco Nori. "Quantum simulation". In: *Rev. Mod. Phys.* 86 (1 2014), pp. 153–185.

[273] Cheng Chin et al. "Feshbach resonances in ultracold gases". In: *Rev. Mod. Phys.* 82 (2 2010), pp. 1225–1286.

[274] W. S. Bakr et al. "A quantum gas microscope for detecting single atoms in a Hubbard-regime optical lattice". In: *Nature* 462 (Nov. 2009), pp. 74–77.

[275] Jon H. Shirley. "Solution of the Schrödinger Equation with a Hamiltonian Periodic in Time". In: *Phys. Rev.* 138 (4B 1965), B979–B987.

[276] Hideo Sambe. "Steady States and Quasienergies of a Quantum-Mechanical System in an Oscillating Field". In: *Phys. Rev. A* 7 (6 1973), pp. 2203–2213.

[277] F Gesztesy and H Mitter. "A note on quasi-periodic states". In: *Journal of Physics A: Mathematical and General* 14.4 (1981), p. L79.

[278] Wilhelm Magnus. "On the exponential solution of differential equations for a linear operator". In: *Communications on Pure and Applied Mathematics* 7.4 (1954), pp. 649–673.

[279] S. Blanes et al. "The Magnus expansion and some of its applications". In: *Physics Reports* 470.5–6 (2009), pp. 151 –238.

[280] E.B. Feldman. "On the convergence of the magnus expansion for spin systems in periodic magnetic fields". In: *Physics Letters A* 104.9 (1984), pp. 479 –481.

[281] M. Matti Maricq. "Application of average Hamiltonian theory to the NMR of solids". In: *Phys. Rev. B* 25 (11 1982), pp. 6622–6632.

[282] T. P. Grozdanov and M. J. Rakovi ć. "Quantum system driven by rapidly varying periodic perturbation". In: *Phys. Rev. A* 38 (4 1988), pp. 1739–1746.

[283] Saar Rahav, Ido Gilary, and Shmuel Fishman. "Effective Hamiltonians for periodically driven systems". In: *Phys. Rev. A* 68 (1 2003), p. 013820.

[284] Saar Rahav, Ido Gilary, and Shmuel Fishman. "Time Independent Description of Rapidly Oscillating Potentials". In: *Phys. Rev. Lett.* 91 (11 2003), p. 110404.

[285] N. Goldman and J. Dalibard. "Periodically Driven Quantum Systems: Effective Hamiltonians and Engineered Gauge Fields". In: *Phys. Rev. X* 4 (3 2014), p. 031027.

[286] Andre Eckardt and Egidijus Anisimovas. "Consistent high-frequency approximation for periodically driven quantum systems". In: *ArXiv e-prints* (2015).

[287] Marin Bukov, Luca D'Alessio, and Anatoli Polkovnikov. "Universal high-frequency behavior of periodically driven systems: from dynamical stabilization to Floquet engineering". In: *Advances in Physics* 64.2 (2015), pp. 139–226.

[288] André Eckardt. "Colloquium: Atomic quantum gases in periodically driven optical lattices". In: *Rev. Mod. Phys.* 89 (1 2017), p. 011004.

[289] André Eckardt and Martin Holthaus. "Avoided-Level-Crossing Spectroscopy with Dressed Matter Waves". In: *Phys. Rev. Lett.* 101 (24 2008), p. 245302.

[290] M. Heyl and S. Kehrein. "Nonequilibrium steady state in a periodically driven Kondo model". In: *Phys. Rev. B* 81 (14 2010), p. 144301.

[291] Luca D'Alessio and Anatoli Polkovnikov. "Many-body energy localization transition in periodically driven systems". In: *Annals of Physics* 333 (2013), pp. 19 –33.

[292] Luca D'Alessio and Marcos Rigol. "Long-time Behavior of Isolated Periodically Driven Interacting Lattice Systems". In: *Phys. Rev. X* 4 (4 2014), p. 041048.

[293] P. Ponte et al. "Periodically driven ergodic and many-body localized quantum systems". In: *Annals of Physics* 353 (Feb. 2015), pp. 196–204.

[294] Marin Bukov et al. "Heating and many-body resonances in a periodically driven two-band system". In: *Phys. Rev. B* 93 (15 2016), p. 155132.

[295] Angelo Russomanno, Alessandro Silva, and Giuseppe E. Santoro. "Periodic Steady Regime and Interference in a Periodically Driven Quantum System". In: *Phys. Rev. Lett.* 109 (25 2012), p. 257201.

[296] Achilleas Lazarides, Arnab Das, and Roderich Moessner. "Periodic Thermodynamics of Isolated Quantum Systems". In: *Phys. Rev. Lett.* 112 (15 2014), p. 150401.

[297] Vladimir Gritsev and Anatoli Polkovnikov. "Integrable Floquet dynamics". In: *SciPost Phys.* 2 (3 2017), p. 021.

[298] Roberta Citro et al. "Dynamical stability of a many-body Kapitza pendulum". In: *Annals of Physics* 360 (2015), pp. 694 –710.

[299] Pedro Ponte et al. "Many-Body Localization in Periodically Driven Systems". In: *Phys. Rev. Lett.* 114 (14 2015), p. 140401.

[300] Achilleas Lazarides, Arnab Das, and Roderich Moessner. "Fate of Many-Body Localization Under Periodic Driving". In: *Phys. Rev. Lett.* 115 (3 2015), p. 030402.

[301] D. A. Abanin, W. De Roeck, and F. Huveneers. "Theory of many-body localization in periodically driven systems". In: *Annals of Physics* 372 (Sept. 2016), pp. 1–11.

[302] Marin Bukov et al. "Prethermal Floquet Steady States and Instabilities in the Periodically Driven, Weakly Interacting Bose-Hubbard Model". In: *Phys. Rev. Lett.* 115 (20 2015), p. 205301.

[303] Tomotaka Kuwahara, Takashi Mori, and Keiji Saito. "Floquet–Magnus theory and generic transient dynamics in periodically driven many-body quantum systems". In: *Annals of Physics* 367 (2016), pp. 96 –124.

[304] Takashi Mori, Tomotaka Kuwahara, and Keiji Saito. "Rigorous Bound on Energy Absorption and Generic Relaxation in Periodically Driven Quantum Systems". In: *Phys. Rev. Lett.* 116 (12 2016), p. 120401.

[305] Dmitry A. Abanin, Wojciech De Roeck, and François Huveneers. "Exponentially Slow Heating in Periodically Driven Many-Body Systems". In: *Phys. Rev. Lett.* 115 (25 2015), p. 256803.

[306] D. A. Abanin et al. "Effective Hamiltonians, prethermalization, and slow energy absorption in periodically driven many-body systems". In: *Phys. Rev. B* 95.1, 014112 (Jan. 2017), p. 014112.

[307] Elena Canovi, Marcus Kollar, and Martin Eckstein. "Stroboscopic prethermalization in weakly interacting periodically driven systems". In: *Phys. Rev. E* 93 (1 2016), p. 012130.

[308] Thomas Iadecola, Titus Neupert, and Claudio Chamon. "Occupation of topological Floquet bands in open systems". In: *Phys. Rev. B* 91 (23 2015), p. 235133.

[309] Daniel Vorberg et al. "Nonequilibrium steady states of ideal bosonic and fermionic quantum gases". In: *Phys. Rev. E* 92 (6 2015), p. 062119.

[310] G. Goldstein, C. Aron, and C. Chamon. "Driven-dissipative Ising model: Mean-field solution". In: *Phys. Rev. B* 92 (17 2015), p. 174418.

[311] T. Shirai et al. "Effective Floquet-Gibbs states for dissipative quantum systems". In: *New Journal of Physics* 18.5, 053008 (May 2016), p. 053008.

[312] T. Qin and W. Hofstetter. "Spectral functions of a time-periodically driven Falicov-Kimball model: Real-space Floquet dynamical mean-field theory study". In: *Phys. Rev. B* 96.7, 075134 (Aug. 2017), p. 075134.

[313] N. Goldman et al. "Periodically driven quantum matter: The case of resonant modulations". In: *Phys. Rev. A* 91 (3 2015), p. 033632.

[314] Takashi Oka and Hideo Aoki. "Photovoltaic Hall effect in graphene". In: *Phys. Rev. B* 79 (8 2009), p. 081406.

[315] Hernán L. Calvo et al. "Tuning laser-induced band gaps in graphene". In: *Applied Physics Letters* 98.23, 232103 (2011).

[316] Takuya Kitagawa et al. "Transport properties of nonequilibrium systems under the application of light: Photoinduced quantum Hall insulators without Landau levels". In: *Phys. Rev. B* 84 (23 2011), p. 235108.

[317] Eric Suárez Morell and Luis E. F. Foa Torres. "Radiation effects on the electronic properties of bilayer graphene". In: *Phys. Rev. B* 86 (12 2012), p. 125449.

[318] Netanel H. Lindner, Gil Refael, and Victor Galitski. "Floquet topological insulator in semiconductor quantum wells". In: *Nat Phys* 7.6 (2011), pp. 490–495.

[319] Netanel H. Lindner et al. "Topological Floquet spectrum in three dimensions via a two-photon resonance". In: *Phys. Rev. B* 87 (23 2013), p. 235131.

[320] Jérôme Cayssol et al. "Floquet topological insulators". In: *physica status solidi (RRL) – Rapid Research Letters* 7.1-2 (2013), pp. 101–108.

[321] Pierre Delplace, Álvaro Gómez-León, and Gloria Platero. "Merging of Dirac points and Floquet topological transitions in ac-driven graphene". In: *Phys. Rev. B* 88 (24 2013), p. 245422.

[322] Álvaro Gómez-León, Pierre Delplace, and Gloria Platero. "Engineering anomalous quantum Hall plateaus and antichiral states with ac fields". In: *Phys. Rev. B* 89 (20 2014), p. 205408.

[323] Y. H. Wang et al. "Observation of Floquet-Bloch States on the Surface of a Topological Insulator". In: *Science* 342.6157 (2013), pp. 453–457.

[324] Adolfo G. Grushin, Álvaro Gómez-León, and Titus Neupert. "Floquet Fractional Chern Insulators". In: *Phys. Rev. Lett.* 112 (15 2014), p. 156801.

[325] Liang Jiang et al. "Majorana Fermions in Equilibrium and in Driven Cold-Atom Quantum Wires". In: *Phys. Rev. Lett.* 106 (22 2011), p. 220402.

[326] Guocai Liu et al. "Topological superfluid transition induced by a periodically driven optical lattice". In: *Phys. Rev. A* 86 (1 2012), p. 013639.

[327] Qing-Jun Tong et al. "Generating many Majorana modes via periodic driving: A superconductor model". In: *Phys. Rev. B* 87 (20 2013), p. 201109.

[328] Manisha Thakurathi et al. "Floquet generation of Majorana end modes and topological invariants". In: *Phys. Rev. B* 88 (15 2013), p. 155133.

[329] Arijit Kundu and Babak Seradjeh. "Transport Signatures of Floquet Majorana Fermions in Driven Topological Superconductors". In: *Phys. Rev. Lett.* 111 (13 2013), p. 136402.

[330] Zi-bo Wang et al. "Floquet Majorana fermions in driven hexagonal lattice systems". In: *Solid State Communications* 215–216 (2015), pp. 18 –26.

[331] M. Thakurathi, D. Loss, and J. Klinovaja. "Floquet Majorana fermions and parafermions in driven Rashba nanowires". In: *Phys. Rev. B* 95.15, 155407 (Apr. 2017), p. 155407.

[332] Jelena Klinovaja, Peter Stano, and Daniel Loss. "Topological Floquet Phases in Driven Coupled Rashba Nanowires". In: *Phys. Rev. Lett.* 116 (17 2016), p. 176401.

[333] N. Fläschner et al. "Experimental reconstruction of the Berry curvature in a Floquet Bloch band". In: *Science* 352.6289 (2016), pp. 1091–1094.

[334] Mikael C. Rechtsman et al. "Photonic Floquet topological insulators". In: *Nature* 496.7444 (2013), pp. 196–200.

[335] Kejie Fang, Zongfu Yu, and Shanhui Fan. "Photonic de Haas-van Alphen effect". In: *Opt. Express* 21.15 (2013), pp. 18216–18224.

[336] Kejie Fang, Zongfu Yu, and Shanhui Fan. "Realizing effective magnetic field for photons by controlling the phase of dynamic modulation". In: *Nat Photon* 6.11 (2012), pp. 782–787.

[337] P. Roushan et al. "Chiral ground-state currents of interacting photons in a synthetic magnetic field". In: *Nat Phys* (2016).

[338] Jens Koch et al. "Time-reversal-symmetry breaking in circuit-QED-based photon lattices". In: *Phys. Rev. A* 82 (4 2010), p. 043811.

[339] M. H. Devoret. "Quantum Fluctuations in Electrical Circuits". In: *Fluctuations Quantiques/Quantum Fluctuations*. Ed. by S. Reynaud, E. Giacobino, and J. Zinn-Justin. 1997, p. 351.

[340] N. Jia et al. "Time Reversal Invariant Topologically Insulating Circuits". In: *Phys. Rev. X* 5 (2015), p. 021031.

[341] Victor V. Albert, Leonid I. Glazman, and Liang Jiang. "Topological Properties of Linear Circuit Lattices". In: *Phys. Rev. Lett.* 114 (17 2015), p. 173902.

[342] M. Serra-Garcia et al. "Observation of a phononic quadrupole topological insulator". In: *ArXiv e-prints* (Aug. 2017).

[343] S. Imhof et al. "Topolectrical circuit realization of topological corner modes". In: *ArXiv e-prints* (Aug. 2017).

[344] C. W. Peterson et al. "Demonstration of a quantized microwave quadrupole insulator with topologically protected corner states". In: *ArXiv e-prints* (Oct. 2017).

[345] Michael A. Nielsen and Isaac L. Chuang. *Quantum Computation and Quantum Information: 10th Anniversary Edition*. Cambridge University Press, 2010.

[346] F. Verstraete, J. J. García-Ripoll, and J. I. Cirac. "Matrix Product Density Operators: Simulation of Finite-Temperature and Dissipative Systems". In: *Phys. Rev. Lett.* 93 (20 2004), p. 207204.

[347] Adrian E. Feiguin and Steven R. White. "Finite-temperature density matrix renormalization using an enlarged Hilbert space". In: *Phys. Rev. B* 72 (22 2005), p. 220401.

[348] Thomas Barthel, Ulrich Schollwöck, and Steven R. White. "Spectral functions in one-dimensional quantum systems at finite temperature using the density matrix renormalization group". In: *Phys. Rev. B* 79 (24 2009), p. 245101.

[349] A. Nocera and G. Alvarez. "Symmetry-conserving purification of quantum states within the density matrix renormalization group". In: *Phys. Rev. B* 93 (4 2016), p. 045137.

[350] Steven R. White. "Density matrix formulation for quantum renormalization groups". In: *Phys. Rev. Lett.* 69 (19 1992), pp. 2863–2866.

[351] Steven R. White. "Density-matrix algorithms for quantum renormalization groups". In: *Phys. Rev. B* 48 (14 1993), pp. 10345–10356.

[352] U. Schollwöck. "The density-matrix renormalization group in the age of matrix product states". In: *Annals of Physics* 326 (Jan. 2011), pp. 96–192.

[353] Tomaz Prosen, Thomas H. Seligman, and Marko Znidaric. "Theory of Quantum Loschmidt Echoes". In: *Progress of Theoretical Physics Supplement* 150 (2003), pp. 200–228.

[354] A. Goussev et al. "Loschmidt Echo". In: *ArXiv e-prints* (June 2012).

[355] Erik Sjöqvist et al. "Geometric Phases for Mixed States in Interferometry". In: *Phys. Rev. Lett.* 85 (14 2000), pp. 2845–2849.

[356] O. Viyuela, A. Rivas, and M. A. Martin-Delgado. "Uhlmann Phase as a Topological Measure for One-Dimensional Fermion Systems". In: *Phys. Rev. Lett.* 112 (13 2014), p. 130401.

[357] Brian Swingle et al. "Measuring the scrambling of quantum information". In: *Phys. Rev. A* 94 (4 2016), p. 040302.

[358] O. Viyuela et al. "Observation of topological Uhlmann phases with superconducting qubits". In: *ArXiv e-prints* (July 2016).

[359] R. Islam et al. "Measuring entanglement entropy through the interference of quantum many-body twins". In: *ArXiv e-prints* (Sept. 2015).

[360] Luca D'Alessio et al. "From quantum chaos and eigenstate thermalization to statistical mechanics and thermodynamics". In: *Advances in Physics* 65.3 (2016), pp. 239–362.

[361] F. Borgonovi et al. "Quantum chaos and thermalization in isolated systems of interacting particles". In: *Physics Reports* 626 (2016). Quantum chaos and thermalization in isolated systems of interacting particles, pp. 1 –58.

[362] Takuya Kitagawa et al. "Topological characterization of periodically driven quantum systems". In: *Phys. Rev. B* 82 (23 2010), p. 235114.

[363] A. Gómez-León and G. Platero. "Floquet-Bloch Theory and Topology in Periodically Driven Lattices". In: *Phys. Rev. Lett.* 110 (20 2013), p. 200403.

[364] Mark S. Rudner et al. "Anomalous Edge States and the Bulk-Edge Correspondence for Periodically Driven Two-Dimensional Systems". In: *Phys. Rev. X* 3 (3 2013), p. 031005.

[365] Frederik Nathan and Mark S Rudner. "Topological singularities and the general classification of Floquet–Bloch systems". In: *New Journal of Physics* 17.12 (2015), p. 125014.

[366] L. J. Maczewsky et al. "Observation of photonic anomalous Floquet topological insulators". In: *Nature Communications* 8, 13756 (Jan. 2017), p. 13756.

[367] Cornelius Lanczos. "An iteration method for the solution of the eigenvalue problem of linear differential and integral operators". In: *J. Res. Natl. Bur. Stand. B* 45 (1950), pp. 255–282.

[368] Ernest R. Davidson. "The iterative calculation of a few of the lowest eigenvalues and corresponding eigenvectors of large real-symmetric matrices". In: *Journal of Computational Physics* 17.1 (1975), pp. 87 –94.

[369] J. Eisert, M. Cramer, and M. B. Plenio. "Colloquium: Area laws for the entanglement entropy". In: *Reviews of Modern Physics* 82 (Jan. 2010), pp. 277–306.

[370] U. Schollwöck. "The density-matrix renormalization group in the age of matrix product states". In: *Annals of Physics* 326 (Jan. 2011), pp. 96–192.

[371] R. Orús. "A practical introduction to tensor networks: Matrix product states and projected entangled pair states". In: *Annals of Physics* 349 (Oct. 2014), pp. 117–158.

[372] J. C. Bridgeman and C. T. Chubb. "Hand-waving and interpretive dance: an introductory course on tensor networks". In: *Journal of Physics A Mathematical General* 50.22, 223001 (June 2017), p. 223001.

[373] Shiing-Shen Chern and James Simons. "Characteristic Forms and Geometric Invariants". In: *Annals of Mathematics* 99.1 (1974), pp. 48–69.

[374] E. Witten. "Topological quantum field theory". In: *Communications in Mathematical Physics* 117 (Sept. 1988), pp. 353–386.

université PARIS-SACLAY

ÉCOLE DOCTORALE
Physique en île-de-France (EDPIF)

Titre: États de Floquet topologiques, champs de jauge artificiels dans des fluides quantiques fortement corrélés

Mots clés: Physique de la matière condensée, Phases topologiques, Systèmes fortement corrélés, Méthodes numériques, Simulateurs quantiques, Ingénierie de Floquet

Résumé: Dans cette thèse nous abordons des aspects topologiques de la matière condensée. Les états topologiques sont insensibles à un large spectre des perturbations externes et au désordre – une propriété indispensable dans le domaine d'information quantique. L'effet des interactions dans des systèmes topologiques est pourtant loin d'être bien maîtrisé à ce jour. Dans ce travail, nous étudions la corrélation entre la description topologique et l'effet des interactions. Afin d'accomplir notre but, nous utilisons des méthodes analytiques et numériques. Nous nous intéressons aussi à des sondes expérimentales qui peuvent être utilisées pour vérifier nos prédictions théoriques. Tout d'abord, nous étudions la version bosonique en interactions du modèle de Haldane – le modèle célèbre qui décrit l'effet Hall anomal. Nous proposons son implémentation expérimentale dans des circuits quantiques, basée sur l'application de perturbation périodique dépendantes du temps – méthodologie qui s'appelle l'ingénierie de Floquet. En poursuivant ces idées, nous étudions la version bosonique du modèle de Kane-Mele d'un isolant topologique. Ce modèle possède un diagramme de phase très riche. En particulier, lorsque les interactions sont fortes, nous observons l'apparition d'un modèle de magnétisme frustrée présentant une variété d'états exotiques. La mise en œuvre de ces modèles dans des réseaux d'atomes ultra-froids ou des circuits quantiques permettra de sonder expérimentalement les propriétés exotiques que nous avons observées. Ensuite, nous abordons d'une manière plus détaillée la réalisation expérimentale des modèles topologiques dans des circuits quantiques, en considérant le cas particulier du modèle de Su-Schrieffer-Heeger en couplage fort. Nous testons aussi des nouvelles sondes qui peuvent être utilisées afin de mesurer la phase de Zak et en déduire la topologie du système. Finalement, nous nous intéressons aux sondes hors d'équilibre et des méthodes pour tester les propriétés spectrales de systèmes quantiques, en utilisant l'approche de purification, pertinent pour le numérique et les expériences.

Title: Topological Floquet states, artificial gauge fields in strongly correlated quantum fluids

Keywords: Theoretical condensed matter, Topological phases, Strongly correlated quantum fluids, Numerical techniques, Quantum simulators, Floquet engineering

Abstract: In this thesis we study the topological aspects of condensed matter physics, that received a revolutionary development in the last decades. Topological states of matter are protected against perturbations and disorder, making them very promising in the context of quantum information. The interplay between topology and interactions in such systems is however far from being well understood, while the experimental realization is challenging. Thus, in this work we investigate analytically such strongly correlated states of matter and explore new protocols to probe experimentally their properties. In order to do this, we use various analytical and numerical techniques. First, we analyze the properties of an interacting bosonic version of the celebrated Haldane model – the model for the quantum anomalous Hall effect. We propose its quantum circuit implementation based on the application of periodic time-dependent perturbations – Floquet engineering. Continuing these ideas, we study the interacting bosonic version of the Kane-Mele model – the first model of a topological insulator. This model has a very rich phase diagram with an emergence of an effective frustrated magnetic model and a variety of symmetry broken spin states in the strongly interacting regime. Ultra-cold atoms or quantum circuits implementation of both Haldane and Kane-Mele bosonic models would allow for experimental probes of the exotic states we observed. Second, in order to deepen the perspectives of quantum circuit simulations of topological phases we analyze the strong coupling limit of the Su-Schrieffer-Heeger model and we test new experimental probes of its topology associated with the Zak phase. We also work on the out-of-equilibrium protocols to study bulk spectral properties of quantum systems and quantum phase transitions using a purification scheme which could be implemented both numerically and experimentally.

Université Paris-Saclay
Espace Technologique / Immeuble Discovery
Route de l'Orme aux Merisiers RD 128 / 91190 Saint-Aubin, France